People's Democratic Republic of Algeria
Ministry of Higher Education and Scientific Research
Echahid Cheikh Larbi Tebessi university



Faculty of Exact Sciences and Natural and Life Sciences

Department: Earth and Universe Sciences

Option: Applied Hydrogeology

Contribution of the Hydrogeological Study of Some Thermo-mineral Springs in the North-East of Algeria, Case study of Guelma, Souk Ahras, Tebessa, and Khenchela

Submitted in Partial Fulfillment of the Requirements for the Doctorate Degree (Third Cycle - LMD)

Prepared by: **Djaafri Ibtissem**

Jury members:

President:	Baali Fathi	Professor	Echahid Cheikh Larbi Tebessi University
Supervisor:	Seghir Karima	MCA	Echahid Cheikh Larbi Tebessi University
Examiner:	Boubaya Djamel	Professor	Echahid Cheikh Larbi Tebessi University
Examiner:	Boumezbeur Abderrahmane	Professor	Larbi Ben M'hidi, Oum El Bouaghi University
Examiner:	Bouaicha Foued	Professor	Constantine 1 – Frères Mentouri University

2024-2025



IN THE NAME OF ALLAH, THE MOST MERCIFUL AND MOST GRACIOUS

Acknowledgment

This journey would not have been possible without Allah, the Almighty, who opened the doors of success for me. I am deeply grateful for His guidance and blessings throughout this path.

First and foremost, I would like to express my heartfelt appreciation to Mrs. Seghir Karima, Associate Professor (Class A) at the Faculty of Earth Sciences at the University of Tebessa, for her invaluable guidance, patience, and oversight. Her scientific rigor and insightful advice have been instrumental in helping me successfully complete this work.

To Pr. Joel José Carrillo Rivera, to whom I am deeply grateful. Throughout all the years of developing this work, he stood by me with unwavering support. His help at any time, his patience, guidance, advice, generosity, and kindness were beyond measure. His impact will last forever, and his legacy will live on through the work he did. May Allah grant him Jannah.

I am sincerely appreciative of Pr. Baali Fethi, who has done me the great honor of serving as the chair of my jury.

I also extend my thanks to Pr. Boubaya Djamel, Pr. Boumezbeur Abderrahmane, and Pr. Bouaicha Foued, for agreeing to serve as members and examiners.

I would like to express my heartfelt gratitude to Mr. Vincent Valles from the Hydrogeology Laboratory at Avignon University, France, and to Mr. Laurent Barbiero from the Institute of Research for Development, Geoscience and Environment Toulouse, CNRS, University of Toulouse, France, for their invaluable help and assistance.

I would also like to express my sincere gratitude to Pr. Mr. Bouaicha Foued for the valuable documents he has always provided me.

Dedication

I dedicate this modest work to my dear parents, for everything they have done for me and for guiding me to be the person I am today. Their endless love and sacrifices have been my greatest source of strength.

To my beloved husband, for his steadfast support and help, and for being a good understander and my pillar of strength and encouragement until the very end, and to my little princess Yakine, who shared countless precious moments with me while I prepared this work, and to my dear son Amir, who shared this journey with me from within, though he left us at birth.

To my brothers, Aymen and Anis, and my sisters, Nardjesse and Soundous, who have stood by me every step of the way, offering love, support, and encouragement, and for always believing in me even during the toughest times.

To my entire family, your support and prayers have meant the world to me. And to my family-in-law, especially my mother-in-law, and to my dear father-in-law, may Allah accept him in His vast paradise.

To all my friends, and to everyone who has helped me, near or far, in the development of this modest work. I am also deeply grateful to all my professors at every level of my education. Thank you for your guidance, inspiration, and belief in me.

Djaafri Ibtissem

Abstract

Thermo-mineral springs are widely distributed across northeastern Algeria and represent both a natural resource and a potential sector for therapeutic and tourism development. These waters exhibit significant variability in temperature, discharge, and chemical composition, reflecting heterogeneous hydrogeological conditions. This study aims to characterize the regional variability of hydrothermal systems in Guelma, Souk Ahras, Khenchela, and Tebessa, and to interpret groundwater circulation within the framework of hierarchical flow systems. For the first time in this region, the conceptual model of gravitational groundwater flow systems defined by József Tóth is applied to interpret hydrothermal circulation patterns. The methodological approach combines classical hydrogeological investigation with the gravitational flow system theory, incorporating hydrochemical analyses, isotopic measurements of $\delta^{18}O$ and $\delta^{2}H$, characteristic ionic ratios, geothermometric estimations using Na/K, Na–Li, and Na–K–Ca geothermometers, and multivariate statistical analyses (principal component analysis and hierarchical cluster analysis). This integrated approach is used to identify the factors controlling water composition, the origin of recharge, and circulation pathways within hydrothermal units across a regional basin scale comprising hierarchical groundwater systems. Results show water temperatures ranging from 18 °C to 94.7 °C, and total mineralization varying from 424 mg/L in F6 (Khenchela) to 15,992 mg/L in S13 (Tebessa), reflecting contrasting circulation depths and degrees of water–rock interaction. Three dominant hydrochemical facies: calcium bicarbonate, calcium sulfate, and sodium chloride, which correspond to local, intermediate, and regional flow systems within the hierarchical groundwater circulation framework. Isotopic compositions confirm a meteoric origin for all thermal waters. Regionally, the Guelma province forms a distinct hydrothermal domain characterized by higher temperatures and specific mineralization patterns. Geochemical temperature estimations indicate that S7 (Guelma) and S13 (Tebessa) exhibit ion ratios and geothermometric signatures of chemically mature groundwater, suggesting prolonged circulation and stable hydrochemical evolution. This integrated framework enhances the understanding of hydrothermal processes and supports the sustainable development and management of geothermal resources in northeastern Algeria.

Keywords: Thermal springs; Hydrochemistry; Stable isotope; Gravitational flow systems; Regional hydrogeology; Principal component analysis (PCA)

Résumé

Les sources thermo-minérales sont largement répandues dans le nord-est de l'Algérie et représentent à la fois une ressource naturelle et un potentiel secteur de développement thérapeutique et touristique. Ces eaux présentent une variabilité importante en termes de température, de débit et de composition chimique, reflétant des conditions hydrogéologiques hétérogènes. Cette étude vise à caractériser la variabilité régionale des systèmes hydrothermaux dans les régions de Guelma, Souk Ahras, Khenchela et Tebessa, et à interpréter la circulation des eaux souterraines dans le cadre des systèmes d'écoulement hiérarchisés. Pour la première fois dans cette région, le modèle conceptuel des systèmes d'écoulement gravitaire des eaux souterraines défini par József Tóth est appliqué pour interpréter les schémas de circulation hydrothermale. L'approche méthodologique combine l'investigation hydrogéologique classique avec la théorie des systèmes d'écoulement gravitaire, en intégrant des analyses hydrochimiques, des mesures isotopiques de $\delta^{18}O$ et $\delta^{2}H$, des rapports ioniques caractéristiques, des estimations géothermométriques utilisant les géothermomètres Na/K, Na–Li et Na–K–Ca, ainsi que des analyses statistiques multivariées (analyse en composantes principales et analyse hiérarchique par regroupement). Cette approche intégrée est utilisée pour identifier les facteurs contrôlant la composition des eaux, l'origine de la recharge et les voies de circulation au sein des unités hydrothermales à l'échelle d'un bassin régional comprenant des systèmes d'eaux souterraines hiérarchisés. Les résultats montrent que les températures des eaux varient entre 18 °C et 94,7 °C et que la minéralisation totale varie de 424 mg/L dans F6 (Khenchela) à 15 992 mg/L dans S13 (Tebessa), reflétant des profondeurs de circulation contrastées et des degrés d'interaction eau–roche différents. Trois faciès hydrochimiques dominants : bicarbonate de calcium, sulfate de calcium et chlorure de sodium, qui correspondent respectivement aux systèmes d'écoulement local, intermédiaire et régional dans le cadre hiérarchique de la circulation des eaux souterraines. Les compositions isotopiques confirment une origine météorique pour l'ensemble des eaux thermales. À l'échelle régionale, la province de Guelma constitue un domaine hydrothermal distinct caractérisé par des températures plus élevées et des patterns de minéralisation spécifiques. Les estimations géothermométriques montrent que S7 (Guelma) et S13 (Tebessa) présentent des signatures d'eaux chimiquement matures, suggérant une circulation prolongée et une évolution hydrochimique stable. Ce travail intégré améliore la compréhension des processus hydrothermaux et soutient le développement durable et la gestion des ressources géothermiques dans le nord-est de l'Algérie.

***Mots-clés* :** ; Sources thermales ; Hydrochimie ; Isotopes stables ; Ecoulement gravitationnel ; Hydrogéologie régionale ; Composantes principales (ACP).

الملخص.

نتشر الينابيع الحرارية المعدنية على نطاق واسع في شمال شرق الجزائر، وتمثل موردًا طبيعيًا هامًا وقطاعًا واعدًا للتطوير العلاجي والسياحي. وتظهر هذه المياه تباينًا كبيرًا في درجات الحرارة والتدفق والتركيب الكيميائي، مما يعكس ظروفًا هيدروجيولوجية غير متجانسة. يهدف هذا العمل إلى دراسة الاختلاف الإقليمي للأنظمة الحرارية الجوفية في ولاية قالمة، سوق أهراس، خنشلة وتبسة، وتفسير مسارات الجريان الجوفي ضمن إطار الأنظمة الهرمية للجريان. ولأول مرة في هذه المنطقة، يُطبق النموذج التصوري لأنظمة الجريان الجوفي الجاذبي الذي حدده József Tóth لتفسير أنماط دوران المياه الحرارية .تجمع المنهجية بين الدراسة الهيدروجيولوجية التقليدية ونظرية نظام الجريان الجاذبي، مع دمج التحاليل الهيدروكيميائية، وقياسات النظائردالتا أكسيجين-18 $\delta^{18}O$ و دالتا ديتيريوم $\delta^{2}H$، والنسب الأيونية المميزة، والتقديرات الجيوحرارية باستخدام معايير Na/K و Na–Li و Na–K–Ca، بالإضافة إلى التحليل الإحصائي متعدد المتغيرات (التحليل بالمكوّنات الرئيسية والتحليل العنقودي الهرمي). وتُستخدم هذه المنهجية المتكاملة لتحديد العوامل التي تتحكم في تركيب المياه، وأصل التغذية، ومسارات الجريان داخل الوحدات الحرارية على نطاق حوض إقليمي يشمل أنظمة مياه جوفية هرمية. أظهرت النتائج أن درجات حرارة المياه تتراوح بين 18 °م و94.7 °م، وأن الملوحة الكلية تتراوح بين 424 ملغ/لتر في F6 (خنشلة) و15,992 ملغ/لتر في S13 (تبسة)، مما يعكس أعماق تدوير مختلفة ودرجات متفاوتة من تفاعل الماء مع الصخور. وتم تحديد ثلاث أنماط هيدروكيميائية رئيسية: بيكربونات الكالسيوم، كبريتات الكالسيوم، وكلوريد الصوديوم، تتوافق مع أنظمة الجريان المحلي، المتوسط، والإقليمي ضمن الهيكل الهرمي لتدوير المياه الجوفية. وتؤكد التراكيب النظيرية الأصل المطري لجميع المياه الحرارية. وعلى المستوى الإقليمي، تُعد ولاية قالمة نطاقًا حراريًا مميزًا يتسم بدرجات حرارة أعلى وأنماط ملوحة خاصة. وتشير التقديرات الجيوحرارية إلى أن العينتين S7 (قالمة) و S13 (تبسة) تظهران خصائص مياه ناضجة كيميائيًا، مما يدل على دوران طويل واستقرار في التطور الهيدروكيميائي .يساهم هذا الإطار المتكامل في تعزيز فهم العمليات الحرارية الجوفية ويدعم التنمية المستدامة وإدارة الموارد الجيوحرارية في شمال شرق الجزائر.

الكلمات المفتاحية : الينابيع الحرارية؛ الكيمياء المائية؛ النظائر المستقرة؛ أنظمة تدفق الجاذبية؛ الهيدروجيولوجيا الإقليمية؛ تحليل المكونات الرئيسية (PCA).

Table of Contents

General introduction **18**

Hydrogeological Characteristics of Thermal Springs: 21

A Classical Approach 21

Chapter One 22

I. Geographical Situation **1**

II. Spring's Location **1**

III. Physio-graphical Aspect **2**

IV. Hydrology **5**

V. Vegetation Cover **6**

VI. Climate **7**

VII. Conclusion **8**

Chapter Two 9

I. Introduction **10**

II. The Regional Geological Framework **11**

1. The Internal Domain 11

1. The Flysch Domain 11

II. The External Domain 11

1. The Tellian Nappes 12

2. The Para-autochthonous Foreland Domain 13

III. The Litho-stratigraphic Setting **13**

1. The Mesozoic 13

1.1 Trias 13

1.2 Jurassic 14

1.3 Cretaceous 15

2. The Cenozoic 19

2.1 Paleogene 19

2.2 Neogene 20

2.3 Quaternary 21

IV. Structural and Tectonic Setting **25**

I.1 Introduction to the Tectonic Context 25

1. Folds 27

2. Faults 28

I.2 Structural Tectonic Implications 30

a) **Hydrogeological Impact on Groundwater Flow and Storage** 30

b) **Potential Recharge Zones** 31

c) **Implications for Groundwater Quality and Mineralization** 31
IV.3 Hydrogeological Implication; Fault-Spring Relationship 31
V. Conclusion **34**
Chapter Three 35
I. Introduction **36**
II. Analysis of Climatic Factors **36**
II.1 Precipitation 36
1. Guelma 37
2. Souk Ahras 39
3. Tebessa 40
4. Khenchela 42
II.2 **Temperature** 43
1. Guelma 43
2. ***Souk Ahras*** 44
3. Tebessa 45
4. Khenchela 46
II.3 Temperature-Precipitation Relationships 48
1. The Ombrothermic Diagram 48
2. Determination of Aridity (De Martonne Index) 51
3. Determination of Soil Moisture (Euverte method) 52
III. Hydrological Balance **53**
III.1 Notion of Potential and Actual Evapotranspiration 54
III.1.1 Potential Evapotranspiration (PET) 54
III.1.2 Actual Evapotranspiration (A.E.T) 55
1. Turc's Formula 55
2. Water Balance According to the THORNTHWAITE Method 56
3. Runoff (R) 64
4. Water Infiltration (I) 64
5. The Depth of Runoff (E) 65
6. Interpretation of the Water Balance 65
IV. Conclusion **68**
Chapter Four 69
I. Introduction **70**
II. Hydrogeological Identification and Characterization of Aquifers **70**
1. The Region of Guelma 70
1.1 The Alluvial Aquifer of Guelma 71

1.1.1 The Lower Terrace (the current aquifer) 71
1.1.2 The Upper Terrace (the ancient aquifer) 71
1.1.3 The Middle Terrace (the travertine limestone aquifer) 71
1.2 The Aquifer of the Carbonate Formations of Heliopolis-Fedjoudj 73
1.3 The Aquifer of Carbonate Formations: Region of Ras El Agba-Sellaoua-Announa 74
1.4 The Aquifer of Carbonate Formations in the Bouhachana–Ain Larbi Region 75
2. The Region of Souk Ahras 75
2.1 Shallow Aquifer in Mio-Plio-Quaternary Formations 75
2.2 Heterogeneous Aquifers in Eocene and Oligocene Formations 76
2.3 Deep Confined Aquifer in Maastrichtian-Campanian Formations 76
2.4 Triassic Evaporites Aquifer 76
2.5 Jurassic Carbonate Aquifer 76
3. The Region of Tebessa 79
3.1 The plain of Tebessa 79
3.2 The plain of Morsot- El Aouinet 83
3.3 The plain of El-Meridj-El Ouanza 84
4. The Region of Khenchela 86
4.1 The Quaternary aquifer 87
4.2 The Miocene aquifer 87
4.3 The Cretaceous aquifer 87
III. Cross-Regional Findings **90**
1. Aquifer Types 90
2. Flow Patterns 92
3. Hydraulic Gradients 92
4. Recharge Zones 92
5. Condition at the Emergence of Thermal Waters **93**
a. Spring of Hammam Ouled Ali (S1) 93
b. Spring of the Cascade 1(S2) 95
c. Spring of Hammam Guerfa (S5) 97
d. Spring of Hammam Belhacheni (S6) 97
e. Spring of Hammam N'bails (S7) 98
f. Spring of Hammam (Ouled Zaid) Ouled Driss (S10) 99
g. Spring of Hammam Tessa (S11) 100
h. Spring of Hammamet (S12): (Borehole) 100
i. Spring of Hammam Sidi Yahia (S13) 101
j. Spring of Hammam Salhine (S14) 102

k. Spring of Hammam Knif (S15) ... 103
6. Conclusion ... **105**
Chapter Five ... 106
Section One ... 107
I. Introduction ... **108**
II. Study of Physico-Chemical, Statistical, and Isotopic Analyses ... **108**
1. Methodology and Materials ... 108
1.1. Sampling and Field Measurements ... 108
2. Study of Physico-Chemical Parameters: ... 110
2.1 Temperature (T°C) ... 110
2.2 Hydrogen Potential (pH) ... 111
2.3 Conductivity (µs/cm) ... 111
2.4 Mineralization ... 112
2.5 Total Dissolved Solids TDS (mg/l) and Salinity ... 113
2.6 Alkalinity ... 114
2.7 Chemical Characteristics ... 115
3. Chemical Facies ... 124
3.1 Stabler Classification ... 124
3.2 Piper Diagram ... 125
3.3 Schoeller-Berkaloff Classification ... 128
4. Saturation Index ... 130
5. Temperature Influence on Mineral Saturation : ... 132
6. Principal Geochemical Processes: Binary Diagrams ... 134
a) Na^+/Cl^- ... 134
b) HCO_3^-/Ca^{2+}, HCO_3^-/Mg^{2+} ... 135
c) SO_4^{2-}/Ca^{2+} ... 137
d) $Ca^{2+} + Mg^{2+}/HCO_3^- + SO_4^{2-}$ ... 137
e) HCO_3/SO_4 ... 138
7. Principal Components Analysis and Hierarchical Components Analysis (PCA, HCA) ... 139
7.1 Principal Components Analysis (PCA) ... 139
7.2 Hierarchical Components Analysis (HCA) ... 146
7.3 Principal Component Analysis of the Combined Dataset ... 148
7.3.1 Data Preprocessing: Normality and Distribution Check ... 148
7.3.2 Principal Component Analysis Results ... 150
7.4 Agglomerative Hierarchical Clustering of Regional Hydrogeochemical Profiles ... 153
8. Contribution of Water Stable Isotopes: δ^2H and $\delta^{18}O$ ... 154

8.1 Introduction 154
8.2 Concepts of d-excess and ^{17}O-excess 154
8.3 Diagram of $\delta^{18}O/\delta^{2}H$ and Groundwater Origin 157
Section two 159
I. Geothermometry **160**
1. Reliability of Geothermometers 160
2. Chemical Geothermometers 161
2.1 Geothermometer of Na-k: 161
2.2 Geothermometer of Na-Li 161
2.3 Geothermometer of Mg-Li 162
2.4 Geothermometer of Na-K-Ca 162
3. Geothermal Gradient 163
4. Estimation of Groundwater Circulation Depths and Temperatures 164
5. Thermal Water Depth and Temperature of the Reservoir: Plotting the Results 168
5.1 General Trends Across All Geothermometers 168
6. Cross-Validation of Geothermometer Reliability Through Index of Maturity and Ternary Diagrams 171
6.1 Maturity Index 171
6.2 Ternary Diagram of Giggenbach Na-K-$Mg^{1/2}$ 171
6.3 Ternary Diagram of SO4-Cl-HCO3 173
6.4 Interpretation and Hypotheses 175
III. Conclusion **176**
Gravitational Flow Systems in Modern Hydrogeology: **180**
Insights from Tóth's Theory and Application **180**
I. History and Definition **182**
II. Groundwater Flow Theory: Basic Concepts and Practical Applications **183**
A. The Basic Concepts: The Sub-Theory of the "Hydraulics of Basin-Scale Flow Systems": 183
1. Flow Patterns in Unit Basins and Their Extension to Complex, Composite Basins: 183
B. The Practical Utilization: The Sub-Theory of the "Geologic Agency of Flow Systems" . 185
B.1 Chemical Processes 186
B.2 Physical Processes 187
B.3 Kinetic or transport processes 187
III. Groundwater Flow Theory: A Fundamental Paradigm Change in Hydrogeology **188**
IV. Gravitational groundwater flow system and the science of hydrogeology **189**
V. From Recharge to Discharge: The Study Zone from a Tothian Perspective **192**
V.1 Practical Utilization: Data Projection and Analysis of Primary Indicators 192

A. Surface Indicators of Groundwater 192
B. Chemical Indicators 196
V.2 Innovations in Groundwater Analysis 199
A. Influence of Faults 200
B. Conceptual Model 202
VI. Conclusion **205**
General Conclusion **207**
References **209**
Appendices **221**

List of Figures

Figure 1. Geographical situation map and Springs' locations 1
Figure 2. The major watersheds of the North-East of Algeria and the spring locations 6
Figure 3. Major Geological Domains with Active Faults in Northern Algeria (Yelles-Chaouche et al., 2022) 10
Figure 4. Synthetic Cross-Section of Maghrebides in Eastern Algeria (Constantinois Region) (Vila, 1977) 12
Figure 5. Excerpt of the Geological Map of the Northern Part of the Study Area (after Vila, 1978) 23
Figure 6. Excerpt of the Geological Map of the Khenchela Region (after Geological Map of Algeria, 1977, Sheet N°203) 24
Figure 7. Rose Diagram of Fault Direction in the Study Zone 30
Figure 8. Map of Faults Density of the Northern Part of the Study Zone 31
Figure 9. Fault - Spring Map. According to the Geological Map of Vila, 1978 33
Figure 10. Fault - Spring Map of the Khenchela Region (Digitized from Satellite Imagery) 33
Figure 11 Precipitation Map of the Study Area for 2021 (Ordinary Kriging, GEE Data) 37
Figure 12 Monthly average precipitation in the Guelma Region (2000-2022) 38
Figure 13 Annual Average Precipitation in the Guelma Region (2000-2022) 38
Figure 14. Monthly average precipitation in the Souk Ahras region (2000-2022) 39
Figure 15. Annual average precipitation in the Souk Ahras region (2000-2022) 40
Figure 16 Monthly Average Precipitation in the Tebessa Region (2000-2022) 41
Figure 17 Annually Average Precipitation in the Tebessa Region (2000-2022) 41
Figure 18 Monthly Average Precipitation in the Khenchela Region (2000-2022) 42
Figure 19 Annual Average Precipitation in the Khenchela Region (2000-2022) 42
Figure 20 Monthly Average Temperature in the Guelma Region (2000-2022) 43
Figure 21 Annual Average Temperature in the Guelma Region (2000-2022) 44
Figure 22 Monthly Average Temperature in the Souk Ahras Region (2000-2022) 44
Figure 23 Annual Average Temperature in the Souk Ahras Region (2000-2022) 45
Figure 24 Monthly Average Temperature in the Guelma Region (2000-2022) 45
Figure 25 Annual Average Temperature in the Tebessa Region (2000-2022) 46
Figure 26 Monthly Average Temperature in the Khenchela Region (2000-2022) 46
Figure 27 Annual Average Temperature in the Khenchela Region (2000-2022) 47
Figure 28 Ombrothermic Diagram of the Guelma Region (2000-2022) 48
Figure 29 Ombrothermic Diagram of the Souk Ahras Region (2000-2022) 49
Figure 30 Ombrothermic Diagram of the Tebessa Region (2000-2022) 49
Figure 31 Ombrothermic Diagram of the Khenchela Region (2000-2022) 50
Figure 32 Evaluation of Soil Moisture Using the Euvrete Method 52
Figure 33 Graphic Representation of Thornthwaite's Water Balance Sheet of the Guelma Region (2000-2022) 57
Figure 34 Graphic Representation of the Hydrological Balance of the Guelma Region (2000-2022) 57
Figure 35 Graphic Representation of Thornthwaite's Water Balance Sheet of the Souk Ahras Region (2000-2022) 59
Figure 36 Graphic Representation of the Hydrological Balance of the Souk Ahras Region (2000-2022) 59
Figure 37 Graphic Representation of Thornthwaite's Water Balance Sheet of the Tebessa Region (2000-2022) 61
Figure 38 Graphic Representation of the Hydrological Balance of the Tebessa Region (2000-2022) 61
Figure 39 Graphic Representation of Thornthwaite's Water Balance Sheet of Khenchela Region (2000-2022) 63
Figure 40 Graphic Representation of the Hydrological Balance of the Khenchela Region (2000-2022) 63
Figure 41 Piezometric Map of the Alluvium Aquifer of Guelma, April 2009 (Benmarce, 2015) 72

Figure 42 Hydrogeological Cross-Section in the Guelma Plain (Gaud, 1974)..... 73
Figure 43 Hydrogeological Cross-Section of the Taoura Region (Djabri et al., 2020)..... 77
Figure 44 Piezometric Map of the Shallow Aquifer (Djabri et al., 2020)..... 78
Figure 45 Boundary Conditions and Flow Directions in the Plain of Tebessa (Rouabhia et al., 2010)..... 81
Figure 46 Piezometric and Geologic Map of the Plain of Tebessa (February 2022)(Saad et al., 2024)..... 82
Figure 47 Hydrogeological Cross-Section Across the Plain of Tebessa (Saad et al., 2024)..... 83
Figure 48 Piezometric Map (2006) of the Morsot-El Aouinet Plain (Fehdi et al., 2011)..... 84
Figure 49 Piezometric Map of El-Meridj-El-Ouanza Region (2016)(Stamboul, 2017)..... 86
Figure 50 Piezometric Map of the Quaternary (Boubelli, 2017)..... 88
Figure 51 Piezometric Map of the Miocene (Boubelli, 2017)..... 89
Figure 52 Piezometric Map of the Cretaceous (Boubelli, 2017)..... 90
Figure 53 Geological Cross-Section of Hammam Ouled Ali (Vila et al., 1986)..... 94
Figure 54 Hydrogeological Cross-Section of Hammam Ouled Region (Gaud 1947)..... 94
Figure 55 Geological Cross-Section of Hammam Debegh (S2) in Dib H, 1985)..... 96
Figure 56 Geological Cross-Section of Hammam Knif (In Dib H, 1985)..... 104
Figure 57 Field Equipment for Water Sampling and Alkalinity Titration Process..... 110
Figure 58 Spatial Variation of Conductivity Concentration (µS/cm) in the study zone at 25°C..... 112
Figure 59 Spatial Variation of Calcium Concentration (mg/l) Across Study Zones..... 115
Figure 60 Spatial Variation of Magnesium Concentration Across the Study Zone..... 116
Figure 61 Spatial Variation of Bicarbonate Concentration Across the Study Region..... 117
Figure 62 Spatial Variation of Chloride Concentration Across the Region..... 118
Figure 63 Spatial Variation of Sodium Concentration Across the Study Zone..... 119
Figure 64 Spatial Variation of Potassium Concentration Across the Study Zone..... 120
Figure 65 Spatial Variation of Sulfate Concentration Across the Study Zone..... 121
Figure 66 Spatial Variation of Nitrates Concentration Across the Study Zone..... 122
Figure 67 Spatial Variation of Strontium Concentration Across the Study Zone..... 123
Figure 68 Spatial Variation of Lithium Concentration Across the Study Zone..... 124
Figure 69 Chemical Facies of Waters Across the Region According to Stabler Classification (2018- 2019)..... 125
Figure 70 Piper Diagram of Groundwater Samples from the First Sampling Campaign (2018)..... 126
Figure 71 Piper Diagram of Groundwater Samples from the Second Sampling Campaign (2019)..... 126
Figure 72 Schoeller-Berkaloff Diagram Comparing the Hydrochemical Profiles of the 2018 Samples in the Study Area..... 129
Figure 73 Schoeller-Berkaloff Diagram Comparing the Hydrochemical Profiles of the 2019 Cold and Thermal Samples in the Study Area..... 129
Figure 74 Temperature vs Saturation Index for the Following Minerals: Calcite (a), dolomite (b), anhydrite (c), aragonite (d), gypsum (e), strontianite (f), halite (g)..... 133
Figure 75 Ionic Ratio Plot of Cl^-/Na^+ for All Samples..... 135
Figure 76 Ionic Ratio Plot of HCO_3^-/ Ca^{2+} for All Samples..... 136
Figure 77 Ionic Ratio Plot of HCO_3^-/Mg^2 for All Samples..... 136
Figure 78 Ionic Ratio Plot of Ca^{2+}/SO_4^{2-} for All Samples..... 137
Figure 79 Ionic Ratio of $Ca^{2+} + Mg^{2+}$ vs $HCO_3^- + SO_4^{2-}$ for All Samples..... 138
Figure 80 Ionic Ratio of SO_4^{2-} vs HCO_3 for All Samples..... 139
Figure 81 Histogram of Eigenvalues and Cumulative Variability..... 141
Figure 82 Principal Component Analysis Biplot of PC1 and PC2..... 145
Figure 83 Distribution of Samples Plot According to PC1 and PC2..... 146
Figure 84 Hierarchical Cluster Dendrogram of All Water Samples in the Study Region..... 147

Figure 85 Quantile - Quantile (Q-Q) Plots of Electrical Conductivity (EC) and Nitrate (NO_3^-) Before and After Logarithmic Transformation. (a) Raw EC, (b) Raw NO_3^-, (c) Log-transformed EC, (d) Log-transformed NO_3^- 150
Figure 86 Distribution of pH, Temperature, Log (EC), and Log (Concentration) in the Score Plots: (a)PC1-PC2 and (b) PC3-PC4 152
Figure 87 Distribution of Samples in the Factorial Plots: (a) PC1-PC2 and (b) PC1-PC3 152
Figure 88 Agglomerative Hierarchical Dendrogram of Regional Sample Groups Based on Hydrochemical Similarity 153
Figure 89 δ^2H vs $\delta^{18}O$ of Thermal Waters in the Study Zone, GMWL is the Global Meteoric Water Line, WMMWL is the Western Mediterranean Meteoric Water Line 158
Figure 90 Geothermal Gradient Map of the North-East of Algeria (Adapted from Bouchareb-Haouchine, 2012) 164
Figure 91 Plots Illustrating the Depth and Temperature of Thermal Waters in the Study Area 170
Figure 92 Giggenbach 1988 Ternary Diagram for All Water Samples 172
Figure 93 Cl-SO4-HCO3 Ternary Diagram (Giggenbach, 1988) Showing the Position of the Water Samples from the Study Area 173
Figure 94 General Groundwater Flow System Conceptual Model 184
Figure 95 Overview of the Historical Evolution of the Science of Hydrogeology 190
Figure 96 Surface Geological Framework of The Study Area Showing Spring Locations, Major Faults, and The Position of the Cross-Section (Figure 100) 195
Figure 97 The Schematic Diagram of Groundwater Flow Systems Illustrates Various Processes and Manifestations. The Flow Order, Local, Intermediate, and Regional, is represented by Green, Red, and Black Flowlines, respectively. The two Red Areas Signify Internal Water Traps, While the Yellow Area Indicates a Basin Floor. The Scale is determined by the geological Framework 197
Figure 98. Hydrochemical facies classification using the Piper Diagram 198
Figure 99 Effects of Barrier Fault on Groundwater Flow Patterns in the Unit Basin:(a) vertical fault, (b) horizontal fault, (c) fault dipping opposite to the direction of regional flow, (d) fault dipping in the direction of regional flow (Toth J, 2009) 201
Figure 100 Effect of Faults on Groundwater Flow Patterns in the Unit Basin : (a) vertical fault, (b) horizontal fault, (c) fault dipping opposite to the direction of regional flow, (d) fault dipping in the direction of regional flow (Toth J, 2009) 202
Figure 101 N - S Cross-Section of the Region Illustrating the Hierarchical Flow Systems (credit by Tatiana Aguilar Castillo) 203
Figure 103. Cascade of Guelma highlights (Appendices) 229

List of Tables

Table 1. Spring Projected Coordinates (WGS84 / UTM Zone 32N) 2
Table 2. Monthly average precipitation in the Guelma region (2000-2022) 37
Table 3. Monthly average precipitation in the Souk Ahras region (2000-2022) 39
Table 4. Monthly average precipitation in the Tebessa region (2000-2022) 40
Table 5. Monthly average precipitation in the Khenchela region (2000-2022) 42
Table 6. Monthly average of temperature of Guelma region (2000-2022) 43
Table 7. Monthly average of temperature of Souk Ahras region (2000-2022) 44
Table 8. Monthly average temperature in the Tebessa region (2000-2022) 45
Table 9. Monthly average temperature in the Khenchela region (2000-2022) 46
Table 10. Aridity index according to De Martonne 51
Table 11. Classification of climate type according to aridity index values 51
Table 12. Classification of types of regimes according Euverte method 52
Table 13. Variation of P/T ratio values in the study zone 52
Table 14. Correlation coefficient of each month 54
Table 15. Water balance for Guelma region (2000 to 2022) 56
Table 16. Water balance for the Souk Ahras region (2000-2022) 58
Table 17. Water balance for the Tebessa region (2000-2022) 60
Table 18. Water Balance of Khenchela Region (2000-2022) 62
Table 19. Estimation of runoff across the region 64
Table 20. Estimation of water infiltration across the region 65
Table 21. Estimation of the depth of runoff across the region 65
Table 22. Variation of pH in the study zone 111
Table 23. Classification of water samples by mineralization levels 113
Table 24. Salinity and TDS variation in the study zone (2018/2019) 114
Table 25. Alkalinity measurements: TA and TAC for thermal waters 114
Table 26. The calculated index of saturation SI 130
Table 27. Descriptive statistics for the study parameters of the second campaign 141
Table 28. Eigenvalues and percentage of explained variance by factorial axes from PC1 to PC13 142
Table 29. Different variables and PCs 142
Table 30. Correlation matrix between parameters (high values are in bold) 143
Table 31. Descriptive statistics for the study parameters of the combined dataset 149
Table 32 Shapiro-Wilk test results for Raw and Log-transformed distributions of (EC) and (NO_3^-) 149
Table 33. Correlation matrix of hydrochemical parameters 151
Table 34. Eigenvalues and variance contribution of principal components PC1 to PC4 152
Table 35. Isotopic measurements and excess values for oxygen and hydrogen isotopes 155
Table 36. Estimated temperature in °C in the study zone by different chemical geothermometers 166
Table 37. Estimation of the depths of deep reservoirs in the study area 167
Table 38. Estimation of the depths of deep reservoirs in the study area 167
Table 39. Calculation of Maturity Index of all samples in the Study area 171
Table 40. Calculated Mineralization of all samples (Appendices) 221
Table 41. Air Temperature in the region of Guelma during the preiod 2000 to 2022 downloaded from GEE (Appendices) 222
Table 42. Precipitation of the region of Guelma during the period 2000 to 2022 according to GEE (Appendices) 223
Table 43. Air temperature of the Souk Ahras region in the period from 2000 to 2022(Appendices) 224
Table 44. Precipitation of the region of Souk Ahras from 2000 to 2022 (Appendices) 224

Table 45. Air temperature of the region of Tebessa from 2000 to 2022 (Appendices) 225
Table 46. Precipitation data of Tebessa from 2000 to 2022 (Appendices)..... 226
Table 47. Air temperature of Khenchela region from 2000 to 2022 (Appendices) 226
Table 48. Precipitation of Khenchela region during 2000 to 2022 (Appendices) 227

List of Photos

Photo 1. The spring of Hammam Ouled Ali (S1) (2019)..... **Erreur ! Signet non défini.**
Photo 2. The thermal spring (S2) of Hammam Debegh (The Cascade 1) (2019)..... **Erreur ! Signet non défini.**
Photo 3. The thermal spring of Hammam Guerfa (S5) (2018) ..... **Erreur ! Signet non défini.**
Photo 4. The thermal spring of Hammam Belhecheni (S6) (2018)..... 98
Photo 5. The thermal station of Hammam Ouled Driss (S10) (2018) ..... **Erreur ! Signet non défini.**
Photo 6. The thermal station of Hammam Tessa (S11) (2019) ..... **Erreur ! Signet non défini.**
Photo 7. Thermal water discharge from the Hammamet (S12) borehole (2018)..... **Erreur ! Signet non défini.**
Photo 8. The thermal station of Sidi Yahia (S13) (2019) ..... **Erreur ! Signet non défini.**
Photo 9. The thermal station of Hammam Salhine (2019) ..... **Erreur ! Signet non défini.**
Photo 10. Geothermal steam room and bath from Hammam Knif (2019)..... **Erreur ! Signet non défini.**

General Introduction

General introduction

﴿أَوَلَمْ يَرَ الَّذِينَ كَفَرُوا أَنَّ السَّمَاوَاتِ وَالْأَرْضَ كَانَتَا رَتْقًا فَفَتَقْنَاهُمَا ۖ وَجَعَلْنَا مِنَ الْمَاءِ كُلَّ شَيْءٍ حَيٍّ ۖ أَفَلَا يُؤْمِنُونَ﴾

[الأنبياء: 30]

English - Sahih International

21:30 Have those who disbelieved not considered that the heavens and the earth were a joined entity, and We separated them and made from water every living thing? Then will they not believe?

The Qur'an, in Surah Al-Anbiya (21:30), reminds us: “And We made from water every living thing. Then will they not believe?” This verse summarizes the profound truth that water is the origin and sustainer of all life, a gift and necessity that has no equal. Without water, life as we know it would not exist, and its presence shapes our planet and sustains every ecosystem.

Water is mankind's most precious resource, unique in its properties and invaluable in its role. It is the only substance on Earth that exists naturally in all three states: liquid, solid, and gaseous, demonstrating a versatility that has allowed it to sculpt landscapes and create fertile grounds for life. Though composed of one of the smallest molecules, water has an immense influence on geological and ecological systems, carving rivers, eroding mountains, and nurturing soil.

Despite being thoroughly studied, water still holds mysteries that inspire curiosity and investigation. Known as the "Blue Gold," it remains a focus of scientific inquiry worldwide. Researchers continue to unravel the secrets of water, from its molecular properties to its vast global cycle, to better understand how this essential substance sustains life and shapes our world.

Among Earth's water resources, groundwater is particularly valuable. The term groundwater is generally reserved for the subsurface water found beneath the water table in soils and geologic formations that are fully saturated. Groundwater constitutes about 30% of the world’s fresh water, making it the second-largest source of fresh water after glaciers and polar ice caps. Stored in vast underground aquifers, it plays an essential role in sustaining rivers, wetlands, and springs, especially during dry periods.

Given its vital importance, a clear and logical understanding of groundwater's functioning and effective management is paramount. Groundwater not only serves as the primary source of water in many arid and semi-arid regions, but it also provides a more protected and reliable source than surface water, particularly in areas with scarce precipitation or pollution concerns.

Thermal springs are natural discharges of groundwater that have been heated within the subsurface, mainly due to the geothermal gradient and, in some cases, proximity to magmatic or tectonic activity. As infiltrating meteoric water circulates to greater depths through fractures and permeable geological formations, it acquires heat and dissolves minerals from the surrounding rocks. This process results in waters with diverse temperatures and chemical compositions that reflect the geological context and depth of circulation (Arnorsson S, 2000; Boden, 2016). Because of their mineral content and elevated temperatures, thermal springs have long been valued for bathing and traditional therapeutic uses (Porowski, 2019; Toth J, 2009). They also provide important information for understanding groundwater flow systems, geothermal processes, and subsurface water–rock interaction ((Fournier, 1991).

The structure of this thesis is divided into two main parts. The first part, comprising five chapters, covers the foundational aspects of the study, including a description of the study area, climatology, geological framework, hydrogeology, and hydrochemistry, all examined through classical hydrogeological methods. The second part is dedicated exclusively to modern hydrogeological approaches, specifically the application of Tóth's Gravitational Groundwater Flow System Theory. While many previous studies on thermal springs in the region have focused on individual provinces, our study is unique in examining these systems across northeastern Algeria as a whole, integrating the Tóthian perspective for the first time in this area. This original approach aims to provide a comprehensive understanding of the hydrothermal characteristics across the region, which is essential for the sustainable management and development of these valuable water resources.

This naturally leads us to fundamental questions that this research seeks to address:

- What are the key hydrogeological and hydrochemical characteristics of the thermo-mineral springs in the northeastern regions of Algeria, and how do they vary within and among the different hydrothermal units?
- What geochemical and isotopic indicators reveal about the recharge sources, processes, and interconnected nature of the thermo-mineral waters across the four provinces?
- To what extent do the thermo-mineral springs across the four northeastern provinces of Algeria exhibit signs of a cohesive hydrothermal system?
- How does Toth's flow system theory help explain the origin, circulation, and emergence conditions of the thermal waters in the study area, and what does this suggest about potential regional-scale hydrothermal connectivity?

Through addressing these questions, this thesis aims not only to advance our scientific understanding of northeastern Algeria's hydrothermal systems but also to contribute to the sustainable management of these vital water resources.

Part I

Hydrogeological Characteristics of Thermal Springs: A Classical Approach

Chapter One

The Description of the Study Area

I. Geographical Situation

Located in the northeastern part of Algeria, the region comprising Gulema, Souk Ahras, Tebessa, and Khenchela is home to numerous springs of significant flow and vital importance, and these springs are the focus of our study. To simplify matters, the geographical limits chosen for the study area form a rectangle with the following approximate coordinates: N 36.851666°, E 8.400806°, S 35.242649°, and W 6.824964°, and cover about 20,000 Km^2 of surface. It occupies a central part of the four wilayas (Figure 1). These latter are part of the Tellian Atlas and the Saharian Atlas of Algeria and demonstrate an integrated geographical relationship by forming a network of borders where the presence of the others determines the boundaries of one wilaya. Because of their proximity to one another and their interconnection, the four territories' geographical arrangement has an impact on each state's natural resources, transportation, socioeconomic and development operations, and more, on the geological framework, and on environmental management.

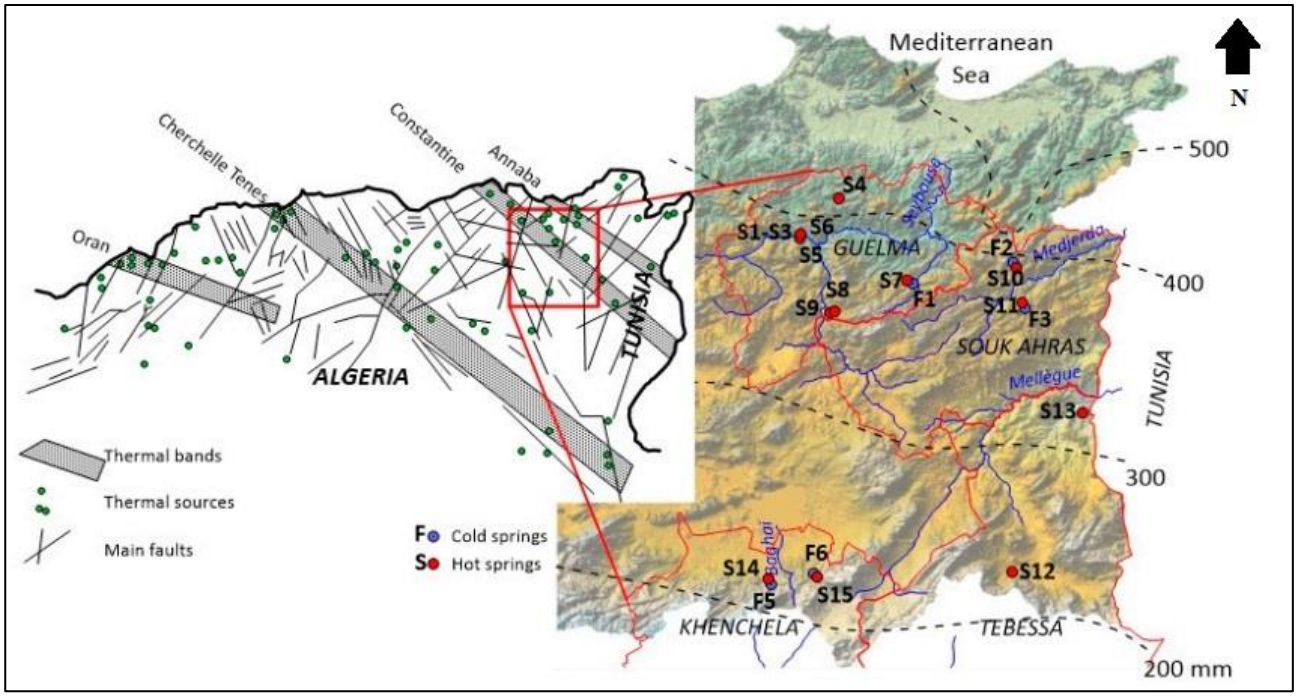


Figure 1. Geographical situation map and Springs' locations

II. Spring's Location

The following factors were taken into account while selecting the dispersed springs for this study: relevance to the research objectives, ecological value, hydrological significance, diversity of geography, water quality and quantity, and feasibility of the research; to study the subject on a regional scale concerning the continuing geological media, which may enhance the understanding of the

aquifer's behavior and determine if they are connected naturally or have similarities. Sampling of the representative samples took place within these coordinates (Table 1) to adequately depict the characteristics and spatial distribution of the chosen springs, while cold springs were sampled for reference purposes.

Table 1. Spring Projected Coordinates (WGS84 / UTM Zone 32N)

Springs	ID	X	Y	Z	Springs	ID	X	Y	Z
Ouled Ali	**S1**	355223.76	4048993.3	223	**H. Tessa**	**S11**	414187.97	4010088.57	628
Cascade 1	**S2**	344928	4036340	315	**Hammamet**	**S12**	405459.24	3923486.47	
Ain chfa	**S3**	344939	4036473	299	**Sidi Yahya**	**S13**	430937	3973789	513
Cascade 2	**S4**	345116.18	4036350.57	303	**H. Salhine**	**S14**	326282.54	3923292.88	1086
Guerfa	**S5**	350876	4012622	661	**H. Knif**	**S15**	341462	3928488	338
Belhacheni	**S6**	350566	4011295	728	**N'bails F**	**F1**	377957	4020683	504
H. N'bails	**S7**	378369	4020961	476	**Ain Souda**	**F2**	411450	4024388	850
C.interne	**S8**	344681	4035229	372	**Tessa F**	**F3**	414729	4008923	681
C.externe	**S9**	344669	4035201	367	**Silene**	**F5**	326370	3923037	1123
Ouled Driss	**S10**	411463.11	4024375.89	828	**Mosque**	**F6**	341297	3928584	1019

III. Physio-graphical Aspect

The orography of the study zone is characterized by a diversified relief, between plains, hills, and mountains, each with its own morphological characteristics and geological structures. The region of Guelma is known by a mountainous cover of 37.82%, whereas the highest peaks are Mohouna, which rises 1411 m; Houara, with 1292 m; Taya (Bouhamdane), with 1208 m; and Debegh, with 1060 m.

To the northwest, the last steep limestone slopes of the Debar (1060 m) sink into the softer marl or sandstone formations. Moving westward, the Djebel Taya limestone chain divides the Oued Bouhamdane basin to the south and the Oued Safsaf basin to the north. The western part comprises very varied reliefs, ranging from the wide and deep valley of the Cherf Wadi upstream, which flows from south to north, from the high plains of the region of Ain Makhlouf, Ras El Agba (700–800 m) to the deep valleys of Guelma downstream.

The south of Guelma includes the central chain of the Medjerda, where the important massif of Ras El Alia is imposed. A sequence of Eocene limestone entablements, of which Djebel Bardou (1261m) and Djebel Zouara (1292m) are the principal ones. To the south-east, the high chain continues with the Senonian limestone massifs of Djebel El Arous (1160m) and the Eocene limestone of Djebel Safiet, then by the mountains of Ain Seynour covered by the Numidian sandstone. The

whole massif constituting the high central chain of the Medjerda mountains plunges under the plains of Sellaoua.

Eastward, the wooded peaks of the Medjerda Mountains' northern slopes—including kef Erramoul (797m) and kef Djemmel (812m)— drop abruptly in steps to the Seybouse Wadi Valley. Most of the slope is covered by the thick Numidian clayey sandstone formation that characterizes the landscape up to the Algerian-Tunisian border. The peaks are rounded without sharp edges, and the massive shapes and valleys are shallow. It is the same for the Triassic formations of Ain Seynour-Nador, which rise in massive cliffs above the plain of Bouchegouf.

Beyond the northern boundaries of the area in question, to the north, are the Ain Berda mountains, which divide the Guelma depression from the Lake Fetzara depression. The rest of the relief is composed of (27.22%) plains and plateaus, (26.29%) hills and foothills.

To the east lies the wilaya of Souk Ahras, characterized by a predominantly hilly region with rugged peaks and deep valleys. The northern part, averaging 1000 meters in altitude, is mountainous, forested, and consists of 12 communes covering an area of 1,879.58 km². In contrast, the southern part, with an average altitude of 650 meters, comprises high plains and pastureland, covering 14 communes over an area of 2,480.07 km².

The province is characterized by two distinct geomorphological features:

- The northern part, north of Oued Medjerda, is characterized by very rugged mountainous terrain, from east to west and from north to south, the mountains encountered are:

Aïn Zana, M'Cid, El Hammam, Guern Djedi, Medjene, Koudiet ben Ahmed, Bouallegue, Boubakouch.

- The southern part extends from the Sidi Lehmissi station (near the Algerian-Tunisian border) in the east to Djebel Zaarouria in the west. Its relief is formed from east to west by:
  Djebel Graout, Mesla, Bou Rzine, Ouled Soltane, Boukebch and Zaarouria.

To the north of Djebel Graout lies the Oued el Berriche – Oued Medjerda basin, while to the south extends the Merahna – Taoura basin.

To the south of Souk Ahras, the wilaya of Tebessa appears distinguished by mountains that comprise a continuous chain with peaks that range in elevation from about 1000 to 1700 meters. They extend from west to east, and represent in fact the main Atlasic tectonic structures of the region; (Djebel Bouziane 1308 m, Djebel Tazbent 1252 m, Djebel Mestiri 1274 m, Djebel Dokkane, and Djebel Troubia) dispersed over a considerable area, and occupying almost 40% of the land.

The relief in the northern part of the Tebessa consists of isolated, steep-form massifs (Djebel Ouenza 1200 m, Djebel Harraba 1060 m) as well as slightly sloping domes (Djebel Dyr 1472 m) rising over vast plains with height fluctuations of 400–510 meters.

The Djebel Ouenza is a massive anticline, oriented NE-SW that rises to a height of roughly 1200 meters. Above all, the Djebel Meridef (780 m) has a short, Aptian-aged blade that is extremely straightened and goes in a NE-SW orientation. It is divided by a longitudinal fault that descends the SE portion. It has a remarkable resemblance to Djebel El Ouenza and is impacted by three injections of Triassic.

In the middle, the Tebessa plain corresponds to a sizable collapse basin that slices the folds of the S-NE axis orthogonally. The sinking of the graben was inevitably followed by large fractures that dislocated these old structures. At an average elevation of 800 meters, the vast plain is bordered on two sides by rough mountains, high limestone masses (Bou Roumane, 1545 meters), and rocky ridges, which are crossed by mountains of Bekkaria and Tenoukla.

Regarding plains, one of the Serdies is a large, open basin in a strong Emscherian marl series, bordered to the south by Djebel Troubia and to the west by the straight ridges of Djebel Serdies, and demonstrates a plain shape caused by erosion.

As a result of accumulation, the dextral component of the highest Plio-Quaternary pressure has caused the Hammamet Plain, which is situated in a subsiding graben, to be heavily sedimented by Quaternary-age deposits.

Meanwhile, the Tebessa Plain is full of recent sediments from the Quaternary period, which are mostly made up of clays, marls, limestone pebbles, and fine to medium sand. The Tebessa - Hammamet Plain's Quaternary filling map reveals abundantly that these strata's thickness has reached 550 meters in the plain's center.

Finally, the Khenchela wilaya lies right next to the western limit of Tebessa, at the foothills of the Aures massifs, with the highest peak in eastern Algeria, the Chelia Mountain (2,326 m amsl), and is characterized by four major geographical sets, which are listed below:

- The mountains: They are mainly found in the western part of the wilaya (the Aures), in the central area (the Nememchas mountains; Djebel Dokhana 1,712 m), and in the northeast (Ain-Touila; Djebel Tefrent 1,349 m amsl).
- The plateaus: They cover the communes of Mahmel and Ouled Rechache and are situated in the northeast (O. Rechache plateau).

- The plains: these structures are located in the north and northwest of the wilaya; they include Remila, Bouhmama, and M'toussa. It should be noted that these last two sets are sometimes called the high plains.
- The steppe landscape and depressions, which cover 56% of the natural terrain of the province they are located in the southern part of Khenchela. They are characterized by sandy lands and the presence of chotts. These chotts serve as the convergence points for the wadis draining the southern part of the wilaya.

IV. Hydrology

This area is part of four drainage basins (Figure 2): **a**) the Seybouse, which covers 6471 km^2, has five dams, and approximately 181 boreholes scattered throughout the basin mobilize a volume of 82 hm^3/year, and 35 among them are not exploited. 66% of the mobilized volume is destined to alimentation in drinking water, whereas 8% to industries supply, and 26% to irrigation. covers about 7 wilayas (Annaba, El Tarf, Skikda, Oum El Bouaghi, Constantine, Souk Ahras and Guelma), sixty-eight (68) municipalities; where thirty-three (33) of them are totally included and the rest of thirty-five (35) are only partially included, the basin is characterized by twenty-five (25) points of precipitation's measuring data that gives information that the pluviometry of the region is ranging between an average of 450 mm at South, to 735 mm at North according to ABH (2002) assessment, **b**) the Coastal Center Constantinois basin, which covers 5582 km^2, presenting a section from the Coastal Constantinois watershed that covers 11.509 Km^2, the basin is divided into one hundred thirty-two (132) municipalities and ten (10) wilayas. Eighty-eight (88) municipalities are entirely within the watershed, while forty-four (44) are partially included. Precipitation increases from south to north, measuring an average between 650 and 1200 mm. The Coastal Center Constantinois basin is the wettest, with rainfall sometimes reaching 1800 mm. Across the entire Constantine coastal basin, there are forty-five (45) rainfall stations and twelve (12) hydrometric stations monitored by the National Agency for Water Resources (ANRH). For the period 2004-2007, the basin has seven (7) boreholes that serve as measurement points for water quality. **c**) the basin that flows from the High Plateaus of Constantinois, which covers 9615 km^2, is composed of seventy-six (76) municipalities and five (5) wilayas. Thirty-four (34) municipalities are entirely within the basin, while forty-two (42) are partially included. Precipitation increases from east to west, averaging between 318 mm in the eastern part of the basin and 700 mm in the west. Across the entire High Plateaus of Constantinois, there are seventeen (17) rainfall stations and six (06) hydrometric stations, also monitored by the National Agency for Water Resources (ANRH). and **d**) the Medjerda-Mellegue basin, which covers 7942 km^2. (Hydrographic basins agency Constantinois-Seybouse- Mellegue, 2009), and divided into four (04)

wilayas are partially included within the basin, and according to (Derradji, 2023); the annual average precipitation ranges from 374.74 mm in Tebessa to 716.86 mm in Souk Ahras, and it has four (4) points of water quality measurements.

These watersheds are traced by a very developed hydrographic network with large wadis such as: Seybouse, Oued El Kebir West, Oued Bounamoussa, Oued El Kebir East, Oued Medjarda, Oued Mellegue, and Oued Baghai, all of them have internal drainage network except for Oued Mellègue and Oued Medjarda which drain part of Tunisia, except for Seybouse, which has an East-West direction upstream before becoming straight with a South-North direction downstream, the majority of the valleys are oriented South-North; however, some wadis in Khenchela flows to the South towards the chotts (Guaraet et tarf) which represent extensive zones with continuous groundwater discharge that merge with outflow from wadis in the South of the state.

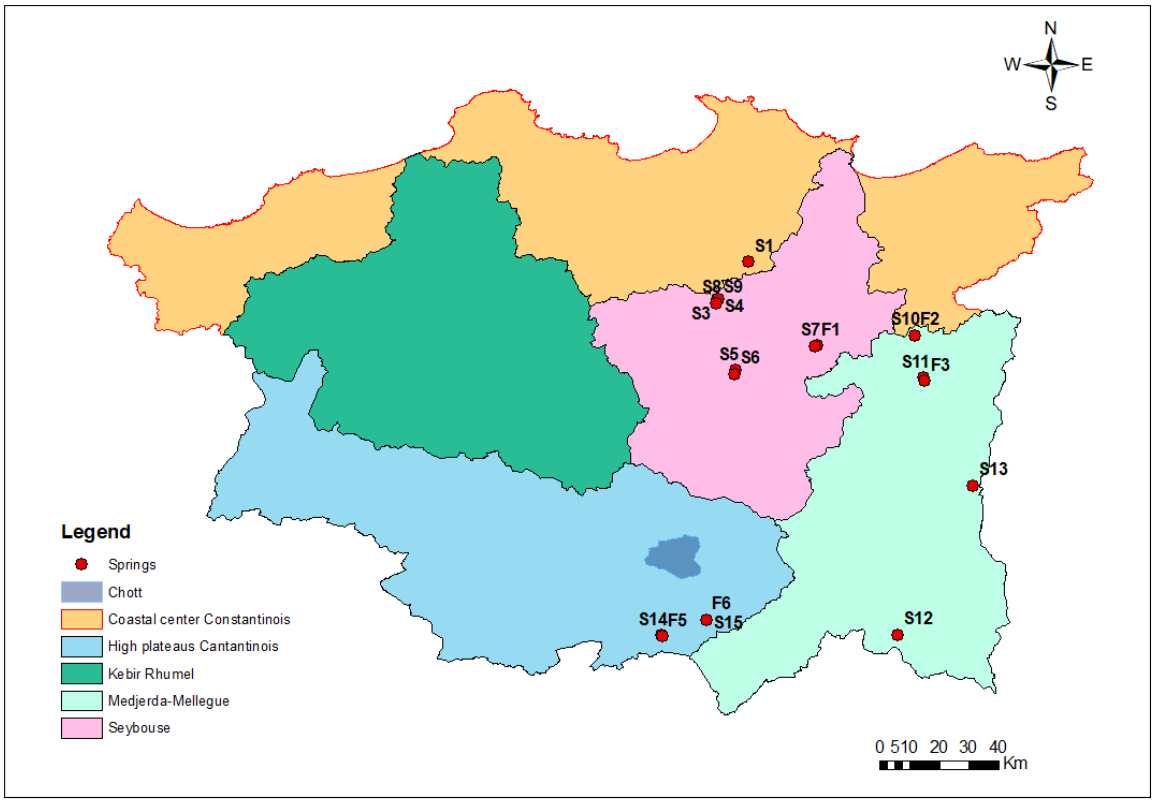


Figure 2. The major watersheds of the North-East of Algeria and the spring locations

V. Vegetation Cover

Despite environmental factors like the chemical and physical characteristics of the soil and topographic considerations like high slope, the vegetation cover is fairly diverse, it is differentiated

from the north by a highly dense cover with woody forests locally known as Oued Soudan Forest, Bouredine Forest, Ouarda Forest, Ben Mezzline Forest, Beni Ahmed Forest, and El Hachani Forest, etc. Elevation decreases gradually towards the south, where vegetation diverges to trees, shrubs, and perennial plants according to varied natural conditions. At the high plains, it is common to find low vegetation as Armoise or Chih (Artemisia Alba), Guetaf (Atriplex), Salsola, and Jujubier (Zizyphus). From plains and plateaus to depressions classification of the following is well known as Tarfa (Tamarix), R'tem (Retama), Aleppo Pine, Cedar, Holm Oak, Black Pine, Cypress, Ash, there are also palm trees, juniper, willow, jujube, tamarind, and fruit trees (apple, pomegranate, apricot, pear, fig, olive, almond, etc. A mention might be made about the types of roots in vegetation. In the south the plants are predominantly deep rooted which could have a direct relation to the hydraulic elevation.

VI. Climate

From a climatic perspective, the area is divided into the northern and central parts, which have Mediterranean and continental climates, respectively. These regions are distinguished by a cold, humid winter that lasts from October to May, followed by a dry, hot summer for the rest of the year. Figure 3 in chapter two shows an example of the annual precipitation of the year 2021. The southern region's persistent aridity hints at an almost desert-like climate.

Climatic data refers to a broad spectrum of meteorological parameters, including precipitation, temperature, wind patterns, evapotranspiration, and more. These data points serve as vital indicators of the atmospheric conditions within the region over time. They offer invaluable insights into climate variability, trends, and potential impacts on ecosystems, agriculture, and human activities.

Accurate data on the several variables influencing climate variability are necessary for any hydroclimatological investigation. In our country there are two main factors, one is linked to altitude and thus to the effect of continentality; it is a geographical factor, and the other is related to the Saharan bottom and the Mediterranean bottom; it is a meteorological factor.

Let us recall that our study area is part of the following watersheds: the Seybouse, covering 6471 km^2 with an average of 450 mm at South, to 735 mm at North of precipitation, the Coastal Center Constantinois basin, which covers 5582 km^2, with an average between 650 mm and 1200 mm of precipitation, besides the High Plateaus of Constantinois spans an area 9615 km^2, and presents 318 mm in the eastern part of the basin and 700 mm in the west, and finally the Medjerda-Mellegue basin occupying 7942 km^2, and characterized by an average of precipitation from 374.74 mm to 716.86 mm according to the ANRH database.

VII. Conclusion

The study area is defined by its varied topography, which includes the mountainous regions of Guelma and the Medjerda ranges of Souk Ahras, alongside the plateaus and plains of Tebessa and Khenchela. Coupled with a semi-arid climate and extensive watersheds featuring a developed hydrographic network, these characteristics significantly influence variations in water quality, storage capacities, and recharge rates, thereby shaping the region's hydrogeological profile.

The watershed, as a fundamental unit controlling water flow across the terrain, is essential for hydrological studies. By integrating climatic data with watershed assessments, researchers can uncover intricate relationships between rainfall patterns, surface runoff, groundwater recharge, and water quality. This comprehensive approach enhances our understanding of hydrological processes, facilitating informed decision-making in water resource management, land use planning, and environmental conservation.

Chapter Two

The Geological Settings

I. Introduction

Geological data are among the primary surface elements to analyze for understanding the structure and history of a region, and are of primordial importance to understand groundwater flow systems and the aquifer functioning. The geology serves as the host for groundwater. The type, structure, and composition of geological formations determine the storage, movement, quantity, and quality of groundwater, making it a critical factor in understanding and managing water resources.

The geological framework of Algeria can be divided into two main structural units (Figure 3). In the north, the Tellian domain is characterized by the Alpine chain, also known as the Maghrebides, and the Atlas chain, which together define the region's general geology. To the south lies the Saharan platform, separated from the northern part by the South-Atlas Flexure (Fabre, 1976). The geological context further controls the presence, water flow, and direction of groundwater flow, and its physicochemical characteristics; the interaction of groundwater with tectonic activity, surface water and climate are also relevant, due mainly to the developed geomorphological features, permeability of the media, and basement rock depth which in turns control the position of the water-table (Toth, 2009). Several authors have contributed their research to the geological studies of the area in question, such as Darest de la Chavane. J.C. (1909, 1910), Durand Delga (1955), Vila J.M. (1966, 1980), Lahondère. J. C. (1987), Chouabi. A.M (1987), R. Laffitte (1939), R. Guiraud (1973), C.G.G. (1969), B. Houha (1996 et 2007), Raoult. J. F. (1974),

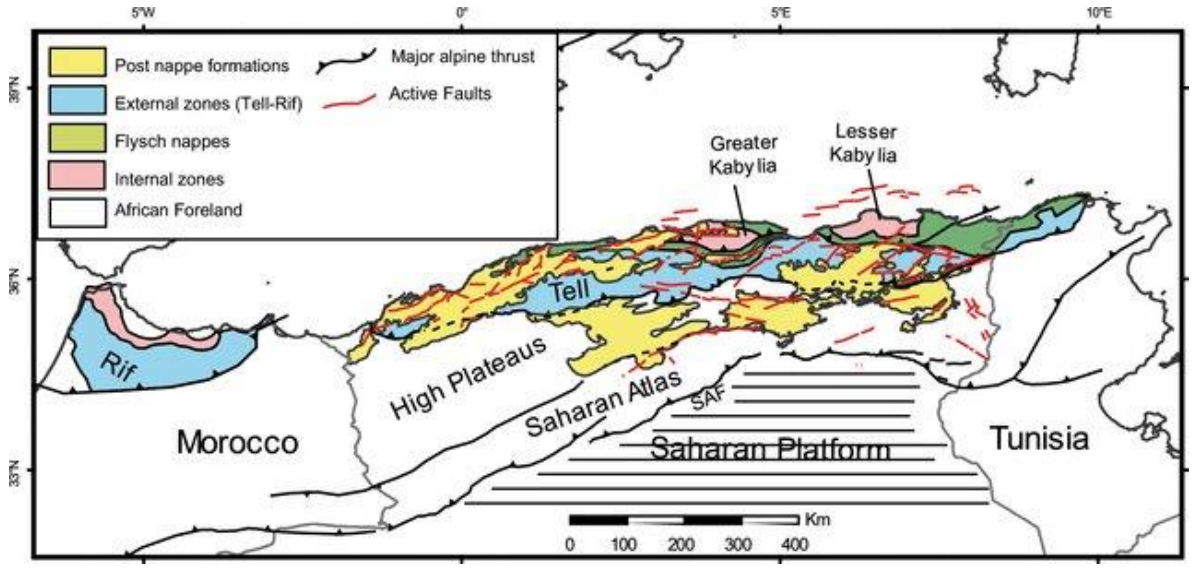


Figure 3. Major Geological Domains with Active Faults in Northern Algeria (Yelles-Chaouche et al., 2022)

II. The Regional Geological Framework

Several structural units have been identified by geologists working in Eastern Algeria, arranged from north to south: (Figure 4)

1. The Internal Domain

According to Ben Ali et al. (2014), it contains the Kabyle basement of variable nature and its sedimentary cover from the Paleozoic to the Tertiary; it is bounded to the south by the Kabyle basement or limestone chain.

1. The Flysch Domain

In the context of sedimentation, a flysch is a sequence of sedimentary rocks commonly deposited in deep marine environments, frequently on a base resembling oceanic crust. Two flysch species are distinguished from each other: the Mauritanian and the Massylian flysch, which vary from one another with respect to their environment and source material. The Numidium, which spans the Oligocene to the lower Burdigal Period, covers the entire region. These sequences are named after their facies.

1.1.1 Flysch Mauritanian

These geological series feature alternating layers of clay (soft), limestone, and sandstone (harder), creating multiple hard and soft rock pairs. The sequence begins with Dogger-Malm red radiolarites and ends with the Paleocene conglomerate layer.

1.1.2 Flysch Massilyan

It contains a pelito-quartzitic series of Lower Cretaceous age overlain by a pelito-micro-brecciated series of Upper Cretaceous age, with a significant portion of marls and clays. The hard beds (sandstone and limestone) are very thin and do not prevent erosion.

1.1.3 Flysch Numidian

It corresponds to the upper unit and is characterized by an Oligo-Aquitanian sandstone flysch, extending into the Burdigalian.

II. The External Domain

It is located south of the flysch domain and corresponds to the formations of the northern margin of the African plate. The basement rock of the Tellian domain does not outcrop anywhere and is probably of continental crust type. Some authors as (Vila J. M, 1980) consider the Edough Massif to be the basement of the external domain. The latter includes the units of the Tellian nappe and the foreland units of the Tellian domain (Chabbi, 2017). The Tellian units form a complex stack of nappes

with southward vergence, overlying the pre-Saharan autochthon of the high plains to the south (high and rigid zones that separate the coastal ranges from the Saharan Atlas).

1. The Tellian Nappes

2.1.1 The Ultra-Tellian Nappes

Cretaceous- Lutecian are composed of Cretaceous formations which are generally light in color, and refer to the series that are abnormally superimposed on the Neritic Cretaceous of the Constantinois in the Djebel Debar and Douar Bouzitoune areas in the Guelma region, as designated by Durand Delga in 1969. and were defined at Djebel Bou-Sba, north of the province, by Vila (1986).

2.1.2 The Tellian Sensu-Stricto Nappes

Triassic- Lutetian consists of dark Cretaceous and Eocene formations, and comprises a complex stack of carbonate nappes.

- Tellian nappe of Hammam Ouled Ali.
- Tellian nappe of Ras El Agba-Sellaoua Announa region: constituted by the Tellian unit with Globigerina, and the Tellian nummulites unit.

2.1.3 The Peni-Tellian Nappe

Lias – Eocene are composed of neritic Eocene facies very similar to the pre-Saharan autochthonous.

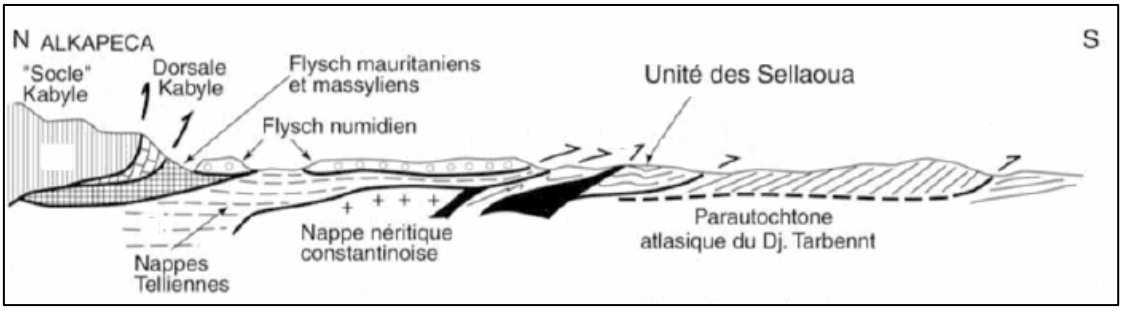


Figure 4. Synthetic Cross-Section of Maghrebides in Eastern Algeria (Constantinois Region) (Vila, 1977)

2. **The Para-autochthonous Foreland Domain**: Is represented by:
   a) The Neritic Constantinois nappe (Vila J.M. 1980, Chadi M. 1991),
   b) The scaled domain of the Sellaoua (Voute 1967)
   c) The north-Auresian domain. (Chabbi 2017).

III. The Litho-stratigraphic Setting

A general description of the lithological composition of the geological units in the area includes formations from Triassic to Quaternary ages (Figures 35 and 36). A basic stratigraphical column of the region in question is as follows:

1. The Mesozoic

1.1 Trias

The start will be with the region of Guelma; It forms the study area's oldest terrain. It is mostly evaporitic and can be seen as injected sheets along fault lines and large diapiric outcrops in the eastern region and south of Bouchegouf. The Triassic formations of the Nador N'Bails and Mechrouha region are composed of a combination of sandstones, cargneules, dolomites, and dolomitic limestones, all enveloped in red clays and gypsums. (Chouabi 1987). According to (J.M. Vila 1972), as is the case of south of the Nador station, over the Neogene molasses of the Guelma basin, the Triassic strata frequently emerge in an overthrust position over the surrounding terrains. A detailed investigation of the contours reveals that the Triassic formations mark the abnormal connections that resulted in the creation of the large molassic basin of Guelma (Chouabi 1987). similar to the case of the Mechrouha-Ain Tahmamine basin.

Elsewhere, in the next wilaya, the Triassic outcrops are located around the town of Souk Ahras, to the North; those of Nador N'bails and Mechroha (mentioned earlier) are considered parts of the diapiric zone by some authors (Perthuisot et al., 1978) and as allochthonous Triassic units (nappe zones) by others (Vila, 1980; Chouabbi). These formations typically show NE-SW-oriented bands over about ten (10) kilometers, shifting to a nearly North-South direction at the western end.

In the Tebessa wilaya, it's represented by well-developed formations that form the calcareous and clayey substrate. As well as diapiric injections dislocating the overlaying formations, outcropping at the edge of Tebessa-Morsott's basin and in the Bekkeria area (Djebel Djebissa), Bir Dheb (Djebel Belkfif), and to the north of Morsott.

these formations are characterized by the presence of red clay, fragmented crystals with limestone and dolomite lenses, outcrops in the North and South of Hammamet. Meanwhile, the 1/50000 geological map shows that it outcrops around Youkous-les-bains (Othmamine 1987)

At Djebel Ouanza, which is an anticline trending NE-SW, three diapiric injections of Triassic formations converge. One of these diapirs is emplaced along an NE-trending fault, extending from the base to the peak of the mountain.

Finally, these outcrops are numerous and highly localized around Khenchela, where they separate Miocene from Cretaceous layers along a 4-5 km long and 300-400 m wide strip. Notably, in the Djebel El Krouma and Djebel Knif areas, they are in abnormal contact with the Albian, Cenomanian, and Coniacian layers.

The most commonly encountered mineral is gypsum, which can be found as white to greyish saccharoid masses or big crystals. The amount of salt present is notable, especially in the diapirs of Khenchela and Krouma.

The most common rocks at these outcrops are varicolored clays and marls, ranging in color from greenish to reddish to purplish. Additionally, there are well-stratified calcareous-dolomitic layers, usually gray to black, sometimes with marly interbeds, frequently found within the Triassic complexes.

1.2 Jurassic

It is absent in outcrops and in oil drillings in the Algerian-Tunisian border region (Dubourdieu, 1956; Chevenine et al., 1989). However, nearby, between Guelma and Souk-Ahras in the Hammam N'Bail basin, it appears with dolomitic outcrops. At Djebel Nador, there are Middle Lias protrusions considered tectonic (David, 1956). These outcrops are part of a sedimentary horizon (Vila, 1980). North of Guelma, the Jurassic appears at Djebel Debar, the eastern continuity of the neritic platform of Constantine (Vila and Magne, 1969; Durand-Delga, 1969). Furthermore, in the Aures region, it is characterized by a significant development of carbonate facies (dolomitic limestone), sometimes clayey (clay shales, and siliceous and berchic clayey limestone). These formations sometimes contain intercalations of yellow and red marls, with thicknesses reaching up to 400 meters. The total thickness of these deposits in the region can be estimated at 4000 to 6000 meters.

1.3 Cretaceous

a) Guelma

At Douar Bou-Zitoune, outcrops of ***Neocomian*** formations, near Hiliopolis village, are represented by dark limestones, sometimes micritic and/ or dolomitic. These limestones form very thick banks and show an east-west alignment over 2.5km. They are surmounted in concordance by the complete marly series of the *Middle and Upper Cretaceous* (Dareste de la Chavane, J.C. 1910).

Towards the east and west ends of this strip of limestone of the *Lower and Middle Neocomian*, the *Middle and Upper Cretaceous* series, formed of marls and marl-calcareous rocks, appear stretched and compressed in such a way that the calcareous ones with *Senonian* inocerams come to rest almost directly on the *Neocomian* limestones (Dareste de la Chavane, J.C., 1910).

These phases of stretching and detachment of strata seem to be at the origin of the update of the mineralization (calamine (mixture of zinc oxide and ferric oxide), galena, antimony, and barite), which appear mainly at the two ends of this limestone massif, especially in Hammam Berdaa. Two other small outcrops of limestone similar to the previous are observed west of Heliopolis.

Barremian formations outcrop about 4km southwest of the city of Guelma on the right bank of the Seybouse, as well as in the ravine of Châbet El Biade, near Dra El Krouche and Djebel Bou Sba (Vila, J. M. et al., 1968). They are represented mainly by marls and marl-limestones and covered to the west by sandstone; while to the north and east, they are covered by gypsy clays and molasses of the *Miocene,* as well as by the *Pliocene* travertines of Guelma.

The ***Aptian*** formations are visible at Koudiat Enchir, Djebel Djabana, and Bou Zitoune. These formations consist of blue-gray limestone, sometimes oolitic, with beds reaching up to 6 meters thick. Above them are thicker layers of micritic blue limestone containing a diverse fauna.

In addition, the ***Albian*** formations outcrop on the southeast slope of Djebel Bou Sba. They consist of black or gray schistose marls. These marls contain small beds of blackish or greenish micritic limestone towards the top. The microfauna, which is sparse in these formations, is mainly represented by rare Hedbergella fossils (Lahondère, J. C., 1987).

But the ***Vraconian*** formations are represented by about ten meters of green marls interspersed with decimetric beds of green micritic limestone. Sometimes, the Vraconian formations begin with thick beds of blueish micritic limestone containing radiolarians. The Vraconian formations outcrop at the eastern end of Djebel Debagh (Lahondère, J. C., 1987).

The ***Cenomanian*** begins with an alternation of small decimetric beds of green micritic limestone and green marls. The significance of the green marl levels increases towards the top of the series. This initial sequence can exceed 50 meters in thickness. The upper parts of this stage become more marly, with micritic limestone beds spaced more than 1 meter apart, while the green hues remain. The thickness of this upper sequence varies between 10 and 20 meters (Lahondère, J. C., 1987). The Cenomanian outcrops to the west of Djebel Bou Sba (Vila J. M., 1980).

The ***Turonian*** is represented by very reduced limestone formations containing debris of sea urchins, inoceramids, and melobesians. These Turonian limestones outcrop at Kef Hahouner (Raoult, J. F., 1974).

The formations of the ***Coniacian*** are difficult to separate. They are represented by alternations of biomicrites and marls, which become more prominent at the top (Lahondère, J. C., 1987).

Meanwhile, the ***Santonian*** outcrops at Djebel Bou Sba. It is represented by layered blue marls at the base, overlain by greenish clayey marls (Lahondère, J. C., 1987).

Campanian formations outcrop to the southwest of Guelma at Koudiat Djebissa. It begins with bluish marls that include levels of biomicrite, which become more frequent towards the top of the series. The thickness is around 100 meters. Furthermore, the ***Maastrichtian*** formations outcrop around Djebel Bou Sba and are represented by pyritous gray to blue marls, overlain by light biomicritic limestones (Lahondère, J. C., 1987).

b) Souk Ahras

The ***Lower Cretaceous*** formations can be summarized as follows: ***Albo-Cenomanian*** formations are primarily composed of marls, siltstones, and marl limestones. They outcrop in the extreme northeast near the boundary at Koudiet El Hemimib. ***Aptian*** outcrops are primarily represented in the Sidi Ameur and Ras El Guema mountains.

To the southeast of Taoura, ***Lower Cretaceous*** outcrops are recognized in the form of exotic blocks within the Senonian marls.

The ***Albo-Cenomanian*** formation consists of marls, siltstones, and limestones. It surfaces to the north in the Oued Mougras anticline (including Sidi el Hemessi, Djebel Graouet, and Bourzine) and extends to the Tunisian border. It is also found in the Djebel Ladjbel anticline at the edge of the El Ouasta Triassic diapir (O.R.G.M., 1997, 2000).

The ***Turonian*** is primarily composed of limestones, though the proportion of limestone to marl varies. It constitues Koudiet Henchir Ellouz and Koudiet el Msala in Oued Mougras and is also

present in Djebels Shrachif Messaouda, Sahaba, and Ouasta. In the northern region, the ***Turonian*** exceeds 200 meters in thickness, while in the southern region it is less than 100 meters.

The ***Coniacian*** consists of marls, marl limestone, and limestone marl, found in the northeast at the borders of Algeria and Tunisia. The ***lower Santonian*** appears as isolated outcrops of limestone and marl. The ***Upper Santonian*** to ***Lower Campanian*** consists mainly of marls with some limestone layers, varying in compactness from soft to very compact, often showing confused stratification and scrubby flow. These formations outcrop in the Djebels of El Ogla, Baba Embarek, Zellez, and Kef Ellouz (Kriviakine et al., 1989b; Fatna, 2018; Hadji, 2013).

The ***Upper Campanian*** is composed of grey limestone with 80 to 100 meters thick layers of marl. These formations outcrop on the southern flanks of Djebels Boussessou, Ogla, and Baba Embarek. Scattered peaks are also observed along the wadis El Hammam, Boudrhis, and Guelib Hachem, and appear at Djebels Serrou and Cherif.

The ***Maastrichtian*** starts near the top of the intermediate marl and primarily consists of the second limestone bar and the upper marl. Notably, Cretaceous limestones are present in the Ain Soltane Mountains and on the flanks of the Dra Taoura Mrahna synclines and Bordj M'Raou, where they are overlain by Miocene sandstone and Quaternary alluvia. Thicknesses can reach up to 300 meters.

c) Tebessa

A carbonate formation represented by large layers of cracked limestone and ***Cretaceous*** marl; this formation is very clear at the edges of the Tebessa-Morsot plain.

The ***Aptian*** formations consist of limestone beds containing Orbitolines, frequently brecciated and cemented with dolomite or calcite. In the southern region of Djebel Belkfif, these limestones are incorporated into the diapiric Triassic, with a thickness of more than 100 meters.

Meanwhile, ***Albian*** outcrops are found near Djebel Bouroumane and are composed of 90 meters of thick brown limestone beds. This formation is not present in the study area, possibly due to significant diapirism during that period. However, based on the latest article of J-M. Vila (2001), they are near Djebel Belkfif. And also presented by a well-developed formation of *Vraconian* in the Bouroumane and Hammaimat areas, and it probably exists at depth in the Hammamet trough. It's characterized by a series of grayish limestone and marl limestone plates containing Ammonite imprints.

In addition, ***Vraconian*** formations are well-developed in the Bouroumane and Hammaimet areas and probably exist at depth in the Hammamet trough. This stage is characterized by a series of grayish limestone and marl limestone slabs containing ammonite imprints.

Cenomanian: It outcrops in the northwestern part of the Hammamet trough, east of Djebel Essen, in the form of purple-blue marls with intercalations of limestone breccias. These marls are also known south of Djebel Belkfif in the Hammaimet anticline and in the eastern zone of Djebel Ozmor (Tella).

The ***Turonian*** period is split into two parts: the ***Lower Turonian***, which begins with approximately 60 meters of greyish marly limestone and ends with beige limestone cliffs at sites such as Djebel Essen, Djebel Belkfif, Kef Daheche, and Djebel Tella (Ozmor range); and the ***Upper Turonian***, characterized by alternating grey and green marls, with a thickness of around 150 meters.

The ***Santonian*** and ***Coniacian*** stages consist of a substantial and consistent sequence of grey or green marls. Towards its upper part, it includes levels of limestone breccias spanning 250 meters in thickness.

The ***Campanian*** period, divided into lower and upper stages, consists primarily of a 200-meter-thick sequence of grey marls. Transitioning from the upper Campanian to the lower Maestrichtian, there is a noticeable shift into marly formations, forming a new ridge between the Turonian and Maestrichtian periods.

The ***lower Maestrichtian*** is characterized by scree deposits at the base of relief features, while the upper Maestrichtian is marked by substantial layers of well-bedded, massive white limestone containing numerous Inoceramid impressions. These limestone layers range from 80 to 100 meters thick, expanding to 200 meters in thickness southwest of Youkous (Hammamet).

d) Khenchela

Marly-limestone deposits characterize the ***Upper Cretaceous*** deposits, whereas reef limestone deposits compose the Lower Cretaceous are found in the Albian-Aptian outcrops of the Khenchela anticline**.**

The ***Lower Cretaceous*** sandstone series (Berriasian to Albian) extends across significant portions of the Chelia Anticline, Khenchela Anticline and is also found at Kef Tifekressa, Ras Serdoun, Djebel Chenntgouma, Djebel Faraoun, and Djebel Aidel. R. Laffitte (1939) provided detailed descriptions of most facies, which served as the basis for R. Guiraud's (1973). This schematic

diagram summarizes the primary variations observed, incorporating some modifications and additions to Laffitte's original finding.

2. The Cenozoic

2.1 Paleogene

2.1.1 Paleocene and Eocene

In Guelma, the ***Paleocene*** formations are represented by black marls with globigerina and globorotalia, outcropping above the Maestrichtian formations of the Bou Zitoune massif, with a thickness of 20 to 25 meters (Lahondère, J. C. 1987). North of the Seybouse Valley, above the lower Paleocene layers with echinoderms, there is a significant bed of blue-gray to black limestones and marl-limestones with intercalated beds of black flint nodules, first reported by J.C. de la Chavane (Lahondère, J.C. 1987). Where Upper Eocene and Oligocene Formations are characterized by flysch-type formations, with typical sandstone and clay-sandstone facies. They cover vast areas in the Guelma region and are generally composed of coarse quartzitic sandstones and layered, schistose clays, sometimes intercalated with quartzite and/or marl-limestone beds (Lahondère, J.C. 1987). The Numidian flysch formations, prevalent in the Guelma region, form most of the El Houara and northern Beni Marmi massifs. The top comprises quartz sandstones in thick beds, interspersed with clay-sandstone layers. Below, there are yellow schistose clays with clay-sandstone limestone intercalations. The base ends with pinkish-brown schistose clays with black quartzite nodules (Lahondère, J.C. 1987).

Meanwhile, In Souk Ahras, the ***Paleocene*** formations are southeast of Mehars, Ogla, Ain Hallouf, Djebel Sessou, and M'Daourouch. Its thickness ranges from 80 to 200 meters, primarily consisting of marl limestone. From a geographic distribution perspective, the ***Eocene*** is rarely observed in the Souk Ahras area. It appears only in the northern region as fragmented outcrops. It can be found at Djebel Dekma, north of Djebel M’sid, at Djebel Boukebch, and near the Oued Mougras station. This formation consists of Priabonian calcareous marls and lumachelles, which are overlain by Nummulitic limestones and Ypresian Lutetian marls. These deposits have a moderate thickness of 25 to 30 meters and primarily outcrop to the northeast of Taoura.

In the region of Tebessa, the ***Paleocene*** is characterized by a marl formation covered at the top by marl limestones, containing several phosphatic layers with a thickness of 10 to 15 meters. The ***Eocene***, on the other hand, is characterized by very thick calcareous formations with flint nodules and lumachelle balls. It outcrops in the northwestern parts (Gourigeur) and southeast of Hammamet (Tazbent). Additionally, across the Tébessa trough, it appears at Djebel Dyr-Gastel.

The marine Paleogene of Khenchela, starting with the ***Danian*** stage, features marine marly-calcareous layers. In some areas, these layers include intercalations of lacustrine and red layers of lagoonal or continental origin, particularly in the Lower Eocene (Ypresian) and Middle Eocene (Lutetian), which are primarily marine. Furthermore, In the southeast of the Aures, the Nummulitic formations are the most developed. A notable outcrop in this area is of A. Eguelmamene, characterized by flint-bearing limestones. At the beginning of the ***Eocene***, during the Paleocene (Montian and Thanetian periods), the sea appears to have uniformly covered the Aures. In the southeast, the base of the formation features a fauna rich in Turritelles.

2.1.2 Oligocen*e*

In Souk Ahras, the Oligocene is represented by an east-west band that spans north of the zone and crosses Mechrouha, Sidi El Hemissi, and Oued Mougras. It appears as Numidian sandstone, often separated by thin grey marls containing thin limestone beds or schistose clays

2.2 Neogene

2.2.1 Miocene

The ***lower Miocene*** is represented by distinctly marine deposits, consisting of greenish glauconitic sandstones overlying blue and greenish-gray marls. Whereas, the ***middle and upper Miocene*** are successively represented by lagoon-marine, lagoon-brackish, and finally fluvio-terrestrial deposits, consisting of marls, clays, and gypsum. These formations occupy the current large depressions aligned from East to West, which seem to correspond to the ancient flysch deposition basins. The gypsiferous marls of this stage are observed on the flanks of the hills of Mechta El Acheche and Belkhir, about 3 km southeast of Heliopolis.

It does not outcrop in the area of Hammamet (Tebessa) nor in its immediate surroundings. In contrast, the ***Miocene*** diapirism in the vicinity of Ouenza occurred in two consecutive phases. The oldest phase is pobably Burdigalian, while the more recent phase is post-Tortonian. This latter diapirism significantly disrupted the Miocene graben of the Oulad Soukies, causing the Miocene sediments to become verticalized or to be enveloped in Triassic material (W. Kowalski & l', 2000).

In 1862, Coquand first reported a Burdigalian deposit with Pectens near Khenchela and determined the exact age of the red layers in the southern Aures. The Miocene in the study area can be subdivided as follows: The Aquitano-Burdigalian is marked by red conglomerates and outcrops at El Kelaa, Ras Khodalène, and around Ras Serdoun. The Langhian-Serravallian consists of marls, biomicrites, biomicrosparites, and white sandstones, and is observed at El Kelaa Djebel Knif and Ras Ychebrane. The Tortonian is characterized by white sandstones, which outcrop at Tirkabine, Djebel

Kharroub, Djebel Akar, El Mennchar, and Douar Khenchela. The Upper Tortonian is continental, comprising beige and red silty clays and sandstones, and appears only at Draa El Ahmar.

2.2.2 Pliocene

The Pliocene in the Guelma region is marked by two distinct terraced alluvial formations: The first terrace features horizontally layered alluvial deposits, mainly composed of large rolled pebbles, and in several places, found embedded within reddish silt. These ancient alluviums link to a torrential discharge cone at the base of the El Houara sandstone massif, forming the Djebel Zemzouma plateau. The second level includes two continental facies: alluvial deposits and travertine limestone, which fill the ravines of the first terrace at the bottom of the Seybouse valley. The Pliocene alluviums sometimes reach considerable thicknesses. They are composed mainly of large rolled pebbles, predominantly originating from the flysch sandstone formations, which are widespread in this region and easily eroded. These pebbles are most often embedded in red or yellow silt. In the Guelma region, travertine limestone formations appear to laterally connect to a vast layer of lacustrine limestone deposits. These travertinous limestones, located mainly in the western part of the Guelma, do not show homogeneous facies everywhere. In fact, in the center of the basin, these travertine limestones are presented alternately with marly, limestone, and conglomerate beds. In the eastern and northern parts of the basin, these travertines rise regularly on the edges of the basin and especially on the southern edge, thereby marrying the forms of the topography. You can follow them without interruption from Guelma to the foot of the Mahouna massif.

Additionally, the Pliocene of Souk Ahras is characterized by sea limestones, marls, custard stones, sandstones, and red clays. Dissonant continental terrains covering Triassic, Cretaceous, and Miocene strata serve as the series' main features. Its lowermost 150–200 m thick stratum is composed of red clay marl, micropudding stones, conglomerates, and sandstone with clay layers.

Whereas in Tebessa, it is composed of clay and conglomerates, and outcrops near Djebel Befkfif, and in the eastern part of the Morsot fossil, as well as in the eastern part of the Hammamet fossil, to the south of the junction of the road to Bir d'Heb.

2.3 Quaternary

The Pleistocene formations in Guelma are represented in this region by fluvio-continental sediments. They equally show two types of facies: alluvial facies that show an important development in the Seybouse valley. Recent alluvium consists of rolled stones of varying sizes, mostly of the flysch. These elements, often quite voluminous, are either drowned in a clay lemon or in a limestone-calcareous matrix, while travertine deposits are the result of the thermal sources that existed in this

area during the Pleistocene. These travertine deposits are present at many points, either in the form of nappes or in the form of shells or tuff domes (Photo 1). These are observed north of the Seybouse valley near Heliopolis and other points, including Hammam Debagh and Hammam N'bails.



Photo 1 Deposits of Travertine in Hammam Debegh, Guelma Region (2018)

In Souk Ahras, the Quaternary spans over large areas. It is present in all geological layers covering the wilaya. It is generally composed of continental formations such as colluvium, river terraces, boulders, and silts. Depending on their characteristics, old formations are represented by limestone crust, composed of white, yellowish, and pink carbonate rocks, is found in the south of the Medjerda Mountains, and pebbles in the south of Souk Ahras. Whereas, Recent formations are represented by deposits of a heterogeneous nature, containing clay, silt, loam, and colluvium. The latter covers many mountains, such as Djebel Guenbuita, Zaarouria, and Djebel Ladjbel. Meanwhile, the current formations consist of alluvial materials such as pebbles, gravel, sand, and sandy or loamy silt, which have developed in the valleys of Oued Medjerda, Hammam, Tiffech, and other smaller rivers.

Quaternary is represented by the infill of the Hammamet and Tébessa grabens and occupies a significant surface area, mainly in the plains and at the foot of the mountains. This includes: Lower Pleistocene, characterized by pebbles; the Middle Pleistocene, represented by sandy clays; the Upper Pleistocene, formed by pebbles and gravel; the Holocene, composed mainly of materials visible in the valleys of Youkous, and current scree, which is found at the foot of limestone reliefs with extensive

spread. These deposits are largely deposited on the marl series of the Upper Cretaceous. The northern zone of El Ouanza is characterized by deposits found in the lower parts of the reliefs, covering significant areas. These deposits include limestone crusts, silt, scree, gravel, and conglomerates, with a thickness of 10 to 30 meters in the grabens (Dubourdieu, 1956).

In Khenchela, recent formations are also widespread around the periphery of the Aures, whereas they are rare in the center of the massif. In the center, they are represented only by scree and terraces, while in the periphery, they form large and thick alluvial sheets. Quaternary deposits cover most of the plains, consisting of scree with blocks, recent or current alluvium, arable land, ancient alluvium, polygenic glacis draping the reliefs, and limestone crusts. (Figure 6)(Service de la carte géologique de l'Algérie, 1977)

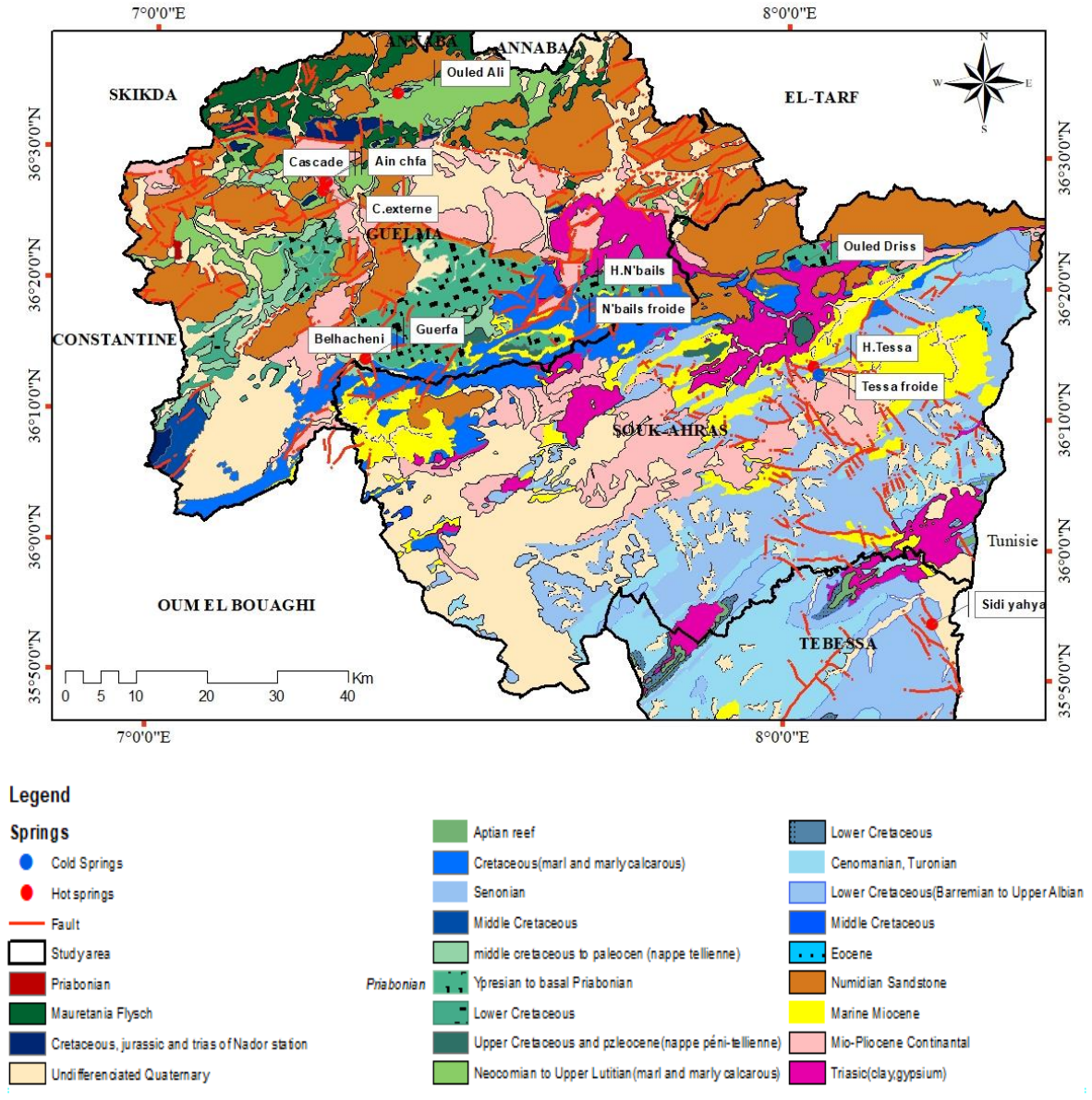


Figure 5. Excerpt of the Geological Map of the Northern Part of the Study Area (after Vila, 1978)

This map represents a digitized excerpt of the original geological map published by Villa (1978). No modifications were made to the geological content.

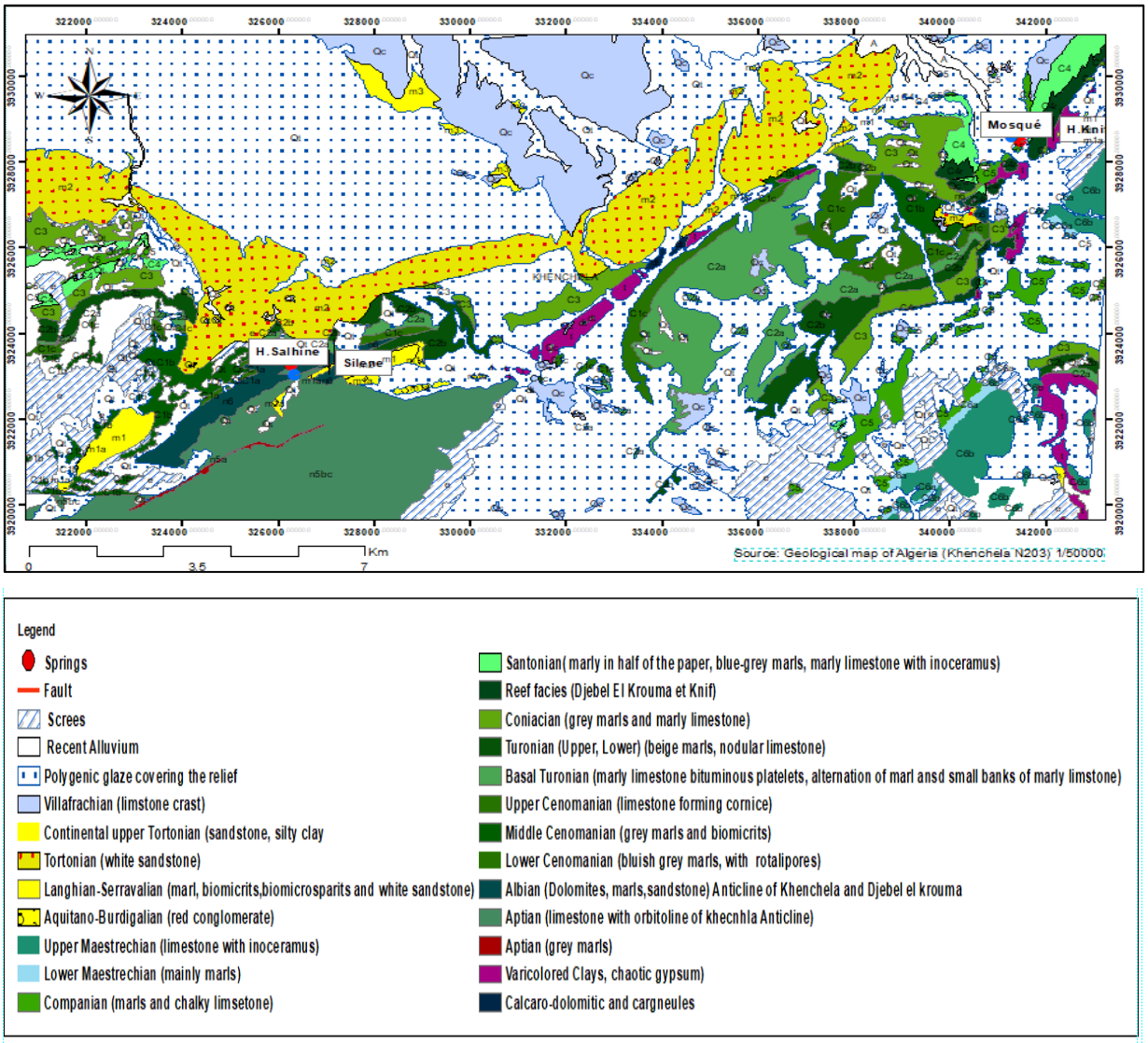


Figure 6. Excerpt of the Geological Map of the Khenchela Region (after Geological Map of Algeria, 1977, Sheet N°203)

Digitized excerpt of the Geological Map of Algeria, Khenchela sheet (First Edition, 1977, Map N°203). No geological features were modified; only georeferencing and vector digitization were performed.

IV. Structural and Tectonic Setting

I.1 Introduction to the Tectonic Context

The northeastern region of Algeria, comprising both the Saharan Atlas and the Tell Atlas, exhibits a complex structural and tectonic setting shaped by the convergence of the African and Eurasian plates. This tectonic activity, progressing at approximately 5-6 mm/year in an NNW direction, has resulted in diverse structural configurations and notable seismicity throughout the region. The Tellian Atlas, characterized by its fold-and-thrust belt system, includes both reverse and strike-slip faults. In the western and central parts, reverse faulting predominates. In contrast, the eastern region, including Guelma and its neighboring provinces, is primarily affected by strike-slip and normal faulting mechanisms, as seen in events like the 2003 Hammam Debegh earthquake (mb = 5.2).

The Guelma region, located between Algeria's coastal zones and high plateaus, is recognized for its distinct tectonic setup. Prominent active structures, such as the Bouchegouf and Hammam N'bails faults, intersect with Quaternary deposits and areas of hydrothermal springs, contributing to the region's seismic relevance. The Guelma seismogenic basin, functioning as a pull-apart basin, predominantly exhibits normal faulting. Notable seismic events, including the Heliopolis earthquake in 1850, the Guelma earthquake in 1937 (mb = 5.4), and the 2003 Hammam Debegh event, highlight the area's persistent tectonic activity. Moreover, field observations reveal NW-SE to NNW-SSE fault orientations, aligned with local geomorphic and hydrothermal features like travertine formations, dykes, ramparts, and cones, all of which point to ongoing neotectonic processes.

The latest significant earthquake impacting the Guelma region occurred on August 17, 2024, registering a magnitude of 3.0. This was part of ongoing minor seismic activity near Guelma, though not unusually strong compared to historical events. In recent years, notable seismic events have included a magnitude 6.0 earthquake in March 2021, located approximately 205 kilometers from Guelma, marking one of the strongest nearby quakes within the past decade according to Earthquakelist.org (2024) and the Earthquake Hazards Program official website.

The structural examination of Souk Ahras, based on geological maps, geophysical data, and borehole profiles, reveals a block configuration of Cretaceous formations defined by diagonal, right-lateral NW-SE faults (such as the M'daourouch transverse fault and the fault bordering the Taoura graben) and left-lateral NE-SW faults associated with E-W trending fractures. These tectonic features are a response to the alternating phases of extension and compression typical of the Atlas domain, as

noted by multiple authors. This dynamic has led to the formation of horsts and grabens, with the Taoura collapse graben standing out as a particularly striking example. Additionally, Triassic salt diapirs have formed along deep-seated faults, further influencing the region's complex structural landscape.

According to the Volcano Discovery GmbH, Germany website, the Souk Ahras region experiences moderate seismic activity, with six earthquakes exceeding a magnitude of 5 since 1970. This indicates that earthquakes of this magnitude likely recur approximately every 5 to 10 years. Based on records from the past 54 years, Souk Ahras and its surroundings average around five seismic events annually, emphasizing the area's consistent, although moderate, tectonic activity. This aligns with historical data, showing a steady pattern of seismicity that highlights the region's vulnerability to occasional stronger earthquakes.

The tectonic evolution of Tebessa reveals a sequence of significant geological phases. The Late Lutetian Compressional Phase, defined by N150° stress, formed N50-60° folds, including the Djebel Troubia syncline and Djebel Gaagaa–Es Senn anticline. During the Miocene Extensional Phase, tectonic forces created the El Ma Labiod basin and fostered diapirism in areas like Djebel Ouanza. Lower Pliocene compression, under N0°-20° stress, generated E-W oriented folds, such as the Bled Tebaga anticline. Lastly, the Plio-Quaternary phase introduced new folds and horst-graben structures along NE-SW and E-W faults, reshaping zones like Djebel Belkfif.

The Tebessa-Morsot plain corresponds to a moderately subsiding sedimentary basin (Dubourdieu, 1956; Kowalski et al., 1997, and G. Durozoy, 1950). It is a tectonically originated trough formed during the Tertiary and Quaternary periods, in which detrital formations have accumulated, resting on a marly substratum in the center of the plain and on limestones at the edges (Kachi et al., 2007).

The fracture analysis of the study area reveals a dense network of structural alignments with significant extensions, facilitating the infiltration and movement of meteoric waters within a karstic system. Fractures, combined with lithological and morpho-structural factors and recent tectonic activity, have strongly influenced the region's water distribution. Since the Eocene, tectonic activity, particularly the orogenic phases, has left its mark on the region, forming the northeastern Saharan Atlas. This structure includes NE-SW-oriented folds intersected by major NW-SE transverse faults, as noted by Morel (1957).

On October 8, 2024, the Research Center in Astronomy, Astrophysics, and Geophysics in Algeria reported a 3.7-magnitude earthquake in Tébessa Province, located in Algeria's far east. The

tremor was recorded at approximately 4:17 PM local time, with its epicenter pinpointed 9 kilometers northwest of Boukhadra, a town in Tebessa Province.

The northeastern foothills of the Aures Mountains are located in northeastern Algeria (Khenchela), on the northern edge of the African plate, where it meets the Eurasian plate. Since the Triassic period, the Saharan Atlas has experienced alternating subsidence and uplift, driven by tectonic shifts. This tectonic movement has shaped the region's structure, notably forming the Djebel Aures syncline with its asymmetrical flanks, the Khenchela anticline, the Djebel Djehfa syncline, and the Djebel Chelia anticline. South of Foum El-Gueiss Dam and Koudiat Medouar, these formations align along faults parallel to the fold axes.

The major faults in the structural outline of the Aures region are associated with significant fracturing, characterized by parallel or slightly oblique networks to the main directions, leading to their multiplication and disorganization (Yelles-Chaouche et al., 2006). Among these faults, one can identify: reverse faults, conjugate faults, collapse faults (normal faults), strike-slip faults, combinations of strike-slip and reverse movements, tectonic traces, and Triassic ejecta.

Khenchela experiences relatively few earthquakes, with only three recorded events exceeding magnitude 5 since 1970, suggesting that strong earthquakes of this magnitude likely occur approximately every 15 to 20 years. The most recent earthquake reported by the Research Center in Astronomy, Astrophysics, and Geophysics (CRAAG, n.d.)occurred on August 30, 2024, measuring 3.2 in magnitude and located 5 km southwest of Bouhmama.

1. Folds

In the Guelma region, the East-West-oriented folds are represented in the Taya-Debagh range and extend eastward through the Bou Zitoun massif and Djebel El Hourara. Some folding axes with a North-South orientation, likely pre-existing and dating back to the Hercynian or Mesozoic era, were reactivated and resulted in folds oriented in the North-South direction. However, these are less pronounced than those with a Southwest-Northeast orientation. For the North-South alignments, the Barremian inliers of Guelma and Djebel Bou Sba provide a very illustrative example. Another alignment can be observed further east, indicated by the Triassic outcrops of Djebel Tifech, Ras El Alia, Hammam N'Bail, and the Nador massif. According to Dareste de la Chavane (J.C. 1910), in these alignment systems, the orientation of each fold segment tends from East-West to curve towards the Northeast as it moves eastward, approaching the North-South folds, which act as hinge axes. This successive inflection of the East-West-oriented fold segments towards the North determines the general direction of the orographic lines, which are roughly Southwest-Northeast.

Further to the East, in the Souk Ahras region, the folds take directions from NE-SW to W-E, influenced by the N–S strike-slip faults. At Djebel Es Sayah, an anticline oriented roughly W–E has been identified. A syncline may be seen at Koudiet Oum Zana, located west of Djebel Bouallegue and north of Oued Djedra. Another fold transgressive over the Cretaceous and Paleocene, with a Lower Miocene core, is found near Chaabet el Ballout. This fold is inverted and inclined towards the SSE.

The Algeria-Tunisia border region is characterized by folds with large curvature radii, primarily formed by Cretaceous limestones. The anticlines, often substituted by vast synclinal structures and pierced by Triassic diapirs at their hinges, are oriented NE-SW. Significant anticlines include Ouanza, Boudjaber, Def, Mesloula, and Belkfif, while notable synclines include Oued El Ksob, Aichemia, and Haoud S'ghir. These folds (anticlines and synclines) result from Neogene compressions, mainly between the Eocene and Miocene, due to the discordance between Miocene sediments and those of the Cretaceous and Eocene. Morel (1955) noted two directions of folds in the vicinity of Djebel Belkfif, which are more recent than those of the final phase

The maximum folding phase in the Aures begins at the end of the Lutetian; it corresponds to the movements of the Pyrenean orogenesis (Vila, 1977). The Cretaceous anticline of Djebel Amrane, which divides the Remila plain into two synclines, features fairly steep dips, reaching up to 50°. The Khenchela syncline, a large and regular structure, is composed of the following geological successions: the Lower Cretaceous, with thick predominantly continental series formed by limestone, marly-limestone, and marly-limestone clay deposits. This region, characterized by a sedimentary substratum inherited from marine transgressions of the Secondary and Tertiary periods, experienced an extremely active orogenic phase towards the end of the Oligocene, leading to the uplift of the Saharan Atlas.

2. Faults

Fault contact type in Guelma is generally observed around domes and brachy-anticlines (structural domes) composed of Eocene and Cretaceous reef limestones in the Taya Debagh chain. For example, in the Taya and Djebel El Grar massifs, due to the collapse of the central part of the dome, they lie in discordance on the marly beds of the Barremian.

The tectonics of the Souk Ahras region are characterized by the dominance of a family of NE-SW faults and a second family oriented perpendicularly, NW-SE. The presence of these two fault networks has facilitated the upward movement of abundant Triassic materials in the region.

The Maastrichtian layers demonstrate fractures in two main directions: N110°E and N20°E. The substrate, consisting of NE-SW-oriented horsts and grabens, shows that ancient fracturing hasn't significantly shaped the landscape but has greatly influenced erosion. Since the Eocene, faults have facilitated folding and the crushing of anticlinal thrust sheets. Post-Miocene tectonics have played a primordial orographic role, creating major NW-SE faults orthogonal to Atlas structures, defining many collapse grabens in the Hammamet-Morsott-Tebessa region.

The various documents published by R. Laffitte report a very small number of faults, some of which are directly directional (in the anticlines of Khenchela, Djebel Aidel, and Chelia), while others are oblique and almost exclusively oriented NW. In fact, fractures are numerous in the Aures massif, generally distributed along directions close to NW-SE (the most frequent), E-W, or 60°E. From north to south, the main fractures are located: South of Djebel Chelia and in the Aidel chain.

2.1 Fault Orientations and Classification

This rose diagram (Figure 7) illustrates the distribution of fault directions within the region, revealing a prominent trend oriented from Northeast (NE) to Southwest (SW). The longest bars, representing the most frequent fault orientations, align primarily around 45°–60° (NE) and 225°–240° (SW). A notable secondary trend is observed near 135°–315° (NW–SE). Moreover, the presence of orientations near 90° further reinforces the East–West component of the pattern, indicating a conjugate fault system.

The area's folds result from polyphased tectonic activity, which has significantly influenced both subsurface structures and groundwater flow patterns. The presence of NE-SW and NW-SE oriented faults plays a critical role in the region's hydrogeological dynamics. These fault orientations affect both groundwater storage and flow pathways by creating fractures and fault zones that facilitate water movement or act as barriers, depending on their properties. This structural complexity highlights the impact of tectonic stresses on groundwater flow, with faults potentially acting as conduits or controls in local and regional hydrogeological systems.

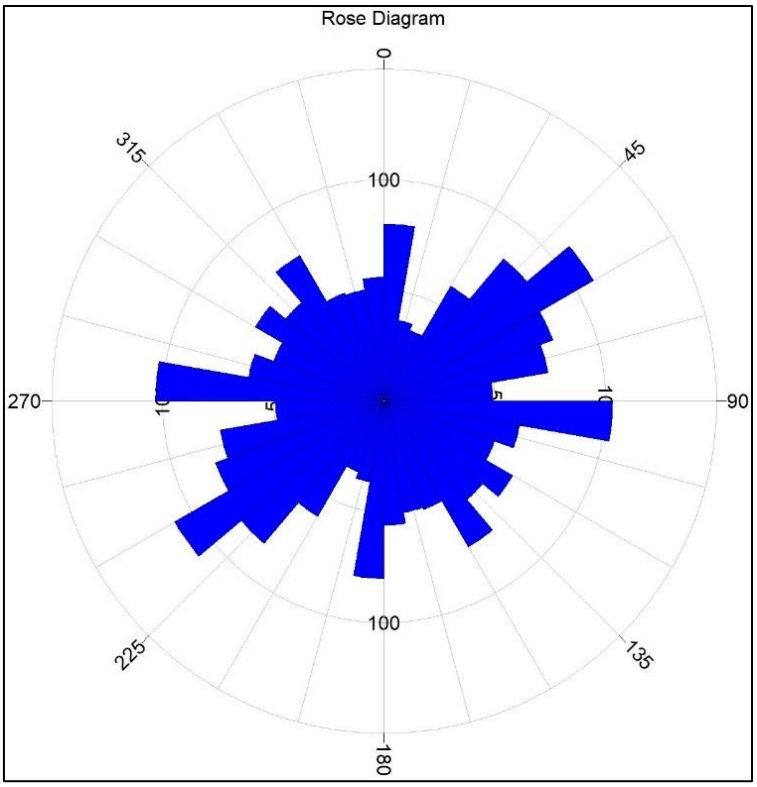


Figure 7. Rose Diagram of Fault Direction in the Study Zone

2.2 Density Map of Faults

Given that high-density fault areas are concentrated in the Northeast (NE) and Northwest (NW) regions, as shown in the map (Figure 8), this pattern could be interpreted in terms of geological and hydrogeological implications as follows:

I.2 Structural Tectonic Implications

The concentration of high-density faults in the NE and NW suggests that these areas have been subject to intense tectonic activity, mostly related to regional stress fields that align with NE-SW and NW-SE orientations. This pattern indicates that tectonic forces have heavily influenced these zones, creating a complex structural framework with overlapping fault networks.

a) Hydrogeological Impact on Groundwater Flow and Storage

In the NE and NW regions, high fault density could enhance groundwater flow, especially if the faults and fractures remain open. These areas may act as conduits for groundwater movement, allowing for increased infiltration and storage. Alternatively, if these faults contain impermeable fault gouge, they could also serve as barriers, compartmentalizing aquifers and affecting regional water flow patterns.

b) Potential Recharge Zones

High-density fault areas, particularly in the NE and NW, are often favorable for groundwater recharge if the faults are permeable, as fractures and fault zones facilitate the downward movement of water. This would make these areas significant for recharging aquifers, especially if surface water bodies or rainfall interact with these faulted regions.

c) Implications for Groundwater Quality and Mineralization

The high density of faults in these regions could also contribute to enhanced mineralization in groundwater due to water-rock interactions along fault zones. As groundwater flows through these faulted areas, it can dissolve minerals, potentially affecting water quality or creating mineral-rich thermal springs if geothermal conditions are present.

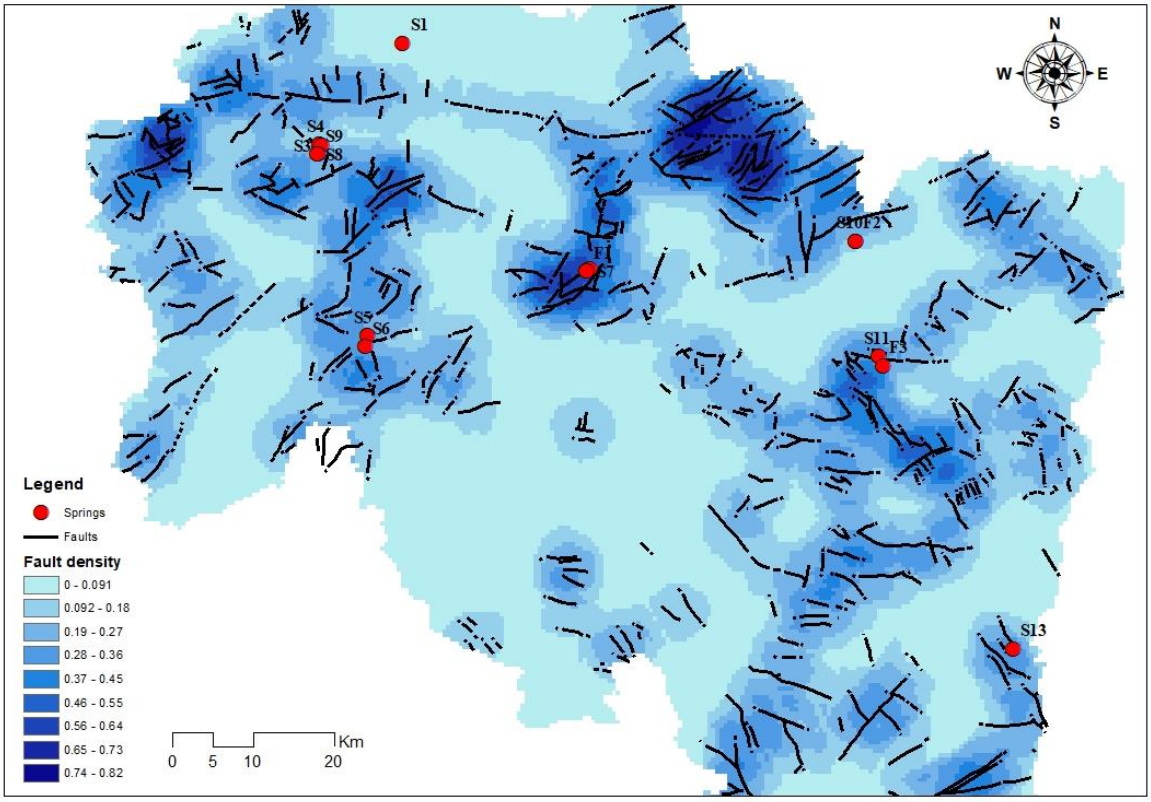


Figure 8. Map of Faults Density of the Northern Part of the Study Zone

IV.3 Hydrogeological Implication; Fault-Spring Relationship

In hydrogeology, faults play a significant role in controlling the distribution, quality, and behavior of groundwater, especially regarding springs. Fault zones in fractured rocks can serve as conduits for groundwater flow, allowing water to penetrate deep within the Earth's crust where it

heats, dissolves minerals, and gains unique hydrochemical properties. Springs often emerge along faults where water reaches the surface due to these fractures.

In regions like the area under investigation, this fault-spring relationship is prominent. Major springs frequently align along fault lines, with the fault orientation affecting water flow rates and temperature. For instance, normal and reverse faults create zones of high permeability, enabling meteoric water to infiltrate and recharge groundwater systems efficiently. Active or recently active faults often correlate with thermal springs, where higher temperatures indicate deeper circulation and increased rock-water interaction.

Additionally, hydrochemical profiles reveal insights into water-rock interactions along fault-controlled paths. For example, elevated levels of calcium, sulfate, or chloride in spring water can result from prolonged mineral dissolution in deep, fault-channeled waters. This interaction enhances mineralization, providing distinct hydrochemical signatures that mark water originating from fault zones.

The elaborated fault-spring maps (figures 9 and 10) reveal the hydrogeological role of faults, making it evident how tectonic activity influences both the distribution and characteristics of groundwater resources. By correlating faults with spring locations, the map underlines the role of structural features in directing groundwater flow and shaping water quality, temperature, and mineralization patterns.

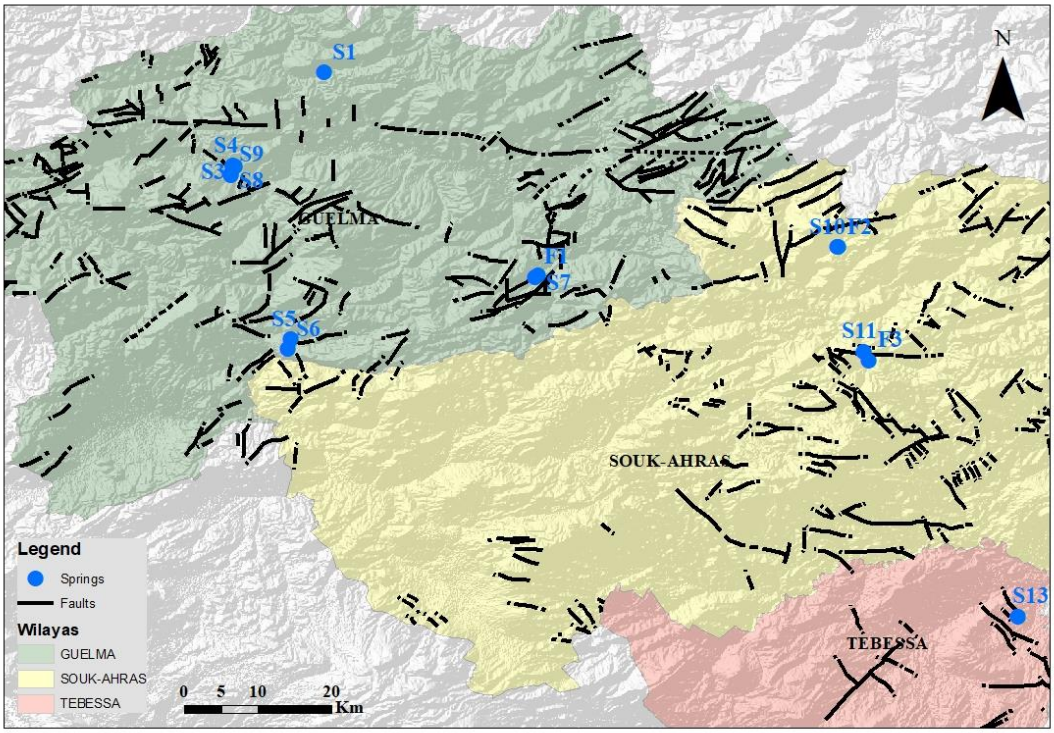


Figure 9. Fault - Spring Map. According to the Geological Map of Vila, 1978

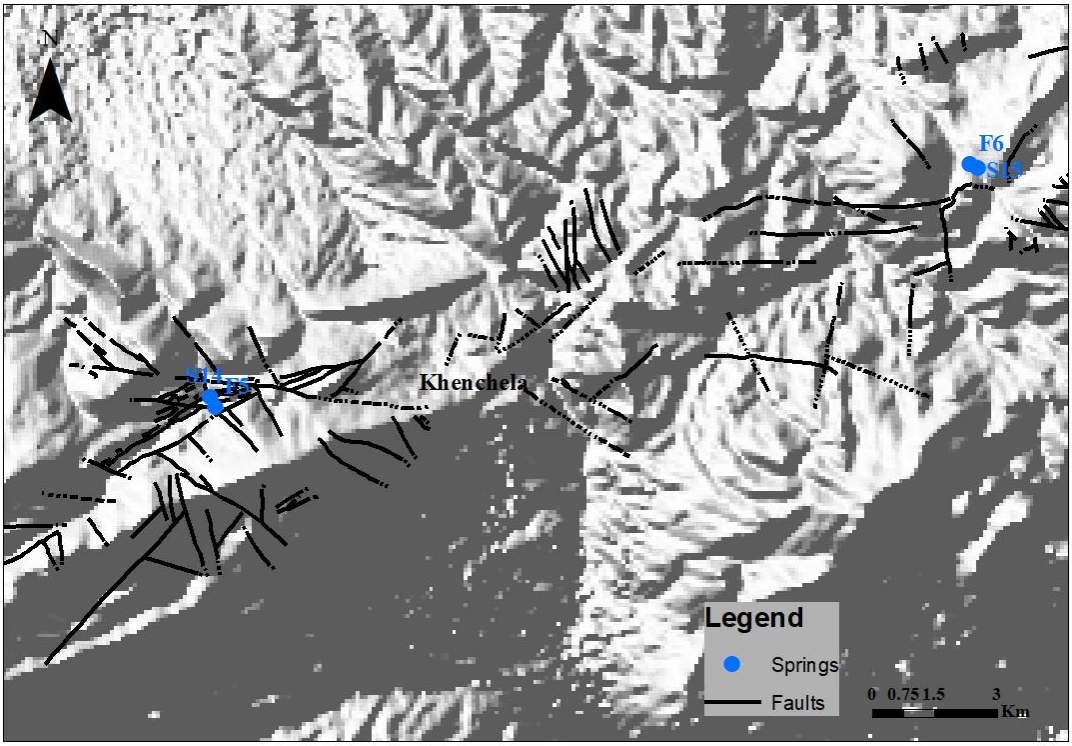


Figure 10. Fault - Spring Map of the Khenchela Region (Digitized from Satellite Imagery)

The intersection of these faults mainly creates pathways that allow groundwater to descend, heat at depth, and then ascend along these structural weaknesses, emerging as thermal springs at the surface. The high-density faults, therefore, play a dual role in both storing and channeling groundwater, affecting the recharge and discharge processes of these aquifers. Moreover, the increased rock-water interactions within these faulted zones contribute to mineralization, potentially enriching the thermal waters.

V. Conclusion

In conclusion, as a whole, this chapter presented a comprehensive review of North East Algeria's geological framework; including the internal, Flysch, external domains, Tellian nappes, and the para-autochthonous foreland domain, reveals the region's geological history and structural evolution, which are of vital importance for understanding the area's groundwater flow systems, highlighting important formations, complicated structural details such as folds and faults and stratigraphy.

The region's geology is particularly complex, the result of enormous tectonic activity that has sculpted practically the entire area. From the Triassic to the Quaternary, the sedimentary strata show considerable variety, with a varied lithology that includes alluvium (sand, gravel, and pebbles), sandstone, marl, shale, clay, flysch, and limestone.

The detailed analysis of the geological features mentioned earlier emphasizes the importance of understanding the region's geology to effectively characterize and manage its thermal water resources. The complex tectonic activity and varied lithostratigraphy form the foundation for the hydrogeological systems, influencing groundwater quantity, quality, and flow dynamics.

The study of fault density and orientation reveals a significant relationship between the region's structural framework and the occurrence of springs, particularly thermal springs. The analysis shows that high fault density zones in the Northeast (NE) and Northwest (NW) are aligned with predominant NE-SW and NW-SE fault orientations, indicating that these areas have experienced intense tectonic stress and deformation. These high-density fault zones, acting as major conduits for groundwater flow, facilitate deep water circulation, which is essential for the formation of thermal springs.

As a conclusion, the orientation and density of faults directly influence the spatial distribution and emergence of springs, especially thermal springs, in the region. These findings highlight the importance of structural geology in understanding hydrogeological dynamics and suggest that the NE and NW fault zones are core areas for further hydrogeological and geothermal studies.

Chapter Three

Climatology Context

I. Introduction

The hydrological study of the watersheds of the zone in question aims to quantify water inputs over time and space. Since the water potential of groundwater is linked to hydroclimatological conditions, the study focuses on the main characteristics that are part of a regional water resource balance sheet and are presented by rainfall and temperature. The parameters of evaporation, infiltration, and runoff determine the infiltration rate required to feed and renew groundwater reserves. The estimation of the climatic characteristics of a watershed plays an important role in understanding the hydrological behavior of watercourses

The climatological data for this study were sourced from Google Earth Engine (GEE), which offers global coverage and high-performance cloud computing. This platform enables consistent analysis across various regions, efficiently processes large-scale datasets, and eliminates the need for additional data sourcing or merging.

II. Analysis of Climatic Factors

We will analyze the climatic factors separately for each of the four wilayas and then compare the findings.

II.1 Precipitation

In establishing the water balance, precipitation—whether in the form of rain, snow, or hail—constitutes the primary input to the hydrological system, as it controls both the behavior of surface watercourses and the potential recharge of groundwater. It therefore governs the circulation of both surface and subsurface waters (Winter et al., 1998). Because liquid precipitation is the dominant component influencing the hydrological behavior of the region, the present study focused specifically on rainfall. Accordingly, a precipitation map for the year 2021 was prepared for the study area using precipitation data extracted from the Google Earth Engine platform and interpolated using Ordinary Kriging (see Figure 11).

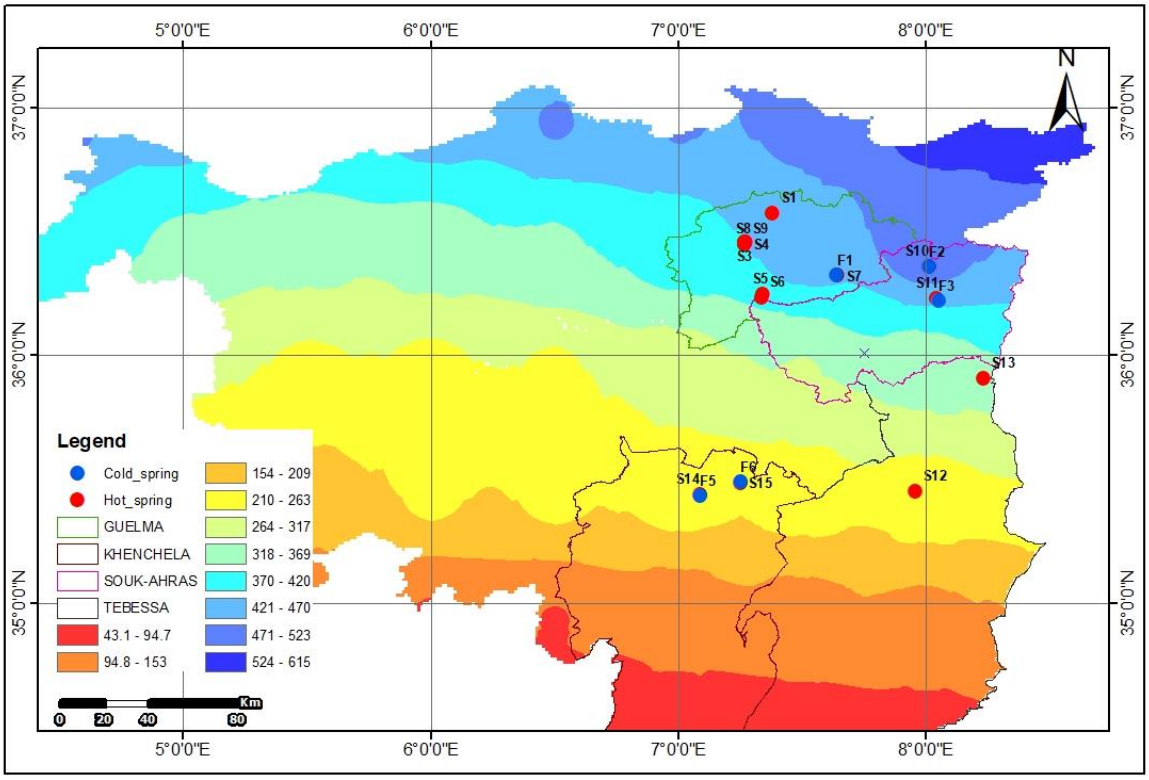


Figure 11 Precipitation Map of the Study Area for 2021 (Ordinary Kriging, GEE Data)

The precipitation data collected by the Google Earth Engine platform (GEE) over 22 years (2000-2022) are summarized in the tables below:

1. Guelma

Table 2. Monthly average precipitation in the Guelma region (2000-2022)

Months	Sept	Oct	Nov	Dec	Jan	Feb	Mar	Apr	May	Jun	July	Aug
P (mm)	39.19	46.13	65.47	82.68	76.63	63.73	69.6	57.09	48.69	15.9	3.77	15.23

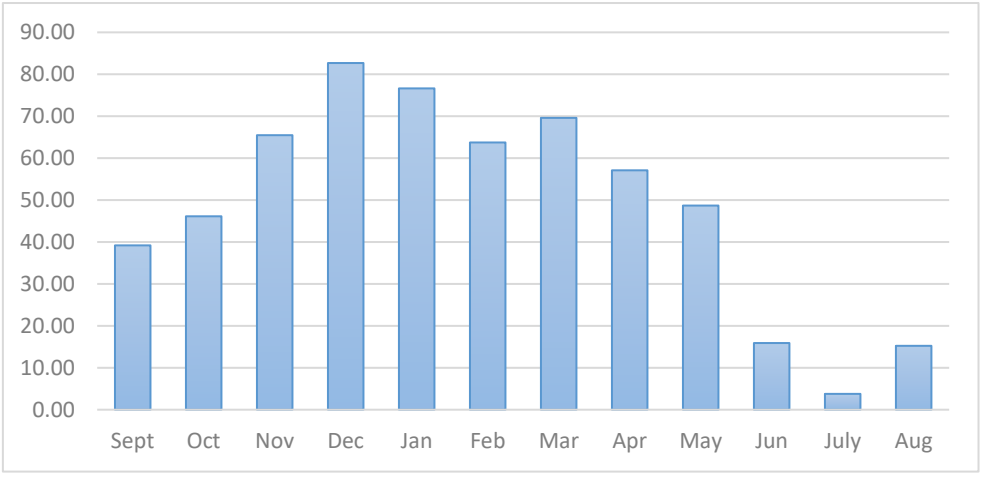


Figure 12 Monthly average precipitation in the Guelma Region (2000-2022)

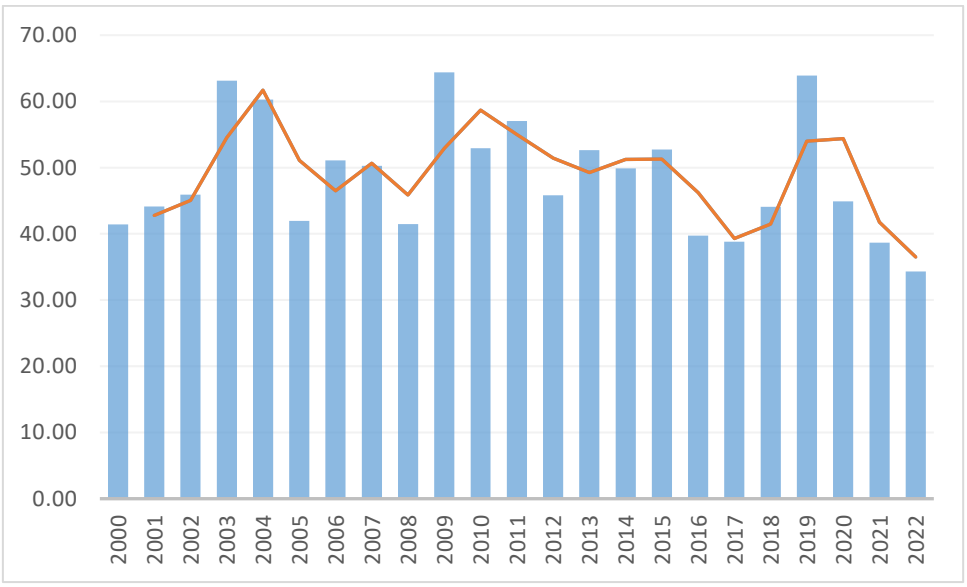


Figure 13 Annual Average Precipitation in the Guelma Region (2000-2022)

❖ *Interpretation*

The histogram of the monthly average of precipitation data (Figure 12) shows that the wettest month is December with an average of 82.68 mm, followed closely by January (76.63mm) and March (69.6mm). The chart suggests a clear seasonality in precipitation, with the winter months being the wettest. meanwhile, the month of July presents a low rainfall average with 3.77 mm, with a slight increase in August. However, the column chart of the annual average (Figure 13) shows that 2009 is the wettest year with 64.39 mm, with 2019 recording 63.88 mm, and 2003 registering 63.14 mm. While 2022 (34.33 mm) depicts the driest year, followed by 2017 (38.81 mm) and 2016 (39.74 mm). The data shows a noticeable fluctuation in precipitation over the years. From 2000 to 2003, there was

an upward trend in precipitation, with values increasing from 41.43 mm to 63.14 mm. After 2003, precipitation levels remained relatively high, peaking in 2009 at 64.39 mm. However, from 2009 onwards, there was a gradual decline in precipitation, reaching a significant decrease by 2019. This downward trend continued, culminating in the lowest average precipitation recorded in 2022 at 34.33 mm. Thus, while there were periods of higher and fluctuating precipitation, the overall pattern indicates a significant reduction in recent years.

2. Souk Ahras

Table 3. Monthly average precipitation in the Souk Ahras region (2000-2022)

Months	Sept	Oct	Nov	Dec	Jan	Feb	Mar	Apr	May	Jun	July	Aug
P (mm)	41.71	49.50	50.24	65.70	69.22	49.16	62.37	57.76	52.46	18.87	9.19	16.27

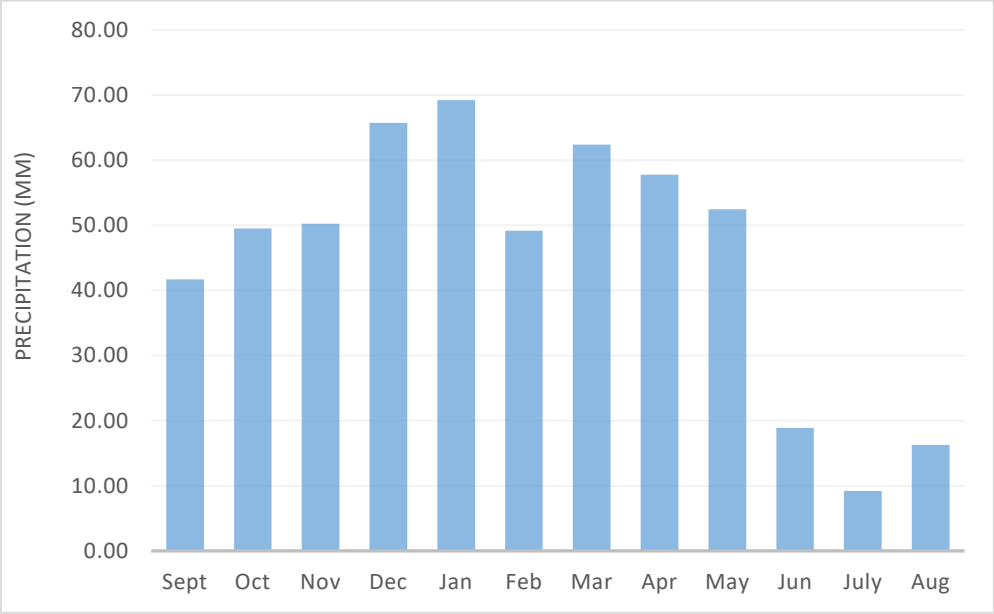


Figure 14. Monthly average precipitation in the Souk Ahras region (2000-2022)

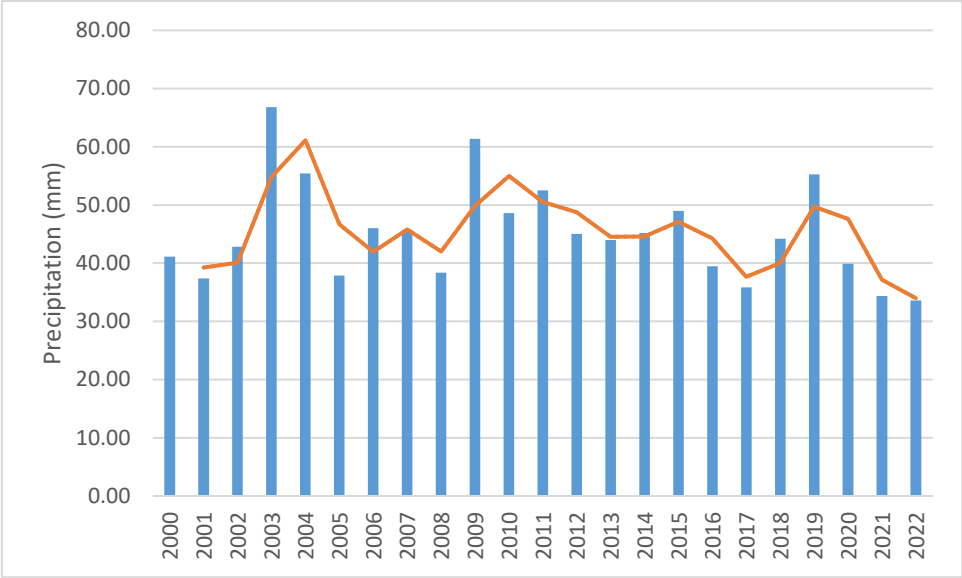


Figure 15. Annual average precipitation in the Souk Ahras region (2000-2022)

❖ *Interpretation*

The data presented in Table 3 and illustrated in Figure 14 clearly demonstrate a seasonal pattern, with January marking the peak month with 69.22 mm of precipitation. The period from December through March, with December at (65.70 mm) and March at 62.37 mm, is also notably wet. In contrast, June through August are the driest months, with June at 18.87 mm and July at 9.19 mm, making July the driest month. Meanwhile, the column chart in Figure 15 shows that the wettest year is 2003 with an annual average of 66.78 mm, followed by 2009 with 61.37 mm, and 2019 with 55.28 mm. Conversely, 2022 is the driest year with an annual average of 33.58 mm. The precipitation data reveal a trend of increasing values until 2003, followed by a gradual decrease until 2009, then a new peak, and finally a period of moderate stability until 2019. By 2020, the trend appears to decrease again.

3. Tebessa

Table 4. Monthly average precipitation in the Tebessa region (2000-2022)

Months	Sept	Oct	Nov	Dec	Jan	Feb	Mar	Apr	May	Jun	July	Aug
P (mm)	46.65	35.29	25.73	25.97	19.79	16.18	33.03	38.35	30.48	22.94	10.21	21.70

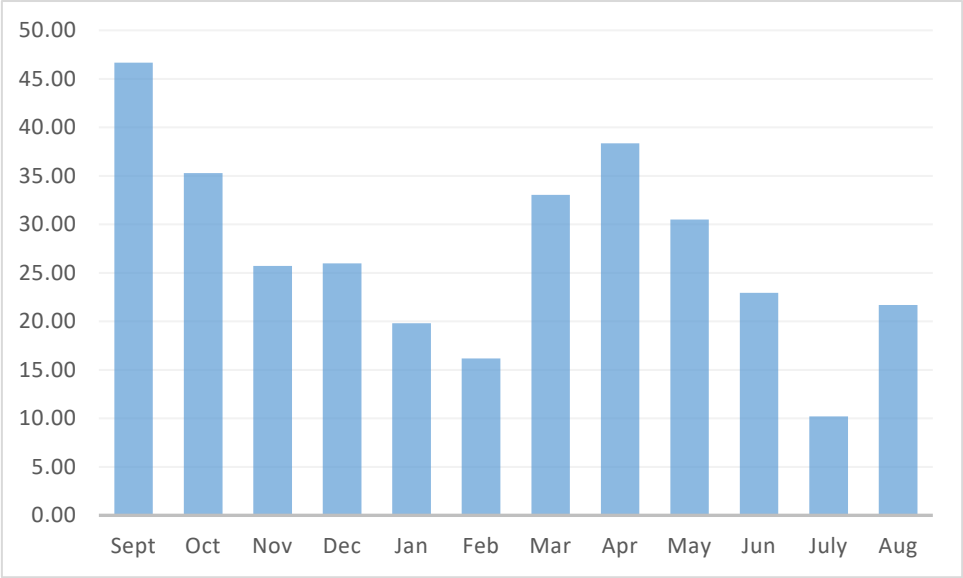


Figure 16 Monthly Average Precipitation in the Tebessa Region (2000-2022)

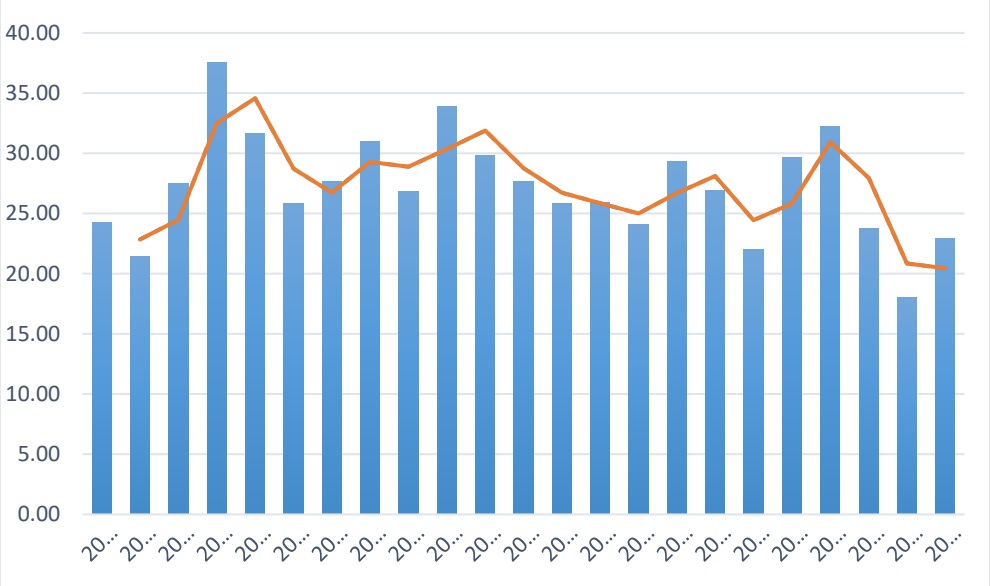


Figure 17 Annually Average Precipitation in the Tebessa Region (2000-2022)

❖ *Interpretation*

Table 4 provides monthly precipitation data (P in mm) for the Tebessa region over 22 years. As it is shown in Figure 16, the highest precipitation values are in September (46.65 mm) and April (38.35 mm). Simultaneously, the driest month is July (10.21 mm), followed by February (16.18 mm). The annual average precipitation column chart (Figure 17) shows that the wettest year is 2003 (37.53 mm). Then it peaks again in 2009 (33.90 mm) and 2019 (32.20 mm). At the same time, it shows that the driest year is 2021, with only 18 mm of precipitation.

4. Khenchela

Table 5. Monthly average precipitation in the Khenchela region (2000-2022)

Months	Sept	Oct	Nov	Dec	Jan	Feb	Mar	Apr	May	Jun	July	Aug
P (mm)	37.92	36.65	36.96	30.87	37.84	27.53	52.01	40.92	45.83	19.98	7.27	20.33

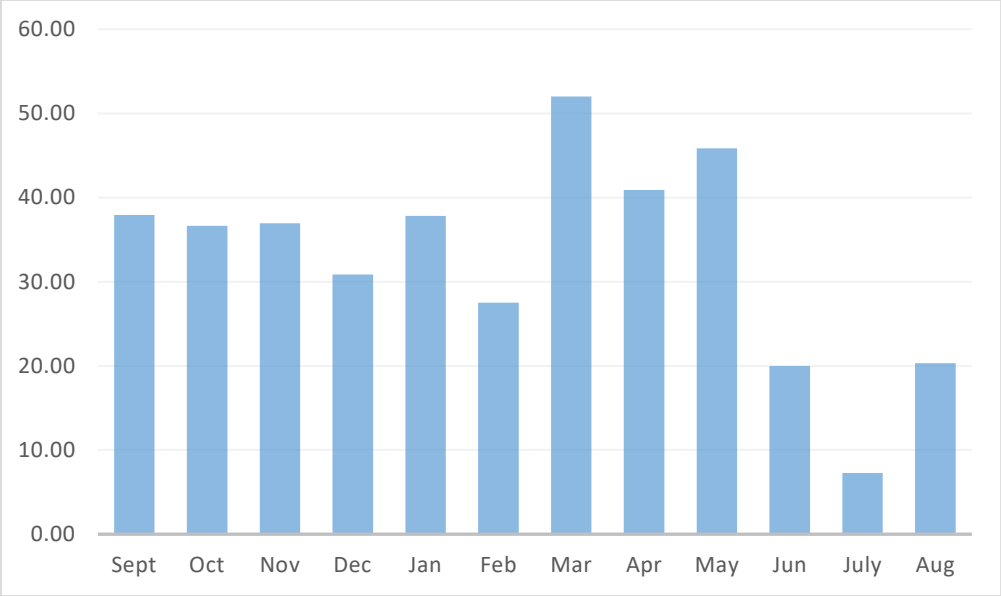


Figure 18 Monthly Average Precipitation in the Khenchela Region (2000-2022)

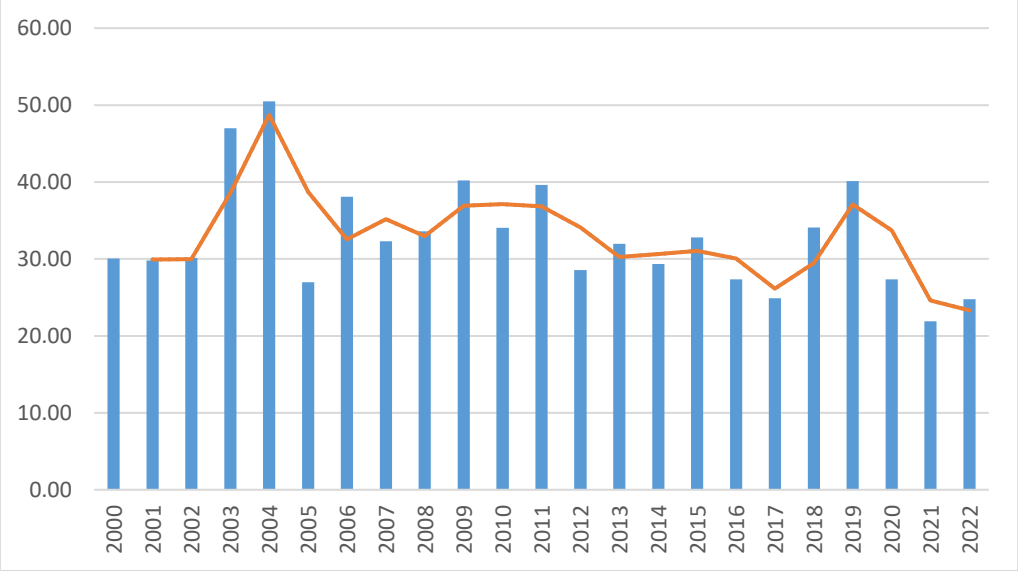


Figure 19 Annual Average Precipitation in the Khenchela Region (2000-2022)

❖ *Interpretation*

The Khenchela region's monthly precipitation data (P in mm) is displayed in Table 5 and illustrated in the histogram (Figure 18). The data reveal that April (40.92 mm), May (45.83 mm), and March (52.01 mm) are the wettest months, showing that the region receives the most rainfall from late winter to early spring. Conversely, July (7.27 mm) recorded the lowest precipitation, with June (19.98 mm) and August (20.33 mm) following closely, indicating a typical dry summer. However, Figure 19 shows that the wettest year was 2004 with 50.46 mm of precipitation, followed by 2003 with 46.99 mm. A relative stability is observed in the years 2009, 2011, and 2019, with nearly the same amount of precipitation (40.20 mm, 39.63 mm, and 40.11 mm, respectively). Additionally, the driest year was 2021 with only 21.89 mm.

II.2 Temperature

Temperature is a very important climatic factor with variations that can significantly influence evaporation, evapotranspiration, as well as the water balance and annual and seasonal runoff deficit. Our data are sourced from Google Earth Engine (GEE) and spanning the period from 2000 to 2022, are represented as follows:

1. Guelma

Table 6. Monthly average of temperature of Guelma region (2000-2022)

Months	Sept	Oct	Nov	Dec	Jan	Feb	Mar	Apr	May	Jun	July	Aug
T (C°)	34.95	28.28	19.36	14.17	13.08	15.08	20.05	23.96	29.64	37.05	41.28	41.25

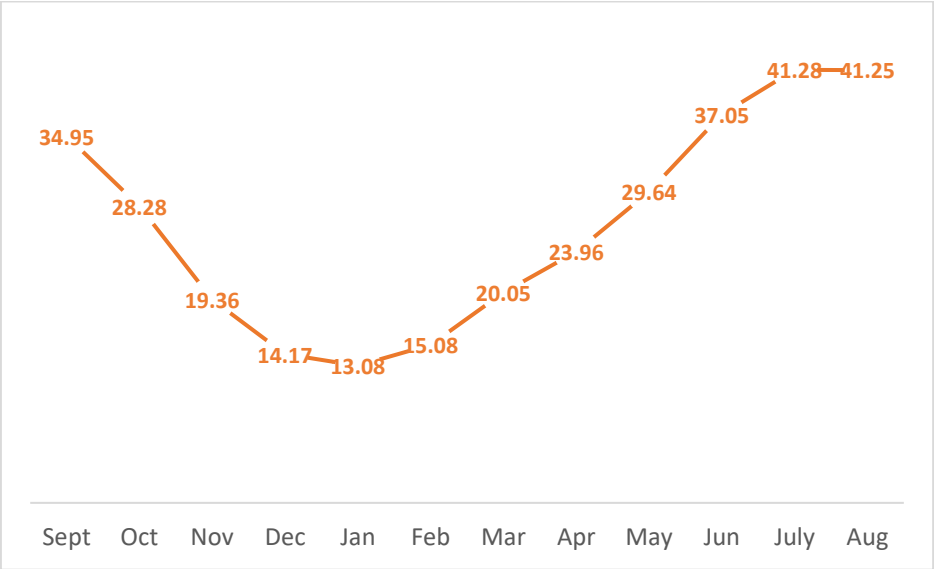


Figure 20 Monthly Average Temperature in the Guelma Region (2000-2022)

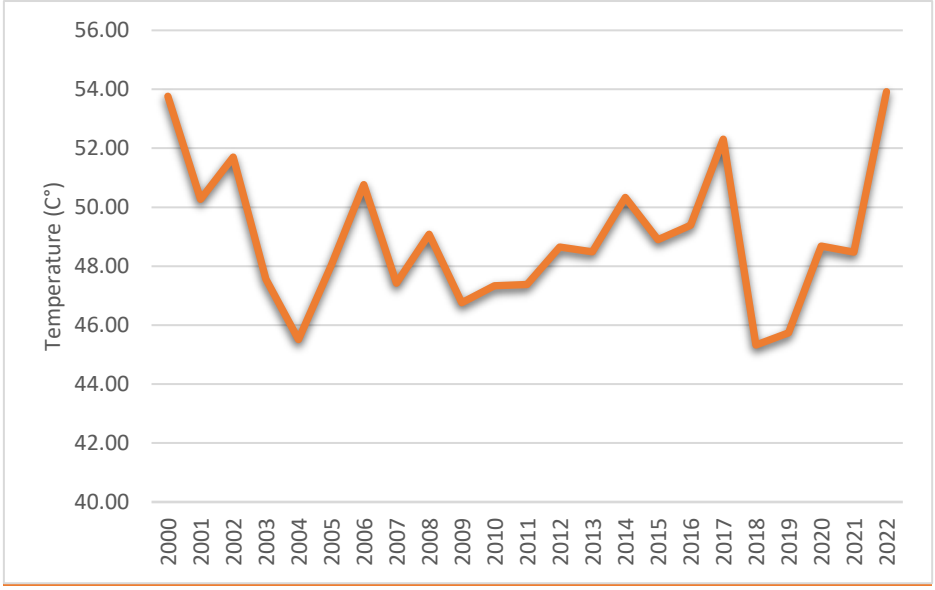


Figure 21 Annual Average Temperature in the Guelma Region (2000-2022)

2. ***Souk Ahras***

Table 7. Monthly average of temperature of Souk Ahras region (2000-2022)

Months	Sept	Oct	Nov	Dec	Jan	Feb	Mar	Apr	May	Jun	July	Aug
T (C°)	21.76	17.60	11.85	8.13	6.83	7.65	10.49	14.00	18.16	23.36	26.90	26.23

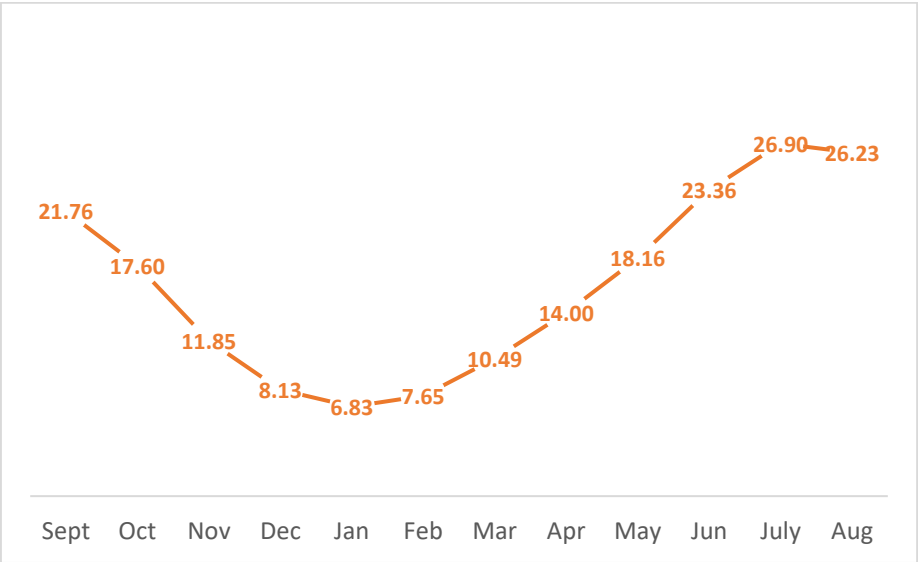


Figure 22 Monthly Average Temperature in the Souk Ahras Region (2000-2022)

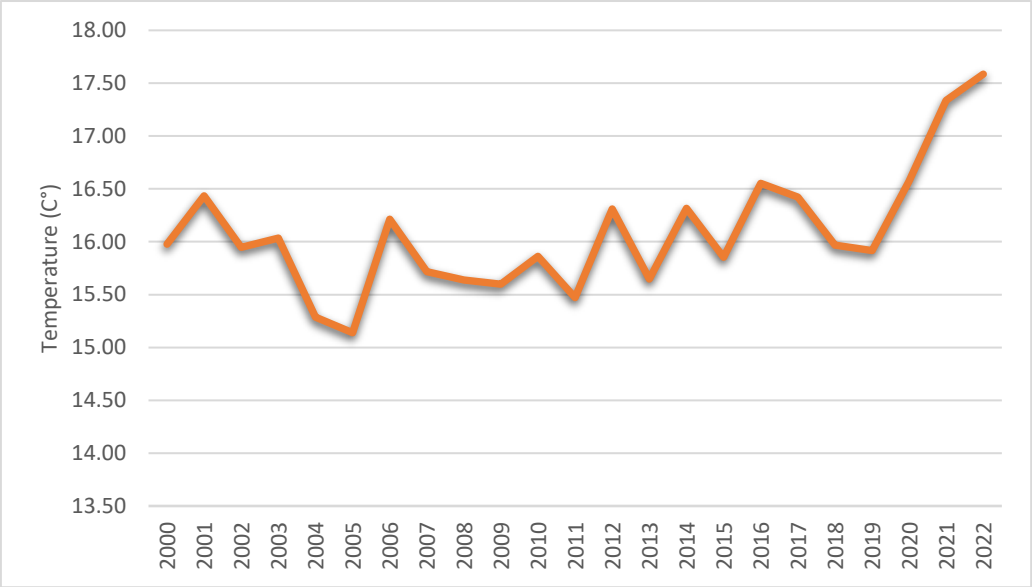


Figure 23 Annual Average Temperature in the Souk Ahras Region (2000-2022)

3. Tebessa

Table 8. Monthly average temperature in the Tebessa region (2000-2022)

Months	Sept	Oct	Nov	Dec	Jan	Feb	Mar	Apr	May	Jun	July	Aug
T (C°)	20.55	15.99	10.02	6.36	5.14	6.10	9.24	13.11	17.49	22.64	26.22	25.23

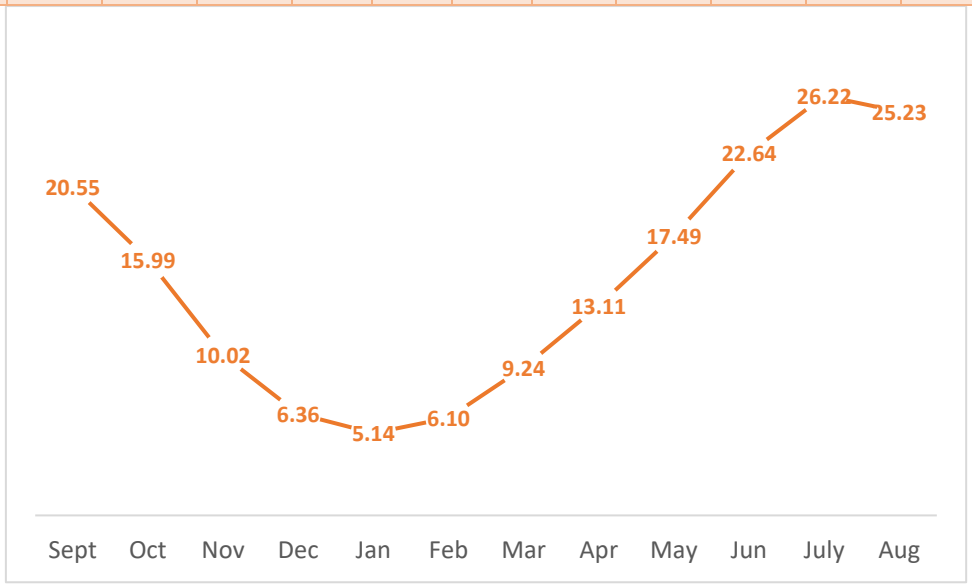


Figure 24 Monthly Average Temperature in the Guelma Region (2000-2022)

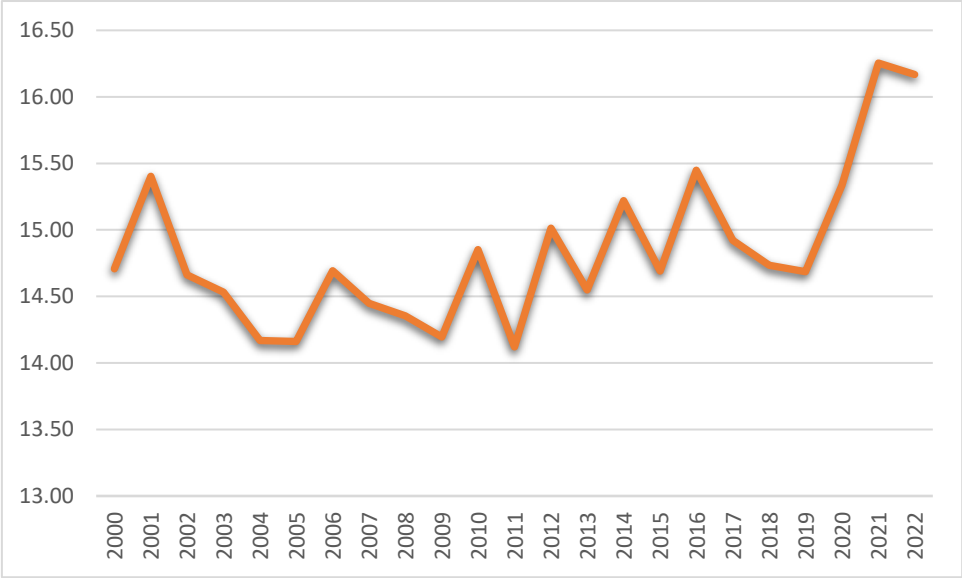


Figure 25 Annual Average Temperature in the Tebessa Region (2000-2022)

4. Khenchela

Table 9. Monthly average temperature in the Khenchela region (2000-2022)

Months	Sept	Oct	Nov	Dec	Jan	Feb	Mar	Apr	May	Jun	July	Aug
T(C°)	20.39	15.62	9.32	5.72	4.56	5.63	8.96	12.87	17.27	22.49	26.18	25.14

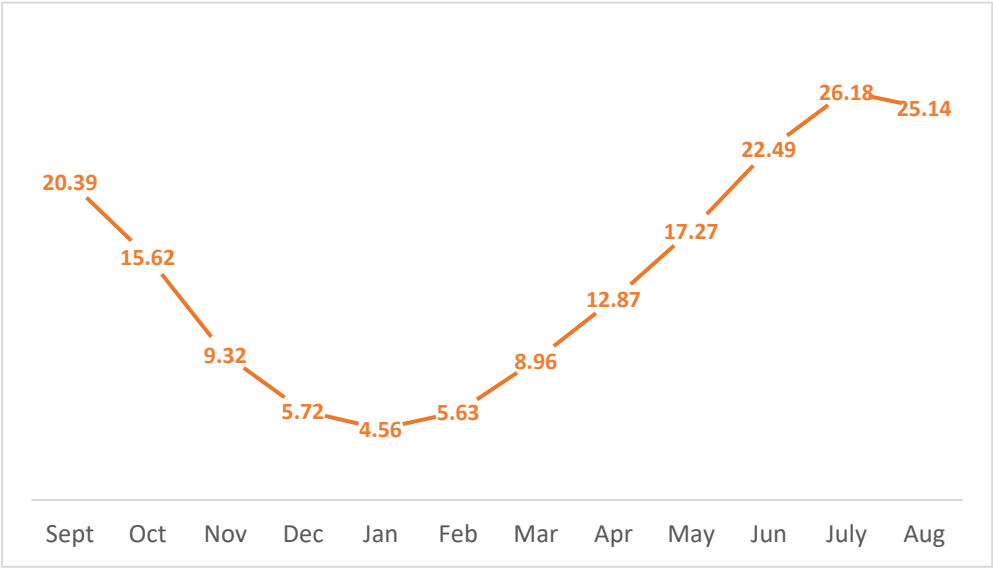


Figure 26 Monthly Average Temperature in the Khenchela Region (2000-2022)

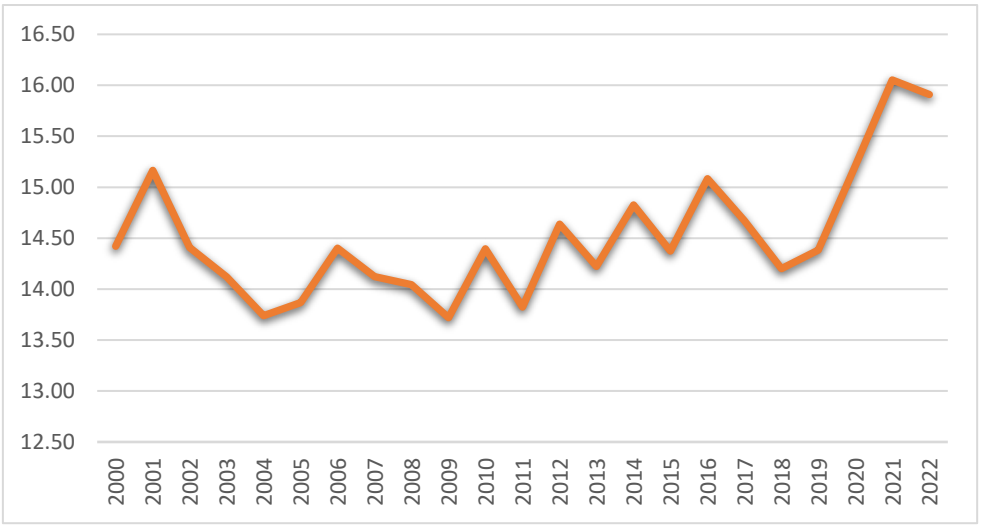


Figure 27 Annual Average Temperature in the Khenchela Region (2000-2022)

❖ *Interpretation*

The line graphs (Figures 20, 22, 24, 26) demonstrate how temperature varies throughout the year. Showing a distinct seasonal pattern. The temperature reaches its highest in June (37.05°C), July (41.28°C) and August (41.25°C) in Guelma, nevertheless in Souk Ahras it attains (23.36 C°) in June, (26.90°C) in July, and (26.23°C) in August, while the region of Tebessa experiences an average of (22.64°C) in June, (26.22°C), and (25.23°C) in August, however, in Khenchela the temperature arrives only at (22.49°C) in June, (26.18°C) in July, (25.14°C) in August. The lowest temperature is observed in January (13.08°C) and December (14.17°C) in Guelma, (6.83°C, 8.13°C) in Souk Ahras, January (5.14°C), February 6.10°C) in Tebessa, and (4.56°C, 5.63°C) in Khenchela. The graph illustrates a gradual rise in temperature from January to July, followed by a continuous reduction from August to December. This trend reflects conventional seasonal changes, with warmer temperatures in the summer and cooler temperatures in the winter months. Additionally, Figures 21, 23, 25, and 27 highlight that the hottest years overall are more recent, specifically 2021 and 2022, whereas lower temperatures were predominantly recorded during earlier years, such as 2004, 2005, and 2011.

II.3 Temperature-Precipitation Relationships

1. The Ombrothermic Diagram

The ombrothermic diagram is a graphical tool used to compare average monthly temperature and precipitation throughout the year. It typically includes two curves:

- Temperature Curve: Monthly mean temperatures are plotted, usually doubled (2T) to allow comparison with precipitation values on the same scale. This highlights seasonal variations between warm and cold periods.
- The precipitation curve: Monthly mean precipitation values are plotted to show how rainfall varies over the year.

A month is considered dry when precipitation (P) is less than or equal to twice the temperature ($P \leq 2T$), according to the Bagnouls and Gaussen, 1957 criterion.

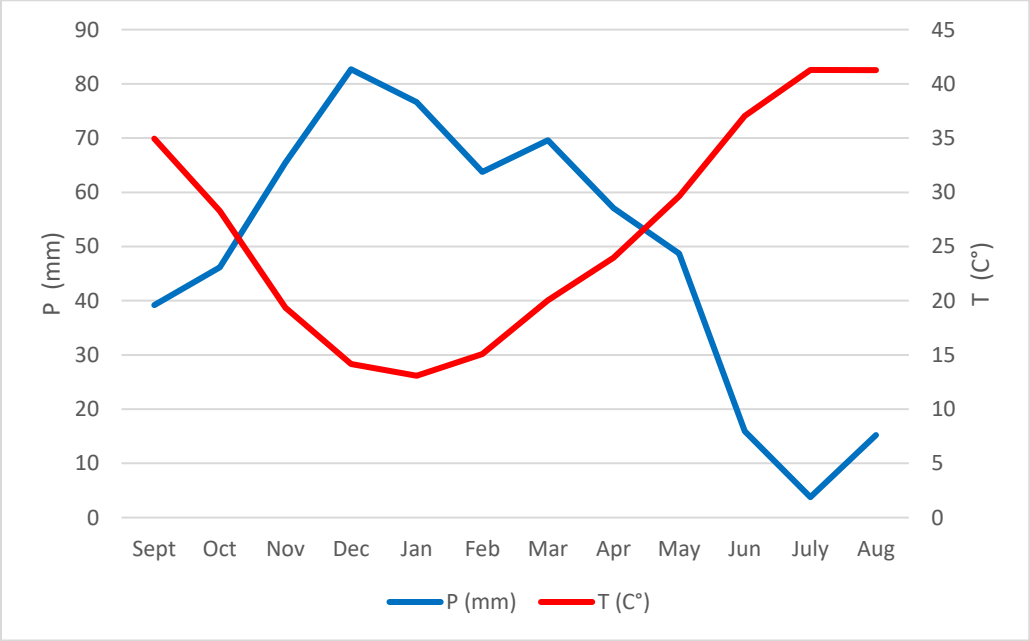


Figure 28 Ombrothermic Diagram of the Guelma Region (2000-2022)

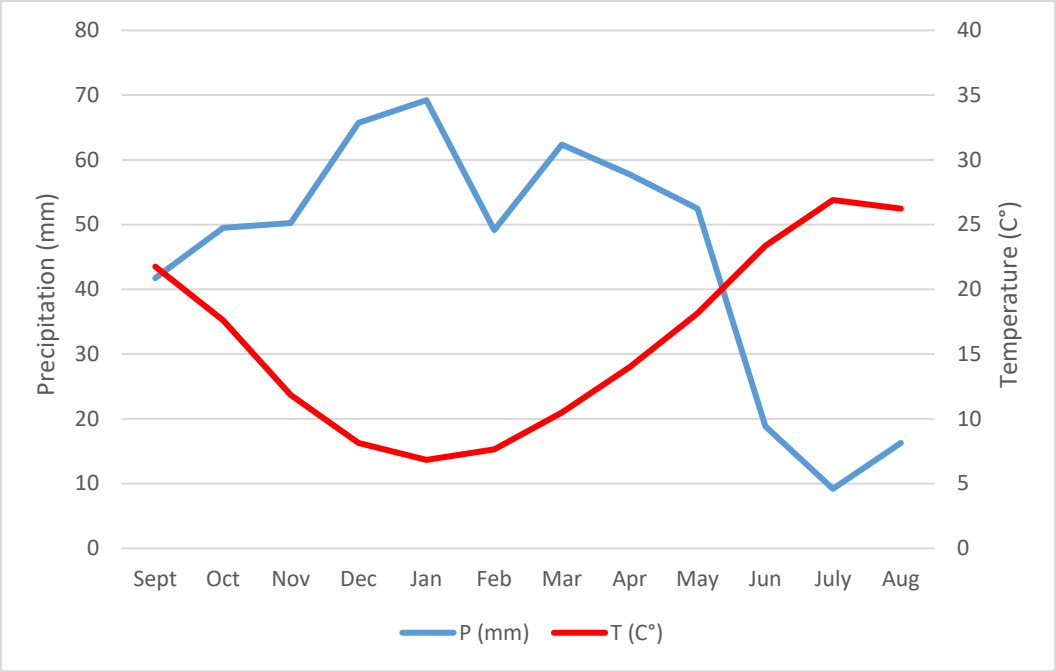


Figure 29 Ombrothermic Diagram of the Souk Ahras Region (2000-2022)

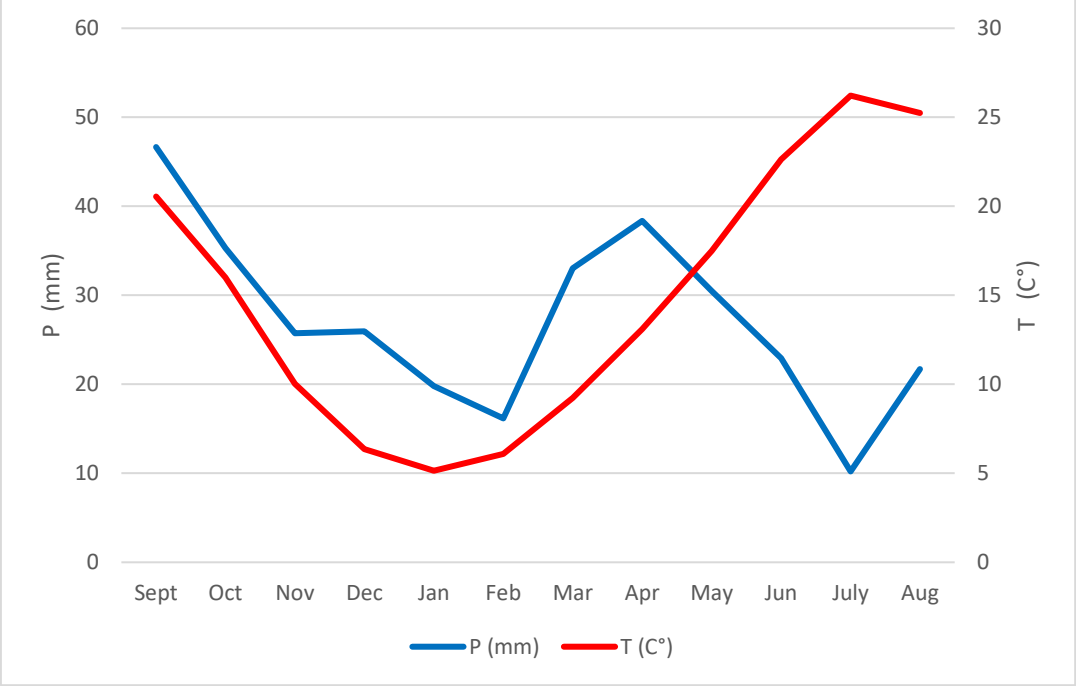


Figure 30 Ombrothermic Diagram of the Tebessa Region (2000-2022)

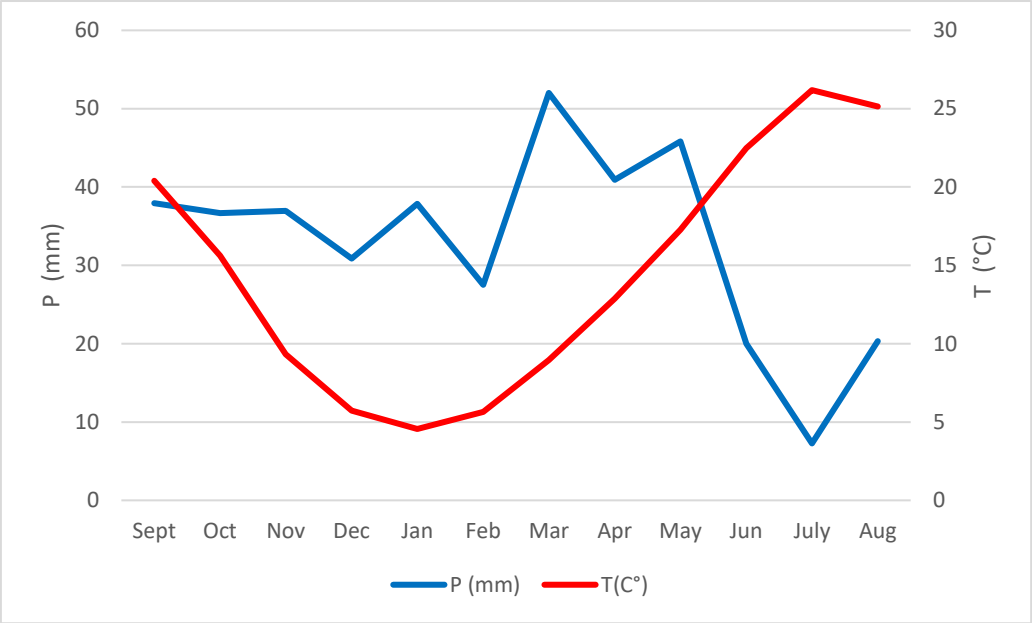


Figure 31 Ombrothermic Diagram of the Khenchela Region (2000-2022)

❖ *Interpretation*

These diagrams (Figures 28, 29, 30, and 31) facilitate understanding of the seasonal climate fluctuations in the study region by illustrating the various wet and dry phases that are crucial for water resource management.

For Guelma:

- Wet and cool periods: Lower temperatures and more precipitation are characteristics of a cooler, wetter season, and these features are present from October through April.
- Dry and hot periods: this period is most evident from May to October, where temperatures rise significantly, and precipitation decreases to minimal levels.

For Tebessa:

- Wet and cool periods: start from September to April, characterized by lower temperatures and relatively higher precipitation. The most notable wet months are September, October, and April.
- Dry and hot: extends from May to August. During this period, the region experiences minimal rainfall and the highest temperatures of the year, indicating a typical hot and dry summer.
- In many cases, September acts as an intermediary month between the hot and dry summer and the colder and wetter autumn. Although there is a chance of rain and a decrease in temperature, the weather is not adequate for what is usually referred to as the "wet and cool" period.

For Khenchela and Souk Ahras:

- Wet and cool period: It seems likely that the cool, wet season in the Khenchela region lasts from September-October through May. During these months, temperatures are generally lower, and there is increased precipitation, especially between December and February. The higher rainfall in March and April further supports the idea that this period is part of the wet season.
- Dry and hot periods: the region is subject to rising temperatures and decreasing precipitation from June to August, being the hottest and driest months.

2. Determination of Aridity (De Martonne Index)

Based on the regime of precipitation and temperatures, De-Martonne in 1923 defined an aridity index (Table 10) by the following relationship:

$$A=P/(T+10)$$

Where:

A: Aridity index

P: Annual average of precipitation (mm)

T: Annual average of temperature (C°)

Table 10. Aridity index according to De Martonne

REGION	P (MM)	T (C°)	ARIDITY INDEX
GUELMA	584.11	26.51	16
SOUK AHRAS	542.44	16.08	20.80
TEBESSA	326.31	14.84	13.14
KHENCHELA	394.09	14.51	16.08

Table 11. Classification of climate type according to aridity index values

I < 5	Hyper-arid climate
5 < I < 7,5	Desert climate
7,5 < I < 10	Steppe climate
10 < I < 20	Semi-arid climate
20 < I < 30	Temperate climate

According to De Martonne (Table 11), an A value between 20 and 30 characterizes a temperate climate with a tendency toward semi-arid conditions in the summer, which describes the Souk Ahras region. While the rest of the study zone, however, falls under the semi-arid climate type.

3. Determination of Soil Moisture (Euverte method)

The Euverte method relies on two essential parameters, which are temperature and precipitation, established every month. The ratio P/T allows for understanding the evolution of soil moisture. This ratio also helps define four types of regimes: (Table 12)

Table 12. Classification of types of regimes according Euverte method

(P/T) < 1	The regime is very dry
1 < (P/T) < 2	The regime is dry
2 < (P/T) < 3	The regime is sub-humid
(P/T) > 3	The regime is humid

Table 13. Variation of P/T ratio values in the study zone

Months	Sept	Oct	Nov	Dec	Jan	Feb	Mar	Apr	May	Jun	July	Aug
P/T Guelma	1.12	1.63	3.38	5.83	5.86	4.23	3.47	2.38	1.64	0.43	0.09	0.37
P/T Souk Ahras	1.92	2.81	4.24	8.08	10.13	6.43	5.95	4.13	2.89	0.81	0.34	0.62
P/T Tebessa	2.27	2.21	2.57	4.08	3.85	2.65	3.58	2.93	1.74	1.01	0.39	0.86
P/T Khenchela	1.86	2.35	3.97	5.39	8.31	4.89	5.81	3.18	2.65	0.89	0.28	0.81

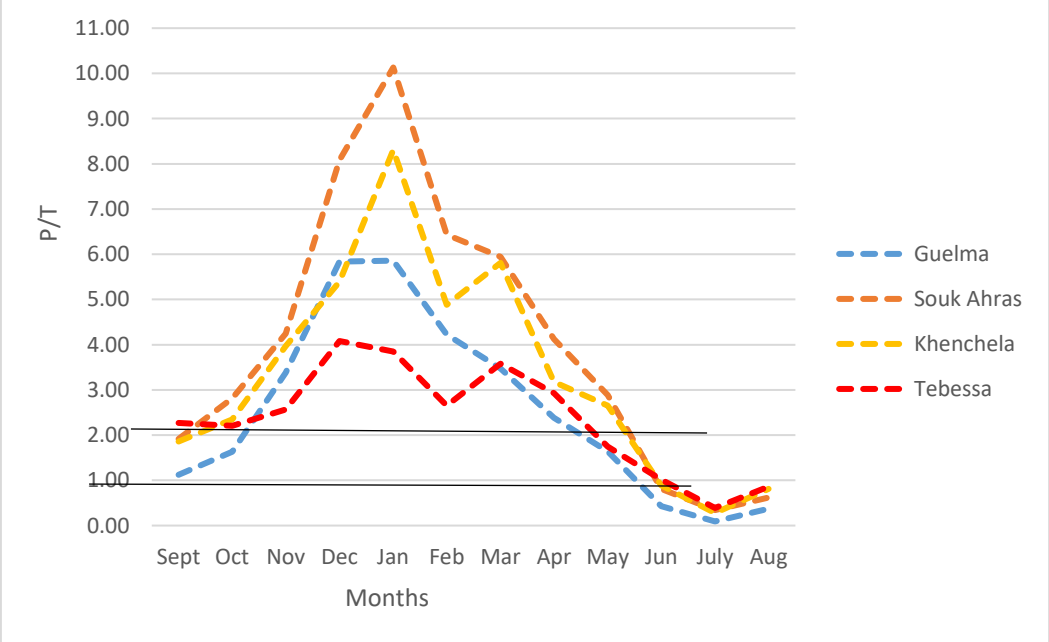


Figure 32 Evaluation of Soil Moisture Using the Euvrete Method

❖ *Interpretation*

The results obtained from the (P/T) ratio, summarized in Table 13 and illustrated in Figure 32, indicate that the humid period begins in November and lasts until April for Guelma and Tebessa, while it starts from October and lasts until May for Souk Ahras and Khenchela, with the highest moisture levels typically occurring between December and February. The sub-humid period in Guelma and Tebessa corresponds to October to November and from April to May, but it starts from September for Tebessa, and characterizes the months of September to late October and from April for Khenchela and May for Souk Ahras to June. The dry period characterizes the months of May to October for Guelma and to June for Tebessa, while it extends from late May to June for Souk Ahras and Khenchela. The very dry regime is dominant in June, July, and August across all regions.

III. Hydrological Balance

The hydrological balance is a quantitative assessment of the inflow, outflow, and storage of water within a specific system, such as a watershed, over a given period of time. It involves calculating the various components, including precipitation, evapotranspiration, surface runoff, water infiltration, and groundwater flow. The hydrological balance helps to understand how water moves through the environment, determining the availability of water resources and the potential for changes in water storage within the system.

The general expression of the hydrological balance represents the equality of water inputs and losses, evaluated over varying periods of time. The formula for the balance is as follows:

$$\mathbf{P = AET + R + I + W}$$

Where:

P: Precipitation

AET: Actual evapotranspiration

R: Runoff

I: Water infiltration

W: change in water storage

III.1 Notion of Potential and Actual Evapotranspiration

Evapotranspiration is paramount in hydrological studies as it affects the water balance and groundwater reserves. It involves two processes: physical evaporation and biological transpiration. Evapotranspiration significantly impacts the water cycle and is influenced by factors such as temperature, air, water, and plant cover etc. We distinguish two different concepts:

- Potential evapotranspiration (PET).
- Actual evapotranspiration (AET).

III.1.1 Potential Evapotranspiration (PET)

Potential evapotranspiration (which expresses the height of the evaporated water layer) is the sum of the amounts of water that can evaporate and transpire from a given surface over a well-defined period, assuming sufficient water availability. Several formulas have been proposed by different authors (Turc 1961, Thornthwaite 1948) for calculating potential evapotranspiration (PET). Thornthwaite established a correlation between the mean monthly temperature and PET, where the evaporative power for each month is determined using the following relationship:

$$\boldsymbol{PETc = 16(10T/I)^{a}.k}$$

With:

$I \sum i$ and $\mathrm{i} = (\frac{T}{5})^{1.514}$ and $a = (1.6/100)I + 0.5$

Where:

PET_C: represents corrected potential evapotranspiration (mm)

T: is the mean monthly temperature (°C)

I: is the annual thermal index

i: is the monthly thermal index

a: is the climate exponent

k: correlation coefficient

The values of (P.E.T) calculated for each month are corrected using a coefficient K (Table 14) according to the follow equation: $PETc = PET \times k$

Table 14. Correlation coefficient of each month

Sept	Oct	Nov	Dec	Jan	Feb	Mar	Apr	May	Jun	July	Aug
1.03	0.97	0.86	0.81	0.87	0.85	1.03	1.10	1.21	1.22	1.24	1.16

III.1.2 Actual Evapotranspiration (A.E.T)

It corresponds to the amount of water evaporated or transpired based on actual climatic influences and the availability of water reserves (open water, soil, vegetation). The actual evapotranspiration (AET) deviates more or less from the potential evapotranspiration (PET) depending on the nature of the evaporative surfaces. Also known as the deficit of runoff (Dr), it is, by definition, the difference between precipitation and runoff.

$$\boldsymbol{Dr = P - Q}$$

Where:

P: It is the average annual height of precipitation that falls on the watershed.

Q: It is the average annual height of the depth of runoff.

1. Turc's Formula

This formula is applicable for all climates and is used to estimate actual evapotranspiration (AET) based on precipitation and temperature data.

$$\mathbf{AET} = \frac{P}{\sqrt{0.9 + \frac{P^2}{L^2}}} \qquad \text{with} \quad L = 300 + 25\,T + 0.05\,T^3$$

P: Average annual rainfall in (mm).

L: Parameter dependent on temperature.

T: Average annual temperature, in °C.

However, for the estimation of actual evapotranspiration (AET), we used the Thornthwaite method, where two main cases are distinguished:

- If P – PET > 0, that is, P > PET, then AET = PET.
- If P – PET < 0, that is, P < PET, there are a couple of possibilities in this case:
  - If P + EUR > PET, then AET = PET.
  - If P + EUR < PET, then AET= P + EUR.

2. *Water Balance According to the THORNTHWAITE Method*

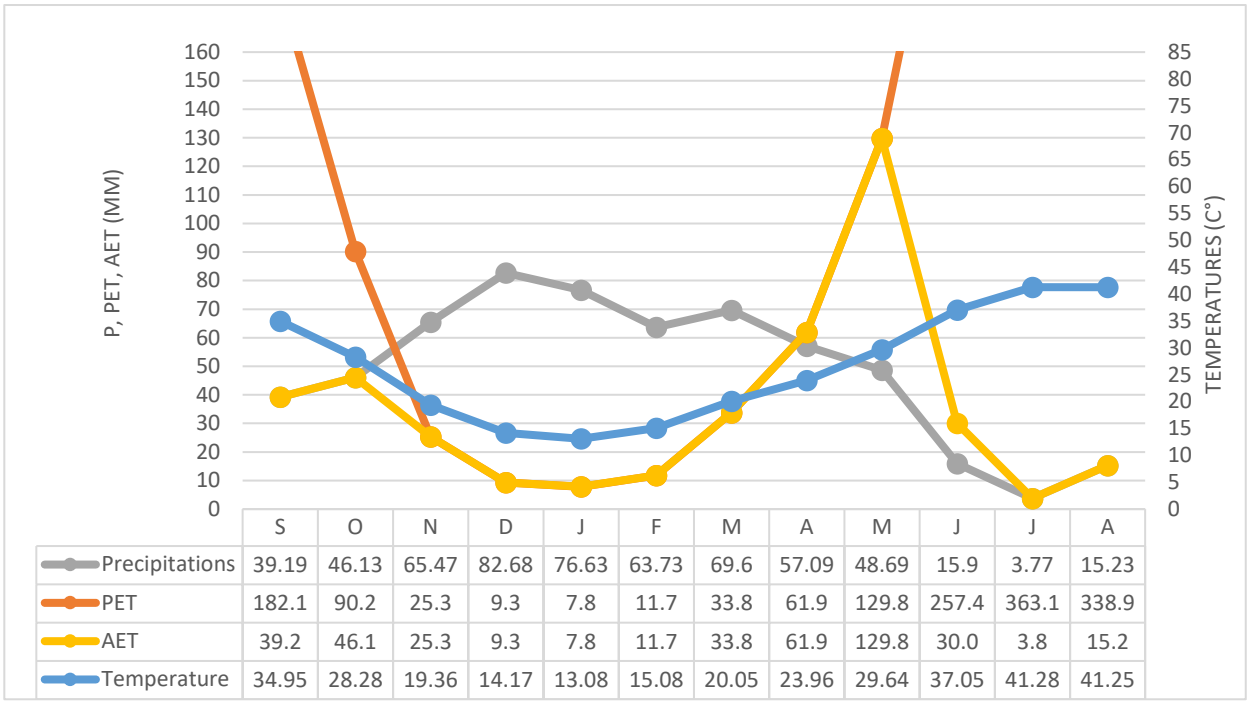
Table 15 displays the water balance for the Guelma region for the years 2000 through 2022:

2.1 Guelma

Table 15. Water balance for Guelma region (2000 to 2022)

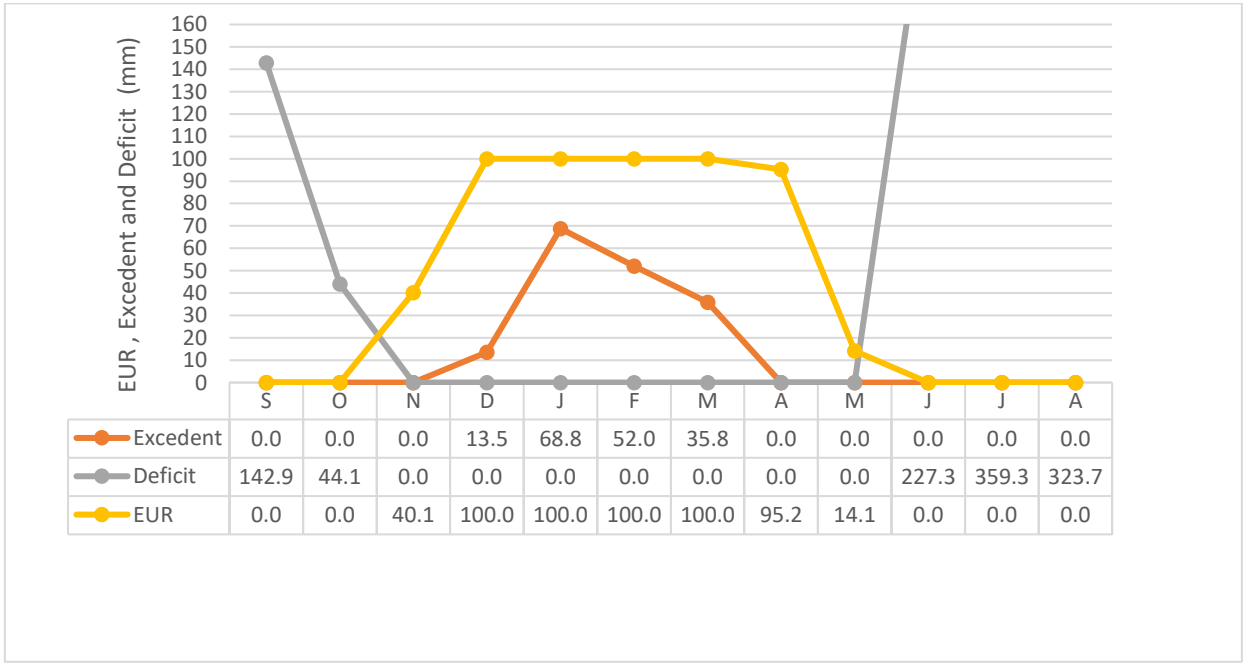
	T	i	LC	PETc	P	WB	WAC	Rv	EUR	AET	Ad	Exc
S	34.95	18.99	1.03	182.05	39.19	-142.86	-0.78	0.00	0.00	39.19	142.86	0.00
O	28.28	13.78	0.97	90.21	46.13	-44.08	-0.49	0.00	0.00	46.13	44.08	0.00
N	19.36	7.76	0.86	25.35	65.47	40.12	1.58	40.12	40.12	25.35	0.00	0.00
D	14.17	4.84	0.81	9.27	82.68	73.41	7.92	59.88	100.00	9.27	0.00	13.54
J	13.08	4.29	0.87	7.81	76.63	68.82	8.82	0.00	100.00	7.81	0.00	68.82
F	15.08	5.32	0.85	11.74	63.73	51.99	4.43	0.00	100.00	11.74	0.00	51.99
M	20.05	8.19	1.03	33.76	69.60	35.84	1.06	0.00	100.00	33.76	0.00	35.84
A	23.96	10.72	1.10	61.88	57.09	-4.79	-0.08	-4.79	95.21	61.88	0.00	0.00
M	29.64	14.80	1.21	129.75	48.69	-81.06	-0.62	-81.06	14.15	129.80	0.00	0.00
J	37.05	20.74	1.22	257.38	15.90	-241.48	-0.94	-14.15	0.00	30.05	227.33	0.00
J	41.28	24.43	1.24	363.08	3.77	-359.31	-0.99	0.00	0.00	3.77	359.31	0.00
A	41.25	24.41	1.16	338.91	15.23	-323.68	-0.96	0.00	0.00	15.23	323.68	0.00
Annually	26.51	158.28		1511.18	584.11	-927.07				413.97	1097.26	170.19

T: monthly temperature in (° C), i: thermal index, LC: latitude coefficient, PETc: Corrected potential evapotranspiration in (mm), P: monthly precipitation in (mm), WB: Water Balance, WAC: Water Availability Coefficient, RV: Reserve volume in (mm), EUR: easily usable reserves in (mm), AET: Actual evapotranspiration in (mm), Ad: Agricultural deficit in (mm), Exc: excess in (mm).



	S	O	N	D	J	F	M	A	M	J	J	A
Precipitations	39.19	46.13	65.47	82.68	76.63	63.73	69.6	57.09	48.69	15.9	3.77	15.23
PET	182.1	90.2	25.3	9.3	7.8	11.7	33.8	61.9	129.8	257.4	363.1	338.9
AET	39.2	46.1	25.3	9.3	7.8	11.7	33.8	61.9	129.8	30.0	3.8	15.2
Temperature	34.95	28.28	19.36	14.17	13.08	15.08	20.05	23.96	29.64	37.05	41.28	41.25

Figure 33 Graphic Representation of Thornthwaite's Water Balance Sheet of the Guelma Region (2000-2022)



	S	O	N	D	J	F	M	A	M	J	J	A
Excedent	0.0	0.0	0.0	13.5	68.8	52.0	35.8	0.0	0.0	0.0	0.0	0.0
Deficit	142.9	44.1	0.0	0.0	0.0	0.0	0.0	0.0	0.0	227.3	359.3	323.7
EUR	0.0	0.0	40.1	100.0	100.0	100.0	100.0	95.2	14.1	0.0	0.0	0.0

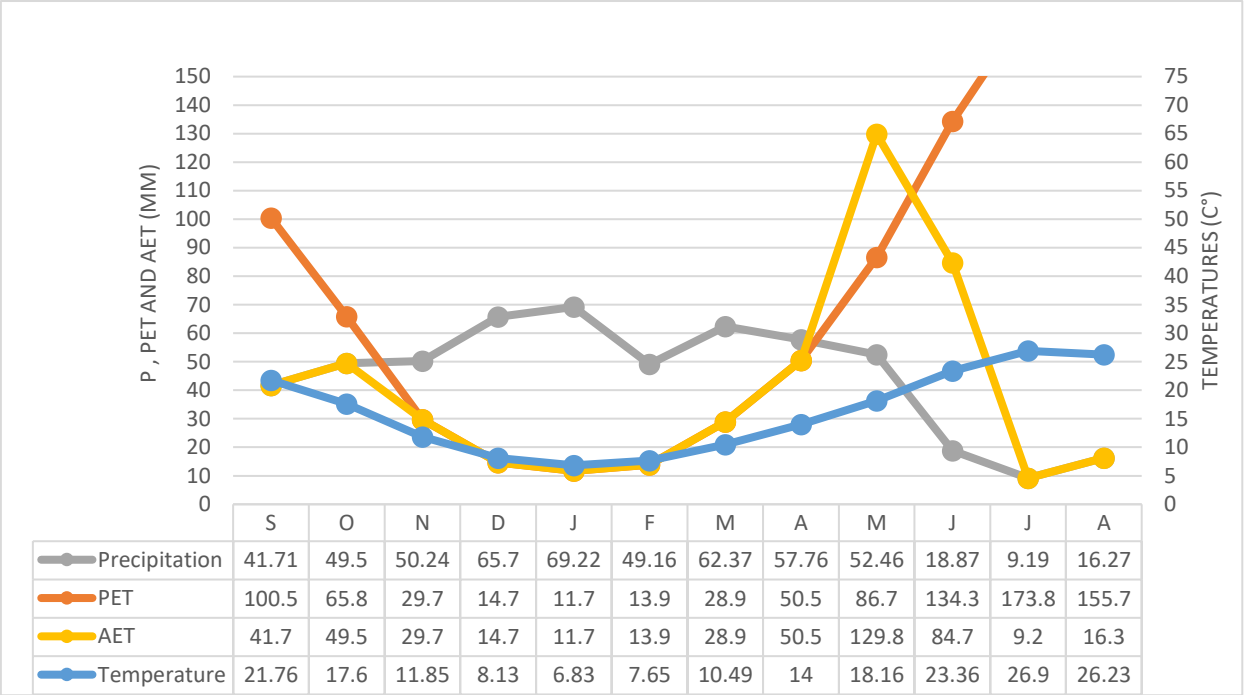
Figure 34 Graphic Representation of the Hydrological Balance of the Guelma Region (2000-2022)

2.2 Souk Ahras

Table 16. Water balance for the Souk Ahras region (2000-2022)

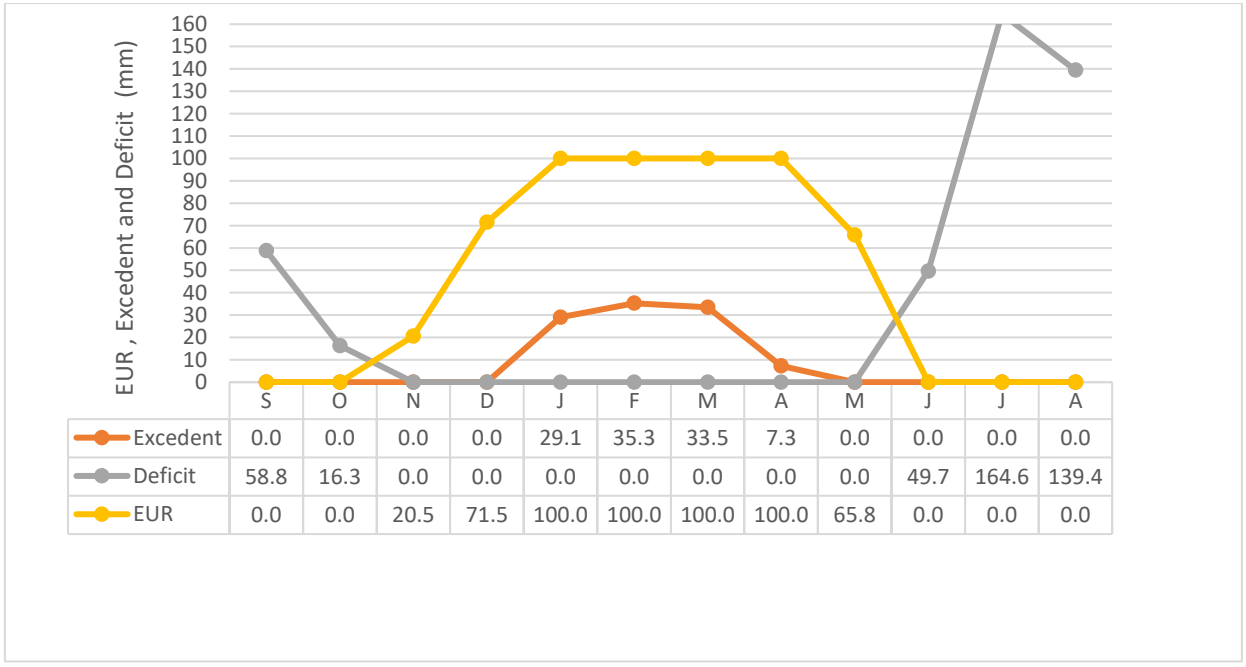
	T	i	LC	PETc	P	WB	WAC	RV	EUR	AET	Ad	Exc
S	21.76	9.27	1.03	100.47	41.71	-58.76	-0.58	0.00	0.00	41.71	58.76	0.00
O	17.60	6.72	0.97	65.85	49.50	-16.35	-0.25	0.00	0.00	49.50	16.35	0.00
N	11.85	3.69	0.86	29.70	50.24	20.54	0.69	20.54	20.54	29.70	0.00	0.00
D	8.13	2.09	0.81	14.69	65.70	51.01	3.47	51.01	71.55	14.69	0.00	0.00
J	6.83	1.60	0.87	11.72	69.22	57.50	4.91	28.45	100.00	11.72	0.00	29.05
F	7.65	1.90	0.85	13.90	49.16	35.26	2.54	0.00	100.00	13.90	0.00	35.26
M	10.49	3.07	1.03	28.88	62.37	33.49	1.16	0.00	100.00	28.88	0.00	33.49
A	14.00	4.75	1.10	50.51	57.76	7.25	0.14	0.00	100.00	50.51	0.00	7.25
M	18.16	7.05	1.21	86.65	52.46	-34.19	-0.39	-34.19	65.81	129.80	0.00	0.00
J	23.36	10.32	1.22	134.34	18.87	-115.47	-0.86	-65.81	0.00	84.68	49.67	0.00
J	26.90	12.78	1.24	173.77	9.19	-164.58	-0.95	0.00	0.00	9.19	164.58	0.00
A	26.23	12.30	1.16	155.71	16.27	-139.44	-0.90	0.00	0.00	16.27	139.44	0.00
Annually	16.08	75.54		866.18	542.45	-323.73				480.54	428.79	105.06

T: monthly temperature in (°C), i: thermal index, LC: latitude coefficient, PETc: Corrected potential evapotranspiration in (mm), P: monthly precipitation in (mm), WB: Water Balance, WAC: Water Availability Coefficient, RV: Reserve volume in (mm), EUR: easily usable reserves in (mm), AET: Actual evapotranspiration in (mm), Ad: Agricultural deficit in (mm), Exc: exceed in (mm).



	S	O	N	D	J	F	M	A	M	J	J	A
Precipitation	41.71	49.5	50.24	65.7	69.22	49.16	62.37	57.76	52.46	18.87	9.19	16.27
PET	100.5	65.8	29.7	14.7	11.7	13.9	28.9	50.5	86.7	134.3	173.8	155.7
AET	41.7	49.5	29.7	14.7	11.7	13.9	28.9	50.5	129.8	84.7	9.2	16.3
Temperature	21.76	17.6	11.85	8.13	6.83	7.65	10.49	14	18.16	23.36	26.9	26.23

Figure 35 Graphic Representation of Thornthwaite's Water Balance Sheet of the Souk Ahras Region (2000-2022)



	S	O	N	D	J	F	M	A	M	J	J	A
Excedent	0.0	0.0	0.0	0.0	29.1	35.3	33.5	7.3	0.0	0.0	0.0	0.0
Deficit	58.8	16.3	0.0	0.0	0.0	0.0	0.0	0.0	0.0	49.7	164.6	139.4
EUR	0.0	0.0	20.5	71.5	100.0	100.0	100.0	100.0	65.8	0.0	0.0	0.0

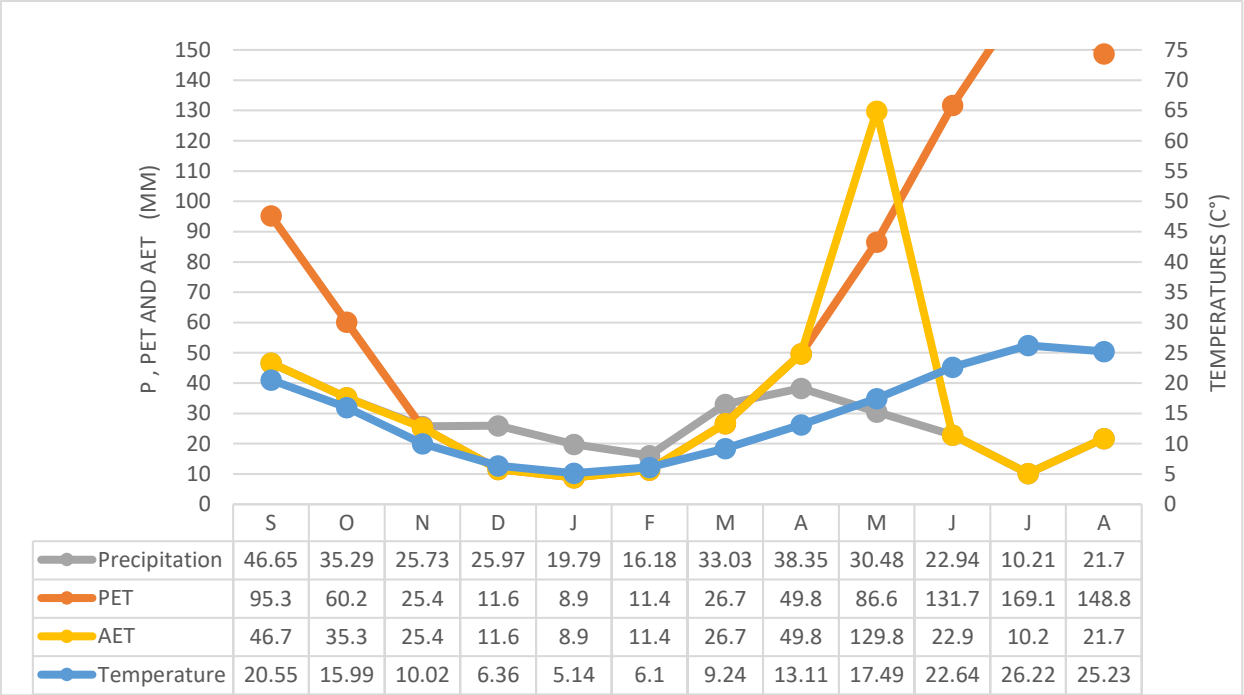
Figure 36 Graphic Representation of the Hydrological Balance of the Souk Ahras Region (2000-2022)

2.3 Tebessa

Table 17. Water balance for the Tebessa region (2000-2022)

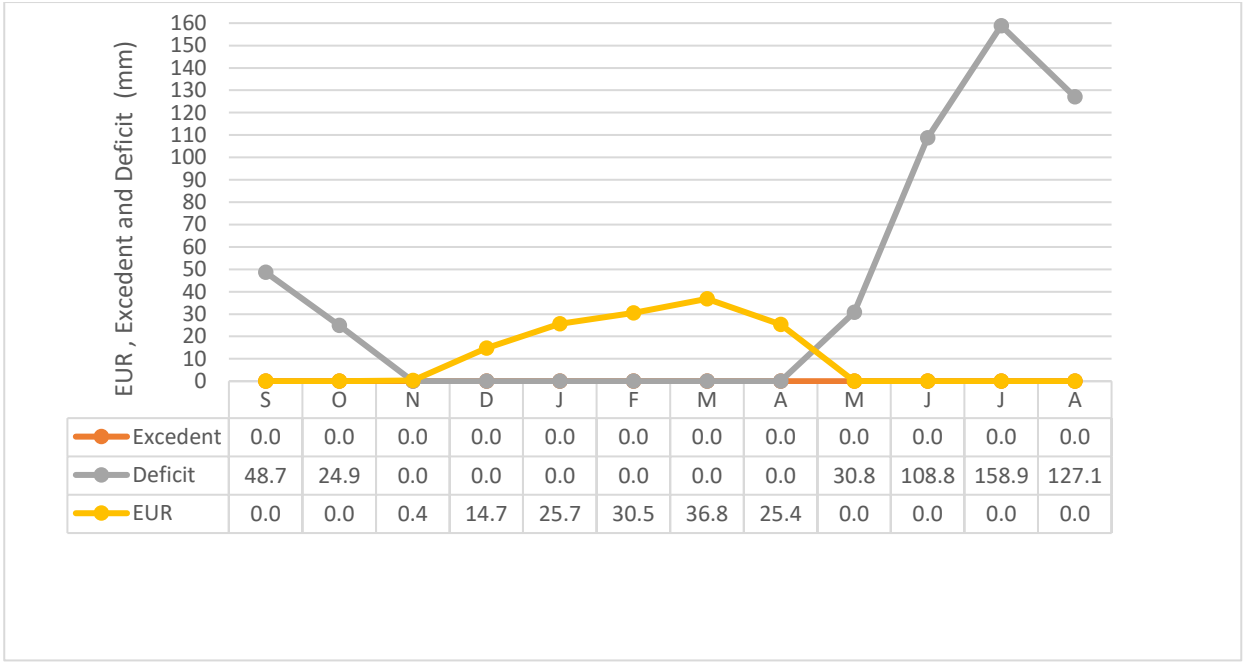
	T	i	LC	PETc	P	WB	WAC	RV	EUR	AET	Ad	Exc
S	20.55	8.50	1.03	95.30	46.65	-48.65	-0.51	0.00	0.00	46.65	48.65	0.00
O	15.99	5.81	0.97	60.20	35.29	-24.91	-0.41	0.00	0.00	35.29	24.91	0.00
N	10.02	2.86	0.86	25.37	25.73	0.36	0.01	0.36	0.36	25.37	0.00	0.00
D	6.36	1.44	0.81	11.59	25.97	14.38	1.24	14.38	14.75	11.59	0.00	0.00
J	5.14	1.04	0.87	8.87	19.79	10.92	1.23	10.92	25.67	8.87	0.00	0.00
F	6.10	1.35	0.85	11.38	16.18	4.80	0.42	4.80	30.47	11.38	0.00	0.00
M	9.24	2.53	1.03	26.70	33.03	6.33	0.24	6.33	36.80	26.70	0.00	0.00
A	13.11	4.30	1.10	49.77	38.35	-11.42	-0.23	-11.42	25.38	49.77	0.00	0.00
M	17.49	6.66	1.21	86.62	30.48	-56.14	-0.65	-25.38	0.00	129.80	30.76	0.00
J	22.64	9.84	1.22	131.70	22.94	-108.76	-0.83	0.00	0.00	22.94	108.76	0.00
J	26.22	12.29	1.24	169.09	10.21	-158.88	-0.94	0.00	0.00	10.21	158.88	0.00
A	25.23	11.59	1.16	148.78	21.70	-127.08	-0.85	0.00	0.00	21.70	127.08	0.00
Annually	14.84	68.23		825.37	326.32	-499.05				400.26	499.05	0.00

T: monthly temperature in (°C), i: thermal index, LC: latitude coefficient, PETc: Corrected potential evapotranspiration in (mm), P: monthly precipitation in (mm), WB: Water Balance, WAC: Water Availability Coefficient, RV: Reserve volume in (mm), EUR: easily usable reserves in (mm), AET: Actual evapotranspiration in (mm), Ad: Agricultural deficit in (mm), Exc: exceed in (mm).



	S	O	N	D	J	F	M	A	M	J	J	A
Precipitation	46.65	35.29	25.73	25.97	19.79	16.18	33.03	38.35	30.48	22.94	10.21	21.7
PET	95.3	60.2	25.4	11.6	8.9	11.4	26.7	49.8	86.6	131.7	169.1	148.8
AET	46.7	35.3	25.4	11.6	8.9	11.4	26.7	49.8	129.8	22.9	10.2	21.7
Temperature	20.55	15.99	10.02	6.36	5.14	6.1	9.24	13.11	17.49	22.64	26.22	25.23

Figure 37 Graphic Representation of Thornthwaite's Water Balance Sheet of the Tebessa Region (2000-2022)



	S	O	N	D	J	F	M	A	M	J	J	A
Excedent	0.0	0.0	0.0	0.0	0.0	0.0	0.0	0.0	0.0	0.0	0.0	0.0
Deficit	48.7	24.9	0.0	0.0	0.0	0.0	0.0	0.0	30.8	108.8	158.9	127.1
EUR	0.0	0.0	0.4	14.7	25.7	30.5	36.8	25.4	0.0	0.0	0.0	0.0

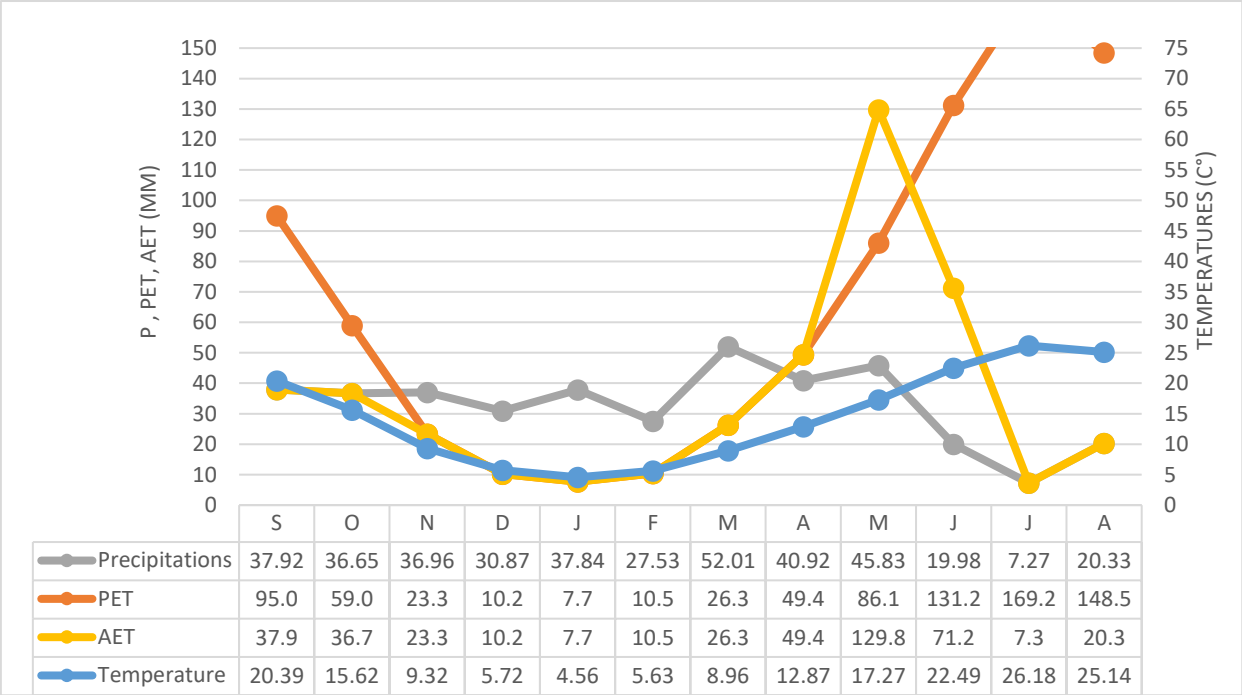
Figure 38 Graphic Representation of the Hydrological Balance of the Tebessa Region (2000-2022)

2.4 Khenchela

Table 18. Water Balance of Khenchela Region (2000-2022)

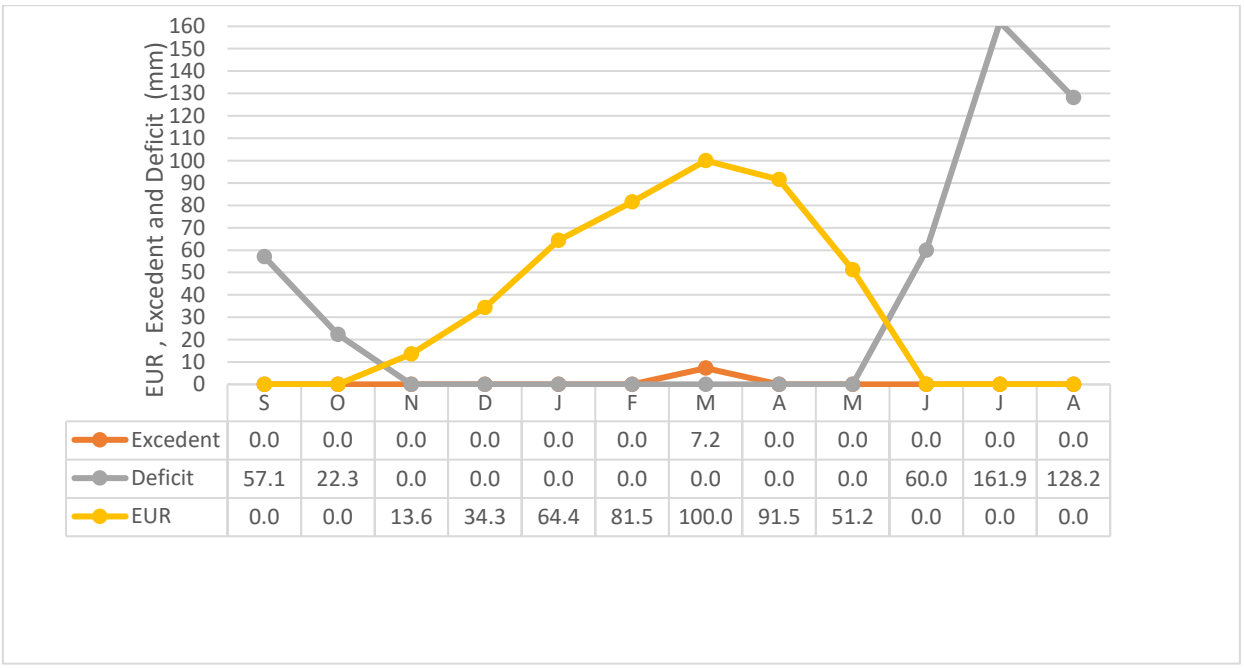
	T	i	CL	PETc	P	WB	WAC	RV	EUR	AET	Ad	Exc
S	20.39	8.40	1.03	95.04	37.92	-57.12	-0.60	0.00	0.00	37.92	57.12	0.00
O	15.62	5.61	0.97	58.99	36.65	-22.34	-0.38	0.00	0.00	36.65	22.34	0.00
N	9.32	2.57	0.86	23.31	36.96	13.65	0.59	13.65	13.65	23.31	0.00	0.00
D	5.72	1.23	0.81	10.23	30.87	20.64	2.02	20.64	34.29	10.23	0.00	0.00
J	4.56	0.87	0.87	7.71	37.84	30.13	3.91	30.13	64.42	7.71	0.00	0.00
F	5.63	1.20	0.85	10.47	27.53	17.06	1.63	17.06	81.48	10.47	0.00	0.00
M	8.96	2.42	1.03	26.25	52.01	25.76	0.98	18.52	100.00	26.25	0.00	7.24
A	12.87	4.18	1.10	49.41	40.92	-8.49	-0.17	-8.49	91.51	49.41	0.00	0.00
M	17.27	6.53	1.21	86.10	45.83	-40.27	-0.47	-40.27	51.25	129.80	0.00	0.00
J	22.49	9.74	1.22	131.23	19.98	-111.25	-0.85	-51.25	0.00	71.23	60.00	0.00
J	26.18	12.26	1.24	169.17	7.27	-161.90	-0.96	0.00	0.00	7.27	161.90	0.00
A	25.14	11.53	1.16	148.53	20.33	-128.20	-0.86	0.00	0.00	20.33	128.20	0.00
Annually	14.51	66.54		816.42	394.11	-422.31				430.57	429.56	7.24

T: monthly temperature in (°C), i: thermal index, LC: latitude coefficient, PETc: Corrected potential evapotranspiration in (mm), P: monthly precipitation in (mm), WB: Water Balance, WAC: Water Availability Coefficient, RV: Reserve volume in (mm), EUR: easily usable reserves in (mm), AET: Actual evapotranspiration in (mm), Ad: Agricultural deficit in (mm), Exc: exceed in (mm).



	S	O	N	D	J	F	M	A	M	J	J	A
Precipitations	37.92	36.65	36.96	30.87	37.84	27.53	52.01	40.92	45.83	19.98	7.27	20.33
PET	95.0	59.0	23.3	10.2	7.7	10.5	26.3	49.4	86.1	131.2	169.2	148.5
AET	37.9	36.7	23.3	10.2	7.7	10.5	26.3	49.4	129.8	71.2	7.3	20.3
Temperature	20.39	15.62	9.32	5.72	4.56	5.63	8.96	12.87	17.27	22.49	26.18	25.14

Figure 39 Graphic Representation of Thornthwaite's Water Balance Sheet of Khenchela Region (2000-2022)



	S	O	N	D	J	F	M	A	M	J	J	A
Excedent	0.0	0.0	0.0	0.0	0.0	0.0	7.2	0.0	0.0	0.0	0.0	0.0
Deficit	57.1	22.3	0.0	0.0	0.0	0.0	0.0	0.0	0.0	60.0	161.9	128.2
EUR	0.0	0.0	13.6	34.3	64.4	81.5	100.0	91.5	51.2	0.0	0.0	0.0

Figure 40 Graphic Representation of the Hydrological Balance of the Khenchela Region (2000-2022)

3. Runoff (R)

Runoff is the water from precipitation (rainfall, snowmelt, etc.) that flows over the land surface into water bodies when the soil is unable to absorb it. This parameter is considered very important from a hydrological point of view. Runoff (Table 19) is calculated using the Tixeront-Berkaloff formula, which depends on precipitation and potential evapotranspiration, namely:

$$R = \frac{P^3}{3(PET)^2}$$

R: Surface runoff calculated in mm.

P: The average annual precipitation in mm.

PET: Refers to the average annual potential evapotranspiration (mm).

❖ *Runoff according to the Tixeront-Berkaloff equation:*

Table 19. Estimation of runoff across the region

	Guelma	Souk Ahras	Tebessa	Khenchela
P	584.11	542.45	326.32	394.11
PET	1511.18	866.18	825.37	816.42
R	29.09	70.92	17.00	30.61

4. Water Infiltration (I)

Based on the general expression of the hydrological balance, which states that inputs and losses are equal over a defined period, infiltration (I) can be determined using the following formula: (Table 20)

$$\mathbf{I = P – R – AET- W}$$

Where:

P: Precipitation in (mm).

AET: Actual evapotranspiration in (mm).

R: Runoff water layer in (mm).

I: Infiltration in (mm).

W: Variation in water reserves in (mm), considered negligible.

❖ *Numerical application*

Table 20. Estimation of water infiltration across the region

	Guelma	Souk Ahras	Tebessa	Khenchela
P	584.11	542.45	326.32	394.11
AET	413.97	480.54	400.26	430.57
R	29.09	70.92	17.00	30.61
I	141.05	0	0	0

5. The Depth of Runoff (E)

$$\mathbf{E = R + I}$$

❖ *Numerical application*

Table 21. Estimation of the depth of runoff across the region

	Guelma	Souk Ahras	Tebessa	Khenchela
E	170.14	70.92	17.00	30.61

The total runoff and infiltrated water in each region (Table 21) is as follows: in Guelma, it is 170.14 mm, representing 29.12% of the average annual precipitation. In Souk Ahras, it is 70.92 mm, accounting for 13.07% of annual precipitation. Khenchela has approximately 30.61 mm, constituting 7.71%, while in Tebessa, the runoff and infiltration depth is 17.00 mm, representing 5.20% of the region's annual precipitation.

6. Interpretation of the Water Balance

The water balance (Figure 33) data for the Guelma region illustrate a marked seasonal variability influenced by precipitation and evapotranspiration:

In months from November to March, during the cooler months, precipitation exceeds potential evapotranspiration (PET) and provides positive water balance values. This period allows for groundwater recharge, reflected by positive values of WAC (Water Availability Coefficient) and RV (Runoff Volume) in November and December, signaling potential contributions to water reserves. From April to October: As temperatures rise, PET surpasses precipitation significantly, leading to negative water balance values (e.g., -323.68 mm in August). This indicates a considerable deficit, with evapotranspiration depleting soil moisture and reducing water availability for recharge. The

negative WB (Water Balance) values during these months highlight intense water loss, limiting runoff and infiltration. Over the year, Guelma shows an annual water deficit of -927.07 mm due to high PET (1511.18 mm) relative to precipitation (584.11 mm). Actual evapotranspiration (AET) meets most of the available precipitation at 413.97 mm, while Excess Water (Exc) and recharge capacity are minimal during the hottest months.

The water balance for Souk Ahras (Figure 34) highlights its semi-arid climate, where annual potential evapotranspiration (PET) of 866.18 mm substantially exceeds annual precipitation (P) of 542.45 mm. This results in a negative water balance (-323.73 mm), signifying that the region's water demand through PET is not met by rainfall, leading to a notable water deficit and limited availability.

From November to April, rainfall temporarily meets or exceeds local demand, leading to a positive balance during these months. December approaches full Easy Usable Reserves (EUR), while January, February, March, and April each reach 100% EUR, representing a period when available rainfall satisfies regional water needs, supports some runoff, and even allows for minor accumulation in the system. As temperatures rise from April onward, PET escalates sharply, driving increasingly high-water deficits. By June, PET far outstrips rainfall, amplifying deficits through the summer months (June to August) when soil moisture and groundwater reserves face substantial depletion. This seasonal fluctuation emphasizes the need for effective water resource planning in Souk Ahras, particularly to mitigate summer shortages.

The water balance for Tebessa (Figure 35) reflects a semi-arid environment characterized by an annual potential evapotranspiration (PET) of 825.37 mm, which significantly exceeds total precipitation (P) at 326.32 mm, resulting in a substantial negative water balance of -499.05 mm. This persistent deficit indicates that the demand for water due to PET is not being met by rainfall, leading to limited water availability throughout the year.

In winter months (November to March), precipitation provides some relief, with relatively lower PET demands. Notably, December (D) and January (J) demonstrate a positive water balance, although only marginally, indicating that rainfall during this period can briefly meet local water needs. However, as spring arrives, the situation becomes more challenging.

From March onward, the PET begins to increase more significantly, leading to greater deficits. April (A) shows a slight negative balance as PET continues to rise, and the situation worsens in May (M) and June (J), where deficits reach alarming levels, reflecting the escalating demand for water. By July (J) and August (A), the water balance indicates a critical decline, with significant negative values implying that both soil moisture and groundwater reserves are under severe stress.

The water balance for Khenchela (Figure 36) reveals a semi-arid climate, characterized by a significant annual potential evapotranspiration (PET) of 816.42 mm compared to total precipitation

(P) of 394.11 mm, resulting in a negative water balance of -422.31 mm. This substantial deficit indicates that the water demand from evaporation and transpiration exceeds the available rainfall, leading to limited water resources throughout the year.

In the winter months (November to March), Khenchela experiences relatively higher precipitation compared to PET, which temporarily alleviates the water stress. Particularly, December (D) and January (J) demonstrate a modest positive water balance, suggesting that rainfall can meet some local water needs during these months. However, as spring approaches, the situation begins to deteriorate.

From March onward, the PET increases significantly, which results in a shift toward negative water balances. April (A) shows a slight negative balance as evaporation demands rise, and this trend continues into May (M), where the deficit deepens further. By June (J) and July (J), the negative water balance becomes pronounced, indicating that the region is unable to sustain its moisture levels as evaporation outpaces precipitation.

In July (J) and August (A), the water balance reaches critical lows, with deficits suggesting severe stress on soil moisture and groundwater resources. The high PET during these months underscores the urgency of implementing effective water management strategies to mitigate the impacts of water scarcity.

Guelma shows a positive infiltration value of 141.05 mm, indicating effective groundwater recharge.

Souk Ahras, Tebessa, and Khenchela exhibit negative infiltration values, suggesting that the combination of high runoff and evapotranspiration results in conditions where infiltration does not occur, which may be influenced by soil saturation or land use practices that enhance surface runoff. This analysis highlights the importance of considering local hydrological conditions and land management practices when evaluating water infiltration in these regions.

The data indicate that, although Guelma receives the highest precipitation, its high potential evapotranspiration limits the amount of water available for runoff. Souk Ahras, despite lower precipitation, shows the highest runoff, reflecting more favorable drainage and storage conditions. In contrast, Tebessa and Khenchela receive the lowest precipitation and exhibit minimal runoff, where most of the incoming water is lost to evapotranspiration and soil infiltration. In Tebessa specifically, the 17 mm of runoff corresponds to baseflow, representing water that infiltrated and was stored during previous wetter periods and is now slowly released from groundwater and soil storage, rather than being generated by current rainfall. This pattern illustrates how the interplay between precipitation, evapotranspiration, and subsurface storage controls hydrological responses in semi-arid regions.

The depth of runoff highlights significant hydrological contrasts among the four regions. Guelma's relatively high runoff depth reflects not only its precipitation regime but also topographic gradients and soil permeability that favor surface flow despite elevated evapotranspiration. Souk Ahras shows a moderate runoff depth, suggesting efficient drainage conditions shaped by a favorable balance between rainfall, evaporation, and landform. In contrast, Khenchela and Tebessa exhibit limited runoff depths, which can be attributed **to** lower precipitation, higher evaporative demand, and soil and terrain characteristics that enhance infiltration and water retention within the subsurface. These factors collectively illustrate how climate, topography, and soil properties interact to control runoff generation and water availability across the study region.

IV. Conclusion

The water balance analysis of Guelma, Souk Ahras, Tebessa, and Khenchela underscores the semi-arid climate's impact on regional water resources, with pronounced seasonal variation in water availability. Winter precipitation provides essential recharge for aquifers and watercourses, especially during the humid period from September to May. Regions like Souk Ahras and Tebessa, and Khenchela benefit from this prolonged sub-humid phase, which supports sustained groundwater recharge and stabilizes water levels. Conversely, high evapotranspiration during the hot, dry summer months drives significant water deficits, particularly in Guelma, where limited rainfall intensifies water scarcity. These findings emphasize the need for adaptive water resource management to optimize recharge during wet periods and mitigate shortages during the arid season.

Chapter Four

Hydrogeological Context

I. Introduction

Water productivity in geological formations is greatly influenced by the characteristics, cohesiveness, and structure of the rock that retains and circulates the water. This is the reason that geological formations are separated into hydrogeological units, each of which is distinguished by a unique hydrodynamic behaviour. Leading to a hydrogeological classification: aquitards, describe a semi-permeable formation with a limited capacity of exploitation, aquifer: constitutes a sufficiently porous and permeable formation to allow the extraction of a significant amount of groundwater, and aquicludes: refer to impermeable formations, making them unusable for groundwater purposes.

The hydrogeological study of the research area is essential for identifying the many existing aquifers and improving our understanding of the various formations that constitute them. The aim is to provide an overview of several recharge and discharge sites, to understand the behavior of the aquifers, which helps address the questions outlined in our research problem.

II. Hydrogeological Identification and Characterization of Aquifers

Given that our study zone is composed of four wilayas, we will examine each one individually. This approach will allow us to gain detailed insights into the specific hydrogeological characteristics and aquifer behaviors within each area. After studying each of the four wilayas individually, we will compare our findings to highlight similarities and differences in their hydrogeological characteristics.

1. The Region of Guelma

In the hydrogeological system of Guelma, the area is characterized by a collapsed zone filled up with Miocene deposits (clays and marls with gypsum) and Quaternary deposits (heterogeneous alluvial terraces). With a great thickness and high permeability, these latter form a significant aquifer recharge by rainwater infiltration and lateral inputs from the Seybouse watershed, which flows between two impermeable thresholds formed by Triassic marls to the east. The infiltrations flow deep underground, creating a large thermal reservoir in the study area and surrounding regions.

With the description of the various geological formations and the interpretation of stratigraphic logs from exploitation and exploration boreholes conducted by DRE Guelma (Water Resources Directorate of Guelma Province), along with geoelectric and gravimetric profiles collected from different studies, it is possible to identify four aquifers as follows:

1.1 The Alluvial Aquifer of Guelma

The Guelma alluvial aquifer is a collapsed basin covering an area of 106 km², located in the Oued Seybouse valley, predominantly on its right bank. The aquifer is traversed by the Oued Seybouse from west to east, extending from Medjez Amar to Nador. Dating from the Mio-Pliocene-Quaternary period (Sogréah, 2005) Its bedrock is formed by Miocene deposits consisting of clays and gypsiferous marls, with Quaternary deposits comprising heterogeneous alluvium arranged in a series of terraces, which can be described as follows:

1.1.1 The Lower Terrace (the current aquifer)

It is the valley in the north through which the current Oued Seybous flows, covering an area of 44 km². It is primarily composed of sand, pebbles, and gravel, with its thickness increasing from west to east, ranging from 8 meters north of the city of Guelma to 16 meters north of Boumahra. It rests on a gypsum marl and Miocene clay bedrock in its western part, and on clay and Numidian sandstone in the east. The aquifer is exploited by ordinary wells and has a transmissivity ranging from 10^{-3} to $8.9 * 10^{-3}$ m²/s.

1.1.2 The Upper Terrace (the ancient aquifer)

It is located to the south of the middle terrace, and composed of two superposed aquifers: an unconfined aquifer located between 0 and 50 meters within the pebbles, sands, and gravels of the Quaternary, and a semi-confined aquifer situated between 70 and 100 meters within coarse Pliocene alluvium. The two aquifers are separated in places by a clay layer 10 to 20 meters thick. In the unconfined aquifer, transmissivity values range between 10^{-3} and 10^{-2} m²/s, and storage coefficients between 4% and 10%, which can be equated to porosity (Castany, 1982). In the semi-confined aquifer, transmissivity is around 10^{-3} m²/s, and the storage coefficient is 1%, which is 10 to 100 times smaller than porosity (Banton et al., 1997).

1.1.3 The Middle Terrace (the travertine limestone aquifer)

It consists of relatively fine detrital material alternating with clay layers. The bedrock is consistently marl with gypsum. (Sogréah, 2005). The surface area of the travertines containing an aquifer is only 12.5 km², with a thickness of 55 meters.

- **Flow Patterns, Piezometry, and Hydrogeological Cross-Section**

For the lower aquifer, there is general drainage through the Oued Seybouse. The average hydraulic gradients are around 0.0043 during high water periods and 0.004 during low water periods. For the aquifer of the upper terraces and Pliocene alluvium, the general flow is directed northward, with a gradient ranging between 0.09 and 0.01, decreasing in the direction of the flow. The travertine

aquifer shows the same flow direction as the upper terrace aquifer, suggesting that it partly feeds the latter. The interactions between the different aquifers consist of the travertine aquifer supplying the alluvium aquifer, and the upper terrace aquifer draining towards the current valley above the gypsum marl threshold, as well as towards the Oued Boussorra valley above the yellow marls with puddingstone.(Benmarce, 2015).

The spacing of the isopiestic lines in the southern part of the aquifer (Figure 41) indicates a laminar subsurface flow diverging towards the watercourses (tributaries of the Oued Seybouse). In the eastern section, an impermeable boundary is observed, while in the northwestern part, there is a noted convergence towards an area of excessive pumping. The travertine aquifer partially feeds the alluvial aquifer. Overall, the flow within the aquifer moves from south to north (Figure 42).

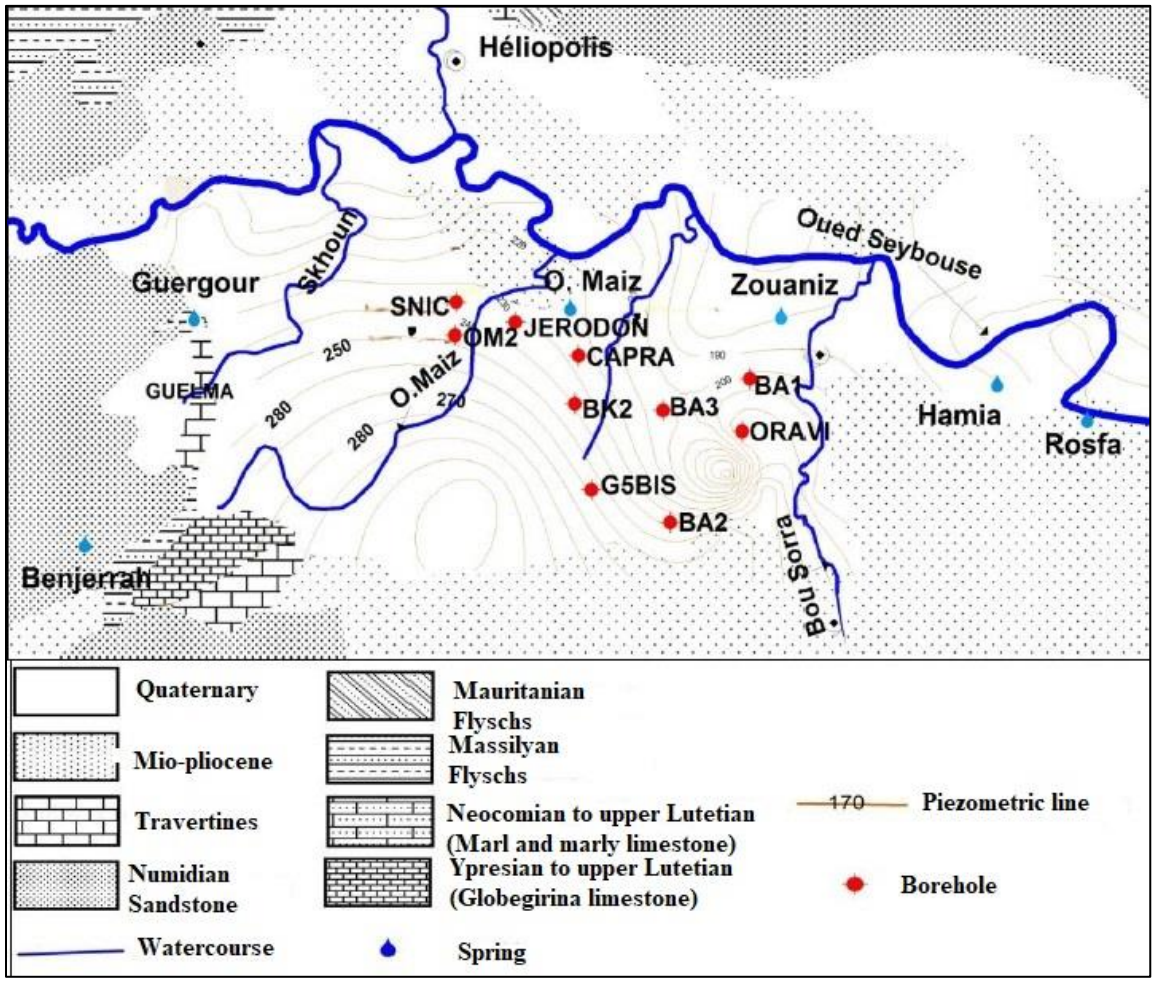


Figure 41 Piezometric Map of the Alluvium Aquifer of Guelma, April 2009 (Benmarce, 2015)

The hydrogeological cross-section (Figure 42) illustrates the connection between the lower terrace aquifer and the upper terrace, which occurs through the middle terrace. Similar aquifer systems are observed extending southward as previously described for the aquifers.

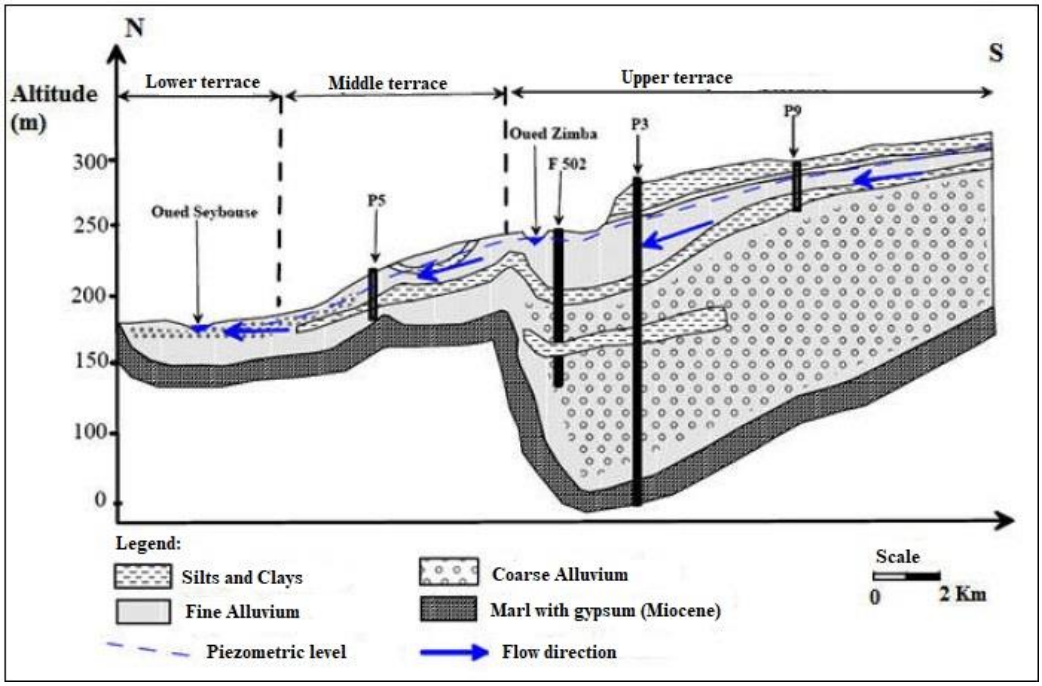


Figure 42 Hydrogeological Cross-Section in the Guelma Plain (Gaud, 1974)

1.2 The Aquifer of the Carbonate Formations of Heliopolis-Fedjoudj

The carbonate formations are represented by neritic limestones, which are part of the northeastern group of the Constantinian neritic series. This aquifer is mainly composed of bio-detrital or micritic limestone and calcareous-dolomitic formations from the Upper Senonian, which are likely to be aquiferous (De Marsily, 1981; Backalowitch and Mangin, 1980). At Ouled Ali (S1), these formations are represented by several dozen meters of Upper Senonian layers, dipping eastward into depth, then reappearing first in the Bouzitoune (Heliopolis) region, and later near the Roman spring (Hammam Bradaa). The depth limits are unknown. The boreholes at El Fedjoudj II, Bouzitoune, and Hammam Bradaa suggest the continuity of these formations along the Djebel Debegh axis towards Hammam Bradaa. From the perspective of system analysis and exploitation, the study area's neritic formations represent a very interesting karstification that is situated at varying depths between 50 and 350 meters.

- **Flow Patterns, and Piezometry**

According to Benmarce (2015)Various piezometric surveys have shown a general flow from west to east. The groundwater flows toward two main borehole areas: one in Bouzitoune and the other in the Hammam Bredaa area.

1.3 The Aquifer of Carbonate Formations: Region of Ras El Agba-Sellaoua-Announa

In this area, two distinct geological units can be identified:

1. ***Tellian Unit***: This unit consists of Eocene marly-limestone terrains that contain aquifer levels. Several springs are found at the base of the Ypresian limestone ridge. According to (Vila J. M, 1980)The limestone formations belong to the Tellian Paleogene series. In the recognition and exploitation boreholes at Ain Brinis, three main layers are identified, from top to bottom: (i) Lutetian gray marls, (ii) Ypresian massive limestones, and (iii) Paleocene marls with debris.
2. ***Sellaoua Unit***: The springs emerging from these limestone formations are more significant than those of the Tellian unit. The main springs are Ain Beida and A. Karma (Sellaoua Announa).

- **Flow Patterns and Piezometry :**

The flow directions vary depending on the water levels in the boreholes and their location. In the northern flank (Sellaoua unit), the flow moves toward the Oued Cherf (a southern tributary of the Oued Seybouse), while in the western flank (Tellian unit), the flow heads toward the Oued Bouhamdane (a western tributary of the Oued Seybouse. The limited available data revealed at least two main groundwater flow directions:

- A south-to-north flow along the northern flank of Djebel Announa, where the Ain Karma and Ain Beida springs emerge.
- A westward flow toward the Ain Sbaa Spring.

1.4 The Aquifer of Carbonate Formations in the Bouhachana–Ain Larbi Region

Nine exploited boreholes in this aquifer produce a total flow rate of 143 l/s, equivalent to 4.5 Hm^3/year. Limestone formations, which surface in certain areas, especially on the right bank of Oued Halia (Bouhachana), are a continuation of the Sellaoua Announa series. Stratigraphic logs from the boreholes reveal fissured and karstified zones at depths between 70 and 100 meters, as evidenced by water losses and the absence of cuttings during drilling. This carbonate formation constitutes a significant aquifer that once supplied Guelma before the Hammam Debagh dam waters were utilized. The former Halia Spring, which flowed at nearly 100 l/s before the first boreholes were drilled, is a clear indicator of the aquifer's capacity.

2. The Region of Souk Ahras

As a whole, the study area's hydrogeology is characterized by two distinct zones. The northern region is mountainous, predominantly composed of Triassic gypsiferous, sandstone, and clayey formations, interspersed with rock fragments of various sizes. This diapiric structure is not favorable for the development of significant aquifer potential. In contrast, the southern region is highly tectonized and subsiding, which supports the formation of multi-layered aquifers connected through an expanded network of faults.

Between these two contrasting hydrogeological zones lies the Medjerda Valley, with a permanently flowing river deeply embedded between eroded anticline ridges. The river traverses the contact between Oligocene sandstones and limestones, and then over alternating marl and marl-limestone Cretaceous formations. Although these formations possess conditions favorable for reservoir development, the narrow basin geomorphology, steep slopes, and elevated Maastrichtian and Campanian outcrops do not support large, high-capacity water reservoirs.

According to many research sources (Bekkouche mohamed faouzi, 2016; Bouroubi Ouadfel et al., 2021; Bouroubi-Ouadfel et al., 2018; Djabri et al., 2020; Hadji, 2013; Rouaibia & Djabri, 2017) the Souk Ahras region has a complex and multilayered aquifer system, mainly featuring the following aquifers:

2.1 Shallow Aquifer in Mio-Plio-Quaternary Formations

The shallow aquifer in the Souk Ahras region is primarily composed of unconsolidated sediments, including sandstone and clay alluvium (both recent and old), gravels, sands, conglomerates, and marl, deposited during the Mio-Pliocene-Quaternary period. Its depth varies, but

it generally lies close to the surface. The aquifer's structure can range from unconfined to semi-confined, depending on the presence of overlying impermeable layers. Due to its proximity to the surface, this aquifer is particularly vulnerable to contamination from agricultural runoff, industrial pollutants, and other sources of pollution.

2.2 Heterogeneous Aquifers in Eocene and Oligocene Formations

The Eocene and Oligocene formations contain heterogeneous aquifers composed of marls, clays, and calcareous schists. While these formations can store and transmit water, they are less important compared to the overlying Mio-Plio-Quaternary and the deeper Jurassic and Maastrichtian-Campanian aquifers. The water from these aquifers is sometimes influenced by precipitation and snowmelt, particularly at higher altitudes where some cold springs are found.

2.3 Deep Confined Aquifer in Maastrichtian-Campanian Formations

The deep confined aquifer, located within the Maastrichtian-Campanian karstic formations, consists primarily of fractured limestone. This aquifer is under higher pressure and accessed through deep wells, typically ranging from 150 to 350 meters in depth. Its depth and confinement provide natural protection, making it less vulnerable to pollution compared to shallow aquifers. The Maastrichtian chalky limestone aquifer is a vital water resource, known for numerous springs with flow rates generally below 15 liters per second. It is primarily exploited via deep boreholes, which tap into its significant reserves.

2.4 Triassic Evaporites Aquifer

The Triassic evaporites aquifer is located in the northern mountainous region and is characterized by diapiric structures composed mainly of clay-gypsum-salt diapirs and located along major faults or associated with the crestal parts of faulted anticlines. which can limit its aquifer potential. It may be associated with saline groundwater due to the presence of evaporite minerals.

2.5 Jurassic Carbonate Aquifer

The Jurassic carbonate aquifer is a deep aquifer formed in massive limestone formations. It is known for its high permeability, which facilitates efficient groundwater flow. This aquifer is often associated with thermal springs (S10), which emerge through deep faults affecting various geological formations. It plays a significant role in the hydrogeological dynamics of the region.

Flow Patterns, Piezometry, and Hydrogeological Cross-Section

A noteworthy example of a superimposed aquifer system is found in the Taoura syncline (Figure 43). Here, two distinct aquifers coexist:

The first aquifer is unconfined, with an approximate thickness of 40 meters. It is contained within the Mio-Plio-Quaternary formations, rich in marls, conglomerates, sands, and gravels, filling the Taoura syncline. This aquifer is primarily tapped by domestic wells in the northeastern part towards Merahna.

The second aquifer is considered confined, composed of fissured marls and limestones dating from the lower Maastrichtian to the middle Campanian. This aquifer occupies the central part of Taoura and disappears towards the southwest due to the formation of the anticlinal chain towards Madour.

These superimposed aquifers, separated by a thin layer of marl, highlight the complex hydrogeological setting of the Souk Ahras region, where multiple water-bearing units can interact and influence groundwater flow and quality

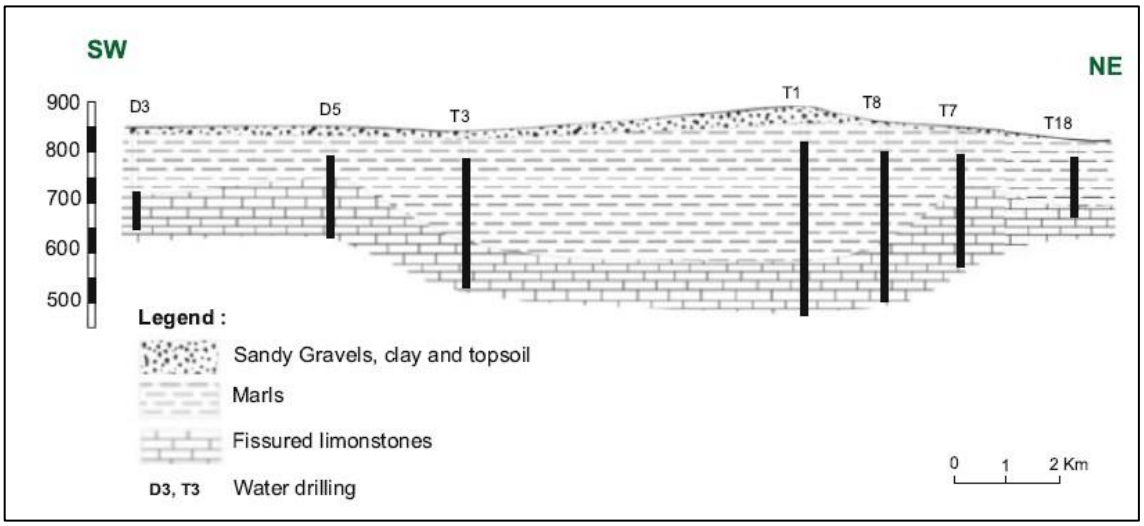


Figure 43 Hydrogeological Cross-Section of the Taoura Region (Djabri et al., 2020)

The thermal karst aquifer of the Taoura syncline is well-known for its discharge through various springs, particularly Hammam Tessa (S11), which emerges due to a major fault. The presence of travertine deposits indicates the former activity of now-extinct thermal springs. The groundwater quality in this aquifer largely depends on factors such as residence time, the lithological nature of the

reservoir, and the types of rocks it flows through. Moreover, the presence of Triassic diapirs near the surface negatively impacts the water quality.

The piezometric map (Figure 44) from 2012 (Djabri et al., 2020) illustrates that groundwater in the Taoura Plain flows from the periphery toward the center, suggesting a lateral recharge contribution. In the southern part of the region, a piezometric dome is observed, which is possibly due to the presence of a groundwater divide. This divide could be the source of two distinct groundwater flow patterns in the area. Recharge primarily originates from the zone between the surrounding relief and the northern part of the plain, particularly within the syncline bordered by the adjacent mountains.

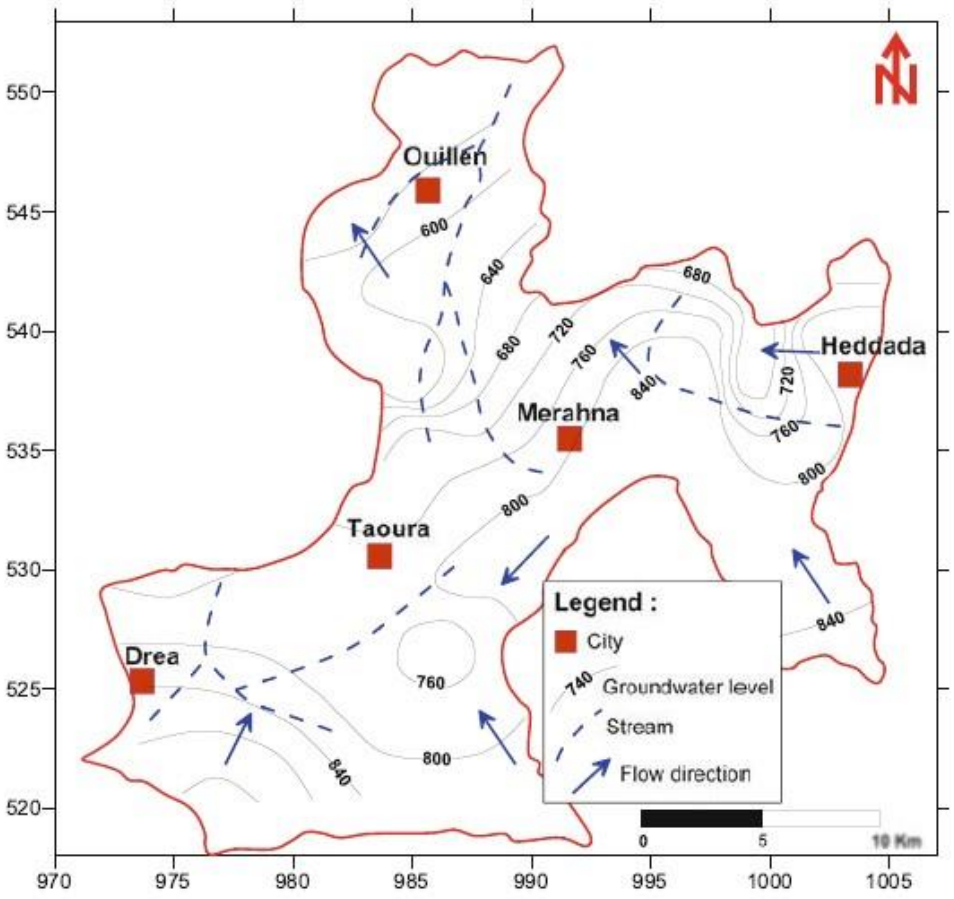


Figure 44 Piezometric Map of the Shallow Aquifer (Djabri et al., 2020)

3. The Region of Tebessa

The Tebessa region was separated into three plains: the Tebessa plain, the Morsot plain, and the El Ouanza plain to cover a large area and discover multiple aquifers. This division allows for a more detailed investigation of the hydrogeological characteristics and aquifer systems within each plain, ensuring a comprehensive understanding of groundwater resources across the region.

3.1 The plain of Tebessa

The analysis of stratigraphic logs and geophysical data in the Tebessa plain reveals three distinct aquifer types:

5.1.1 The Alluvial Aquifer

This aquifer consists of unconsolidated detrital sediments of Mio-Pliocene-Quaternary filling the central basin of the plain. These sediments lie on a marly substratum and extend all over the plain, up to 500 meters thick in some places. The resistivity of this aquifer changes with location; near the limestone borders, it is between 50 and 200 ohm-meters because of the coarser deposits. Contrarily, the resistivity values central to this plain are much lower than 20 ohm-meters, hence indicating finer sediments and higher salinity. With these features, the alluvial aquifer becomes very important yet complex with regard to supply and management, having variability in salinity and permeability in space that allows infiltration from surface waters.

5.1.2 The Karst Aquifer

In contrast, the karst aquifer is primarily composed of fractured limestone formations from the Maastrichtian, Turonian, and Eocene periods, which are essential for its significant hydraulic potential. This aquifer extends to depths of up to 5 km and is characterized by its substantial flow, particularly at notable springs such as Youkous. A key feature of the karst aquifer is its interaction with surrounding geological structures, especially the Maastrichtian limestone outcrops. For instance, S12 Hammamet, classified as a calcium bicarbonate water type (Ca^{2+} - HCO_3^-), reflects the influence of these carbonate reservoir rocks. The abundance of major ions in S12 is ordered as $Ca^{2+} > Na^+ > Mg^{2+} > K^+$ and $HCO_3^- > SO_4^{2-} > Cl^- > NO_3^-$, indicating significant geochemical interactions within the aquifer system. The dominance of calcium bicarbonate facies among various springs, as depicted in the Piper diagram, further emphasizes the aquifer's complex hydrological dynamics and its reliance on carbonate formations for groundwater chemistry.

5.1.3 The Triassic Aquifer

The Triassic formations in the Tebessa region, found near Jebel Djebissa, Jebel Belkfif, and Jebel Hamaimet, also function as aquifers, although their properties vary depending on the specific

geology. The formations consist of sandstones, marls, and evaporites (such as gypsum and halite). The sandstone layers in these formations can act as productive aquifers, particularly where faulting has increased permeability. The Triassic aquifers are not as heavily exploited as the alluvial or karst aquifers, but can provide important deep groundwater resources. The complexity of these formations, especially due to the presence of evaporites and tectonic displacements, can result in variable water quality, with some areas exhibiting higher salinity.

Flow Patterns, Piezometry, and Boundary Conditions of Tebessa Plain

The establishment of the boundary conditions map (Figure 45) is based on the geological formations surrounding the watershed and the arrangement of piezometric curves relative to the topographic limits of the basin. This map has enhanced the understanding of the hydraulic behavior of the aquifer system and the relationship between the existing water tables. The boundary conditions map for the aquifer is obtained from the Hydraulic Directorate of the Wilaya of Tebessa, which was created in 1975 by the CGG company.

The analysis of the elaborated map (Figure 45) allowed us to determine the following boundaries:

- North Boundary: Outflow limit.
- South Boundary: Composed of a complete stratigraphic series from Bekkaria to Ain Chabro, spanning from the Lower Aptian to the Mid Maastrichtian, as well as fractured limestones that constitute an inflow limit (recharge of the aquifer system).
- Northwest Boundary: Inflow limit, as indicated by the established piezometric map. (Figure 47)
- Northeast Boundary: Impermeable limit made up of sandy clays from the Pliocene and Cenomanian marls, with an inflow limit provided by Eocene and Campanian limestones.
- East Boundary: Inflow limit composed of quartz sands and limestone gravel from the Pliocene, with minor recharge from the Triassic formation (Djebel Djebissa)
- West Boundary: Impermeable limit formed by marly formations and limestone marls from the Lower Cretaceous, besides a partial recharge through the Turonian limestones.

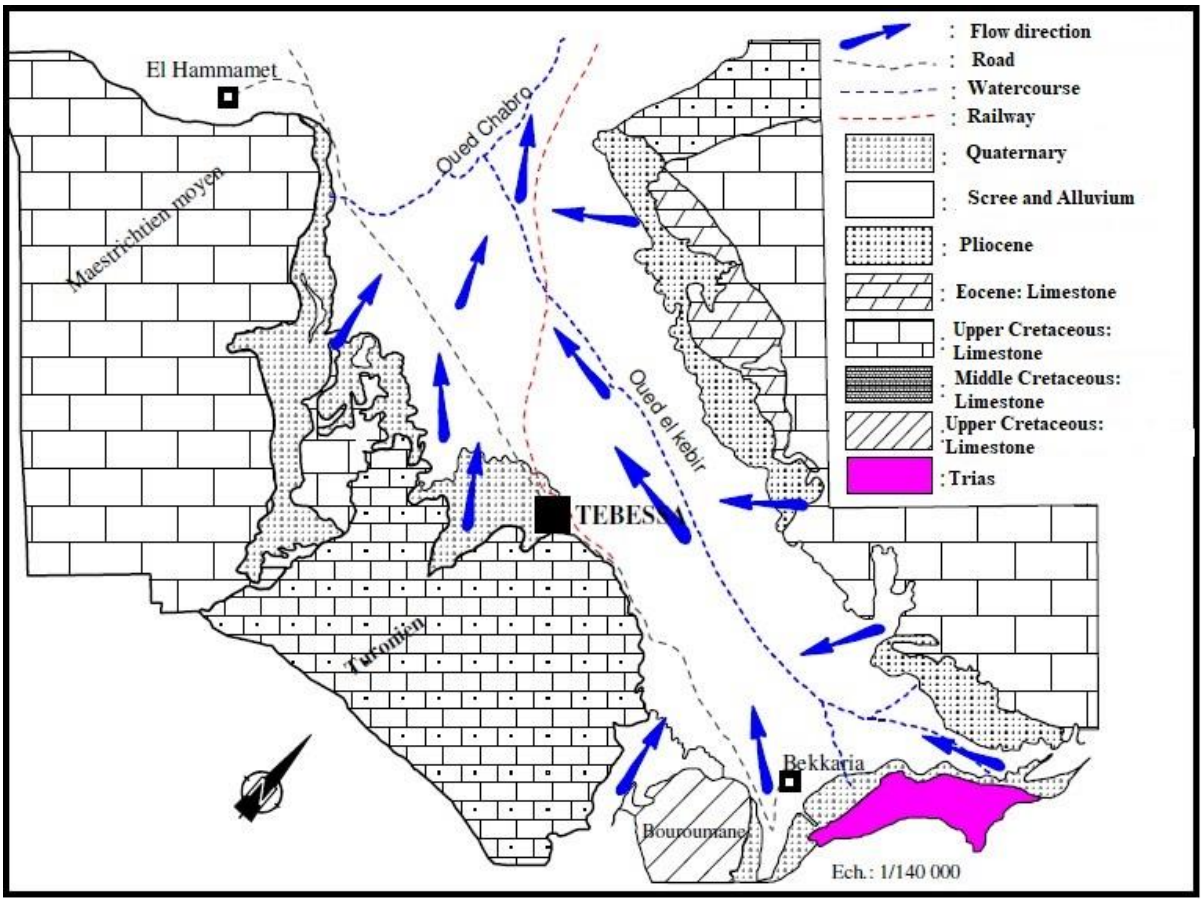


Figure 45 Boundary Conditions and Flow Directions in the Plain of Tebessa (Rouabhia et al., 2010)

The piezometric level (Figure 46) of the area varies from 890 to 760 meters. The analysis of isopiezes curves shows two main directions of flow. First, the southeast-northwest direction follows Wadi El Kebir, then the flow from south to north, starting at El Hammamet and continuing to Morsot. The isopiezes curves become regular in the middle zone, reflecting a homogeneous flow.

In addition, in the southeast, the direction of flow axes diverges, reflecting the recharge from the Djebissa mountain. The contour lines on the map show that the hydraulic gradient is steeper where the lines are closer together toward the center of the plain. The recharge to groundwater through this aquifer is a result of precipitation, irrigation water infiltration, and parts of the eastern part, and the western part, with Serdies Mountain limestone.

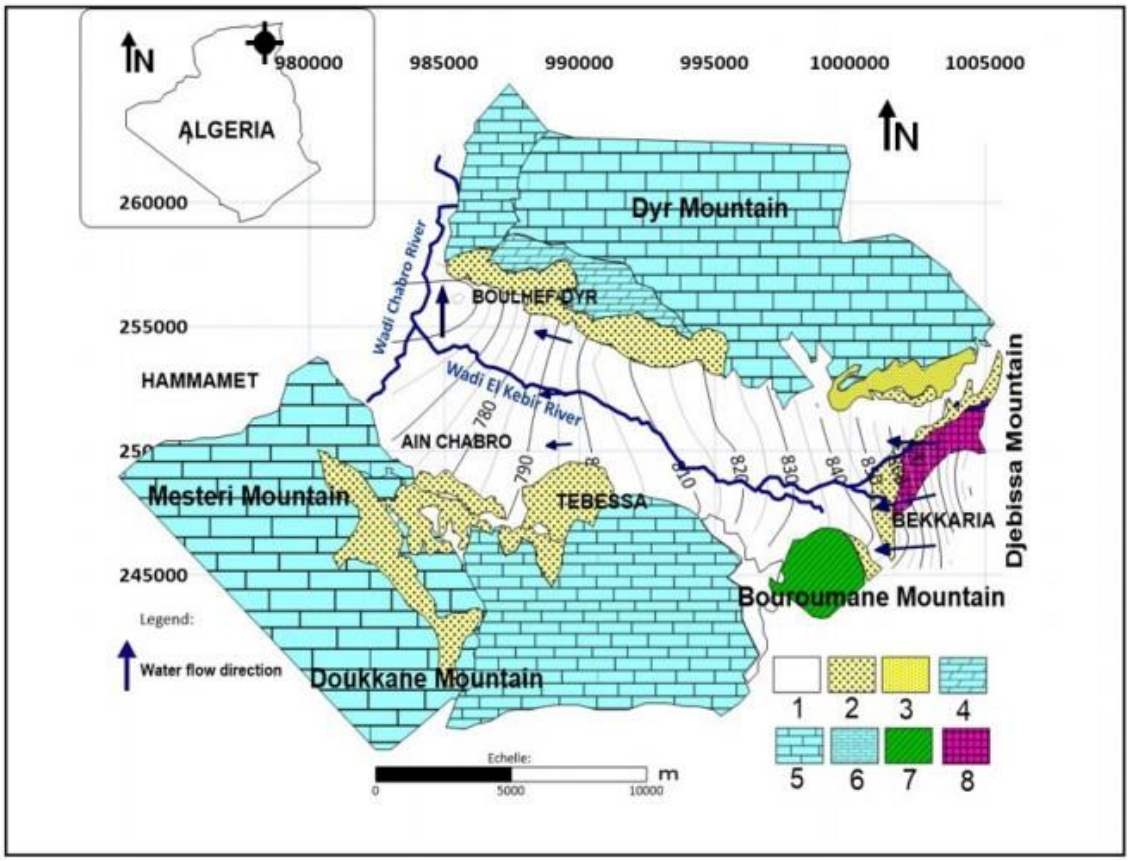


Figure 46 Piezometric and Geologic Map of the Plain of Tebessa (February 2022)(Saad et al., 2024)

The northern Dyr highlands are divided from the southern Doukkane and Mestrie highlands by the plio-quaternary tectonic depression of the Tebessa region. This depression is gradually filled by Mio-Plio-Quaternary detrital sediments (Figure 47). There have been four stages of this depression: the Lower Villafranchien (Upper Pliocene) stage, the Upper Villafranchien (Lower Pleistocene) stage, the Middle Pleistocene stage, and the Upper Pleistocene stage (KOWALSKI et al., 2002). Anticlines and synclines were organized by the Cretaceous limestone deposits that constituted most of the study area. Plio-quaternary and Quaternary formations in the central region are represented by sandstones, gravels, conglomerates, and recent alluvial deposits.(Saad et al., 2024)

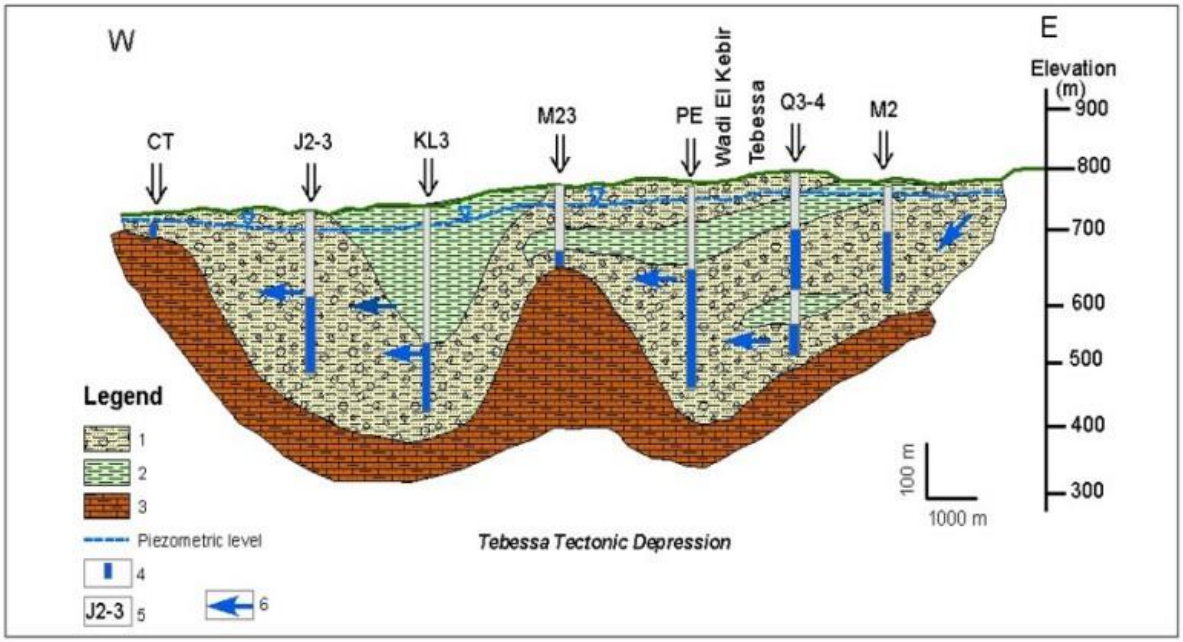


Figure 47 Hydrogeological Cross-Section Across the Plain of Tebessa (Saad et al., 2024)

(1) Permeable zone (marly-limestones, alluvial fans, silts, calcareous crust, conglomerates, and gravels); (2) Impermeable zone (clay and marl); (3) Marly bedrock; (4) Screened interval; (5) Well name. Elevations are above sea level; (6) Water flow direction.

3.2 The plain of Morsot- El Aouinet

The plains of Tebessa and Morsot-El Aouinet exhibit notable similarities in their aquifer systems. Both regions are characterized by comparable geological formations and hydrogeological conditions, which contribute to their aquifers' shared characteristics. A summary analysis of the stratigraphic column of the study area shows the presence of three aquiferous formations, which are:

3.2.1 Plio-Quaternary Aquifer

3.2.2 The Eocene Limestone Aquifer

3.2.3 The Maastrichtian Limestone Aquifer

- **Flow Patterns, Piezometry, and Hydrogeological Cross-Section:**

The groundwater flow system of the Plio-Quaternary aquifer is presented as a groundwater contour map (Figure 48). Two piezometric highs are recognized in the study area; one has a static water level of 800 m and is located in the southeast, and the second is in the north-west of the study area and has a static water level of 690 m. Generally, the groundwater flow direction in this area is converging in the center towards Chabro Wadi.

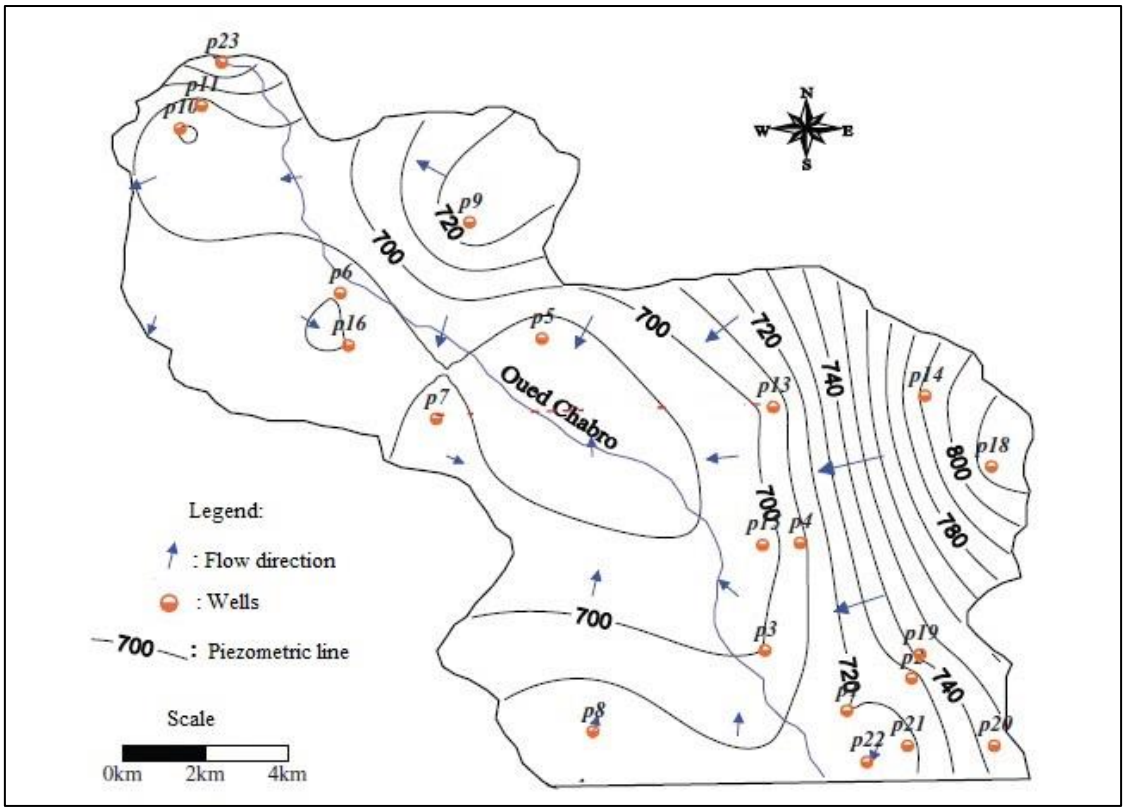


Figure 48 Piezometric Map (2006) of the Morsot-El Aouinet Plain (Fehdi et al., 2011)

3.3 The plain of El-Meridj-El Ouanza

The Ouanza region, as detailed by (Stamboul, 2017), is characterized by several significant aquifers, each exhibiting unique geological and hydrogeological properties that are important for local water supply. These aquifers can be summarized as follows:

3.3.1 The Quaternary Aquifer

Primarily composed of silty alluvium, sand, conglomerates, and sandstone. This aquifer has a thickness of approximately 70 meters and extends from the surface down to a depth of 70 meters. Its resistivity ranges between 20 to 50 ohm-meters, indicating variations in water quality and salinity levels, particularly influenced by fine sediments.

3.3.2 Lower Miocene Aquifer

Consists of sandstones and conglomerates. This aquifer reaches a maximum thickness of 200 meters and is found at depths ranging from 300 to 500 meters. The resistivity of this aquifer is approximately 100 ohm-meters, reflecting its potential for water storage and transmission.

3.3.3 Middle Albian Aquifer

This aquifer is situated in the upper calcareous layers, with a thickness of 225 meters and depths ranging from 500 to 700 meters in the center of the basin. The resistivity of this aquifer varies between 100 and over 500 ohm-meters, suggesting the presence of karstic features, which enhance its ability to store and transmit groundwater. The thermal water sample S13 located at Sidi Yahia emerges mostly from the Albian aquifer, with significant influences from the underlying Triassic formations. The geological study of the area highlights the presence of fractured limestones associated with the Middle Albian and Aptian formations, along with a complex structure featuring faults in a North-West South-East direction that facilitates groundwater movement.

3.3.4 Aptian Aquifer

This aquifer is known for its calcareous rock composition found in Djebel Harraba. This aquifer exceeds a thickness of 430 meters and is situated at depths ranging from 1000 to 1500 meters. The resistivity in this aquifer falls between 80 to 150 ohm-meters, indicating its complex interactions with surrounding geological formations.

Flow Patterns and Piezometry

The constructed piezometric map reveals an irregular piezometric surface, with the morphology of the contours indicating a general flow direction from southwest to northeast (Figure 50). It also identifies three distinct sectors:

- In the western sector, around El Aouinet, the contours are closely spaced, indicating rapid flow in this part of the study area.
- In the Ouanza sector, Oued Mellegue acts as a drainage axis that converges the flows from the surrounding borders.
- In the central zone, there is a convergence of flows associated with the exploitation of the aquifer.

Regarding our thermal spring (S13) located in the northeastern part of the study area, at a lower altitude of 470 m, we can conclude that the groundwater flow from the aquifer converges towards it and likely passes through the spring (the source drains the aquifer). This leads us to suggest that the thermal spring of Sidi Yahia is fed by this aquifer.

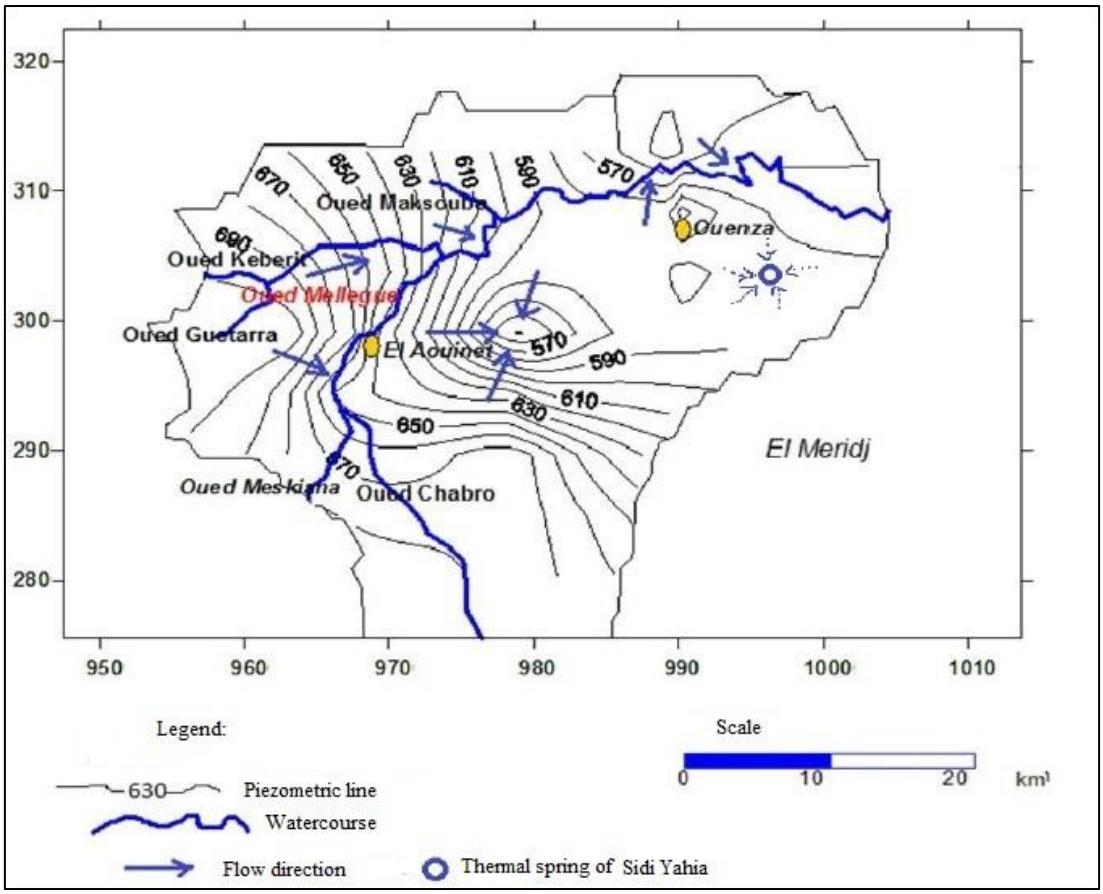


Figure 49 Piezometric Map of El-Meridj-El-Ouanza Region (2016)(Stamboul, 2017)

4. The Region of Khenchela

The examined area is composed of three significant hydrogeological formations. The aquifer system in the semi-arid region of Khenchela is identified by three aquifers: the Quaternary, the Miocene, and the Cretaceous aquifers. In this context, four aquifer systems have been identified. One is a shallow aquifer, with an average depth ranging from 5 to 30 meters. The other is a deeper system, encompassing three aquifers:

1. The collapsed plains aquifer, which is recharged by rainfall and rivers that cross it, with a depth varying between 100 and 200 meters.
2. The fractured limestone aquifer, whose thickness sometimes exceeds 250 meters in certain facies.
3. The continental formations aquifer, with depths ranging from 200 to 600 meters.

4.1 The Quaternary aquifer

Marked by blocky scree, recent alluvium, arable land, polygenic pediments, and calcareous crusts, the base consists of beige and red siliceous clays. Water circulates within these units, which have a thickness ranging from 5 to 30 meters. (Boubelli, 2017)

4.2 The Miocene aquifer

Water circulates through the coarse white sandstones of the Lower Turonian, as well as the biomicritic and biomicroparitic marls and white sandstones of the Langhian-Serravallian. The thickness of this aquifer varies between 100 and 200 meters. (Boubelli, 2017)

4.3 The Cretaceous aquifer

Represented by semi-permeable formations composed mainly of marls and chalky limestones, blue-gray marls, marly limestones, and flaky limestones, water circulates within these formations, which are bounded by a base of red siliceous clays and a roof of gray and blue-gray marls. The thickness of these formations does not exceed 250 meters.(Boubelli, 2017)

- **Flow Patterns and Piezometry**

Three maps were produced by (Boubelli, 2017), each highlighting distinct differences from one another, the piezometric map (Figure 50) created for the Quaternary formations identifies three main sectors:

1. *Western Sector*: The flow direction is from southwest to northeast, with relatively close hydro-isohypse curves, indicating a steep hydraulic gradient.
2. *Eastern Sector*: The flow moves from east to west, and the hydro-isohypse curves are more widely spaced, with a concavity facing westward.
3. *Southern Sector*: The flow direction is from east to west, and the widely spaced hydro-isohypse curves suggest a gentle hydraulic gradient.

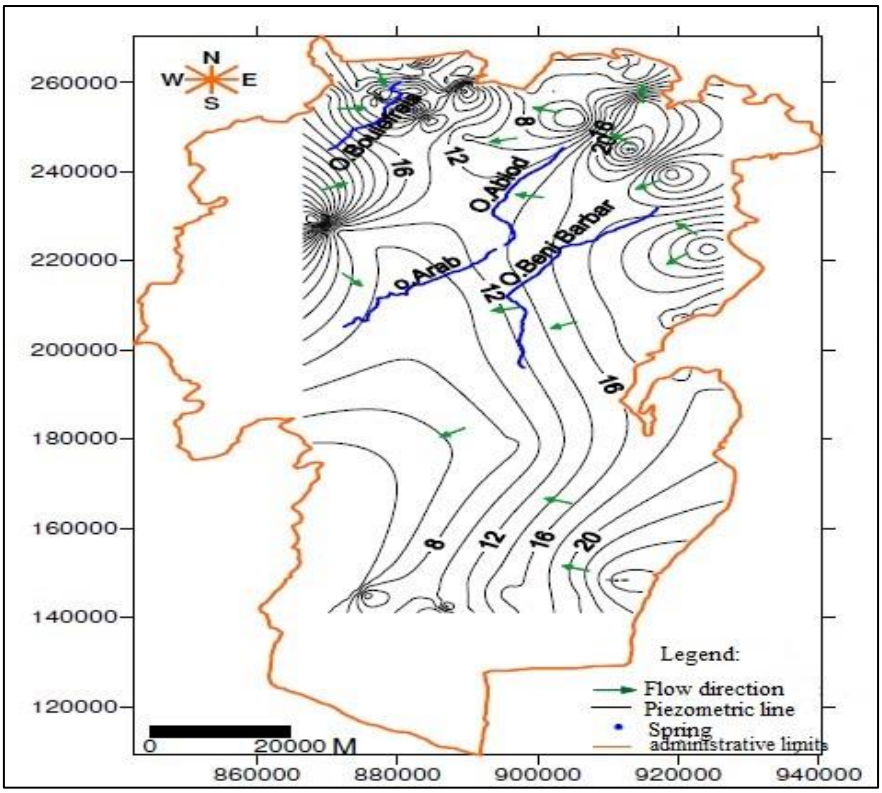


Figure 50 Piezometric Map of the Quaternary (Boubelli, 2017)

Out of the 165 wells reported by the Khenchela DHW in 2008, 13 exploit **the Miocene aquifer**. These boreholes facilitated the development of a piezometric map for the Miocene formations located in the northern part of the Khenchela region. The map (Figure 51) shows a general west-to-east flow direction, with a convergence zone forming piezometric depressions near wells Y-3 and Y-2 in the western part, where tightly spaced curves indicate a steep hydraulic gradient. In contrast, in the eastern part, the flow shifts slightly towards the northeast, with more widely spaced curves, indicating a gentle hydraulic gradient.

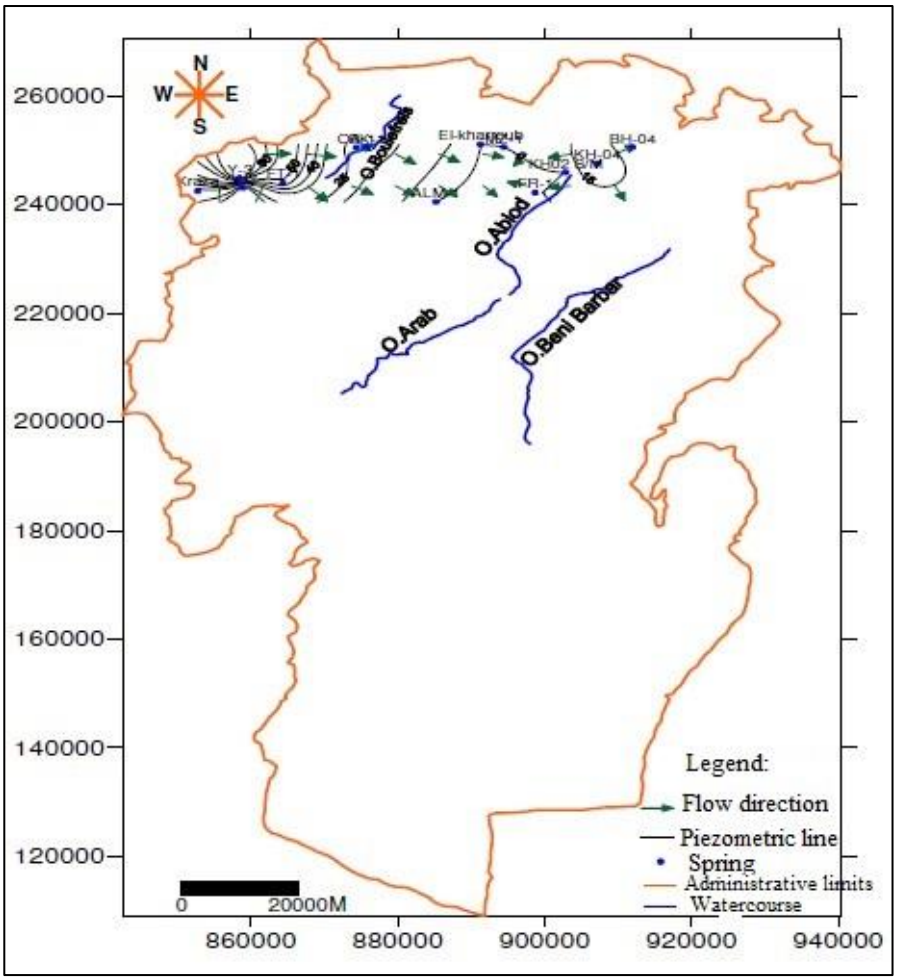


Figure 51 Piezometric Map of the Miocene (Boubelli, 2017)

The creation of the **Cretaceous piezometric map** (Figure 52) is based on data from 36 boreholes located in the Khenchela region. It reveals a flow direction from northwest to southeast in the western part, and from northeast to southwest in the eastern part, with widely spaced curves indicating a low hydraulic gradient. However, in the southeastern area, the tightly spaced curves indicate a steep hydraulic gradient.

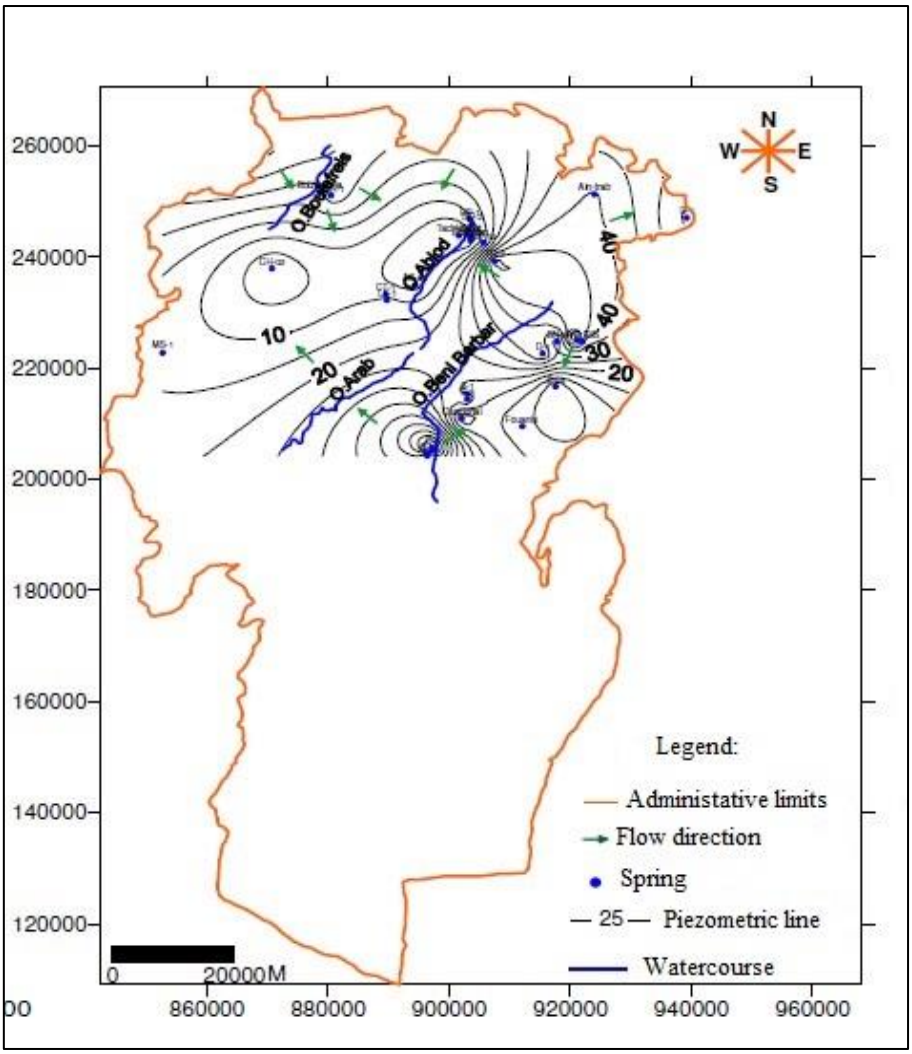


Figure 52 Piezometric Map of the Cretaceous (Boubelli, 2017)

After presenting the aquifers, flow patterns, and piezometric characteristics of the four provinces: Guelma, Souk Ahras, Tebessa, and Khenchela separately, a comparison can highlight the similarities and help develop a regional understanding of the hydrogeological system.

III. Cross-Regional Findings

1. Aquifer Types

The Mio-Plio-Quaternary aquifer is a significant shared water resource across the provinces of Guelma, Souk Ahras, Tebessa, and Khenchela. This widespread, shallow aquifer system is recharged by surface water, precipitation, and occasional recharge from underlying formations. It serves as a primary source of freshwater for both agricultural and domestic use due to its extensive reach and relatively shallow depth. The aquifer's water quality is generally favorable, particularly in Guelma and Khenchela, where groundwater exhibits moderate mineralization, making it suitable for

irrigation and drinking water. This consistent quality enhances its reliability as a sustainable resource. However, in certain areas, such as parts of Tebessa and Souk Ahras, elevated salinity levels are observed, often due to interactions with Triassic evaporites, which can present challenges for agricultural and domestic use. Despite these localized variations, the aquifer remains integral to the agricultural economy of the region, providing water for irrigation, particularly in semi-arid areas where other water sources are limited.

The Eocene aquifer, characterized by its karstified limestone formations, is present across Guelma, Souk Ahras, and Tebessa. Its karst features significantly enhance both porosity and permeability, allowing for substantial groundwater storage and efficient transmission. This makes the Eocene aquifer a highly productive water source, particularly in areas where the karst is well-developed. Its hydrogeological significance lies in its ability to provide important water resources for both irrigation and drinking, making it an essential component of the water supply in these provinces.

The Cretaceous aquifers present in Guelma, Tebessa, Khenchela, and Souk Ahras are significant components of the hydrogeological framework in these regions. Guelma features Senonian karst carbonate formations, while Tebessa includes Maastrichtian, Turonian, and Albian-Aptian layers. Souk Ahras contributes with Maastrichtian Campanian formations, further diversifying the aquifer system. These deeper aquifers are predominantly composed of limestone and carbonate rocks, known for their excellent groundwater storage and transmission capabilities. They share similar recharge mechanisms, primarily relying on rainfall and a network of fractures that enhance water movement. Collectively, these Cretaceous aquifers not only provide critical groundwater resources but also support the overall hydrological balance, making them essential for local communities and agricultural activities across the four provinces.

The Triassic aquifer, characterized by evaporitic formations, is found in both Souk Ahras and Tebessa, reflecting a shared geological history in these provinces. Composed primarily of halite, gypsum, and anhydrite, these formations significantly impact the quality of groundwater, often leading to elevated salinity levels in the regions where they are located. This presents potential challenges for water use, particularly for agricultural and drinking water purposes. It is important to note that while the aquifer is prominent in Souk Ahras and Tebessa, its presence is not exclusive to these provinces, as the aquifer also extends into the remaining provinces, contributing to the regional hydrogeology.

The Jurassic carbonate aquifer, present in Souk Ahras, while not as widespread as other aquifers in the region, contributes additional water storage capacity due to its unique geological

characteristics. This aquifer shares similarities with the Eocene and Cretaceous carbonate formations, which are known for their ability to hold and transmit groundwater effectively. The Jurassic carbonate system is expected to exhibit karst features, enhancing groundwater flow and potentially increasing the aquifer's productivity. These karst characteristics make it a valuable resource for local water supply, particularly in areas reliant on groundwater for irrigation and domestic use.

The aquifer systems of Guelma, Souk Ahras, Tebessa, and Khenchela show significant similarities, particularly in the widespread occurrence of Mio-Plio-Quaternary and carbonate aquifers (Eocene, Cretaceous). These shared features suggest that the provinces are part of a larger, interconnected hydrogeological region, with consistent recharge zones and groundwater flow patterns.

2. Flow Patterns

The groundwater flow patterns observed across Guelma, Souk Ahras, Tebessa, and Khenchela indicate a shared regional flow system. With most regions exhibiting similar directional patterns primarily west-to-east and southwest-to-northeast, it becomes evident that these provinces are interconnected through a common hydrogeological framework. This consistency in flow directions suggests that groundwater movement is influenced by similar topographical features and geological formations, which facilitate recharge and distribution. Consequently, hydrological processes occurring in one province can significantly impact water availability and quality in adjacent areas, reinforcing the notion of a unified regional hydrogeological system.

3. Hydraulic Gradients

The piezometric maps of each province show a mix of steep and gentle hydraulic gradients. Areas with closely spaced piezometric curves, indicating rapid flow, are typically found in regions with fractured limestone formations or more permeable aquifers. Conversely, wider spaced curves indicate slower flow in regions with lower hydraulic conductivity. The presence of both steep and gentle gradients across provinces reflects a regional balance between recharge zones (often in higher elevations) and discharge areas (lower-lying plains).

4. Recharge Zones

In all four regions, the primary recharge areas are located in elevated zones with fractured formations, such as the limestone and marl formations of the Cretaceous and Eocene. Rainfall and surface water contribute significantly to these recharge areas, making them key zones for aquifer recharge across the region.

The comparative analysis of the aquifers in Guelma, Souk Ahras, Tebessa, and Khenchela highlights their interconnectedness through similar geological formations and groundwater flow patterns. This underscores the need for a unified approach to groundwater resource management across these provinces.

5. Condition at the Emergence of Thermal Waters

The discharge zones of thermal waters in the study area are influenced by a combination of geological, thermal, hydrological, and topographical factors. These zones are often located in regions where faults and fractures create pathways for geothermal fluids to rise to the surface. The topography of the area, including elevation and slope, can significantly affect the flow patterns and temperature of the emerging water, while also influencing local evaporation rates and runoff. Additionally, the geological formations, such as marly-calcareous or shale deposits, play a key role in shaping the chemical composition of the waters. In the following section, each spring's discharge zone is characterized individually, focusing on the specific conditions that impact its thermal and chemical profile.

a. Spring of Hammam Ouled Ali (S1)

The thermal spring S1 (Photo 2), located at Latitude 36°34'31.80"N, Longitude 7°22'54.48"E, and an Elevation of 223 meters, is one of several springs found north of Guelma. These springs are situated on the left bank of the Oued El Hammam, to the north of Djebel Debar, within the northeastern neritic formations (Figure 53). In the riverbed, there is an outcropping of marl-limestone and transgressive Senonian black shales. The hot springs emerge along a fault line, as noted by Durand Delga in 1955. On the bank of the river, these waters are clear, with a noticeable sulfurous smell, similar to rotten eggs, and are accompanied by deposits of yellowish sulfide, mud, and algae. The site features several minor outlets alongside the main one, with a high flow rate recorded at 119 L/s (DHW Guelma, 2011).

At the Hammam Ouled Ali region, the limestone formations, which are sometimes solid and other times fractured, form an anticline structure. These limestones hold a confined aquifer with an estimated thickness of 45 meters. The total thickness of the limestone layer is about 320 meters (from Forge HB1). To the west, this formation is covered by thick layers of marl, about 200 meters thick, which act as a cap for the confined aquifer, while also serving as the base for an overlying unconfined aquifer composed of sandy gravels (Figure 54).

The spring (Photo 2) has temperatures ranging from 51.4°C to 54.6°C and a total mineralization of 1235.09 mg/L. The water is of the calcium sulfate type, with the following elemental order: SO_4^{2-}

>HCO_3^-> Cl^-, and Ca^{2+} > Na^+ > Mg^{2+}. The thermal waters at this station have both stimulating and soothing effects, particularly beneficial for treating uterine and skin conditions.

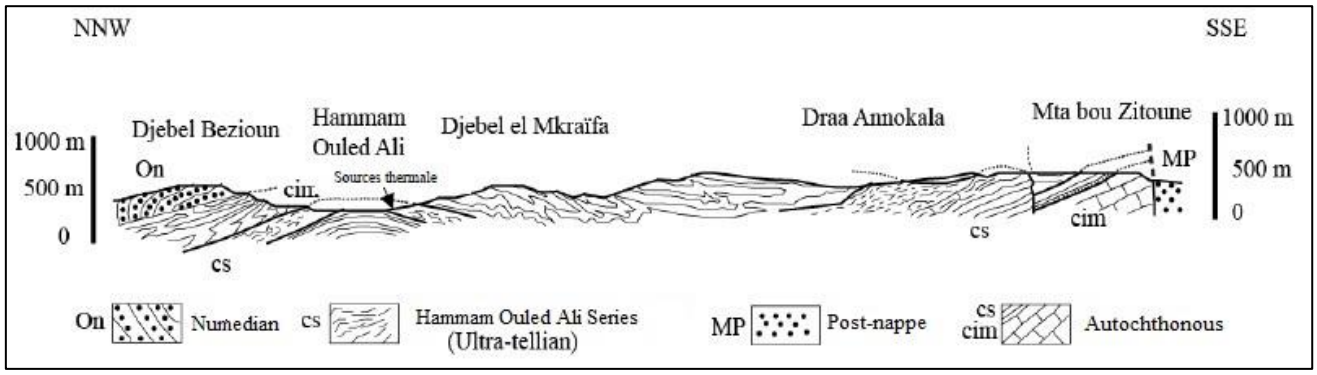


Figure 53 Geological Cross-Section of Hammam Ouled Ali (Vila et al., 1986)

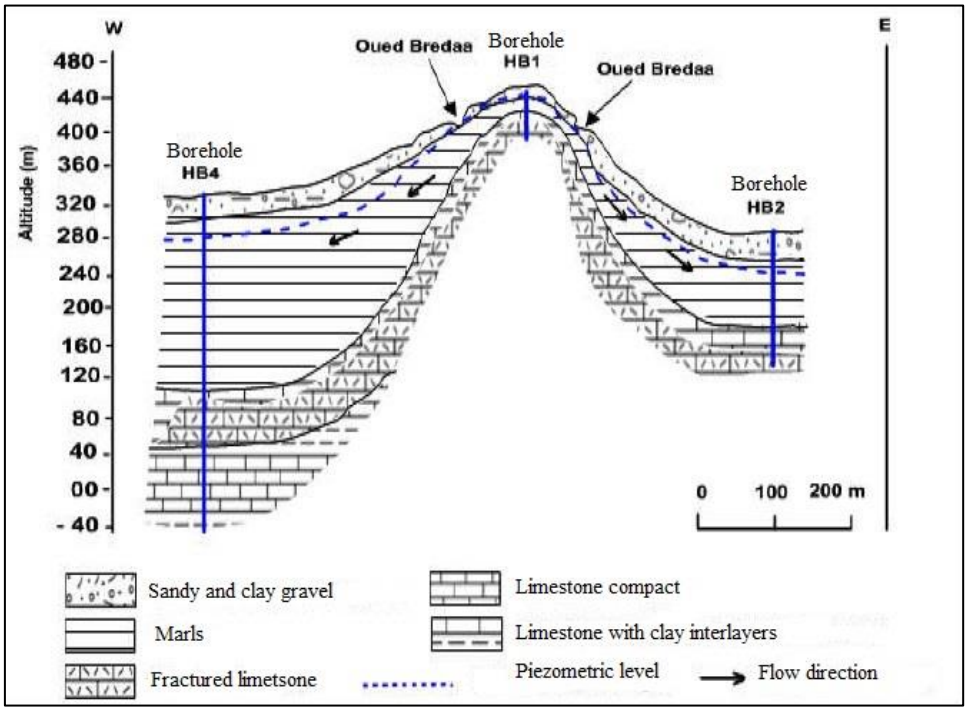


Figure 54 Hydrogeological Cross-Section of Hammam Ouled Region (Gaud 1947)



Photo 2 The Spring of Hammam Ouled Ali (S1) (2019)

b. Spring of the Cascade 1(S2)

The coordinates of the spring (S2) are 36°27'35.28"N, 7°16'9.84"E, at an elevation of 315 meters. The thermal springs in the Hammam Debagh region, including (S2), are located within a Miocene basin and emerge through travertine deposits formed by the thermal waters (Deleau, 1938; 1952; Dib H, 1985; Issaadi, 1992; Verdeil, 1974). These waters flow along a fault-oriented N 20° E (Deleau in Dib, 1985) (Figure 55), which cuts through Aptian limestone formations, Senonian marl-limestone, and reaches down to the dolomitic Jurassic layers. The waters exhibit organoleptic properties similar to those of the Ouled Ali springs but have significantly higher flow rates, with a total discharge of 77.5 L/s from 16 springs (DHW Guelma, 2013).

The spring (photo 3) exhibits temperatures between 94°C and 94.7°C, classified as hyperthermal waters, and has a total mineralization of 1836.98 mg/L. The water is classified as sodium chloride type, with the dominant ions in the following order: $Cl^- > SO_4^{2-} > HCO_3^-$ for anions, and $Na^+ > Ca^{2+} > Mg^{2+}$ for cations. The thermal waters of the Hammam Debagh region possess therapeutic properties and are used to treat various conditions, including rheumatological, dermatological, neurological, and gynecological ailments, as well as respiratory diseases such as pulmonary tuberculosis and sinusitis. In general, these waters are known to strengthen the immune system and promote overall well-being.

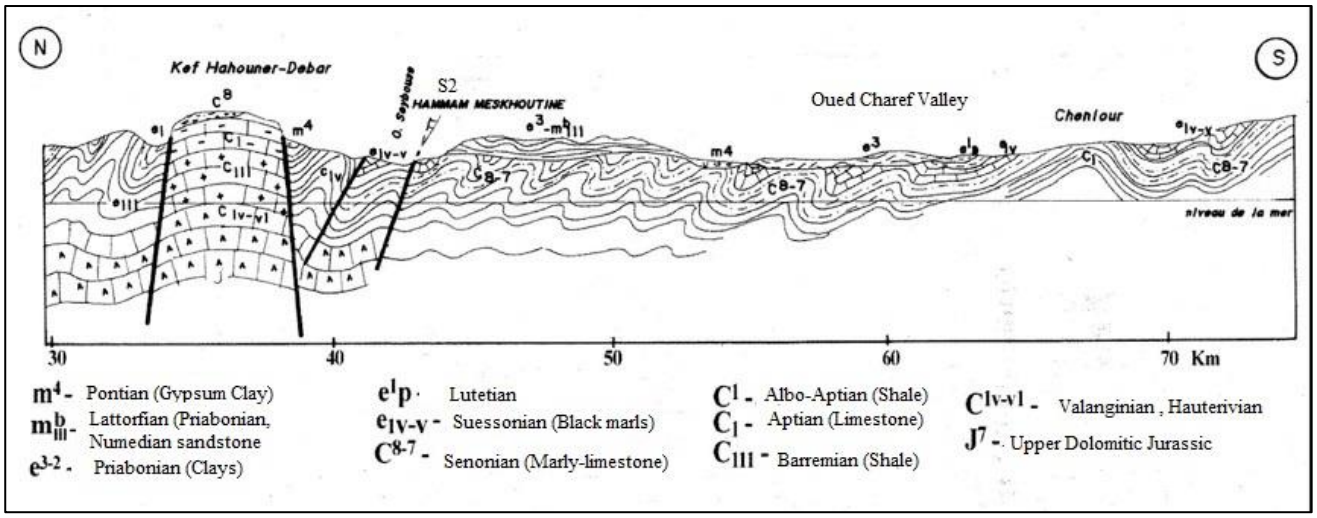


Figure 55 Geological Cross-Section of Hammam Debegh (S2) in Dib H, 1985)



Photo 3 The Thermal Spring (S2) of Hammam Debegh (The Cascade 1)(2019)

c. Spring of Hammam Guerfa (S5)

The Hammam Guerfa Spring (S5) (Photo 4) flows through Quaternary travertines and hydrothermal tuffs with a significant slope. During earthquakes, the water turns a reddish color due to clay particles that appear for a few days, indicating that the spring emerges through an active fault zone in soft formations, such as gypsum and conglomerates. The flow rate is approximately 11 L/s.

The water temperature ranges from 55.3°C to 58°C, with a total mineralization of 2014.75 mg/L. The waters are of the calcium sulfate type, with the following ionic order: $SO_4^{2-} > HCO_3^- > Cl^-$ for anions, and $Ca^{2+} > Na^+ > Mg^{2+}$ for cations. These waters are highly valued for their therapeutic properties, particularly in the treatment of rheumatological and dermatological conditions.



Photo 4 The Thermal Spring of Hammam Guerfa (S5) (2018)

d. Spring of Hammam Belhacheni (S6)

The hammam Belhacheni spring (Photo 5), located at 36°14'6.00"N, 7°20'13.56"E, and at an elevation of 728 meters, lies 10 km from both Ain Makhlouf and Ain El Arbi. The spring emerges in Quaternary travertines and tuffs, which overlay white limestones of Ypresian-Lower Lutetian age. The hot water flows through fissures in the limestone massifs, facilitated by a fault or fold-fault, and is marked by the presence of black marls and gray clays with gypsum, sometimes reddish and

containing conglomerates. This spring maintains a steady flow year-round, with a discharge rate of 15 L/s. The waters are colorless, with a distinct sulfur odor due to the release of H_2S gas (Dib H, 1985). The waters of this spring share similar organoleptic properties with those of Hammam Guerfa (S5).

The water temperature ranges between 62.2°C and 62.8°C, attributed to the rapid circulation of water to the surface, with a total mineralization of 2040.15 mg/L. The waters are of the calcium sulfate type, with the ionic order $SO_4^{2-} > HCO_3^- > Cl^-$ for anions, and $Ca^{2+} > Na^+ > Mg^{2+}$ for cations. These waters are highly appreciated for their therapeutic benefits, similar to those of the Hammam Guerfa springs, located about 3 km away, and are also utilized for irrigation purposes.



Photo 5 The thermal Spring of Hammam Belhecheni (S6) (2018)

e. Spring of Hammam N'bails (S7)

The thermal springs emerge on the right bank of the Oued El Hammam, at coordinates 36°19'33.92"N, 7°38'39.51"E, and an elevation of 476 meters. A significant gypsum complex, dating from the Triassic to Upper Cretaceous period, is present in the area. The hammam naturally exists as several surface outlets due to a major tectonic fault. The sedimentary formations, from the Upper Cretaceous to Eocene periods, are in abnormal contact with the gypsum complex. The presence of

tuff deposits in the Oued El Hammam valley suggests the existence of ancient thermal springs, now dried up (Dib, 2008). The waters of the spring are colorless and odorless, with an estimated flow rate of 6 L/s.

The water temperature ranges between 42.2°C and 42.4°C, with a total mineral content of 7,872.78 mg/L. These sodium chloride-type waters follow the ionic pattern $Cl^- > SO_4^{2-} > HCO_3^-$ for anions and $Na^+ > Ca^{2+} > Mg^{2+}$ for cations. Renowned for their therapeutic benefits, they are particularly effective in treating various forms of rheumatism and skin conditions. However, these waters also contain a notably high level of strontium at 19.7 mg/L, which can pose health risks, particularly affecting bone health if consumed over long periods. Additionally, the presence of lithium at 1.51 mg/L, known for its effects on mental health, can contribute to mood regulation but must be monitored due to potential side effects with prolonged exposure.

f. Spring of Hammam (Ouled Zaid) Ouled Driss (S10)

The Hammam Zaid thermal station is located 18 km northwest of Souk Ahras, along the El Kala Road, in the Ouled Driss douar (Photo 6). The spring emerges on the right bank of the Oued El Hammam, at coordinates 36°21'38.52"N, 8°0'46.08"E, and an elevation of 828 meters, with a flow rate of approximately 3 to 4 L/s. The source emerges from the black marls of the Lutetian and is fed by a fault with a N20°E orientation, clearly visible in the Ypresian limestones. The water temperature ranges between 37.8°C and 38.9°C, with a total mineralization of 1,498.37 mg/L, including a moderately high strontium content of 5.95 mg/L.



Photo 6 The Thermal Station of Hammam Ouled Driss (S10) (2018)

g. Spring of Hammam Tessa (S11)

The Hammam Tessa Spring (Photo 7) is located 15 km southeast of Souk Ahras, along the Souk Ahras-El Kef Road. The spring emerges on the right bank of the Oued El Hammam, at coordinates 36°13'55.56"N, 8°2'40.56"E, and an elevation of 628 meters. The hot water flows from the Senonian white limestones near their contact with Miocene sandstones, in the center of the Djebel Tessa anticline. The water temperature ranges from 38.7°C to 39.2°C, with a total mineralization of 2,844.36 mg/L. The water is of the sodium chloride type and is rich in bicarbonate (1,031 mg/L). The thermal waters of Hammam Tessa are highly sought after by the local population for their chemical properties, particularly for respiratory ailments due to the high chloride and sodium content. However, the elevated strontium level, at 7.51 mg/L, poses potential health risks, as prolonged exposure to high concentrations of strontium can negatively impact bone health. Additionally, the presence of sodium bicarbonate helps alleviate stomach discomfort.



Photo 7 The Thermal Station of Hammam Tessa (S11) (2019)

h. Spring of Hammamet (S12): (Borehole)

The Hammamet spring (Coordinates: 35°27'1.44"N, 7°57'29.04"E, elevation: 887 m, Photo 8) emerges 4 Km from the village of Youkous les Bains and is located 16 km from Tebessa. The geological conditions of the emergence are concealed by continental Quaternary deposits, which form the Tebessa plain. The surrounding hills consist of Senonian chalky limestones, but it is also

noteworthy that Triassic diapir outcrops frequently occur (Guigue, 1947). The water, with low thermal properties (34.5°C to 35°C), is characterized by a low mineralization of 532.91 mg/L. The thermal spring exhibits a calcium bicarbonate chemical facies, with the order of elements as follows: HCO_3^- > SO_4^{2-} > Cl^- for anions and Ca^{2+} > Na^+ > Mg^{2+} for cations. These waters are used in the treatment of skin diseases, rheumatism, and even syphilis.



Photo 8 Thermal Water Discharge in the Hammamet Region (S12) Borehole (2018)

i. Spring of Hammam Sidi Yahia (S13)

The Sidi Yahia thermal station (Photo 9) is located on the Algerian-Tunisian border, southeast of Ouanza, 2 km from the Tebessa-Ouanza national road. The thermal spring emerges from a probable NE-SE fault concealed by Quaternary deposits. The water temperature reaches 34.5°C, but it has the highest mineralization among all the springs, with a concentration of 15,992.03 mg/L. This is likely due to the influence of Triassic or Upper Cretaceous formations. The waters are of the sodium chloride type, with elevated levels of strontium (8.9 mg/L), lithium (1.5 mg/L), and notably nitrates (1,180 mg/L).



Photo 9 Thermal Station of Sidi Yahia (S13) (2019)

j. Spring of Hammam Salhine (S14)

The Khenchela thermal station (Photo 10), one of the best-preserved Roman thermal establishments in Algeria, is located at 35°26'16.80"N, 7°5'9.96"E, with an elevation of 1086 meters, approximately 6 km from Khenchela in the Oued El Kissane valley, southwest of the Khenchela-Batna national road. Numerous springs emerge along the river. The site features two remarkably well-preserved Roman pools: one rectangular and the other circular. The hot water emerges from Lower Cretaceous formations composed of quartzite beds, which are unconformably covered by marl-sandstone deposits from the Lower Miocene. In the vicinity of Khenchela, there is a significant Triassic outcrop consisting of variegated, gypsum-rich clays. The Khenchela region's anticline is affected by longitudinal faults, leading to the disappearance of Lower Cretaceous layers on the northern flanks. These faults are marked by the presence of the Hammam Salhine thermal spring, historically known as Hammam Rhas or Aqua Flavianna (Guigue, 1947). The origin of the thermal water is likely linked to the Triassic formations. The water temperature at emergence ranges between 54.7°C and 58.8°C, with a mineralization of 2,869.75 mg/L. The water has a sodium chloride chemical facies, with the following ion order: $Cl^- > SO_4^{2-} > HCO_3^-$ for anions and $Na^+ > Ca^{2+} > Mg^{2+}$ for cations. The Hammam Salhine thermal station is known for treating dermatological conditions, respiratory asthma, ulcers of all kinds, and rheumatism.



Photo 10 The Thermal Station of Hammam Salhine (2019)

k. Spring of Hammam Knif (S15)

Hammam Knif (Photo 11) is located at 35°29'14.28"N, 35°29'14.28"E, at an elevation of 1020 meters. It lies 10 km northwest of Khenchela, along the national road connecting Khenchela and Ain Baida. The geological conditions of the area can be summarized by the stratigraphic series of Djebel Knif (Figure 56), which includes the following formations:

- Upper Coniacian: This formation consists of alternations of beige marls and nodular limestones, along with dolomitic limestones containing reworked Triassic elements. The thickness of this layer is approximately 80 meters.
- Santonian: Comprised of alternating constructed limestones and brecciated limestones, this formation has a thickness of about 70 meters.
- Campanian: This layer is formed entirely of black marls, with a thickness of 60 meters.
- Lower Maastrichtian: Characterized by alternations of beige marls with mollusks, as well as limestones and black marls.
- Upper Maastrichtian: This formation consists of massive limestones alternating with crumbly limestones, with a thickness of 90 meters.

The geothermal steam emerges from highly fractured massive limestones and is released abundantly from a narrow and deep fissure. The water temperature at the emergence points ranges between 46.5°C and 51°C. The water has a mineralization level of 1851.91 mg/L and is known to be beneficial for treating rheumatic diseases, certain nervous disorders, and epilepsy, which may improve with a stay at Hammam Knif.

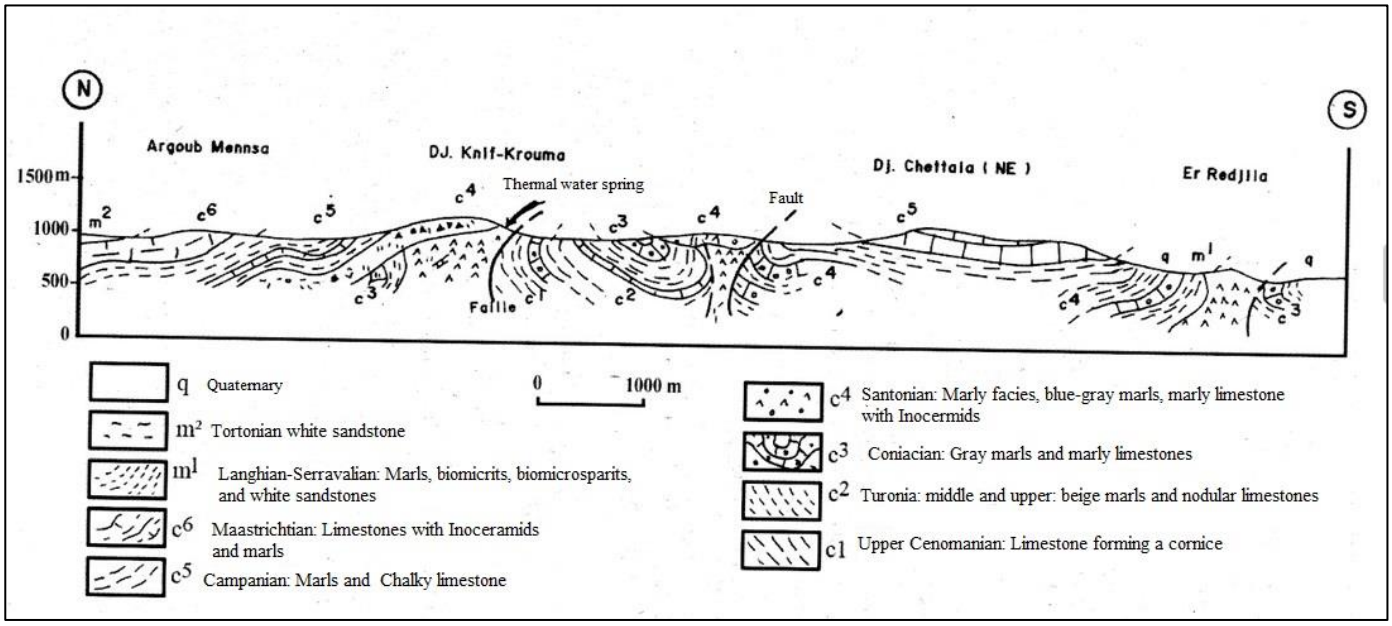


Figure 56 Geological Cross-Section of Hammam Knif (In Dib H, 1985)



Photo 11 Geothermal Steam Room and Bath from Hammam Knif Station (2019)

6. Conclusion

To conclude the chapter on the identification of aquifers, their characteristics, and discharge zones, it is essential to underscore the hydrogeological similarities and interconnectedness of water resources across Guelma, Souk Ahras, Khenchela, and Tebessa. These provinces share common aquifer features, particularly in terms of groundwater recharge patterns driven by rainfall, geological formations such as karstic and alluvial aquifers, and groundwater flow systems that transcend provincial boundaries.

Lithological similarities are also evident across the regions, including the presence of marly-calcareous formations and chalky karstic limestones from the Cretaceous period, which play a crucial role in groundwater storage and flow due to their permeability and porosity. Furthermore, the widespread occurrence of Triassic evaporitic formations—notably gypsum and anhydrite—near thermal springs underscores the influence of tectonic activity and fault systems. These faults create pathways that allow deep, mineralized waters to rise, contributing to the emergence of thermal springs in tectonically active zones.

In terms of water type, the prevalence of sodium chloride waters is a defining feature, particularly for thermal waters with high salinity and temperature. This water chemistry is largely shaped by prolonged interaction with evaporitic formations from the Triassic to Cretaceous periods, reflecting a strong lithological control on groundwater composition. The evolution of groundwater chemistry through water-rock interactions highlights the consistent influence of these geological features across the study regions.

These shared hydrogeological characteristics suggest that a regional approach to groundwater management and conservation would be highly effective. Recognizing the interconnected nature of these aquifers can optimize resource use and address critical challenges related to water scarcity and sustainability, ensuring the long-term viability of these essential water systems across the broader study area.

Chapter Five

Hydrochemistry context

Section One

Study of Physico-Chemical, Statistical, and Isotopic Analyses

I. Introduction

Groundwater chemistry research strongly focuses on comprehending the quality and quantity of subsurface water, the evolution of its chemical characteristics, and the determination of chemical facies, which are closely related to the lithology encountered during the water's residence in the aquifer.

To successfully carry out our research, our study relies on physicochemical and isotopic analyses, which are essential for comprehending the chemical composition of groundwater, its origins, and its interactions with the surrounding media, and for determining recharge, discharge zones. Additionally, statistical approaches will help identify trends, correlations, and patterns within the data, providing an effective understanding of the factors influencing groundwater chemistry. The application of geothermometry, which estimates subsurface temperatures and groundwater circulating depth based on water chemistry and geothermal gradient, is especially of paramount importance in studying thermal aquifers. The combination of these methods will indeed offer a holistic understanding of the aquifer's behavior.

II. Study of Physico-Chemical, Statistical, and Isotopic Analyses

1. Methodology and Materials

Our region represents a significant hydrogeological entity at a regional scale, comprising four wilayas, where we focus on sampling of both thermal and nearby cold springs. The selection of these springs is based on several factors. Comparing the two allows for physicochemical and temperature gradient analyses, evaluation of groundwater hydrochemical evolution in terms of quality and quantity, and the identification of different aquifer systems.

1.1. Sampling and Field Measurements

Two water sampling campaigns were carried out on December 15, 2018, and October 16, 2019 (Figure 57). In 2018, 15 thermal springs were sampled. In 2019, we supplemented these samples with water from 5 nearby cold springs. A seawater sample, referenced from (Lenntech, 2005) has been added to the total sample set for comparison. At each sampling station, three well-rinsed bottles of water were collected: two 150 ml polyethylene bottles, one for cation analysis (acidified with reagent-grade HNO3 to lower the pH below 2) and one for anion analysis; the third was a 50 ml high-density vial for δD and δ18O isotopic analyses. After collection, all samples were stored in an icebox at temperatures below 4°C and transported to the laboratory (APHA, 2005). Before samples were collected, the water was filtered with 0.45 μm membrane filters. Samples for anions and cations were

delivered to Suleyman Demirel University, Sparta, Turkey's Geothermal Energy, Groundwater, and Mineral Resources Research and Application Laboratory, which utilized a flame photometer Jenway PFP7 for metals and - Dionex ICS-3000 ion chromatography (DC: detector chromatography) (SP single pump) + AS auto sampler for ions determination. The isotopic analyses (δ18O and δD) were carried out using cavity ring-down spectroscopy (CRDS) (Steig et al., 2014) on a Picarro L2140-I, and calibrated against V-SMOW in the laboratory of stable isotopes, Almeria University, Spain. In the field, to prevent any modifications a WTW-Inolab level 1 calibrated multiparameter device was used to measure unstable hydrochemical parameters, such as temperature (T), pH, electrical conductivity (EC), salinity and total dissolved solids (TDS) and alkalinity by titration according to the 8th Edition of "Water Analysis" book by Jean Rodier and Collaborators (Rodier et al., 1996).

Before using or discussing the analysis results, it is essential to calculate the ionic balance to confirm the reliability of the water chemistry data and address any discrepancies accurately. The acceptable range for the ionic balance is typically ±5% for most water analyses. However, for high salinity waters, due to their complexity and potential for interference, a wider acceptable range of ±10% may be considered. Our samples fall within this broader range except for S12 in 2018 and S1 and S7 in 2019.



Figure 57 Field Equipment for Water Sampling and Alkalinity Titration Process

2. Study of Physico-Chemical Parameters:

2.1 Temperature (T°C)

It is an important parameter for the study of groundwater, as it allows the distinction between waters circulating near the surface and deep waters. It must be carefully measured right at the emergence point to avoid any cooling or modification at the surface, especially when the atmospheric temperature is either high or low.

Thermal waters are defined by Schoeller, H. (1963) as waters with an emergence temperature greater than 4-5°C over the annual average air temperature. The water temperatures measured at the emergence points range between 18.7 °C (F3 Tessa F) and 94.7 °C (S2 cascade 1), the latter is considered the hottest in Algeria and the second after the geysers of Island (Dib H, 2008).

2.2 Hydrogen Potential (pH)

The pH of a solution is the inverse of the logarithm of the (H_3O^+) ion concentration. It varies depending on temperature and ionic strength. It is a parameter that determines the acidity or alkalinity of water, as well as the equilibrium state of chemical elements in Eh-pH diagrams:

$$pH = - \log [H_3O^+] = - \log [H^+]$$

the obtained results are summarized in the table below:

Table 22. Variation of pH in the study zone

	Max	Min	Average
pH	7.52	6.23	6.86

The measured pH values (Table 22) show that all our springs have values fluctuating around neutrality: from a minimum of 6.23 at (S7) Hammam N'bails in Guelma to a maximum of 7.52 at (F2) Ain Souda in Souk Ahras. It should be noted that pH is influenced by several factors, including temperature, CO_2 concentration, dissolved minerals, flow rate, redox reactions, biological activity, atmospheric gases, human activities, acid rain, and the geological characteristics of the aquifer.

2.3 Conductivity (µs/cm)

Electrical conductivity is considered the property of water that allows it to conduct an electric current. It depends on factors such as temperature, concentration, and the ionization state of dissolved components, as well as the flow rate and direction. This parameter is directly linked to the geological formations encountered along its flow path and offers an approximate estimate of water mineralization. In our study area, the electrical conductivity values range from 530 µS/cm at F6 in the Hammam N'bails area to 16,800 µS/cm at S13 in Hammam Sidi Yahya, Tebessa. Additionally, S7 is placed second with a conductivity of 9,300 µS/cm. The spatial variation of these values is illustrated in Figure 58.

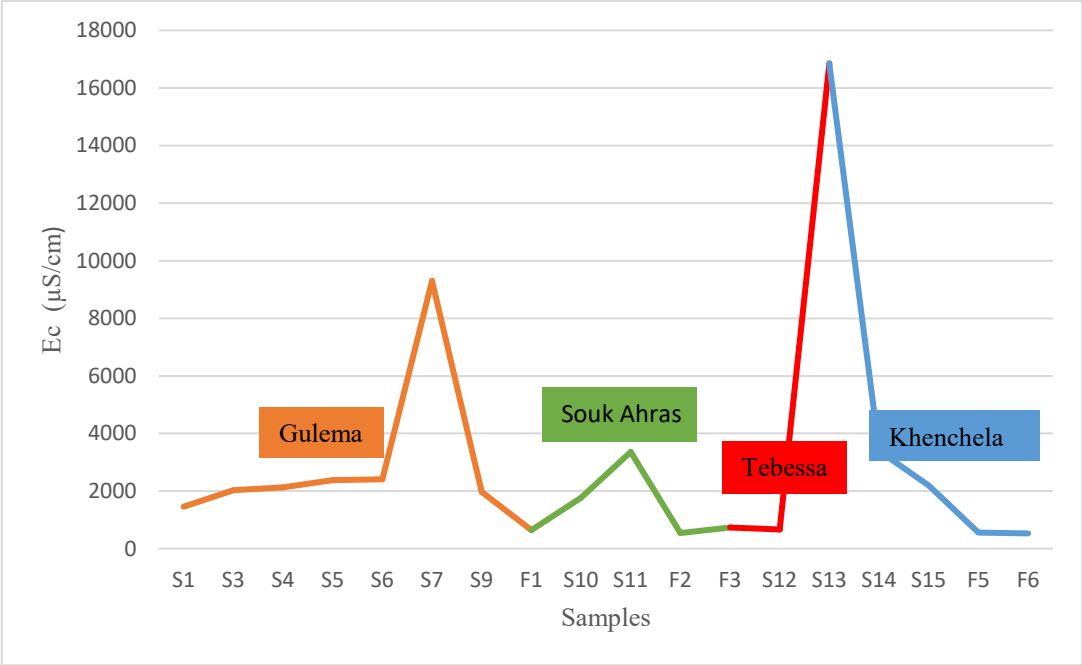


Figure 58 Spatial Variation of Conductivity Concentration (µS/cm) in the study zone at 25°C

2.4 Mineralization

The mineralization of the waters in the study area was calculated based on their measured conductivities using the equation from Rodier et al. (1996). The factor determined according to this method was applied to the conductivity values to obtain the mineralization levels. A summary of the calculated values is presented in Table 40 in the Appendices. Five groups were classified: (Table 23)

- Very low mineralization (< 250 mg/L): Suitable for industrial uses such as steam generation but requires additional dissolved salts for other applications.
- Low mineralization (250 to 500 mg/L): Commonly used in various industrial processes.
- Moderate mineralization (500 mg/L to 1 g/L): Typically, suitable for general industrial purposes.
- High mineralization (1 to 2 g/L): Not recommended for sensitive industrial applications but can be used for irrigation and livestock.
- Very high mineralization (> 2 g/L): Primarily used for thermal or specialized industrial purposes due to its high salt content.

Table 23. Classification of water samples by mineralization levels

Mineralization	Samples
< 250 mg/L	0
250 to 500 mg/L	F2, F5, F6
500 mg/L to 1 g/L	F1, F3, S12
1 to 2 g/L	S1, S3, S4, S9, S10, S15
> 2 g/L	S5, S6, S7, S11, S13, S14

For all the sampled springs, the mineralization varies significantly, ranging from 424.25 mg/l at F6 cold spring in Khenchela to 15,992.03 mg/l at S13 Hammam Sidi Yahya in Tebessa, followed by 7,872.78 mg/l at S7 Hammam N'bails. This wide range reflects the complexity of the hydrogeological and geological settings in the region. The lowest mineralization at F6 suggests relatively low dissolved salts, which may result from a short water residence time within the aquifer and minimal water-rock interaction. Additionally, the low temperature of the water probably limits the dissolution of minerals. In contrast, the highest mineralization observed at S13 indicates highly mineralized thermal water. This can be due to water-rock interactions and extended contact time. Although the water temperature is 34.5°C, it still contributes to the dissolution of minerals such as chloride and carbonate. In like manner, the mineralization at S7, with a value of 7,872.78 mg/l, also points to significant mineral content, owing to geothermal processes. The higher temperature of 42.5°C further enhances mineral dissolution, reflecting the influence of the surrounding geological environment.

2.5 Total Dissolved Solids TDS (mg/l) and Salinity

These two characteristics are directly linked to the mineralization of the waters. Their statistical results are summarized in Table 24. The highest salinity concentration was observed at (10.4 ppt, S13), indicating saline water. Moderate values were recorded at S7 (5.5 ppt) and S11 (2.3 ppt); meanwhile, the lowest values are represented from (0 ppt to 0.9 ppt; F5, S3, respectively). We noticed the same rising tendencies about TDS, especially in S13 and S7. In fact, the device indicated (OFL) for these two springs, meaning that the value exceeds the upper detection limit of the sensor and is too high to be displayed. S11 followed with 1988 mg/l, at the same time, the lowest values were represented by mainly cold springs like F2, F5, and F6 with 0 mg/l.

Table 24. Salinity and TDS variation in the study zone (2018/2019)

Values	Salinity	TDS
Min	0	207
Max	10.4	1988
Average	5.2	1097.5

2.6 Alkalinity

The Total Alkalinity Complete (TAC) values for the water samples varied significantly (Table 25), ranging from 0.1 meq/L in sample S14 to 9.72 meq/L in sample S11. This variability reflects differences in the buffering capacity of the waters, influenced by lithological composition and recharge conditions. Samples such as S10 (6.36 meq/L) and S11 (9.72 meq/L) show notably higher TAC values, indicating an elevated presence of bicarbonate ions, which provide increased buffering capacity. In all samples, the Total Alkalinity (TA) at the initial titration step remained zero, as the phenolphthalein indicator stayed colorless. This result indicates the absence of carbonate (CO_3^{2-}) and hydroxide (OH^-) alkalinity. The alkalinity determined during the subsequent titration with methyl orange, therefore, corresponds entirely to bicarbonate alkalinity (HCO_3^-), in accordance with the standard alkalinity titration procedure described by APHA (2005). Overall, the TAC values indicate a bicarbonate-dominated alkalinity system across the study area, reflecting the geochemical water–rock interactions that govern groundwater chemistry.

Table 25. Alkalinity measurements: TA and TAC for thermal waters

Station	Sample ID	TAC (me/L)	TA
Ouled Ali	S1	1.92	0
Cascade 1	S2	0.52	0
Ain chfa	S3	0.7	0
Cascade 2	S4	0.36	0
C.interne	S8	1.9	0
C.externe	S9	0.52	0
H. N'bails	S7	3.9	0
Guerfa	S5	2.34	0
Belhacheni	S6	3.1	0
H. Salhine	S14	0.1	0
Knif	S15	2.5	0
Hammamet	S12	0.72	0
Ouled Driss	S10	6.36	0
H. Tessa	S11	9.72	0

2.7 Chemical Characteristics

2.7.1 Major Elements

a) Calcium (Ca^{2+})

The presence of this element has two main origins: either the dissolution of carbonates according to the formula:

$$CaCO_3 = Ca^{2+} + CO_3^{2-}$$

Or the dissolution of gypsum

$$CaSO_4, 2H_2O = Ca^{2+} + SO_4^{2-} + 2H_2O$$

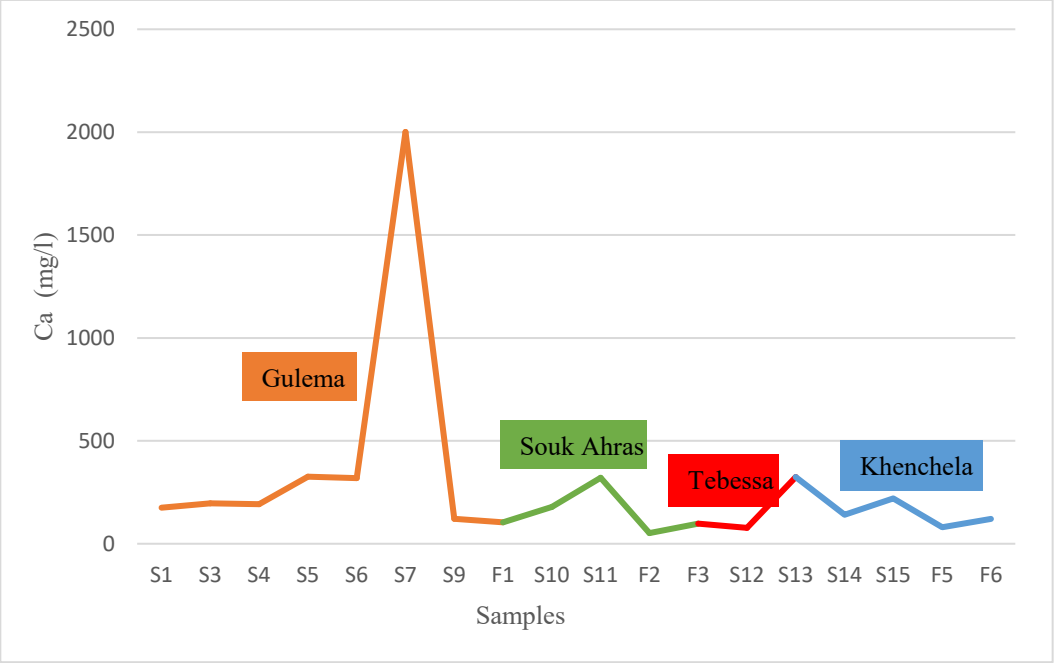


Figure 59 Spatial Variation of Calcium Concentration (mg/l) Across Study Zones

In our study region, the values of Calcium are ranging from 51.74 mg/l at F2, and 2001 mg/l at S7 as the highest content in the area, The graph of spatial variation (Figure 59) clearly shows a gradual increase in calcium concentrations from the central part of the study area, particularly around S7 and F1 located in the southeast of Guelma, extending toward the peripheral areas. Additionally, S13, situated in the northeast of Tebessa, is noted for having a slightly elevated calcium value compared to its surrounding regions.

A low calcium concentration can result from cation exchange processes, where Ca^{2+} in the water is replaced by Na^{+} fixed on clay minerals, leading to a relative depletion of calcium in solution (Appelo & Postma, 2004). It may also reflect limited dissolution of carbonate formations such as limestone and dolomite under the prevailing hydrochemical conditions. In contrast, high calcium concentrations generally indicate active mineral dissolution, particularly of calcite and aragonite ($CaCO_3$) or sulfate minerals such as gypsum and anhydrite ($CaSO_4$) (Freeze & Cherry, 1979).

b) Magnesium (Mg^{2+})

Magnesium is an essential element in water chemistry, contributing to its hardness, which can influence both the quality of the water for drinking and its effects on industrial processes. The origins of magnesium in groundwater are similar to those of calcium, as both result from the dissolution of carbonate formations rich in magnesium, such as magnesite ($MgCO_3$) and dolomite ($CaMg(CO_3)^2$). The dissolution reactions that release magnesium into the water can be represented as follows:

- Dissolution of magnesite :

$$MgCO_3 = Mg^{2+} + CO3^{2-}$$

- Dissolution of dolomite :

$$CaMg(CO_3)^2 = Ca^{2+} + Mg^{2+} + 2CO3^{2-}$$

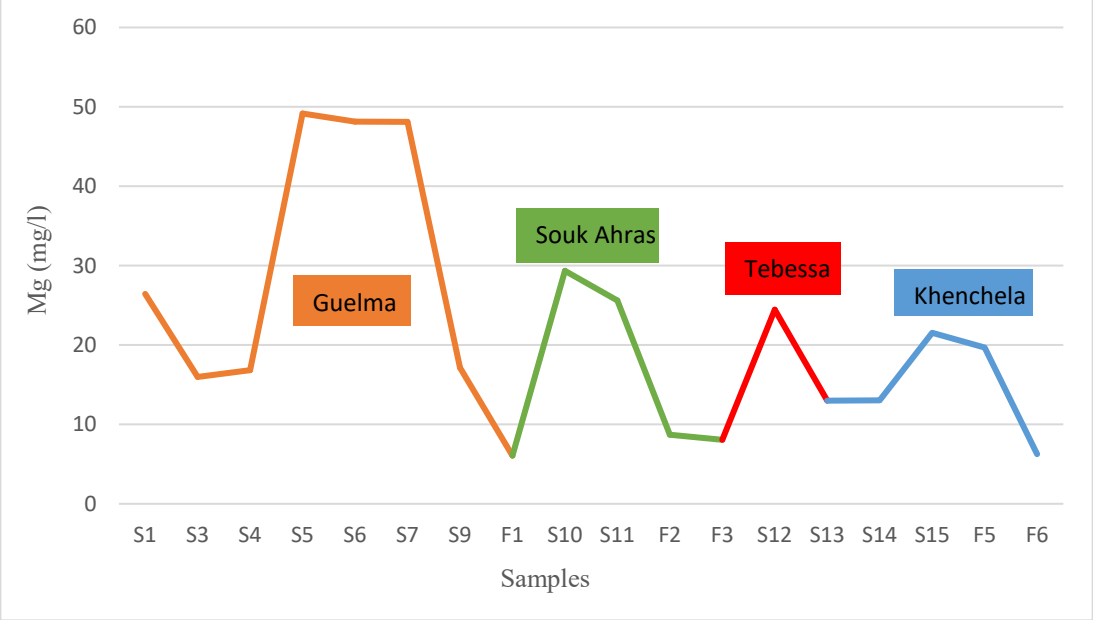


Figure 60 Spatial Variation of Magnesium Concentration Across the Study Zone

Magnesium levels vary from 6.06 mg/l at F1 to 49.16 mg/l at S5. Figure 60 represents the spatial variation graph of magnesium. It suggests a clarified spatial variability in magnesium concentrations, with higher values concentrated in the central region around S5 in the south of Guelma and extended to S7 in Hammam N'bails and S1 in Ouled Ali, and S12 in Tebessa. Additionally, S10 and S11 show relatively high levels of magnesium, with concentrations of 29.35 mg/l and 25.61 mg/l, respectively. Lower values are observed toward the surrounding regions.

A low magnesium content is probably due to both the nature of carbonate formations, which are poor in Mg^{2+}, and saturation or supersaturation with respect to dolomite in the aquifer. Another factor to consider is groundwater flow dynamics and residence time. Meanwhile, high concentrations are normally associated with the dissolution of evaporite minerals or dolomitic rocks under appropriate conditions. The latter includes high salinity, prolonged residence time, and flow dynamics. In some cases, geothermal activity can further stimulate magnesium dissolution by raising the water temperature, while high evaporation rates in the region may concentrate dissolved minerals, including magnesium, in groundwater.

c) Bicarbonates ($HCO3^-$)

The bicarbonate concentrations in our chemical analyses range from 231.8 mg/l at S9 in Guelma to 1.671 mg/l at S13 Sidi Yahya in Tebessa.

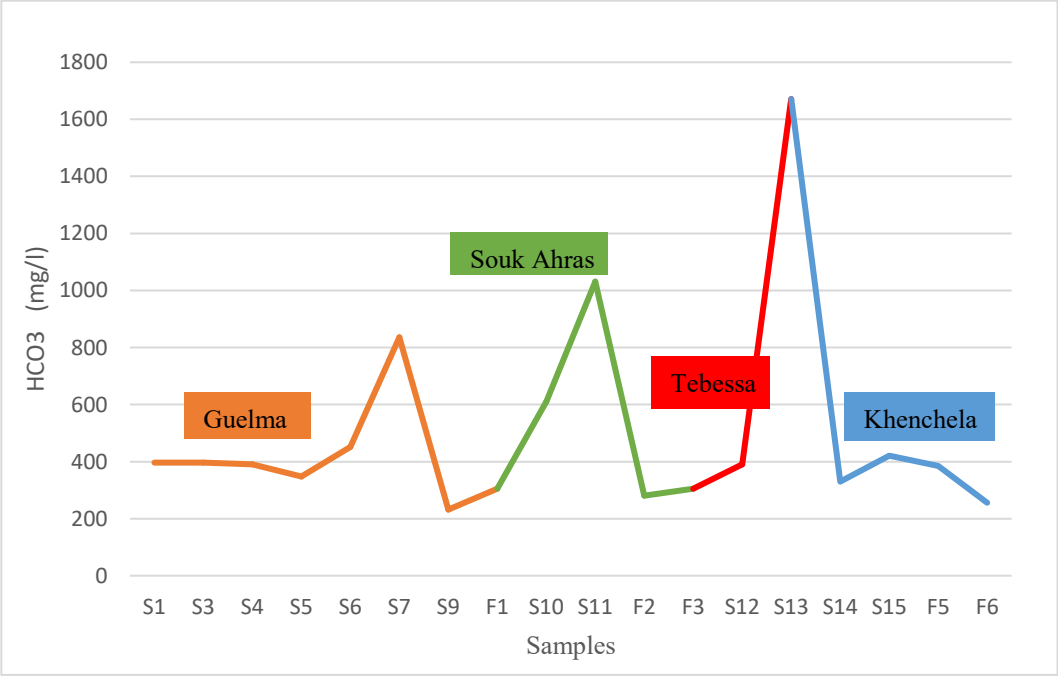


Figure 61 Spatial Variation of Bicarbonate Concentration Across the Study Region

Regarding bicarbonate concentrations, the graph (Figure 61) shows low Bicarbonate concentrations in the majority of the area, especially in the northwest and central regions. This suggests minimal interaction between the groundwater and carbonate rocks or faster groundwater flow, which limits the dissolution of minerals that produce bicarbonates. As we move towards the eastern part of the map, the bicarbonate levels increase gradually around S11 in Souk Ahras and S13 in Tebessa, where they peak at the highest value of 1.671 mg/l.

d) Chloride (Cl^-)

This element is primarily linked to the dissolution of saline formations. In our study area, the low chloride content is mainly observed in the cold springs, with F5 in Khenchela showing the lowest concentration at 14.13 mg/L. In contrast, the chloride level increases significantly and reaches its highest at 6130 mg/L at S13 Hammam Sidi Yahia. This variation suggests that saline formations or evaporite deposits have minimal influence on the cold springs. Meanwhile, the dissolution of these formations, besides the geothermal activity, may contribute to the increase of chloride levels, particularly at S13 in Tebessa and its surroundings, as it shows the spatial variation (Figure 62), as well as at S7 Hammam N'bails in Guelma.

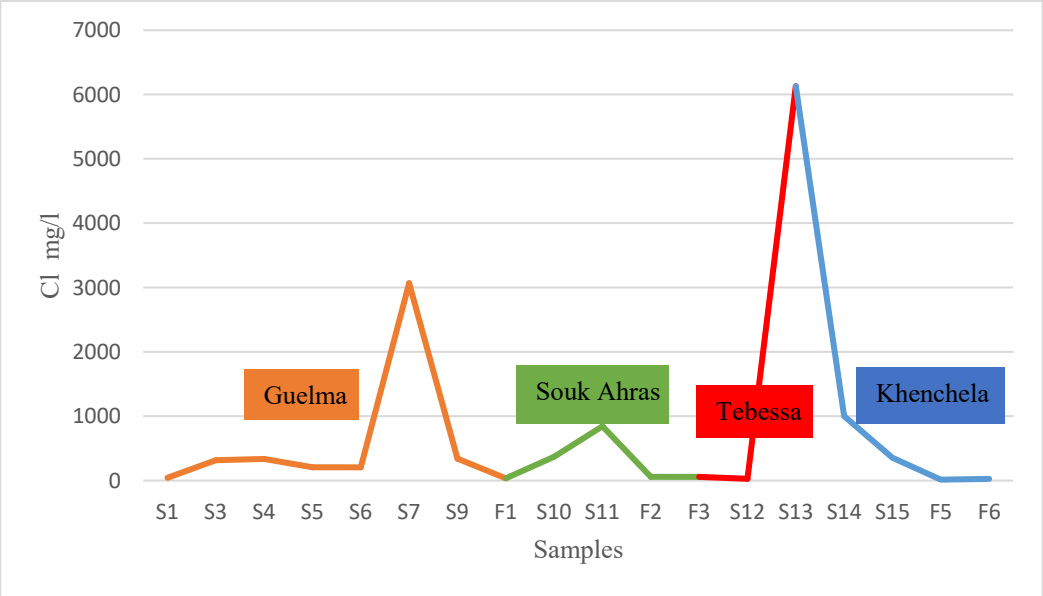


Figure 62 Spatial Variation of Chloride Concentration Across the Region

e) Sodium (Na^{2+})

Similar to the Chloride element, Sodium content is related to the dissolution of saline formations, particularly evaporites such as halite (NaCl), according to the following relationship:

$$NaCl = Na+ + Cl-$$

The sodium concentrations vary between 9.53 mg/L at F5 in Khenchela and reach a high of 4800 mg/L at S13 Sidi Yahya in Tebessa (Figure 63).

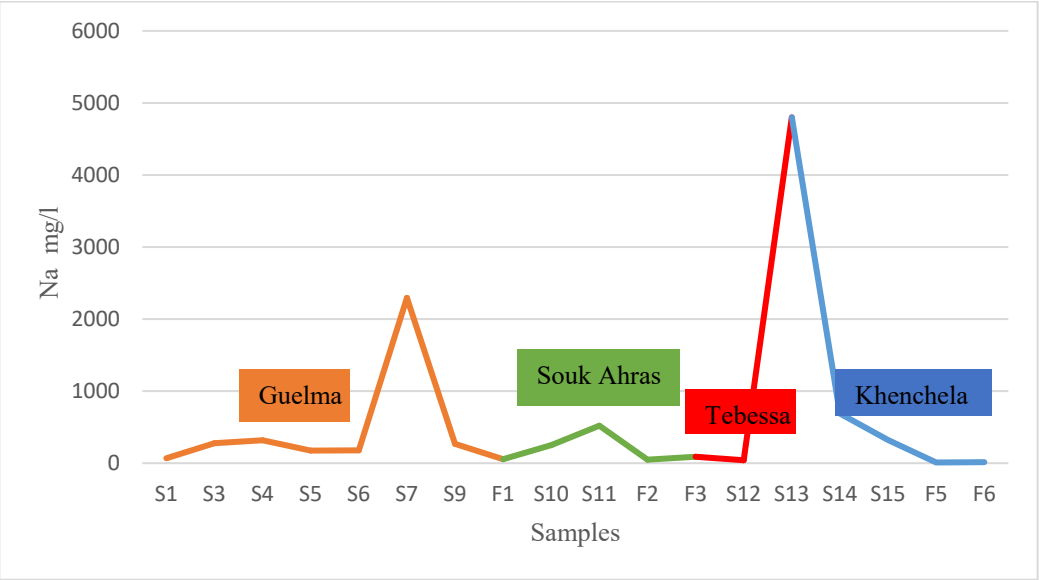


Figure 63 Spatial Variation of Sodium Concentration Across the Study Zone

f) Potassium (K^{2+})

Potassium generally originates from the weathering of silicate formations (gneiss, schist), potassium clays, and the dissolution of chemical fertilizers. Its levels range from 0.24 mg/L at F2 Ain Souda in Souk Ahras to 81.2 mg/L at S7 Hammam N'baïls in Guelma. The distribution of these values across the study area is visually represented in Figure 64, identifying regional variations and major patterns.

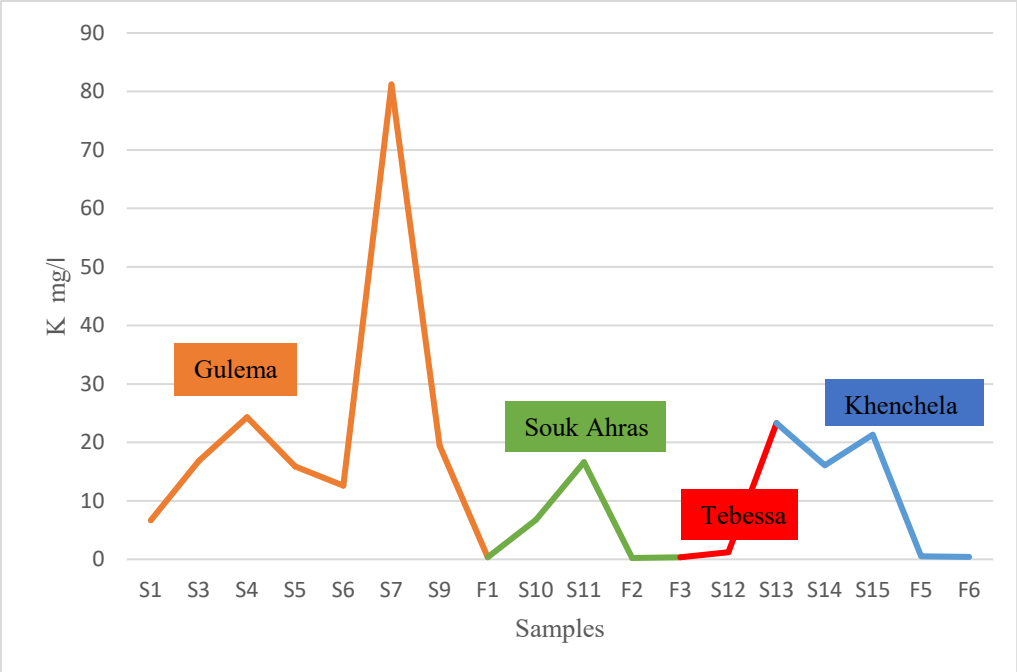


Figure 64 Spatial Variation of Potassium Concentration Across the Study Zone

g) Sulfate (SO_4^{2-})

The origin of sulfates in the study area is attributed to the dissolution of gypsum-bearing formations ($CaSO_4 \cdot 2H_2O$) and anhydrite ($CaSO_4$). These two minerals dissolve very quickly in contact with water. The dissolution reaction of gypsum is represented by the following equation:

$$CaSO_4 \cdot 2H_2O = Ca^{2+} + SO_4^{2-} + 2H_2O$$

High values of sulfates characterize the region of Hammam Belhecheni at S6, with 1060.8 mg/l, and Hammam Guerfa at S5, with 1041.9 mg/l in Guelma. This high level may be interpreted by the presence of evaporite deposits and geothermal activity, both of which play an important role in the formation of sulfates. However, the low content of this element is observed at S10 Ouled Driss in Souk Ahras with a concentration of 12.67 mg/l.

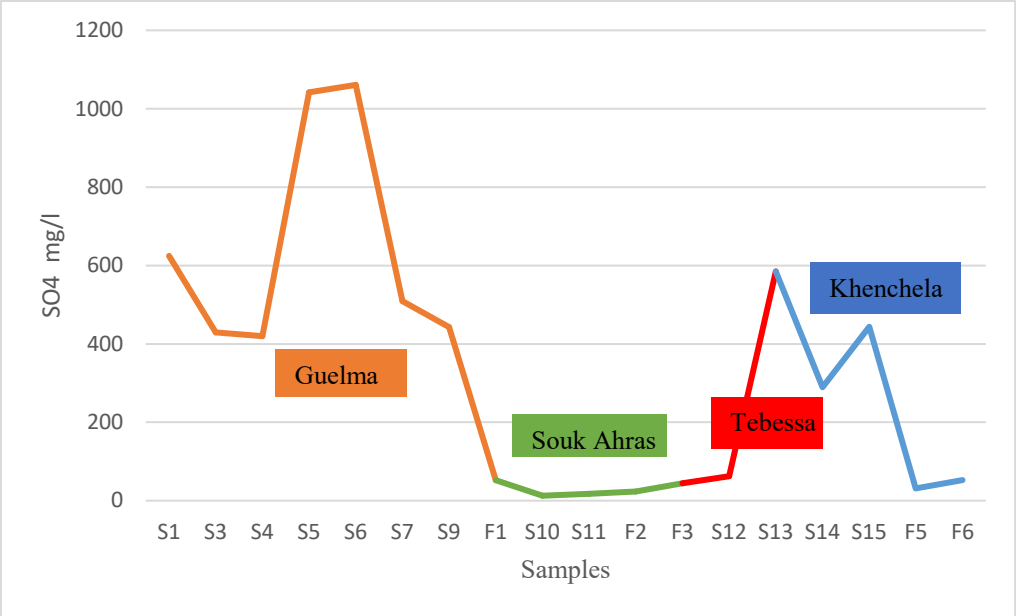


Figure 65 Spatial Variation of Sulfate Concentration Across the Study Zone

2.7.2 Minor Elements

a) Nitrates (NO_3^-) and Nitrites (NO_2^-)

Nitrogen is present in three chemical forms: nitrate (NO_3^-), nitrite (NO_2^-), and ammonium (NH^{4+}). Nitrates represent the most oxygenated form, which is highly soluble. Nitrates are an important nutrient for plant growth. Still, they can become a significant pollutant when present in excess due to human activities, particularly agriculture (fertilizers and animal waste) and wastewater management. They originate as well from natural processes such as soil nitrification and atmospheric deposition. Meanwhile, nitrites represent a less oxygenated and less stable form, acting as an intermediate between nitrates and ammonium.

The values of nitrate (NO_3^-) vary from 2.98 mg/l at F2 Ain Souda in Souk Ahras to 165.85 mg/l at S7 Hammam N'bails in the Guelma region. Given that the World Health Organization (WHO) recommends a maximum concentration of 50 mg/L for drinking water to avoid health risks. However, the content of nitrites is below the detection limit in our samples.

The very high nitrate concentration of 1180 mg/L observed at S13 probably results from both natural and human causes. Agricultural runoff and wastewater may contribute to this, but proximity to an iron mine is a much more important contributor. Mining activities may introduce ammonium nitrate-based explosives into the groundwater, adding a big load of nitrate. Residues of these explosives can leach into the water, significantly raising the nitrate level. Additionally, mining operations can alter the

pattern of water flow, enabling surface runoff or wastewater carrying nitrates to seep more easily into the groundwater. All these reasons together probably explain the unusually high nitrate level at S13 (Figure 66) and stress the importance of monitoring the impact of mining on water quality in the area.

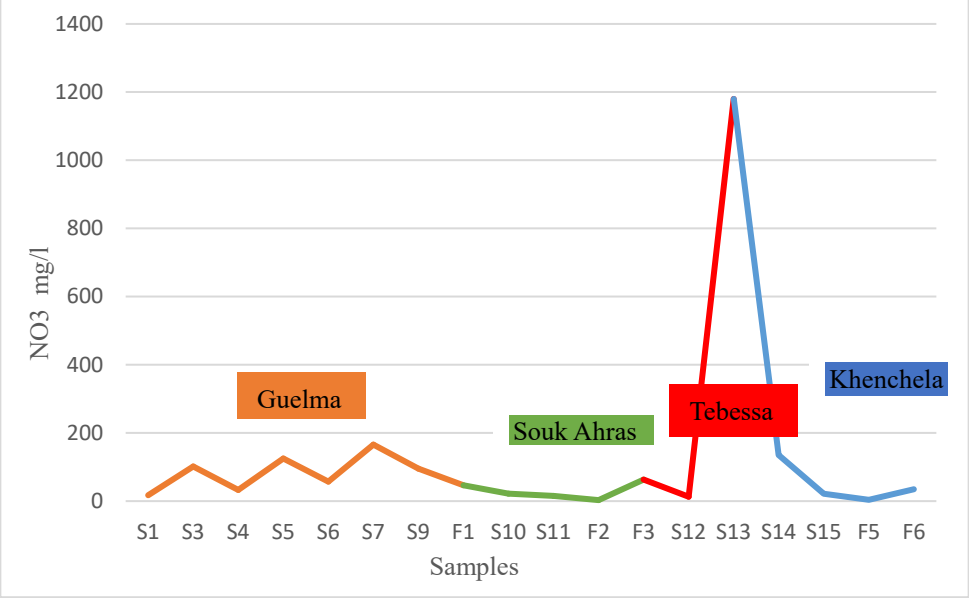


Figure 66 Spatial Variation of Nitrates Concentration Across the Study Zone

2.7.3 Trace Elements

a) Strontium (Sr^{2+})

Strontium is an alkaline earth metal that is most commonly found in nature in the form of strontianite ($SrCO_3$) and celestite ($SrSO_4$). Celestite, in particular, is a good indicator of evaporitic formations and can help determine the origin of sulfates. (Edmunds et al., 1996).

The analysis of the strontium content in our samples revealed that they are low in strontium, with values ranging from 0.26 mg/l at F6 in Khenchela to 19.1 mg/l at S7 Hammam N'bails in Guelma (Figure 67). Low strontium concentrations suggest that sulfates are primarily coming from sulfide oxidation, while high strontium concentrations indicate the presence of strontium-rich evaporitic minerals.

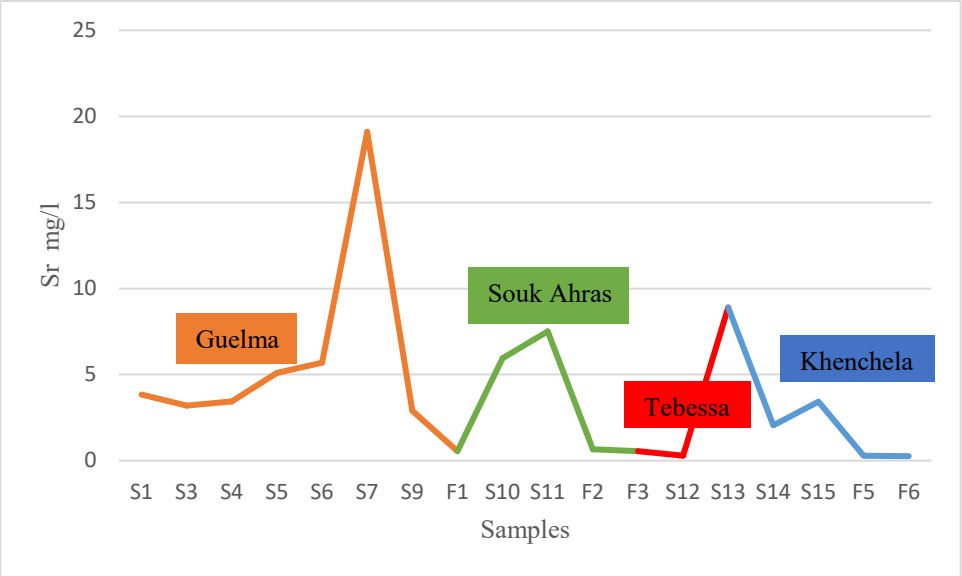


Figure 67 Spatial Variation of Strontium Concentration Across the Study Zone

b) Lithium (Li^{2+})

The lithium content in our samples ranges from 0.01 mg/L at F5 and F6 in Khenchela, S12 in Tebessa, and F1 in Guelma, to the highest level of 1.51 mg/l recorded at S7 Hammam N'bails, in addition to S13 with 1.5 mg/l.

The spatial variation, as shown in Figure 68, points out that lithium concentration is highest in geothermal regions, like Hammam N'bails and Sidi Yahya in Tebessa, where there is likely a strong interaction between geothermal fluids and lithium-rich formations as pegmatites and granites. In contrast, lower concentrations are seen in regions with fewer lithium-bearing minerals, such as spodumene, lepidolite represent the restricted ability for lithium formation in those areas.

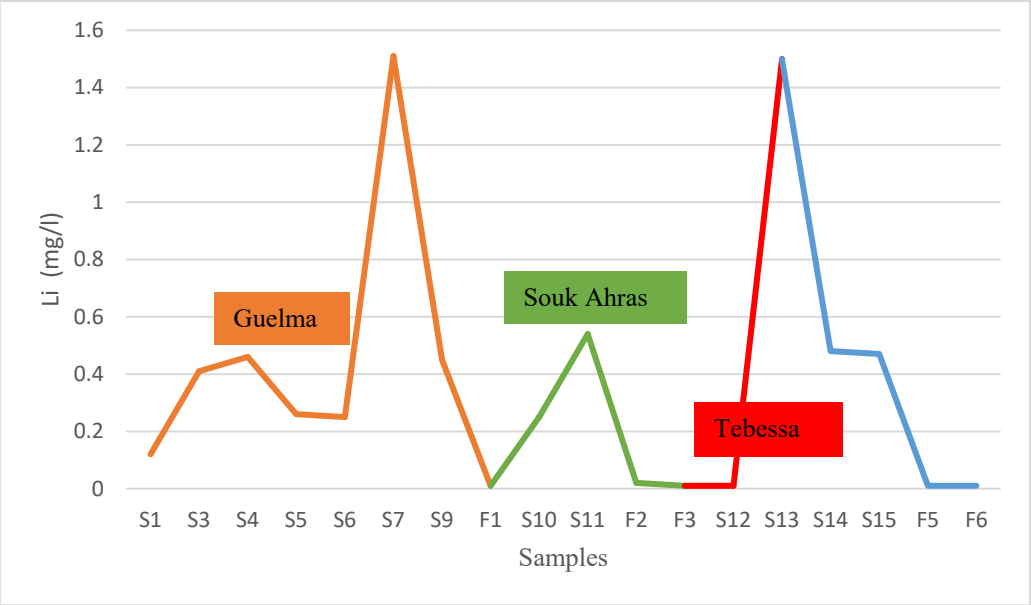


Figure 68 Spatial Variation of Lithium Concentration Across the Study Zone

3. Chemical Facies

To identify water types, geochemical evolution, and understand groundwater flow, mineral interactions, and to determine sources of contamination, it's important to use tools such as Piper, Schoeller-Berkaloff, and Stabler diagrams to graphically represent and interpret the chemical composition of water samples.

3.1 Stabler Classification

The Stabler classification (Figure 69) indicates a chemical homogeneity in the waters. The springs in our region are primarily characterized by a predominance of sulfate over bicarbonate. The samples that were sulfate-dominant in 2018 retained this dominance in 2019. Additionally, new samples in 2019 show bicarbonate dominance. The cations are represented by calcium dominance in some samples and sodium dominance in others. According to this classification, four groups are distinguished:

- Calcium Sulfate ($Ca\text{-}SO_4$) Group: S1, S5, S6
- Sodium Chloride (Na-Cl) Group: S2, S4, S9, S7, S14, S15, S10, S11
- Calcium Bicarbonate ($Ca\text{-}HCO_3$) Group: S12
- Calcium Chloride (Ca-Cl) Group: S8, S3

In the second analysis conducted in 2019, there was a slight shift in the water types.

- Sodium chloride (Na-Cl): S3, S4, S7, S9, S10, S11, S13, S14, and S15, in addition to seawater.
- Calcium sulfate (Ca-SO_4) group: S1, S5, and S6.
- Calcium bicarbonate (Ca-HCO_3) group: F1, F2, F3, F5, F6 and S12.
- It is important to note that samples S2 and S8 were unfortunately lost during transport to the laboratory



Figure 69 Chemical Facies of Waters Across the Region According to Stabler Classification (2018-2019)

3.2 Piper Diagram

The Piper diagram is an effective tool for comparing the chemical compositions of natural waters used widely all over the world. It uses two specific triangles to represent cations and anions, displaying their relative concentrations. The position of an analytical result on these triangles indicates the dominant cations and anions. A diamond shape plots the intersection of lines from the two triangles, representing the overall water chemistry. This helps to identify the water's facies. By plotting multiple samples simultaneously, the Piper diagram allows tracking and monitoring the chemical evolution of waters in space and time, comparing different samples, and understanding potential mixing processes. It offers insights into the lithology of the surrounding media.

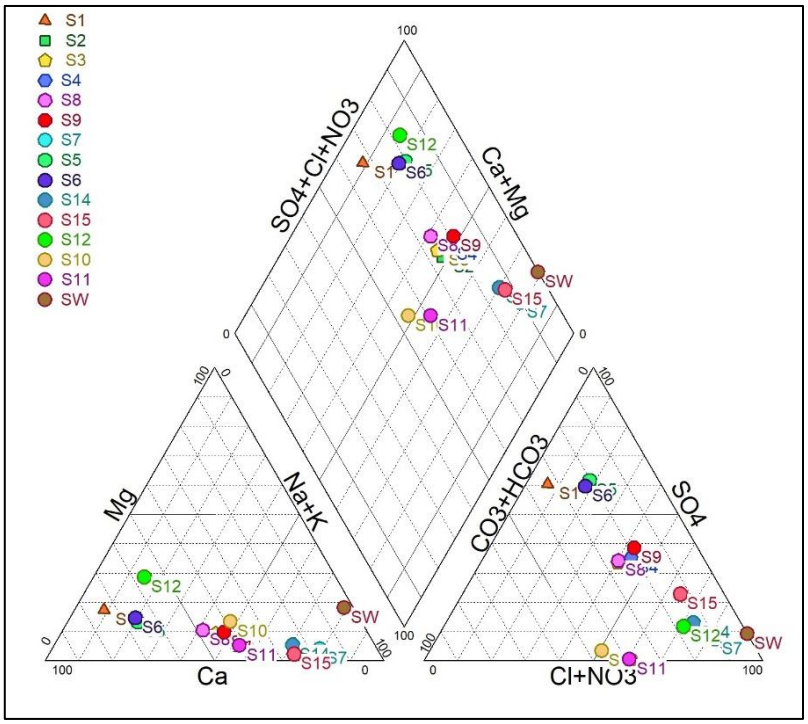


Figure 70 Piper Diagram of Groundwater Samples from the First Sampling Campaign (2018)

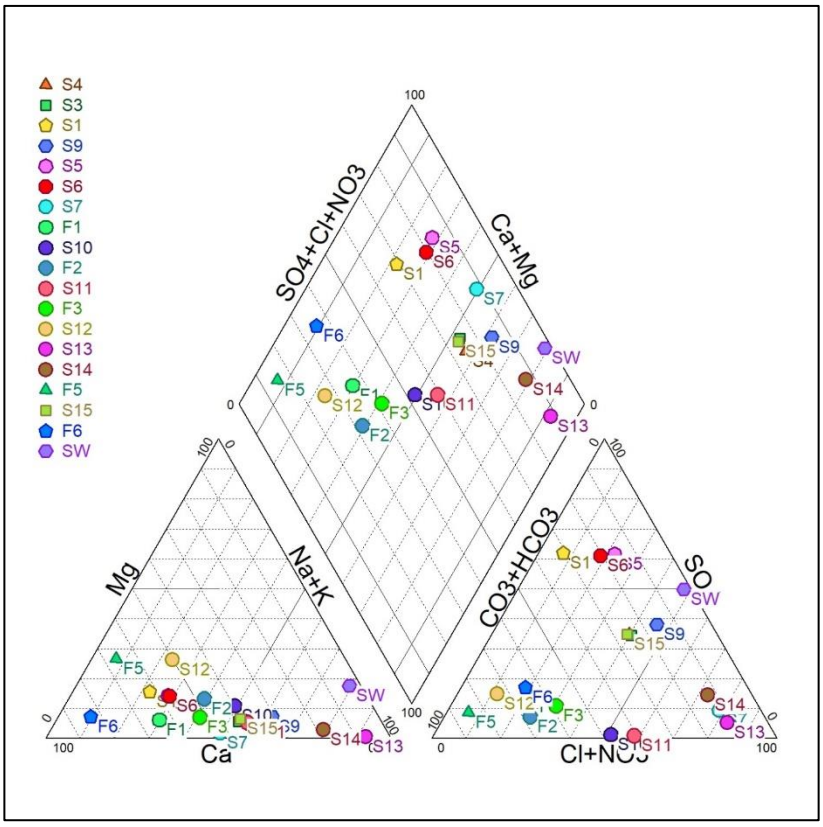


Figure 71 Piper Diagram of Groundwater Samples from the Second Sampling Campaign (2019)

For the 20 samples and the reference sample, the Piper diagram shows that the samples are distributed around three poles (Figures 70 and 71). The Calcium bicarbonate facies is dominant in cold waters (F1, F2, F3, F5, F6). The springs S1, S5, and S6 in Guelma tend towards a different facies, Calcium sulfate. However, S3, S4, S7, S9, S10, S11, S13, S14, S15, and seawater sample (SW) belong to the Sodium chloride water type. Noting that S12 in the first analysis has an ionic balance outside the acceptable range, we decided to accept only the second set of results, and based on this, S12 belongs to the first group and represents a Calcium bicarbonate water type.

- **Sodium chloride facies**: characterises thermal waters with a range of temperature between 34.5°C at S13 Sidi Yahya in Tebessa and 89.1°C at S4 Cascade 2 in Guelma, presenting a high salinity from 0.8 mg/l at S9 in Guelma and S10 in Souk Ahras to 10.4 mg/l at S13 Sidi Yahya in Tebessa, followed by S7 with 5.5 mg/l in Guelma, which contributes high TDS values varying between 815 mg/l and 1988 mg/l as a minimum and maximum at S10 and S11, respectively, in addition to the particularity of S7 and S13, which have values exceeding the detection limit of the measurements (OFL). The elevated values of these two parameters result in increased electrical conductivity that varies between 1770 µs/cm at S10 and 16850 µs/cm at S13.
- **Calcium sulfate facies**: characterizes the second group of our thermal waters, representing a low salinity compared to the first group, ranging between 0.5 mg/l at S1 and 1.7 mg/l at S5, with moderately high values of TDS from 640 mg/l at S1 to 1508 mg/l at S5, and relatively high temperature falls between 51.4°C and 62.8°C. The electric conductivity of this group fluctuates from 1459 µs/cm at S1 to 2410 µs/cm at S6.
- **Calcium bicarbonate facies** are represented by the cold and warm waters in the study zone, with significantly low temperatures ranging from 18.7°C at F3 in Souk Ahras to 29°C at F6 in Khenchela. Despite this, these waters show low salinity (ranging from null to 0.1 mg/L), low TDS values (207 mg/L to 341 mg/L), and consequently, low electrical conductivity (531 µS/cm to 736 µS/cm).

From an anion triangle, for thermal waters the dominant ions are Cl^- and SO_4^{2-}, whereas for cold waters HCO_3^- is the dominant ion. From the cations triangle, Na^{2+} and Ca^{2+} are the dominant ions. The influence of geological formations on water types is evident: carbonate formations and limestone

contribute to bicarbonate facies, whereas evaporite deposits, clay, marls, and gypseous formations lead to the development of chloride and sulfate facies.

3.3 Schoeller-Berkaloff Classification

In addition to the Piper diagram, a Schoeller-Berkaloff diagram is used in the present study to provide a complete understanding of water chemistry, and offer detailed concentration profiles and enabling quantitative comparisons across multiple samples. Schoeller's method, later adapted by Berkaloff, requires using a semi-logarithmic scale to plot the concentrations of anions and cations. The y-axis represents the quantities of ions, while the x-axis displays the chemical elements at regular intervals. This approach is applied to each water sampling location.

The diagrams for the periods of 2018/2019 confirm a Calcium bicarbonate facies related to HCO_3^- and Ca^{2+}; furthermore, a Calcium sulfate facies and Sodium chloride facies related to SO_4^{2-}, $Ca^{2+,}$ and Cl^-, Na^+.

The graphical presentations (Figures 72 and 73) of the samples reveal that the springs with the highest mineralization appear first in the graph. This is the case for seawater (SW), S13, and S7, followed by S14. These springs are characterized by a sodium chloride water type, which is mostly a result of the presence of evaporite deposits and geothermal activity in the region.

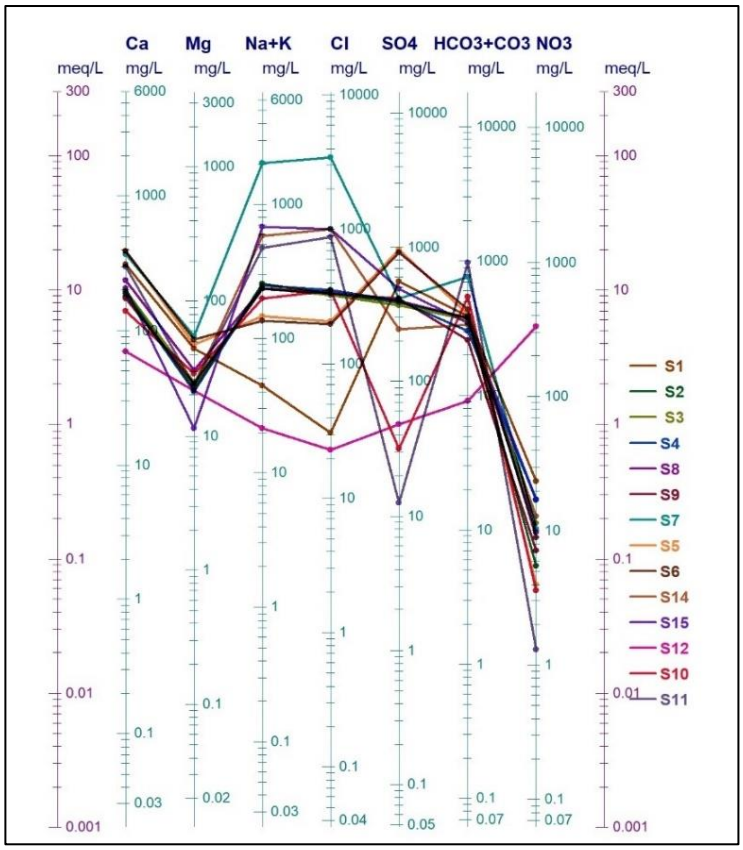


Figure 72 Schoeller-Berkaloff Diagram Comparing the Hydrochemical Profiles of the 2018 Samples in the Study Area

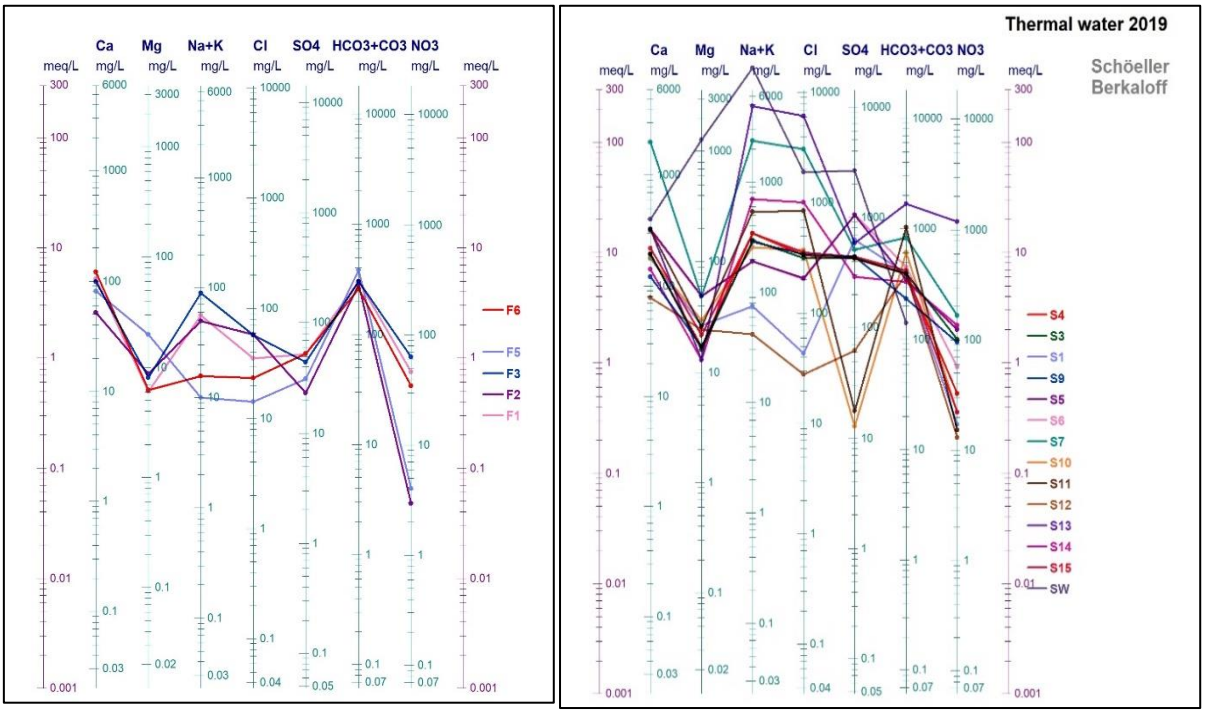


Figure 73 Schoeller-Berkaloff Diagram Comparing the Hydrochemical Profiles of the 2019 Cold and Thermal Samples in the Study Area

4. Saturation Index

Generally, a chemical analysis provides total concentrations of elements in solution. A speciation calculation distributes these totals among aqueous species by using an aqueous model; the results of the speciation calculation are the activities of all of the aqueous species. The activities can be used for calculating saturation indices for minerals, relative to the water. Speciation modeling requires only a SOLUTION data block for each water analysis for which saturation indices are to be calculated.(Parkhurst & Appelo, 2013).

The saturation indices (SI) were calculated for all the sampled springs using the PHREEQC module from Aquachem 4.0 software. The results are presented in Table 26:

Table 26. The calculated index of saturation SI

	Guelma								Souk Ahras				Tebessa		Khenchela			
	S4	S3	S1	S9	S5	S6	S7	F1	S10	F2	S11	F3	S12	S13	S14	F5	S15	F6
Anhydrite	-1.07	-1.05	-0.92	-1.2	-0.6	-0.6	-0.58	-1.98	-2.56	-2.55	-2.33	-2.08	-2.04	-1.23	-1.4	-2.29	-1.01	-1.91
Aragonite	-0.65	-0.02	-0.45	0.08	0.5	0.45	0.33	-0.06	-0.1	0.07	-0.06	0.01	-0.13	-0.13	0.13	0	-0.29	0.33
Calcite	-0.51	0.13	-0.3	0.22	0.64	0.59	0.47	0.09	0.05	0.21	0.08	0.15	0.01	0.02	0.27	0.15	-0.15	0.47
Halite	-5.61	-5.7	-7.16	-5.67	-6.1	-6.1	-3.92	-7.3	-5.66	-7.12	-5.02	-6.88	-7.54	-3.31	-4.82	-8.45	-5.59	-8.03
Dolomite	-1.73	-0.5	-1.09	-0.06	0.8	0.7	-0.3	-0.71	-0.33	0	-0.57	-0.43	-0.12	-0.99	-0.14	0.04	-0.96	0.02
Strontianite	-1.8	-1.21	-1.51	-0.94	-0.71	-0.7	-1.1	-1.74	-0.98	-1.23	-1.1	-1.65	-1.96	-1.1	-1.11	-1.85	-1.5	-1.74
Gypsum	-0.85	-0.83	-0.7	-0.98	-0.38	-0.38	-0.37	-1.76	-2.34	-2.33	-2.11	-1.86	-1.82	-1.01	-1.18	-2.07	-0.79	-1.69

The idea of the saturation index (SI) was applied in order to determine the thermodynamic equilibrium and assess the degree to which thermal fluids had dissolved the host-rock minerals. This tool is expected to provide indications regarding the type of host rock formations that water traveled through. The SI suggests that because of the water's high temperature, it has a relative ability to dissolve more closely related minerals.

According to (Parkhurst & Appelo, 2013) in "Description of Input and Examples for PHREEQC Version 3", the Saturation Index (SI) is used to assess the saturation state of a solution with respect to a mineral. The SI is calculated as:

$$SI = Log\left(\frac{IAP}{Ksp}\right)$$

Where:

IAP is the Ion Activity Product of the dissolved ions that make up the mineral.

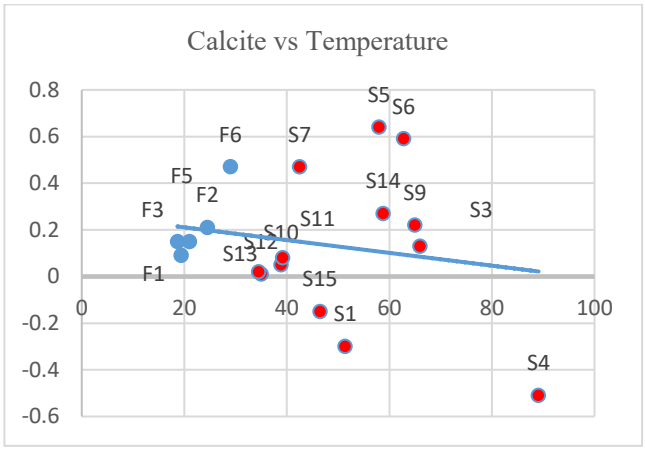
Ksp is the Solubility Product of the mineral.

The value of SI can be interpreted as follows:

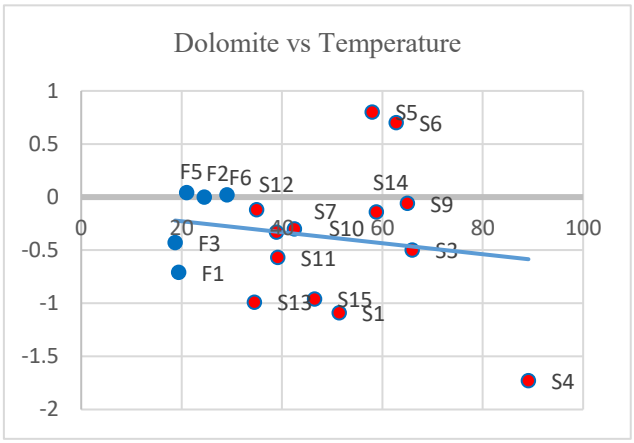
- SI < 0: The solution is undersaturated with respect to the mineral, meaning the mineral can dissolve in the water.
- SI = 0: The solution is saturated, indicating equilibrium between the mineral and the solution, where no dissolution or precipitation occurs.
- SI > 0: The solution is oversaturated, suggesting that the mineral is potentially able to precipitate from the solution.

The Saturation Indices (SI) calculated for anhydrite, halite, strontianite, and gypsum indicate that all samples are undersaturated, suggesting that these waters have the potential to dissolve these minerals. Specifically, samples S1, S3, S4, S10, S11, S12, S13, S15, and F1 are undersaturated with respect to aragonite, while F5 is in equilibrium with this mineral. Regarding calcite, the SI values are positive for all samples except for S1, S4, and S15, which implies that most samples are supersaturated, and calcite may precipitate. For dolomite, the SI values suggest that F2 is in equilibrium, whereas F5, F6, S5, and S6 are undersaturated, indicating that these waters can dissolve dolomite under the current conditions. Carbonate formations tend to precipitate as calcite and dolomite, while evaporite formations, along with strontianite, are always undersaturated and tend to dissolve.

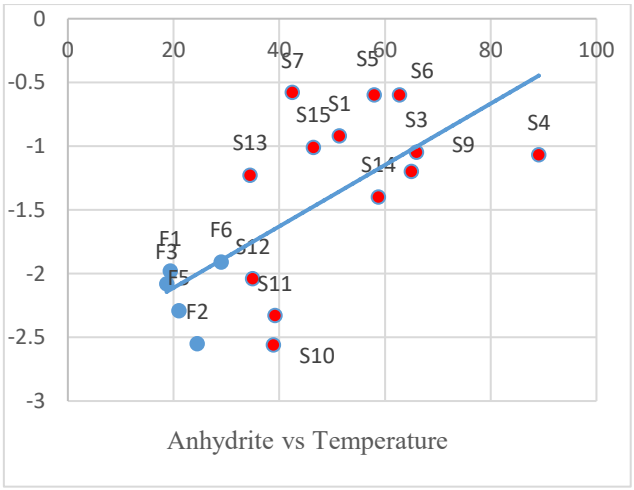
5. Temperature Influence on Mineral Saturation :



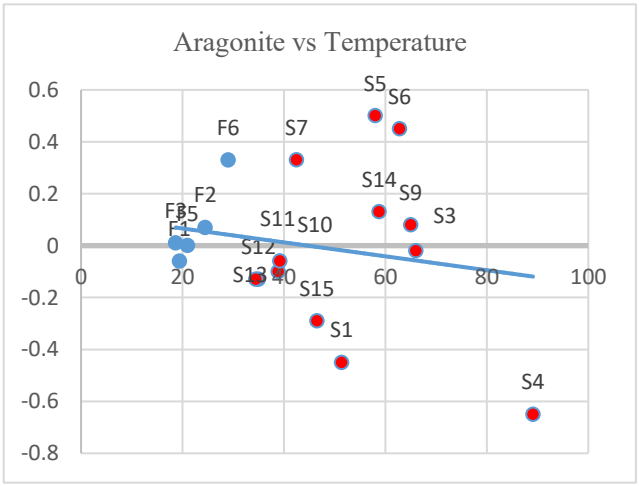
(a)



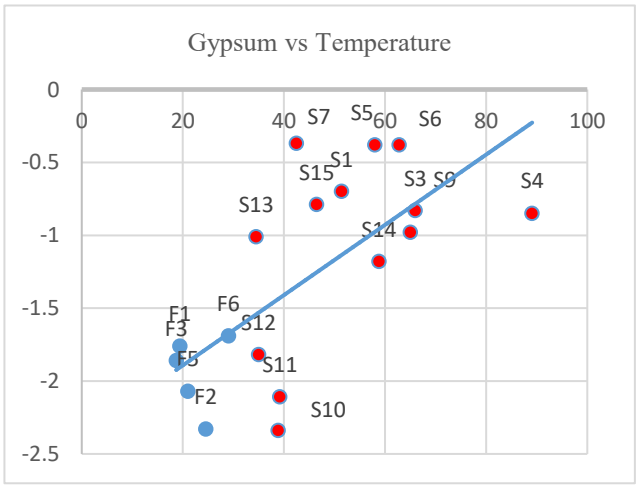
(b)



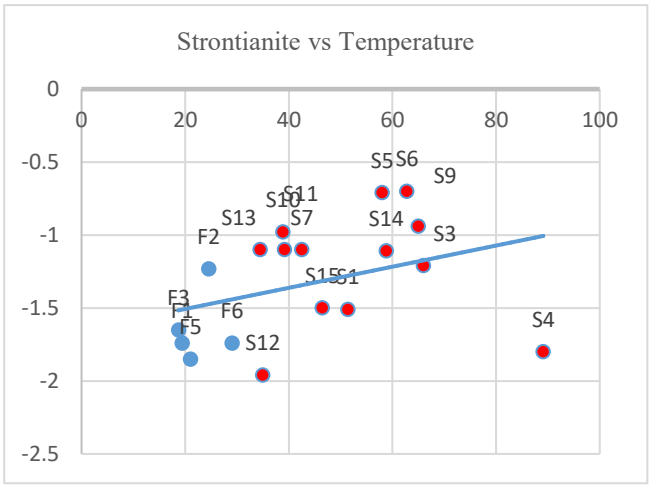
(c)



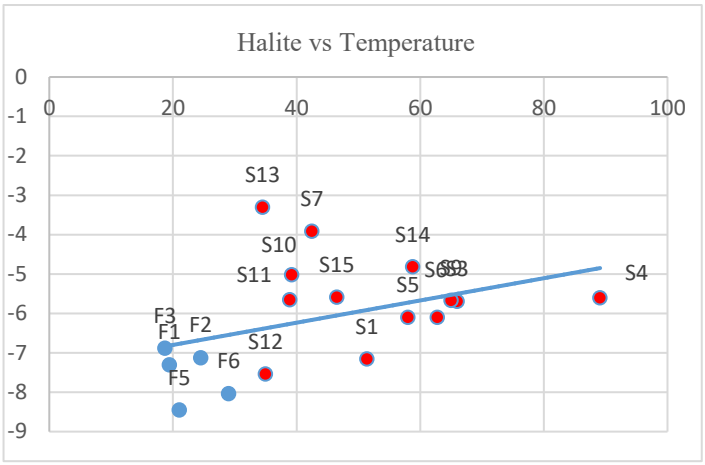
(d)



(e)



(f)



(g)

Figure 74 Temperature vs Saturation Index for the Following Minerals: Calcite (a), dolomite (b), anhydrite (c), aragonite (d), gypsum (e), strontianite (f), halite (g)

The temperature has a significant impact on mineral saturation states in the study area (Figure 74). For carbonate minerals such as calcite, aragonite, and dolomite, a negative correlation with temperature is observed, reflecting increased solubility at higher temperatures under the prevailing hydrochemical conditions, particularly due to the temperature-sensitive CO_2 system and its control on pH and carbonate equilibria (Plummer & Busenberg, 1982; Appelo & Postma, 2004) .In contrast, evaporite minerals such as gypsum, anhydrite, and halite display a strong positive correlation with temperature, indicating decreased solubility and a greater tendency to precipitate under warmer conditions (Langmuir, 1997). Strontianite ($SrCO_3$) shows a positive trend with temperature, which is likely linked to indirect processes such as CO_2 degassing and pH increase, rather than a direct solubility effect. This pattern is characteristic of the geological and hydrochemical setting of the study area and does not represent a universal temperature–solubility relationship. It highlights that the thermal influence on mineral saturation depends on mineral composition, fluid chemistry, and the local hydrogeological context

The combination of water temperature, mineral saturation plots, water type classifications, residence time, and flow rate provides a comprehensive understanding of a water sample's origin and its interaction with surrounding lithology. Water temperature reveals the geothermal influence on the water, indicating whether the water has originated from deep geothermal sources, with higher temperatures pointing to deeper circulation and geothermal heating. Mineral saturation plots show whether the water is undersaturated or supersaturated with respect to various minerals, helping to determine how much interaction has occurred with minerals in the flow path. Water type classifications,

which identify dominant ions, further reveal whether the water has been influenced more by evaporites or carbonates. Additionally, determining the residence time and flow rate of the water provides insights into how long the water has been in contact with the rocks and how rapidly it is moving through the geological formations. Integrating these factors allows for a detailed reconstruction of the water's geological and hydrological history, pinpointing its source, the types of rocks it has interacted with, and its flow path. This approach enhances the understanding of the geochemical processes affecting the water and provides valuable information about the mineral deposits encountered during its journey.

6. Principal Geochemical Processes: Binary Diagrams

Understanding the geochemical mechanisms controlling the major ion chemistry of water can be obtained through the use of ionic ratios.

a) Na^+/Cl^-

The diagram Na^+/Cl^- in (Figure 75) shows a linear correlation between these two elements, representing a coefficient of $R^2 = 0.9$, except for the sample S1. This dissolution releases equal mole concentrations of Na^+ and Cl^- in the solution, and its corresponding reaction can be expressed as $NaCl = Na^+ + Cl^-$ (Yang et al., 2019). It is commonly used to utilize this plot to identify the mechanism of salinity. The milliequivalent per liter (meq/l) ratio of Na^+ vs. Cl^- for all samples plotted around the 1:1 line indicates that the Na^+ and Cl^- derive their concentrations mainly from halite dissolution within host sedimentary formations. Moreover, the SI's values of halite are undersaturated (Table 26), suggesting that more halite could dissolve, particularly in the thermal waters.

In addition to halite dissolution, cation exchange processes with clay-rich formations could explain the increased sodium levels in some samples. This is especially relevant in geothermal environments like S7 and S13, where ion exchange between calcium and sodium can occur, as evidenced by the fact that calcium levels in these springs are lower than sodium levels. However, S13 deviates in terms of NO_3 concentration, indicating additional contamination sources mostly related to human activity. This makes S13 a mixed case of natural mineral dissolution and anthropogenic impact, especially from nearby mining activities (El-Ouanza) or agricultural sources.

Meanwhile, the ratio of Na^+/Cl^- for S1 is less than 1, suggesting that chloride (Cl^-) is not primarily coming from halite dissolution. Instead, the geothermal fluids with a temperature of 51.4°C and the presence of marly-calcareous and shales in the surrounding formations could contribute to the low (Cl^-) concentration.

Using the 2018 analysis results, S1 was plotted aligned with the halite dissolution line, indicating a balanced relationship between sodium (Na^+) and chloride (Cl^-) concentrations. However,

in subsequent analyses, S1 shifted to the Na^+ line, showing a significant -19% ionic imbalance. This shift may suggest influences such as cation exchange, where calcium (Ca^{2+}) is replaced by sodium (Na^+), leading to increased sodium levels while S1 remains classified as calcium sulfate water type.

However, the inaccuracies in the ionic balance raise concerns about potential sampling errors, analytical variability, or interference from other ions during analysis. Changes in halite dissolution dynamics may also contribute to this discrepancy. Overall, this shift reflects evolving groundwater conditions, but further investigation is necessary to determine the precise causes behind the observed changes.

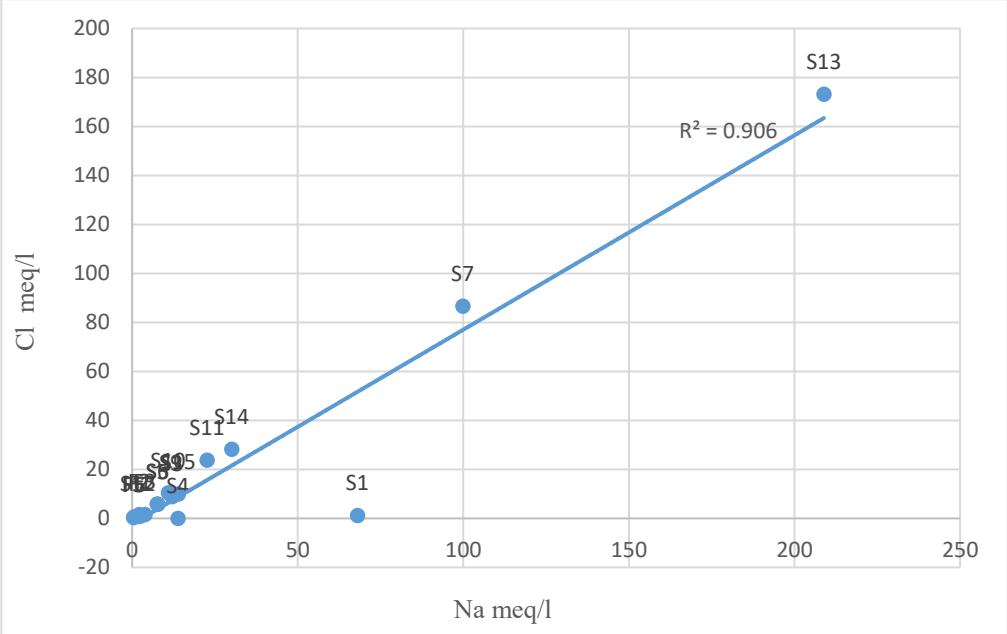


Figure 75 Ionic Ratio Plot of Cl^-/Na^+ for All Samples

b) HCO_3^-/Ca^{2+}, HCO_3^- / Mg^{2+}

The relationship HCO_3^- vs Ca^{2+} (Figure 76) shows no correlation, the positioning of samples on the graph indicates that F2, F5, S12 and closely F3, F1, F6 and S13 belong to the line of limestone dissolution (a slope close to 1:2), while the rest of springs (under the line of correlation) suggests a gypsum origin especially S7 with an excess of Ca^{2+} (2001 mg/l) over HCO_3^- (835.7 mg/l).

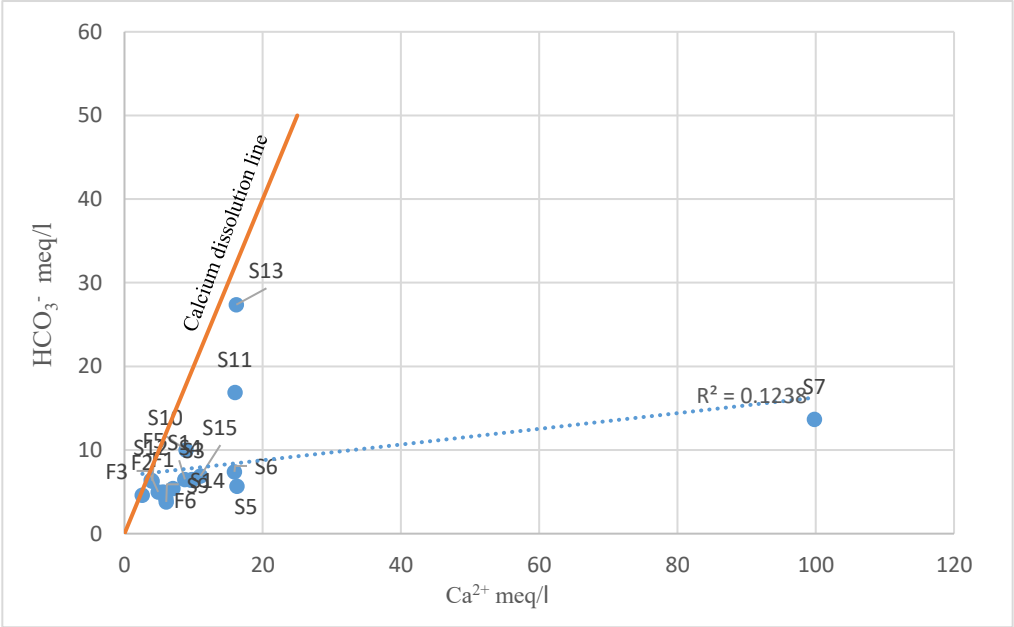


Figure 76 Ionic Ratio Plot of HCO_3^-/ Ca^{2+} for All Samples

Furthermore, the concentrations plotted of Mg^{+2} coupled with HCO_3^- (Figure 77) Indicate a weak correlation and decipher that the Mg^{2+} in most samples is introduced by dedolomitization that is driven by the dissolution of gypsum and/or anhydrite, indicating a gradual depletion of calcium, which might precipitate as calcite, rather than a dissolution of dolomite which is the case of F5, S15, S10, and indicating a gradual enrichment in magnesium.

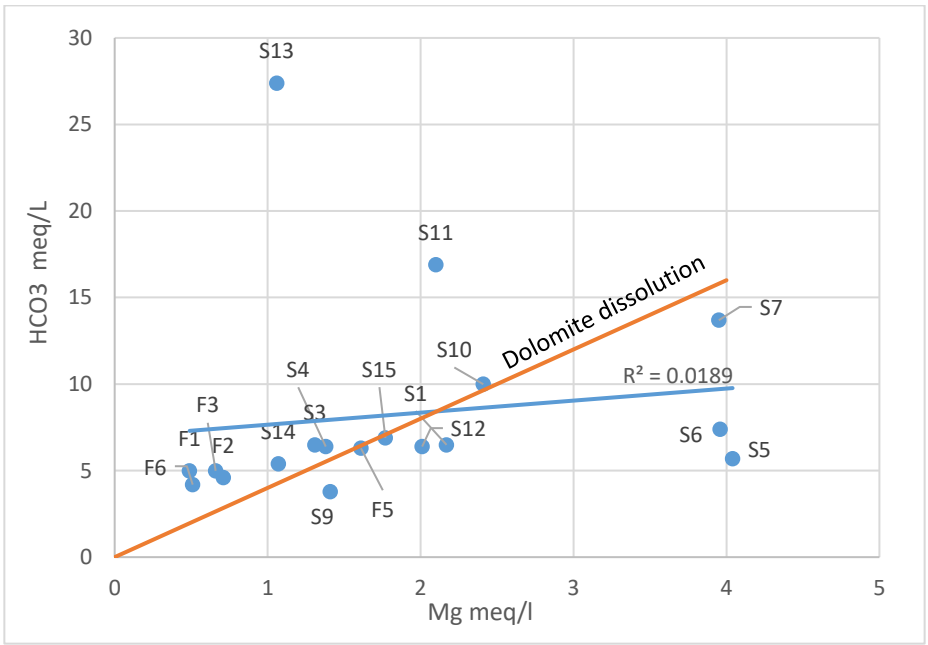


Figure 77 Ionic Ratio Plot of HCO_3^-/Mg^2 for All Samples

c) SO_4^{2-}/Ca^{2+}

The plot ratio (Figure 78) reveals a weak positive correlation between calcium (Ca) and sulfate (SO_4) concentrations across all samples. The theoretical model for gypsum ($CaSO_4 \cdot 2H_2O$) and anhydrite ($CaSO_4$) dissolution indicates that samples near this line, such as S3, S4, S14, and S15, likely derive their (Ca) and (SO_4) from these minerals. Samples above the line, including S6, S1, and S9, could suggest the presence of additional sulfate sources or calcium depletion. In contrast, the other samples positioned below the gypsum/anhydrite line may indicate additional calcium sources or sulfate removal, which applies to the remaining samples. Sample S7 shows a very high (Ca) concentration relative to most other samples, suggesting a distinct contribution to its calcium levels.

The considerable scatter in the data points indicates significant variability in the (Ca/SO_4) ratio among the samples, suggesting that multiple processes or sources are influencing water chemistry.

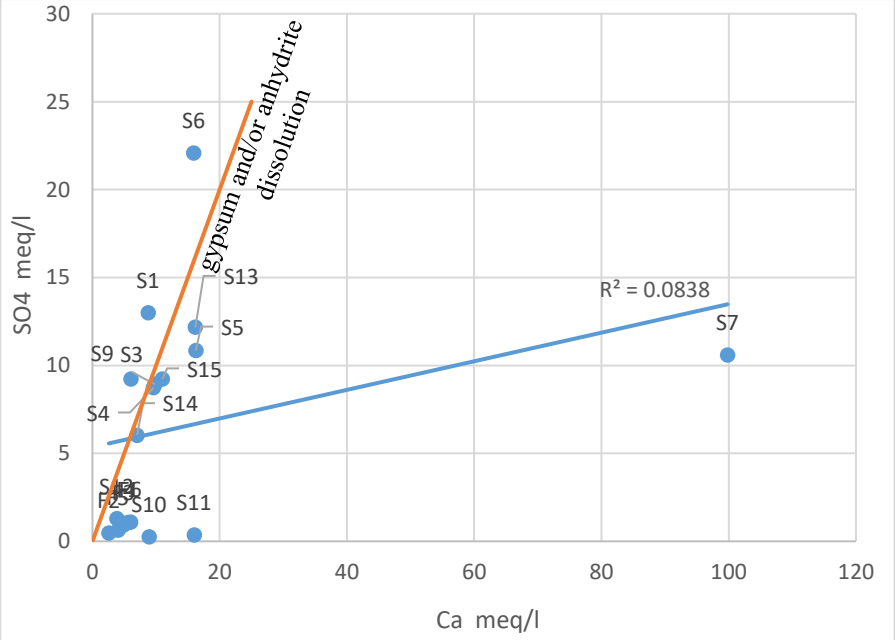


Figure 78 Ionic Ratio Plot of Ca^{2+}/SO_4^{2-} for All Samples

d) $Ca^{2+} + Mg^{2+}/HCO_3^- + SO_4^{2-}$

The (Ca^{2+} + Mg^{2+}) vs (HCO_3^- + SO_4^{2-}) (Figure 79) can be used to analyze the primary geochemical processes at play (Fu et al., 2018). If the anions are governed by the equilibrium of carbonate and gypsum, a 1:1 relationship would be expected. Most samples cluster near this 1:1 line, suggesting that the dissolution of both carbonate and gypsum (or anhydrite) is the primary hydrochemical process affecting water quality and is the main source of Ca^{2+}, Mg^{2+}, HCO_3^-, SO_4^{2-}

(Fisher & Mullican, 1997). However, springs S7, S6, and S13 deviate from this pattern, indicating different influences.

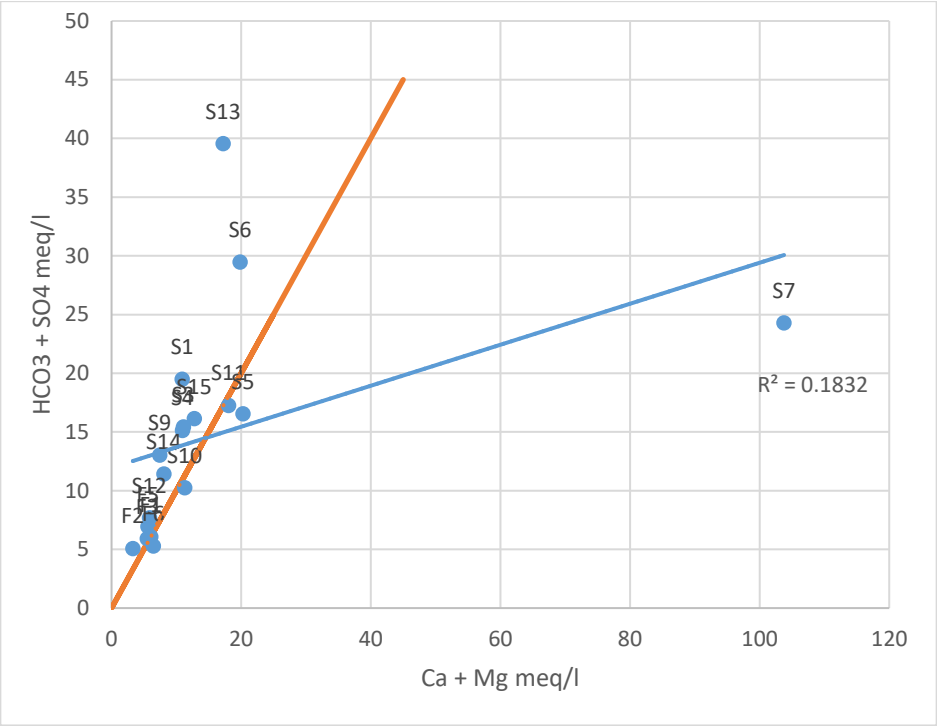


Figure 79 Ionic Ratio of $Ca^{2+} + Mg^{2+}$ vs $HCO_3^- + SO_4^{2-}$ for All Samples

e) HCO_3/ SO_4

The plot HCO_3 vs SO_4^{2-} (Figure 80) shows a similar pattern with a negative correlation. This suggests that as one mole of SO_4^{2-} is produced from the dissolution of gypsum and/or anhydrite, two moles of HCO_3^- are lost during the formation of one mole of calcium carbonate ($CaCO_3$), This process reflects the complex geochemical interactions in hydrothermal systems, where the dissolution of sulfate minerals can lead to a corresponding decrease in bicarbonate levels. Such relationships have been widely documented in various carbonate hydrothermal systems.(Yang et al., 2019)

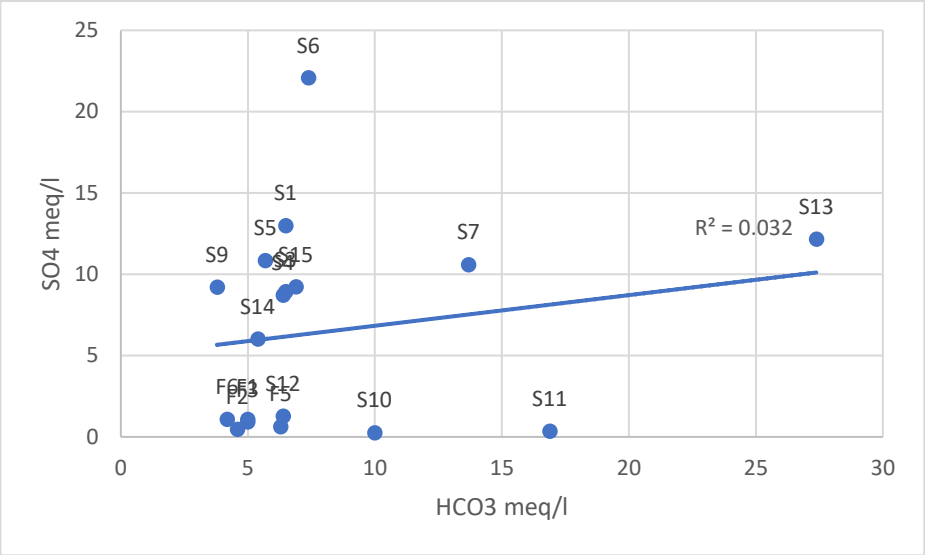


Figure 80 Ionic Ratio of SO_4^{2-} vs HCO_3 for All Samples

7. Principal Components Analysis and Hierarchical Components Analysis (PCA, HCA)

7.1 Principal Components Analysis (PCA)

The principal components are obtained by calculating the eigenvectors (or eigenvalues) of the variance-covariance matrix, developed from the original data matrix (Brown, 1998). Through the evaluation of principal components, the aim is to determine the minimum number of variables that contain the maximum amount of information and to identify which variables are strongly related to each other. The physical significance of the interrelations between the data components is sought to provide a simple interpretation of the processes driving the variation of the variables. This technique was developed by (Hotelling, 1933) , based on (Pearson, 1901)'s original work. The main parameters of concern in PCA are the factor loadings and the total explained variance.

Principal Component Analysis (PCA) aims to enable the visualization of multidimensional data and to explore the structure and relationships among variables. The goal is to provide a simplified representation of the analyzed parameters across different water sampling points on a two-dimensional graph.

In this study, PCA was conducted on the dataset from the second sampling campaign. It was selected as the primary focus because it includes a broader variety of water types, such as thermal and non-thermal springs. This choice provided a more comprehensive view of the hydrochemical variability across the study area

To complement this focused analysis, PCA was also performed on the combined dataset from both campaigns, allowing for a more robust understanding of the multivariate structure of the waters.

While a separate PCA of the first campaign alone could offer insight into temporal differences, the second campaign was prioritized for its spatial and hydrochemical representativeness, making it more suitable for detailed analysis.

The scree plot (Figure 81) illustrates the percentage of total variability explained by each principal component:

- PC1 explains 57.37% of the total variance, meaning that more than half of the variability in the data is captured by this axis. This suggests that PC1 is the most important factor for distinguishing the samples based on their characteristics.
- PC2 explains 20.07% of the variance, adding additional differentiation between the samples.

Together, PC1 and PC2 account for a total of 77.44% of the total variability, which is a significant portion, allowing a reliable two-dimensional representation of the data. The remaining 22.56% of the variability is distributed across other components, which are less critical for explaining the main trends in our dataset.

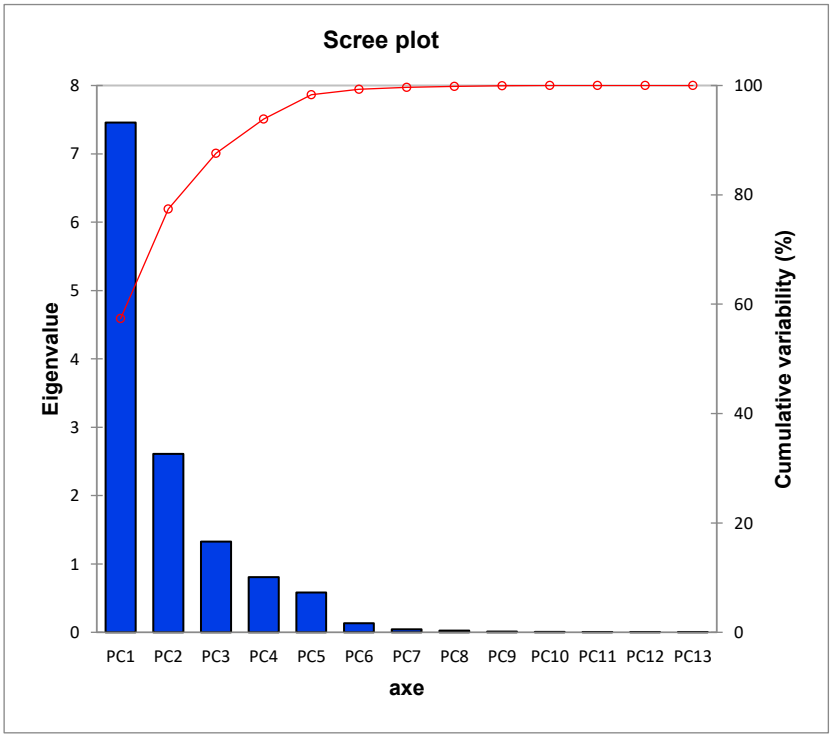


Figure 81 Histogram of Eigenvalues and Cumulative Variability

7.1.1 Descriptive statistics (Quantitative data)

The descriptive statistics (Table 27) help to understand the distribution, variability, and range of each variable, ensuring the data is ready for PCA. They also allow us to identify which variables might be contributing the most to the variation (Table 29) seen in the samples. By standardizing our data, we avoid skewing the PCA results due to differences in variable scales, leading to more reliable and interpretable outcomes.

The descriptive statistics show the wider ranges for **Na**, **Ca**, **NO_3**, **K,** and **Cl** suggest high variability across the samples for these components.

Table 27. Descriptive statistics for the study parameters of the second campaign

Variables	Observations	Obs. with missing data	Obs. without missing data	Minimum	Maximum	Mean	Ecart-type
EC	18	0	18	-0.617	3.565	0.000	1.029
T°C	18	0	18	-1.368	2.370	-0.014	1.016
pH	18	0	18	-1.534	1.327	0.000	1.029
Na	18	0	18	-0.498	3.693	0.000	1.029
K	18	0	18	-0.768	3.539	0.000	1.000
Ca	18	0	18	-0.521	3.920	0.000	1.000
Mg	18	0	18	-1.147	1.937	0.000	1.000
Sr	18	0	18	-0.840	3.284	0.000	1.000
Li	18	0	18	-0.805	2.493	0.000	1.000

Cl	18	0	18	-0.481	3.538	0.000	1.000
SO4	18	0	18	-0.969	2.121	0.000	1.000
NO3	18	0	18	-0.429	3.940	0.000	1.000
HCO3	18	0	18	-0.759	3.285	0.000	1.000

7.1.2 Eigenvalues and PCs :

Eigenvalues are the variation in distances along each principal component. In other words, in PCA, they measure the amount of variation (or spread) in the data along each principal component. Larger eigenvalues mean more variability is captured by that component. Table 28 shows that PC1 explains the largest proportion of the data's variance.

Table 28. Eigenvalues and percentage of explained variance by factorial axes from PC1 to PC13

	PC1	PC2	PC3	PC4	PC5	PC6	PC7	PC8	PC9	PC10	PC11	PC12	PC13
Eigenvalue	7.458	2.609	1.325	0.809	0.581	0.131	0.042	0.025	0.013	0.006	0.001	0.000	0.000
Variabilité (%)	57.371	20.069	10.189	6.224	4.472	1.010	0.321	0.195	0.097	0.045	0.005	0.002	0.000
(%) Cumulative	57.371	77.440	87.629	93.853	98.325	99.335	99.656	99.851	99.948	99.993	99.998	100.000	100.000

Table 29. Different variables and PCs

	PC1	PC2	PC3	PC4	PC5	PC6	PC7	PC8	PC9	PC10	PC11	PC12	PC13
EC	0.948	-0.280	0.130	0.065	-0.041	-0.005	0.016	-0.002	-0.002	-0.023	0.002	-0.009	-0.002
T°C	0.147	0.576	0.566	-0.524	-0.180	-0.130	0.018	-0.044	-0.016	-0.001	0.000	0.000	0.000
pH	-0.683	-0.039	0.228	0.556	-0.373	-0.172	-0.040	-0.001	-0.010	0.000	-0.001	0.000	0.000
Na	0.914	-0.375	0.102	0.067	-0.072	0.013	0.050	-0.014	0.001	-0.020	-0.009	0.011	-0.001
K	0.782	0.484	-0.247	-0.069	-0.287	0.023	0.011	0.071	-0.005	0.019	-0.015	-0.003	0.000
Ca	0.704	0.476	-0.455	0.165	-0.177	0.072	0.020	-0.063	-0.058	0.007	0.009	0.001	0.000
Mg	0.371	0.766	0.065	0.315	0.381	-0.126	0.098	0.023	0.008	0.002	0.001	0.000	0.000
Sr	0.871	0.383	-0.259	0.054	0.049	-0.058	-0.094	-0.074	0.063	-0.001	-0.004	0.000	0.000
Li	0.975	0.019	-0.022	-0.084	-0.175	-0.050	-0.031	0.081	0.028	0.001	0.016	0.004	0.000
Cl	0.921	-0.366	0.079	0.067	-0.071	-0.014	0.038	-0.011	-0.002	-0.032	0.000	-0.004	0.003
SO_4	0.389	0.539	0.672	0.235	0.077	0.198	-0.071	0.015	-0.010	-0.006	0.000	0.001	0.000
NO_3	0.745	-0.545	0.356	0.113	-0.031	0.026	0.046	-0.034	0.018	0.057	0.002	-0.001	0.000
HCO_3	0.853	-0.375	-0.009	-0.055	0.315	-0.130	-0.093	0.018	-0.060	0.011	-0.003	0.001	0.000

7.1.3 Correlation Matrix

Each value indicates the strength and direction of the linear relationship between two variables, the matrix (Table 30) shows:

- Strong positive correlations :
  - Ec vs Na, Cl, Sr, Li, NO_3, and HCO_3
  - K vs Ca, Sr, Li

- Weak negative correlations :
  - pH vs EC, Na, K, Sr, Li, Cl, HCO_3

Based on the correlation matrix results, some adequate insights that can be highlighted are as follows:

- Salinity and conductivity are driven by key ions such as sodium, chloride, lithium, and strontium, indicating that salinity in these waters is heavily influenced by these ions
- Influence of Temperature: Sulfate (SO_4^{2-}) and magnesium (Mg^{2+}) are positively correlated with temperature; however, this pattern does not indicate enhanced gypsum dissolution at higher temperatures. Instead, it reflects dedolomitization, where previously dissolved gypsum provides sulfate that promotes the transformation of dolomite into calcite, releasing Mg^{2+} into solution
- pH Sensitivity: The negative correlation observed between pH and the solubility of certain ions (Na, Li, and Sr) implies that these ions become more soluble in more acidic conditions, which in turn influences the chemistry of the water as a whole.

Table 30. Correlation matrix between parameters (high values are in bold)

Variables	EC	T°C	pH	Na	K	Ca	Mg	Sr	Li	Cl	SO4	NO3	HCO3
EC	**1**	0.026	**-0.555**	**0.993**	**0.580**	**0.493**	0.153	**0.686**	**0.917**	**0.994**	0.316	**0.913**	**0.894**
T°C	0.026	**1**	-0.196	-0.046	0.336	0.060	0.317	0.173	0.219	-0.050	**0.584**	-0.059	-0.109
pH	**-0.555**	-0.196	**1**	**-0.527**	**-0.545**	-0.458	-0.218	**-0.645**	**-0.644**	**-0.532**	-0.063	-0.339	**-0.691**
Na	**0.993**	-0.046	**-0.527**	**1**	**0.523**	0.444	0.055	**0.622**	**0.885**	**0.999**	0.232	**0.934**	**0.886**
K	**0.580**	0.336	**-0.545**	**0.523**	**1**	**0.930**	**0.514**	**0.905**	**0.837**	**0.538**	0.365	0.232	0.399
Ca	**0.493**	0.060	-0.458	0.444	**0.930**	**1**	**0.571**	**0.908**	**0.711**	0.462	0.262	0.132	0.352
Mg	0.153	0.317	-0.218	0.055	**0.514**	**0.571**	**1**	**0.633**	0.287	0.066	**0.673**	-0.093	0.139
Sr	**0.686**	0.173	**-0.645**	**0.622**	**0.905**	**0.908**	**0.633**	**1**	**0.851**	**0.640**	0.382	0.351	**0.626**
Li	**0.917**	0.219	**-0.644**	**0.885**	**0.837**	**0.711**	0.287	**0.851**	**1**	**0.894**	0.335	**0.700**	**0.783**
Cl	**0.994**	-0.050	**-0.532**	**0.999**	**0.538**	0.462	0.066	**0.640**	**0.894**	**1**	0.220	**0.923**	**0.893**
SO_4	0.316	**0.584**	-0.063	0.232	0.365	0.262	**0.673**	0.382	0.335	0.220	**1**	0.261	0.117
NO_3	**0.913**	-0.059	-0.339	**0.934**	0.232	0.132	-0.093	0.351	**0.700**	**0.923**	0.261	**1**	**0.812**
HCO_3	**0.894**	-0.109	**-0.691**	**0.886**	0.399	0.352	0.139	**0.626**	**0.783**	**0.893**	0.117	**0.812**	**1**

7.1.4 Interpretation of Principal Component Analysis Biplot

The biplot (Figure 82) depicts the correlations between variables on the first two principal components, PC1 (57.37%) and PC2 (20.07%), as mentioned earlier, which provides a clear distinction between different water chemistry parameters:

- PC1 (57.37%) :

- Dominated by variables like Cl^-, Na^+, HCO_3^-, EC, and Li, indicating that this component captures much of the variance related to dissolved salts and electrical conductivity. It appears to represent the salinity or mineral content, given the strong associations with variables like Cl^-, Na^+, and HCO_3^-.
- Variables on the right side (positive PC1) are strongly associated with each other and likely represent mineralization processes or salinity.

- PC2 (20.07%) :

- Dominated by variables like Mg^{2+}, T°C, SO_4^{2-}, K^+ and Ca^{2+} contribute strongly to this axis. It might represent the influence of temperature and related chemical processes.
- This could reflect temperature and hardness-related factors, with T°C and Mg^{2+} having a significant impact on PC2.
  - pH is the exception, as it shows little correlation with the other variables and has a negative loading on both PC1 and PC2.

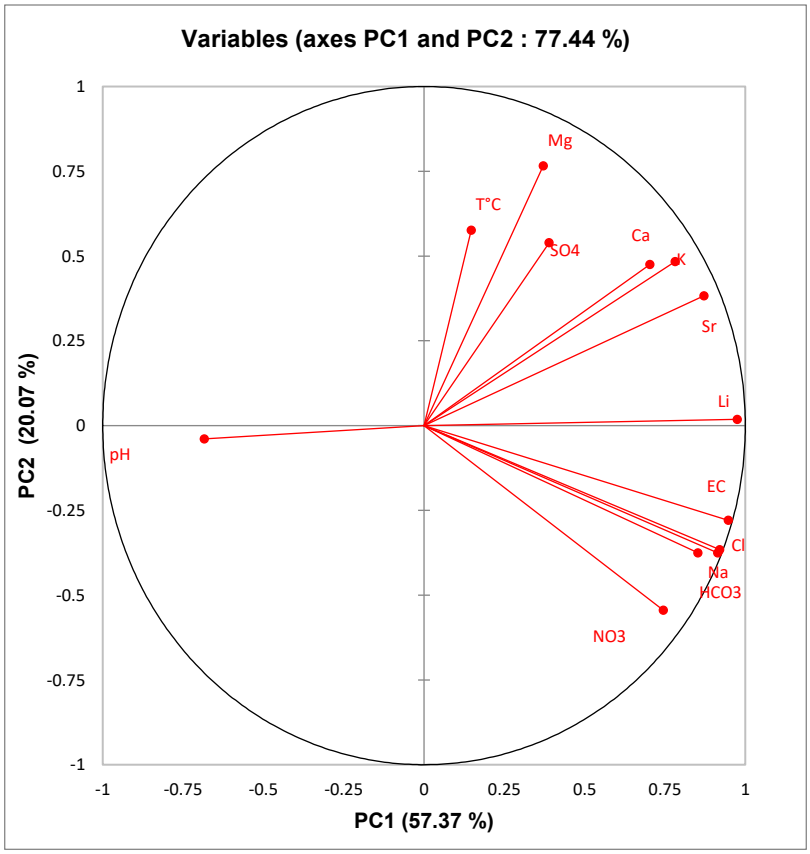


Figure 82 Principal Component Analysis Biplot of PC1 and PC2

The PCA biplot (Figure 82) illustrates the grouping of samples based on the first two principal components (PC1 and PC2), which together explain 77.44% of the variance in the data. The samples are divided into distinct groups as indicated by the color-coded ellipses in Figure 83:

1. **Group 1**: Includes F1, F2, F3, F5, F6, and S12. These samples are characterized by low PC1 and negative PC2 values, suggesting lower conductivity (EC) and moderate to low mineral concentrations. The position of these samples indicates that they represent cooler, less mineralized waters, and the chemical analyses confirm these results.
2. **Group 2**: represents S5, S6, these samples are positioned around higher PC1 and slightly positive PC2 values, suggesting higher temperatures and increased mineralization. The chemical analyses show higher temperature values and elevated mineral content, particularly associated with elements such as calcium and sulfates, indicating that these are likely warmer, more mineral-rich waters.
3. **Group 3**: Contains S1, S3, S4, S9, S10, S11, S14, and S15. These samples are plotted around the origin with moderate contributions to both PC1 and PC2. This group mostly represents

moderately mineralized waters with balanced concentrations of temperature-sensitive ions like Mg^{2+}, Ca^{2+}, and SO_4^{2-}.

4. **Group 4**: S7 and S13, which are outliers positioned far from the other samples, indicating distinct water chemistry. S7 is characterized by high PC1 and PC2 values, suggesting elevated electrical conductivity and concentrations of ions such as Na^+ and Cl^-. S13, although sharing similar mineral content, is distinct along the PC2 axis due to other chemical and environmental factors.

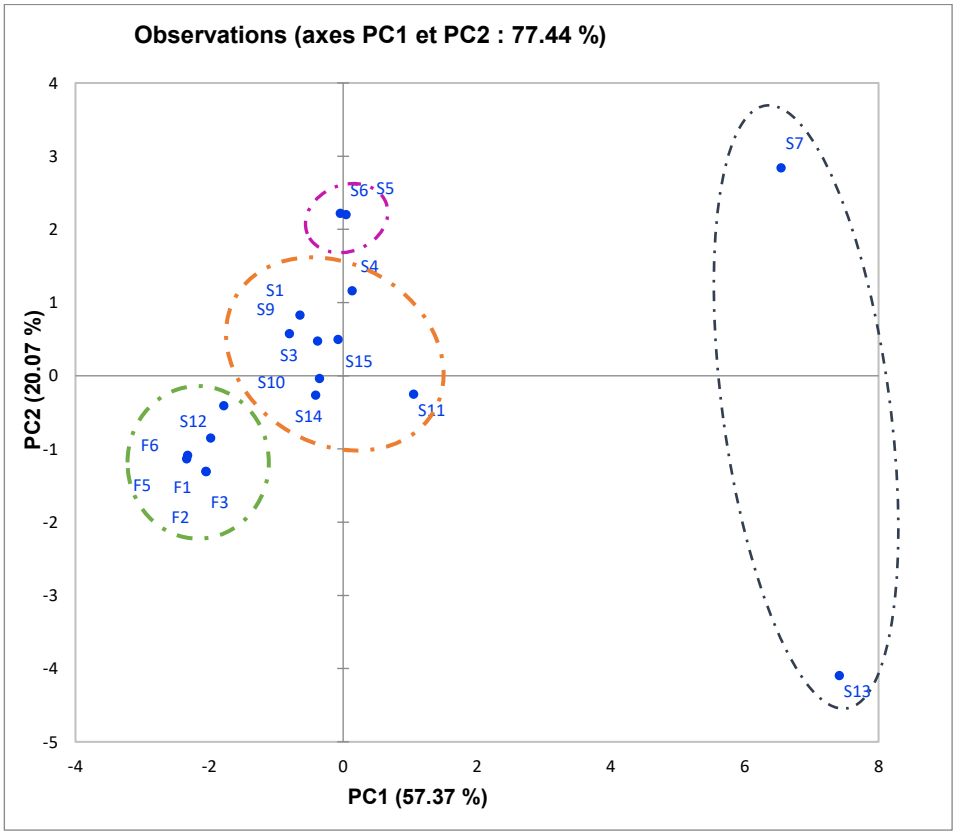


Figure 83 Distribution of Samples Plot According to PC1 and PC2

7.2 Hierarchical Components Analysis (HCA)

Hierarchical Cluster Analysis (HCA) is a statistical method used to group similar objects into clusters based on their characteristics. This technique is particularly useful for understanding patterns and relationships within datasets, such as water quality parameters.

In this analysis, Euclidean distance is employed as the dissimilarity measure. Euclidean distance quantifies the straight-line distance between two points in multidimensional space, making it an

intuitive metric for assessing the similarity between samples (Murtagh et al., 2001). Smaller distances indicate greater similarity, while larger distances suggest more dissimilarity.

Ward's method is used for clustering in this study. This approach minimizes the total within-cluster variance by merging clusters in a way that minimizes the increase in the total variance (Everitt et al., 2001; Ward, 1963). As a result, it tends to create compact, spherical clusters that are well-separated from each other.

The water samples were regrouped into four distinct clusters (Figure 84) based on the hierarchical clustering results:

1. **Group 1**: Comprises S7 and S13
2. **Group 2**: S12, F5, F1, F3, F2, F6,
3. **Group 3** : S5, S6
4. **Group 4**: S10, S11, S3, S9, S14, S4, S1, S15

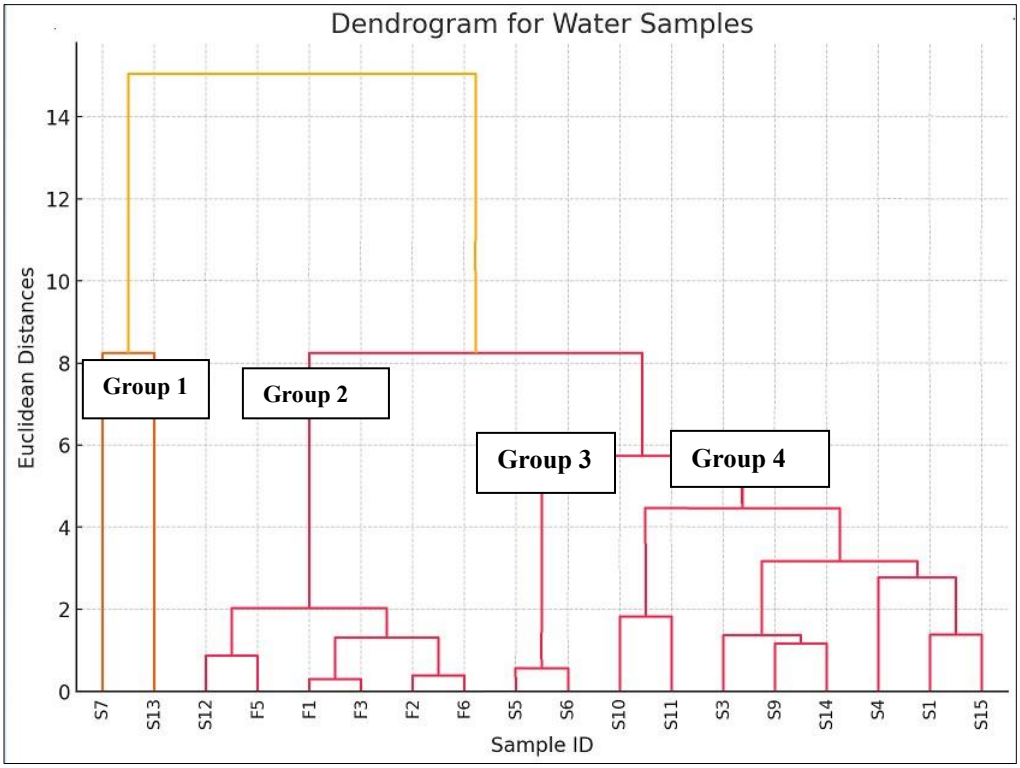


Figure 84 Hierarchical Cluster Dendrogram of All Water Samples in the Study Region

7.3 Principal Component Analysis of the Combined Dataset

To gain a more comprehensive understanding of hydrochemical variability and seasonal influences across the study area, Principal Component Analysis (PCA) was applied to the combined dataset from both sampling campaigns. This approach enabled the identification of consistent patterns and relationships among variables and sampling points under different seasonal and hydrological conditions.(Djaafri et al., 2024)

7.3.1 Data Preprocessing: Normality and Distribution Check

Before conducting the Principal Component Analysis (PCA), descriptive statistics (Table 31) were first applied to examine the distribution characteristics of the dataset, including measures of central tendency, dispersion, and detection of potential outliers. To further evaluate whether the data met the assumptions of normality required for PCA, the Shapiro–Wilk test (Table 32) was used due to its suitability for small datasets ($n < 50$).

The results (Table 32) indicated that the original distributions of electrical conductivity (EC) and nitrate (NO_3^-) significantly deviated from normality ($p < 0.05$). As a corrective measure, logarithmic transformations were applied to these variables. The Shapiro–Wilk test on the transformed data showed clear improvement: the distribution of log (NO_3^-) was consistent with normality, while log (EC) was much closer to a normal distribution.

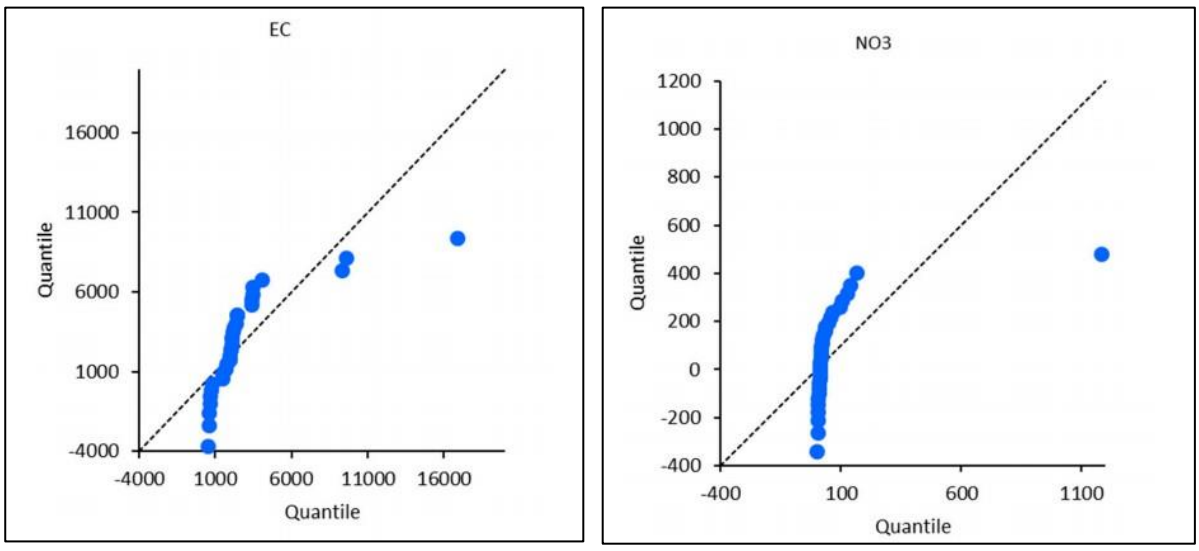
To visually confirm these results, quantile–quantile (Q–Q) plots were generated for EC and NO_3^-, both before and after log transformation. The proximity of the data points to the diagonal line indicates the extent of normality. These plots (Figure 85) confirm the improved distribution following transformation.

Table 31. Descriptive statistics for the study parameters of the combined dataset

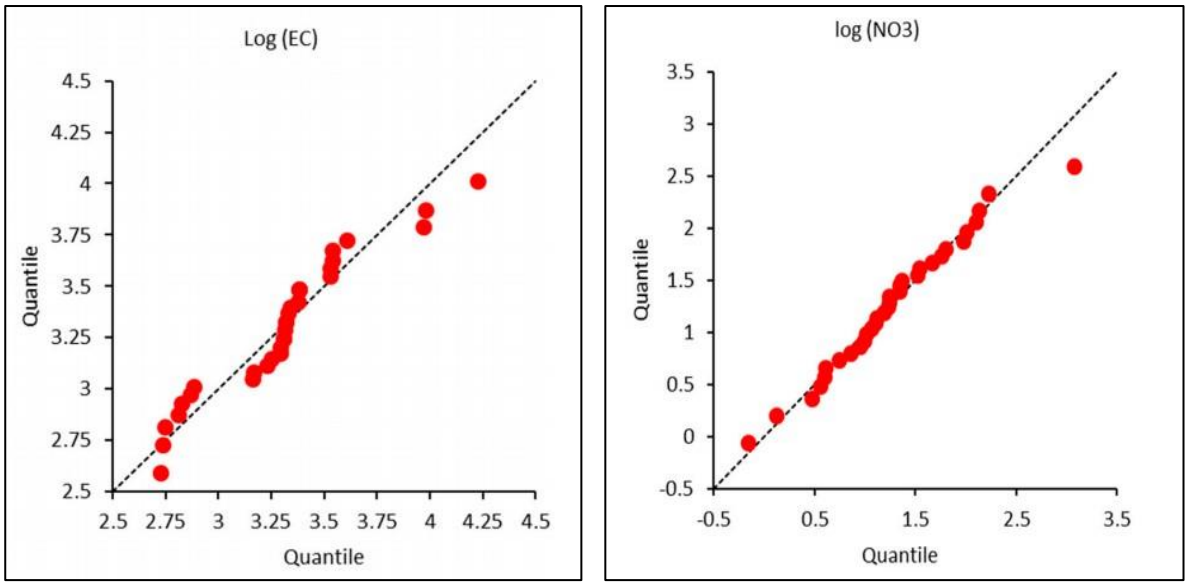
Parameter	Unit	Observations	Minimum	Maximum	Mean
T	°C	32	18.7	94.7	49.2
pH	-	32	5.71	9.88	7.08
EC	µs cm^{-1}	32	531	16,850	2886
Na^+	mg L^{-1}	32	9.53	4800	491
K^+	mg L^{-1}	32	0.24	81.2	15
Ca^{2+}	mg L^{-1}	32	51.74	2001	262
Mg^{2+}	mg L^{-1}	32	6.06	54.85	25.95
Cl^-	mg L^{-1}	32	14.13	6130	696
SO_4^{2-}	mg L^{-1}	32	12.47	1061	368
NO_3^-	mg L^{-1}	32	0.69	1180	71
HCO_3^-	mg L^{-1}	32	91.5	1671	469
Li^+	mg L^{-1}	32	0.01	1.73	0.42

Table 32 Shapiro-Wilk test results for Raw and Log-transformed distributions of (EC) and (NO_3^-)

Parameter	Shapiro–Wilk Test
NO_3^-	<0.0001
Log (NO_3^-)	0.88
EC	<0.0001
Log (EC)	0.02



(a) (b)



(c) (d)

Figure 85 Quantile - Quantile (Q-Q) Plots of Electrical Conductivity (EC) and Nitrate (NO_3^-) Before and After Logarithmic Transformation. (a) Raw EC, (b) Raw NO_3^-, (c) Log-transformed EC, (d) Log-transformed NO_3^-

7.3.2 Principal Component Analysis Results

Following data normalization, PCA was carried out on the transformed dataset to investigate the hydrochemical structure and dominant factors controlling water composition across the study area.

a) Correlation Matrix

The correlation matrix (Table 33) shows that electrical conductivity (EC) is strongly correlated with chloride (r = 0.96), sodium (r = 0.94), and lithium (r = 0.89), indicating that these ions are key contributors to water salinity. Water temperature shows moderate positive correlations with potassium (r = 0.67) and sulfate (r = 0.66), which may reflect seasonal or geochemical influences on ion solubility. Additionally, the strong correlation between Na^+ and Cl^- (r = 0.98) suggests a common origin, likely from halite dissolution.

Table 33. Correlation matrix of hydrochemical parameters

Variables	T	EC	Ca^{2+}	Mg^{2+}	Na^{+}	K^{+}	Cl^{-}	SO_4^{2-}	NO_3^{-}	HCO_3^{-}	H^{+}	Li
T	1											
EC	0.31	1										
Ca^{2+}	0.33	**0.78**	1									
Mg^{2+}	0.36	0.39	**0.61**	1								
Na^{+}	0.31	**0.94**	0.66	0.21	1							
K^{+}	0.67	**0.85**	0.77	0.57	**0.81**	1						
Cl^{-}	0.33	**0.94**	0.66	0.25	**0.98**	0.82	1					
SO_4^{2-}	**0.66**	0.47	0.52	0.40	0.37	**0.63**	0.33	1				
NO_3^{-}	0.11	0.50	0.38	−0.17	**0.51**	0.35	0.41	0.44	1			
HCO_3^{-}	−0.07	**0.70**	0.60	0.27	0.64	0.50	0.63	−0.02	0.33	1		
H^{+}	0.03	0.21	0.05	−0.25	0.28	0.20	0.23	−0.06	0.27	0.16	1	
Li	0.59	**0.89**	0.72	0.42	**0.89**	**0.95**	**0.91**	0.54	0.36	0.53	0.24	1

b) Eigenvalues and PCA Score Plots

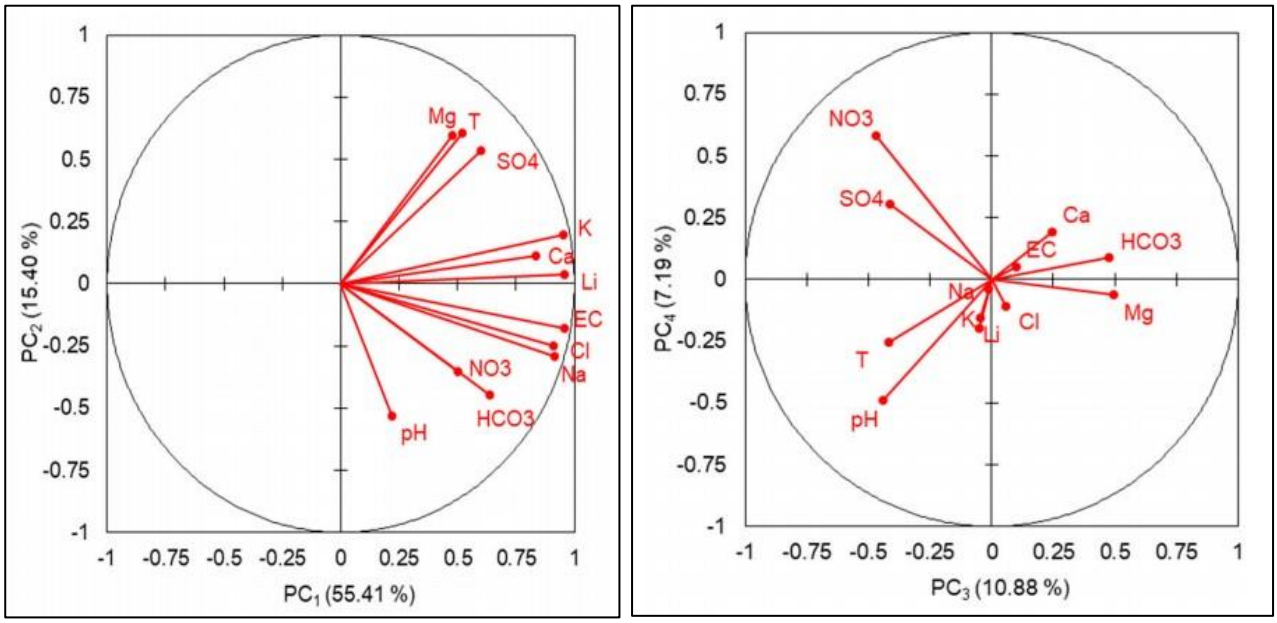
The PCA results reveal that the first four principal components (PCs) explain a significant portion of the variance in the dataset, as summarized in (Table 34) PC1, with an eigenvalue of 6.65, accounts for 55.4% of the variance and is interpreted as a water minerality axis (Figure 86), since it correlates positively with temperature and all major dissolved ions. PC2 (15.41%) is associated with chemical facies, separating warm sulfate- and magnesium-rich waters from cooler bicarbonate and nitrate-rich waters, with sodium–chloride waters in an intermediate position. PC3 further discriminates waters along a thermal gradient, opposing hot sulfate waters to cooler calcium–magnesium bicarbonate types. PC4, contributing only 7.19%, is not clearly associated with specific hydrogeochemical processes.

The spatial distribution of the 32 water samples in the PC1–PC2 and PC1–PC3 planes is illustrated in Figure 88. Logarithmic transformation of the data minimized the influence of extreme values and improved separation between observations. Based on their positions in the PCA space, six hydrochemical groups were distinguished, reflecting both thermal regimes and geochemical evolution:

- **Group 1:** Cold waters from Guelma, Souk Ahras, and Khenchela (F1, F2, F3, F5, F6), along with hypo-thermal waters from Tebessa (S12), all characterized by bicarbonate–calcium composition.
- **Group 2:** High-salinity chloride–sodium hot springs from Guelma and Tebessa (S7, S13), despite their geographic distance.
- **Group 3:** Thermal waters from the Guelma region (S1, S2, S3, S4, S5, S6, S8, S9).
- **Group 4:** Thermal springs from Khenchela (S14, S15) and Souk Ahras (S10, S11).
- **Group 5:** Hot springs from both Guelma and Souk Ahras regions, showing mixed characteristics.
- **Group 6:** A cluster of hot springs from Guelma and Khenchela (S1 to S6, S14, S15)

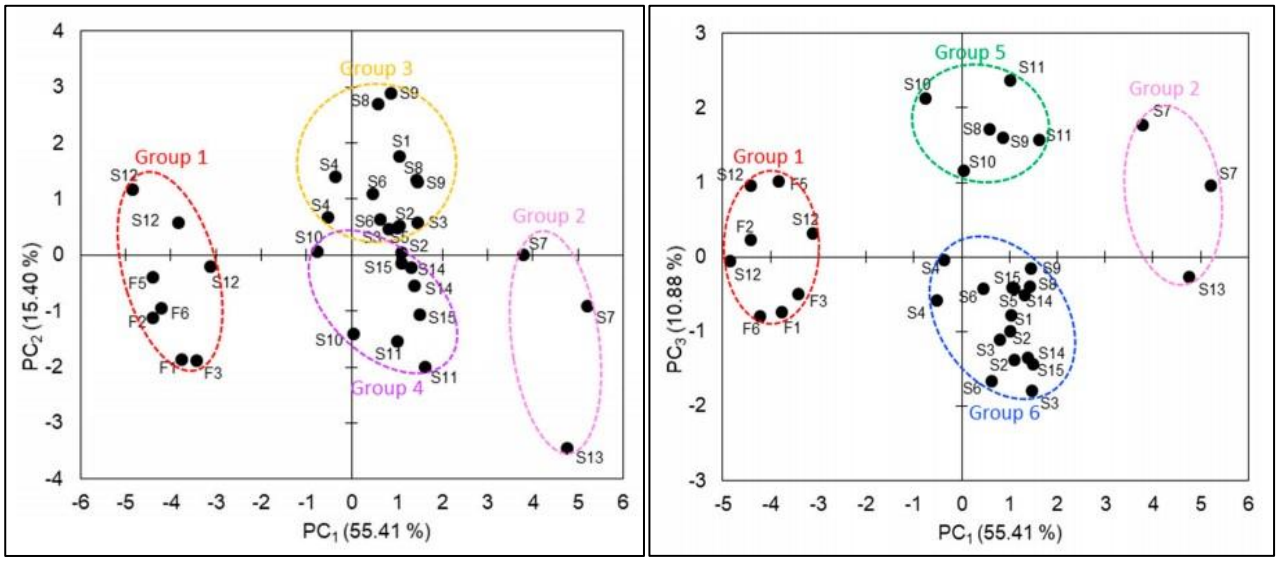
Table 34. Eigenvalues and variance contribution of principal components PC1 to PC4

	PC1	PC2	PC3	PC4
Eigenvalue	6.65	1.85	1.31	0.86
Variance (%)	55.41	15.41	10.88	7.19
Cum. %	55.41	70.82	81.69	88.88



(a) (b)

Figure 86 Distribution of pH, Temperature, Log (EC), and Log (Concentration) in the Score Plots: (a)PC1-PC2 and (b) PC3-PC4



(a) (b)

Figure 87 Distribution of Samples in the Factorial Plots: (a) PC1-PC2 and (b) PC1-PC3

7.4 Agglomerative Hierarchical Clustering of Regional Hydrogeochemical Profiles

Agglomerative Hierarchical Clustering (AHC) (Figure 88) was applied to the regional averages of the hydrochemical data to highlight similarities between the main regions: Guelma, Souk Ahras, Khenchela, and Tebessa. The dendrogram shows that Tebessa and Khenchela are in the same group, indicating shared geochemical characteristics, mostly due to similar geological settings or recharge conditions.

Souk Ahras forms a separate group but connects at the next level, which reflects moderate similarity with the Tebessa–Khenchela group while it maintains distinct features. Guelma appears as the most separate group and connects to the others at a higher dissimilarity level, which suggests significantly different hydrogeochemical conditions. This difference may result from higher temperatures, specific water–rock interactions, or particular geological structures.

This regional clustering clarifies the spatial variation in water chemistry across the study area.

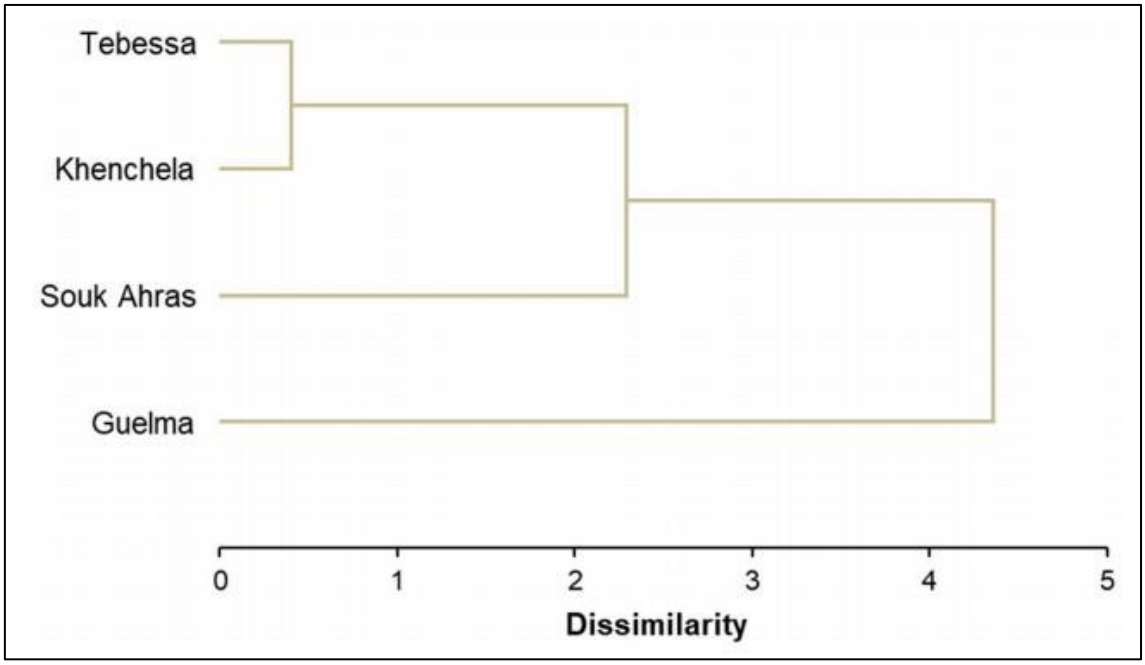


Figure 88 Agglomerative Hierarchical Dendrogram of Regional Sample Groups Based on Hydrochemical Similarity

8. Contribution of Water Stable Isotopes: δ^2H and $\delta^{18}O$

8.1 Introduction

Water is mainly composed of $H_2{}^{16}O$ molecules, but it also contains some heavier molecules such as $H_2{}^{17}O$ (0.004%), $H_2{}^{18}O$ (0.2005%), HDO (0.0155%), and HTO (currently in very small quantities). These different molecules are called isotopologues, or, colloquially, simply "water isotopes. The heavy isotopes $H_2{}^{17}O$, $H_2{}^{18}O$, and HDO are stable, unlike HTO, which is radioactive. The relative proportion of these different molecules is called isotopic composition and is quantified using the notation δ:(Camille Risi, 2009)

$$\delta = \left(\frac{Rsample}{RSMOW} - 1\right).1000$$

With R_{sample} being the ratio of the number of heavy molecules to the total number of molecules in the sample, and R_{SMOW} being the same ratio in an international reference corresponding to average ocean surface water: Standard Mean Ocean Water (SMOW). The delta (δ) is expressed in ‰. Thus, $\delta^{17}O$, $\delta^{18}O$, and δD are defined to quantify the abundance of $H_2{}^{17}O$, $H_2{}^{18}O$, and HDO, respectively. (Camille Risi, 2009)

The data are gathered along a line with a slope of 8 and an intercept of 10, which is called the Meteoric Water Line (MWL). The deviation from this line is quantified by a second-order parameter called deuterium excess, or d-excess, often denoted as d (Craig, 1961; Dansgaard, 1964). Where:

$$\delta D = 8\ \delta^{18}O + 10 \text{ (Craig, 1961)}$$

8.2 Concepts of d-excess and ^{17}O-excess

The d-excess parameter is a measure that reflects the deviation of the observed isotopic composition of precipitation from the expected relationship between deuterium and oxygen-18. It helps to assess the influence of processes like evaporation and rainout on the isotopic composition of precipitation. It is calculated using the formula: (Gat, 1996)

$$d = \delta D - 8.\ \delta^{18}O$$

where:

- δD is the measured isotopic ratio of deuterium in the sample, expressed in per mil ‰ relative to a standard
- $\delta^{18}O$ is the measured isotopic ratio of oxygen-18 in the sample, also expressed in per mil ‰.
- The factor of 8 reflects the typical slope of the Global Meteoric Water Line (GMWL), which describes the expected relationship between deuterium and oxygen-18 in precipitation.

the positive intercept in the GMWL indicates an excess of ^{17}O in meteoric waters with respect to the ocean. An excess (or depletion) of ^{17}O in water is defined as: (Luz & Barkan, 2010)

$$^{17}O\text{-}excess = ln\ (\delta^{17}O + 1) - 0.528(\delta\ ^{18}O + 1)$$

Table 35. Isotopic measurements and excess values for oxygen and hydrogen isotopes

Samples	^{17}O	^{18}O	D	^{17}O-excess	d-excess
S1	-3.64	-6.96	-40.14	42	15.5
S2	-4.15	-7.93	-48.68	44	14.8
S5	-4.16	-7.91	-52.39	26	10.9
S7	-3.65	-6.94	-41.62	27	13.9
S8	-4.04	-7.71	-47.91	36	13.8
S9	-4.05	-7.72	-48.01	32	13.8
S10	-4	-7.64	-44.5	39	16.7
S11	-4.07	-7.77	-48	42	14.2
S12	-4.39	-8.37	-53.42	35	13.5
S13	-3.66	-6.96	-44.92	17	10.8
S14	-4.65	-8.84	-56.65	33	14.1
S15	-4.48	-8.56	-56.16	44	12.3

The d-excess value indicates how much the actual isotopic composition of precipitation deviates from the expected values based on the standard relationship. A positive d-excess value, as seen in our samples (Table 35), suggests that the precipitation has a higher deuterium content relative to oxygen 18 than expected, indicating less evaporation and a more direct source of moisture. A negative d-excess value may indicate significant evaporation or mixing with moisture that has undergone more extensive isotopic fractionation.

Table 35 reveals that samples like S1 (15.5‰) in Guelma and S10 (16.7‰) in Souk Ahras, with relatively high d-excess, suggest that the water in these samples mostly came from a source with dry, cooler conditions. Meanwhile, samples like S13 (10.8‰) in Tebessa and S5 (10.9‰) in Guelma, with

lower d-excess, suggest that their moisture source had higher humidity and potentially warmer conditions, typical of regions with more balanced fractionation during evaporation.

In the same context, values of Deuterium may provide insights into the conditions under which the water samples were formed; the first range of higher D values (less negative) comprises S1 with (-40.14 ‰) and S7 with (-41.62 ‰), suggesting that they originated from sources with higher temperatures and possibly drier conditions. They may have experienced less evaporation, indicated a more direct source of moisture, and recharged in regions with lower altitudes. The second range, comprising the samples S10 (-44.5 ‰), S13 (-44.92‰), S8 (-47.91‰), and S9 (-48.01‰), indicates a moderate level of isotopic fractionation. The moisture sources may have been subject to moderate evaporation processes and have been recharged from intermediate altitude regions. In contrast, the third group of the lowest D values (more negative) is represented by S5 (-52.39 ‰), S12 (-53.42), S15 (-56.16 ‰), and S14 (-56.65 ‰), suggesting that these samples mainly came from higher humidity conditions or sources that experienced significant isotopic fractionation due to extensive evaporation. These conditions often indicate either cooler climates or more humid environments, where the precipitation was less influenced by evaporation before falling. These samples are probably coming from recharge zones located in mountainous regions.

Higher ^{17}O-excess values are typically associated with colder periods, when atmospheric temperatures are lower and the kinetic fractionation processes during evaporation and condensation deviate from typical mass-dependent fractionation (resulting in a higher excess of ^{17}O relative to ^{18}O). In other words, it is associated with dry, arid conditions and low relative humidity during evaporation. The samples S1, S2 in Guelma, S11 in Souk Ahras, and S15 in Khenchela exemplify this trend. Lower 17O-excess values are linked to warmer periods, when more typical isotopic fractionation processes occur during evaporation, and this is observed in S13 in Tebessa.

The δ18O values range from -8.84 to -6.94 ‰ (S14, S7, respectively) for the chloride water type. For the sulfate-bicarbonate water type, values range from -8.37 to -6.96 ‰ (S12, S1, respectively). But 17O represents small values of an interval between (-4.48 ‰ at S15 to -3.64 ‰ at S1)

According to (Craig, 1961; Craig & Gordon, 1965; Dansgaard, 1964; Frohlich et al., 2002; Gat, 1996; Landais et al., 2008; Luz & Barkan, 2010; Nyamgerel et al., 2021), all isotopic measures; ^{18}O, deuterium (D), d-excess, ^{17}O, and ^{17}O -excess indicate a conversely correlated relationship with evaporation. Lower isotopic values imply that the hydrological conditions have been shaped by extensive evaporation in cooler and more humid environments, leading to distinctive isotopic signatures in the water samples. This relationship is very important for understanding the climatic and environmental influences on

water sources, where extensive evaporation has occurred, reflecting moisture sources that have been significantly affected by these processes.

8.3 Diagram of $\delta^{18}O/\delta^{2}H$ and Groundwater Origin

Combined measurements of d-excess and 17O-excess allow researchers to understand more fully the contributions of both temperature and relative humidity to water isotope fractionation (Berman et al., 2013). In our case, one important application of the combined use of $\delta^{2}H$ and $\delta^{18}O$ was to define the origin of thermal waters by analyzing the stable isotopes of hydrogen (deuterium, $\delta^{2}H$) and oxygen ($\delta^{18}O$) in water samples. This analysis helps differentiate the waters and define the processes that influence their chemical signatures relative to the GMWL. This diagram is widely used in hydrology, climatology, and geochemistry to trace water sources and understand hydrological cycles, assess the impact of climatic changes on water isotopic compositions, and evaluate the interaction between surface water, groundwater, and geothermal systems.

As mentioned earlier in this chapter, section on sampling and methodology, the isotopic analyses (δ18O and δD) for 12 thermal water samples, dispersed throughout the study zone, were carried out using cavity ring-down spectroscopy (CRDS) (Steig et al., 2014) on a Picarro L2140-I, and calibrated against V-SMOW (Vienna Standard Mean Ocean Water) in the laboratory of stable isotopes. (Spain)

Figure 89 illustrates the relationship between $\delta^{18}O$ and $\delta^{2}H$ in relation to the established Global Meteoric Water Line (GMWL), showing that thermal waters lie above this line, which is defined by (Craig, 1961) as $\delta^{2}H = 8\ \delta^{18}O + 10$. This positioning may indicate the presence of a specific local meteoric water line or suggest deuterium enrichment resulting from varying recharge water conditions influenced by different humidity levels in the air masses. The recharge from Mediterranean moisture may have been impacted by climatic influences from the Atlantic, as proposed by (Celle-Jeanton et al., 2001) in their definition of the Western Mediterranean Meteoric Water Line (WMWL) as $\delta^{2}H = 8\ \delta^{18}O + 22$.

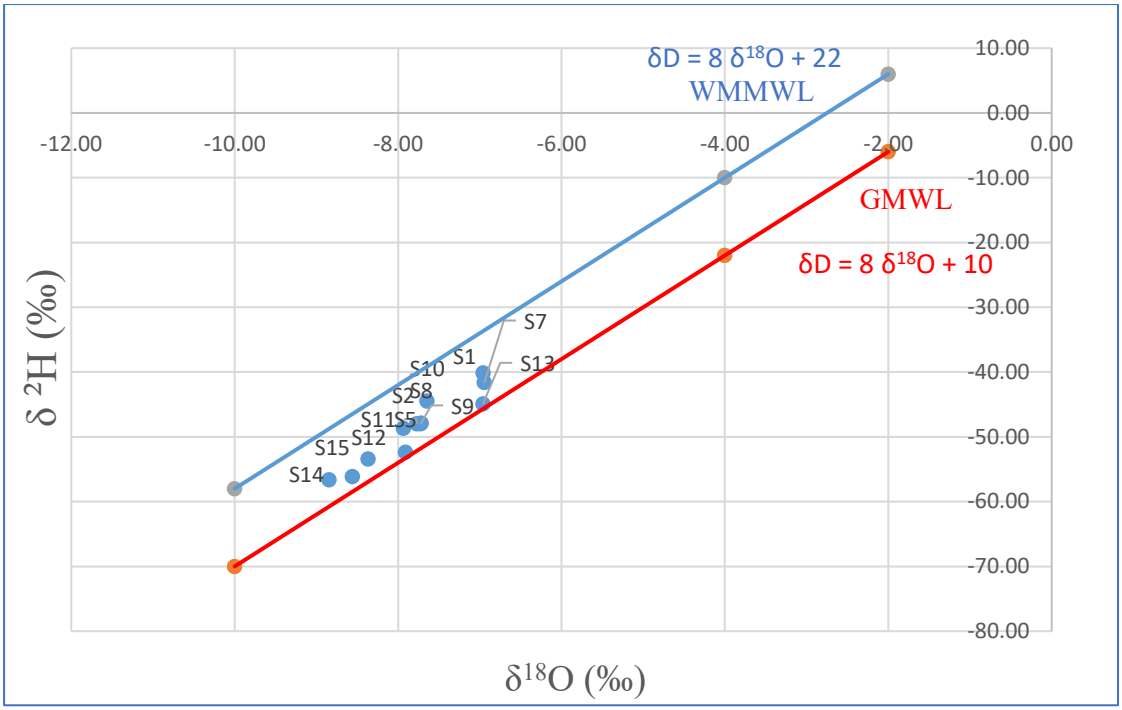


Figure 89 δ^2H vs $\delta^{18}O$ of Thermal Waters in the Study Zone, *GMWL is the Global Meteoric Water Line, WMMWL is the Western Mediterranean Meteoric Water Line*

8.3.1 Comparison to GMWL and WMMWL

- The majority of the samples fall between the WMMWL and the GMWL, with most samples being closer to the GMWL, with S13, S5 belonging to it. The samples' alignment suggests that these waters are mainly of meteoric origin.
- The positioning of samples S5 and S13 indicates that their isotopic signature is still closely similar to those of meteoric waters with little alteration, suggesting a limited interaction with geothermal systems and/or the interaction did not lead to significant isotopic shifts.
- In contrast, S1 and S7 are plotted slightly higher on the graph. This could indicate slight enrichment in both δ^2H and $\delta^{18}O$, suggesting the influence of geothermal processes that alter the isotopic ratios, potentially indicating a shared recharge region at a lower latitude as mentioned previously.
- The grouping of samples like S11, S2, and S9, S1 and S7, S15 and S14 near each other and the WMMWL suggests that these waters may have experienced similar climatic and environmental conditions during recharge, possibly indicating a shared moisture source or recharge zone under Mediterranean climate conditions.

Section two

Geothermometry in the Study Area

I. Geothermometry

One of the major applications of geochemistry in the exploration of geothermal resources involves the estimation of underground temperatures using chemical geothermometers (Arnorsson et al., 1982). According to a geothermal gradient

The sampled water required the selection of a suitable geothermometer based on factors such as element concentration, expected temperature, and the geological media of the study area. In line with these requirements, it is essential to consider certain assumptions (BRGM, 1999) to ensure the accuracy and reliability of geothermometric estimations. These assumptions include the availability of key elements in sufficient concentrations within the host rocks: (Na, K, Ca, Li, Mg), the establishment of chemical equilibrium between the water and minerals, and the necessity for rapid transit of water from the reservoir to the surface, without significant secondary reactions or mixing with shallow waters. Additionally, the reliability of the analytical results must be ensured, from sampling to final measurement.

1. Reliability of Geothermometers

- ***Na/K*** Geothermometers: These are generally reliable for estimating temperatures in high-temperature geothermal systems (typically >120°C) due to their dependence on sodium-potassium equilibrium. They provide consistent results for deeper, hotter systems but may be less accurate at moderate or low temperatures.
- ***Na/Li*** Geothermometers: Well-suited for lower-temperature systems, Na/Li geothermometers are sensitive to lithium concentrations, which can vary widely depending on regional geology. While useful, they may be less reliable in areas where lithium levels are altered by water-rock interactions, such as cation exchange.
- ***Mg/Li*** Geothermometers: Suitable for moderate-temperature systems, Mg/Li geothermometers are often influenced by carbonate systems, which can lead to underestimation of temperatures in hotter geothermal environments. They are particularly useful if magnesium concentrations are significant.
- ***Na-K-Ca*** Geothermometers: These are ideal where calcium plays a prominent role in water chemistry and can be used for moderate to high temperatures. However, they may underestimate temperatures in systems affected by cation exchange or other complex geochemical processes, making Na/K geothermometers generally more reliable for hotter systems.

2. Chemical Geothermometers

2.1 Geothermometer of Na/k:

The relationship between Na/K and temperature was first introduced by White in 1965 and Ellis in 1969 and 1970. It was later formulated as a thermometric relationship by Fournier & Truesdell, in 1973, Truesdell in 1975, and Fournier in 1979 for temperatures above 120°C. However, Kharaka & Mariner (1989) estimate that this geothermometer is only useful for temperatures above approximately 150°C. The Na-K geothermometer is based on the equilibrium reached between a plagioclase and potassium feldspar. This single assumption constitutes a major drawback, as to ensure the existence of such equilibrium, it would be necessary to know the concentration and activity of aluminum at depth.(Serra & Sunjuan, 2004).

A new Na/K geothermometer is proposed by Arnorsson S (2000) based on the thermodynamic properties of albite and K-feldspar. For diluted or slightly saline waters at temperatures below 300°C, the ratio of Na/K activities can be considered as the ratio of their concentrations.

The Na-K geothermometers used in this study are defined by the following equations:

- $\boldsymbol{T°C = \frac{1217}{1.483+\log\frac{Na}{K}} - 273.15}$ (Fournier R., 1979)
- $\boldsymbol{T°C = \frac{933}{0.993+\log\frac{Na}{K}} - 273.15}$ (Arnórsson, 1983)
- $\boldsymbol{T°C = \frac{1390}{1.75+\log\frac{Na}{K}} - 273.15}$ (Giggenbach 1983)

2.2 Geothermometer of Na-Li

The dependence of lithium on temperature is stronger than that of sodium, with a difference of about four orders of magnitude between 0 and 300°C for lithium, compared to approximately two orders of magnitude for sodium. The Na/Li ratio, which is rarely altered during the ascent of the fluid, seems to provide good estimates of deep temperatures (Fouillac and Michard, 1981, Serra & Sunjuan, 2004). In our study, the geothermometer chosen to be used is proposed by (Kharaka et al., 1982)

$$\boldsymbol{T = \frac{1590}{1.30 + \log\frac{Na}{Li}} - 273.15}$$

2.3 Geothermometer of Mg-Li

As noted by White, Fournier, Kharaka, and other researchers, magnesium levels in surface waters are much lower compared to seawater and typically decline with rising temperatures. Conversely, lithium concentrations increase with higher temperatures, indicating that the Mg/Li ratio may be a useful temperature indicator.

Kharaka et al., 1985 were the first to define the Mg/Li geothermometer based on formation water samples from oil fields. Subsequently, (Kharaka & Mariner, 1989) defined a second geothermometer to estimate the deep temperatures of sedimentary basins. In our study, we used the latter.

$$T = \frac{2200}{3.82 + \log\frac{\sqrt{Mg}}{Li}} - 273.15$$

2.4 Geothermometer of Na-K-Ca

Fournier & Truesdell (1973) consider that the addition of calcium to the Na/K geothermometer, proposed by White (1963) and later by Ellis (1970), accounts for a possible cation exchange of Ca^{2+} and Na^{+} between the rock (in the presence of plagioclase) and the solution. The Na-K-Ca geothermometer is expected to be used with a temperature lower than 150° C and with relatively high Ca content, which requires the concentration of ions to be expressed in mol/kgw (moles per kilogram of water).

$$T = \frac{1647}{\log\frac{Na}{K} + \beta\log\frac{\sqrt{Ca}}{Na} + 2.24} - 273.15$$

With :

β = 4/3 Si T< 100 °C

β = 1/3 Si T > 100 °C

How to calculate: (Serra & Sunjuan, 2004)

1. Express the concentrations of major cations in molality (mol/kgw).
2. Calculate the ratio log (√Ca/Na). If the result is negative, calculate log K* for β = 1/3 using the formula:

$$\text{Log } K^* = \log(Na/K) + \beta \log(\sqrt{Ca}/Na)$$

If log(√Ca/Na) is positive, calculate log K* with β = 4/3.

3. The temperature can then be calculated using the equation:

$$T = \frac{1647}{\log\frac{Na}{K} + \beta \log\frac{\sqrt{Ca}}{Na} + 2.24} - 273.15$$

4. If the estimated temperature is higher than 100°C, recalculate the temperature with β = 1/3. If the temperature is lower than 100°C, then use β = 3/4 to estimate it.

3. Geothermal Gradient

The geothermal gradient refers to the variation of the Earth's temperature, which increases with depth. On average, the temperature rises about 3°C per 100 meters, though this can vary significantly depending on the geological and geothermal characteristics of a region. The geothermal gradient is influenced by two main factors: Earth's heat flow and the thermal conductivity of rocks. Through the work conducted on the geothermal gradient and (Ouali Salima, 2015) the geothermal gradient is associated with three principal causes:

a) **Magmatic Origin**: High geothermal gradients are caused by the presence of hot rocks beneath the surface, often linked to volcanic activity or magmatic chambers, or local upwellings of mantle material.
b) **Tectonic Origin**: Heat can also be generated by tectonic plate movements, particularly through friction and deformation along faults due to tectonic stress.
c) **Chemical Origin**: Exothermic chemical reactions, such as the reduction of sulfates, oxidation of iron sulfides, and the transformation of anhydrite to gypsum, along with the decay of radioactive minerals, can contribute to elevated temperatures in the subsurface.

The geothermal gradient map (Figure 90) is fundamental in geothermal exploration because it helps identify geothermal gradient anomalies, which are essential for delineating regions of interest for geothermal applications and for assessing the extent and potential of reservoirs. In the concerned area, the isogradient map (Bouchareb-Haouchine, 2012) shows that the geothermal gradient varies from 3°C per 100 meters in the central part to 4°C per 100 meters in the external parts.

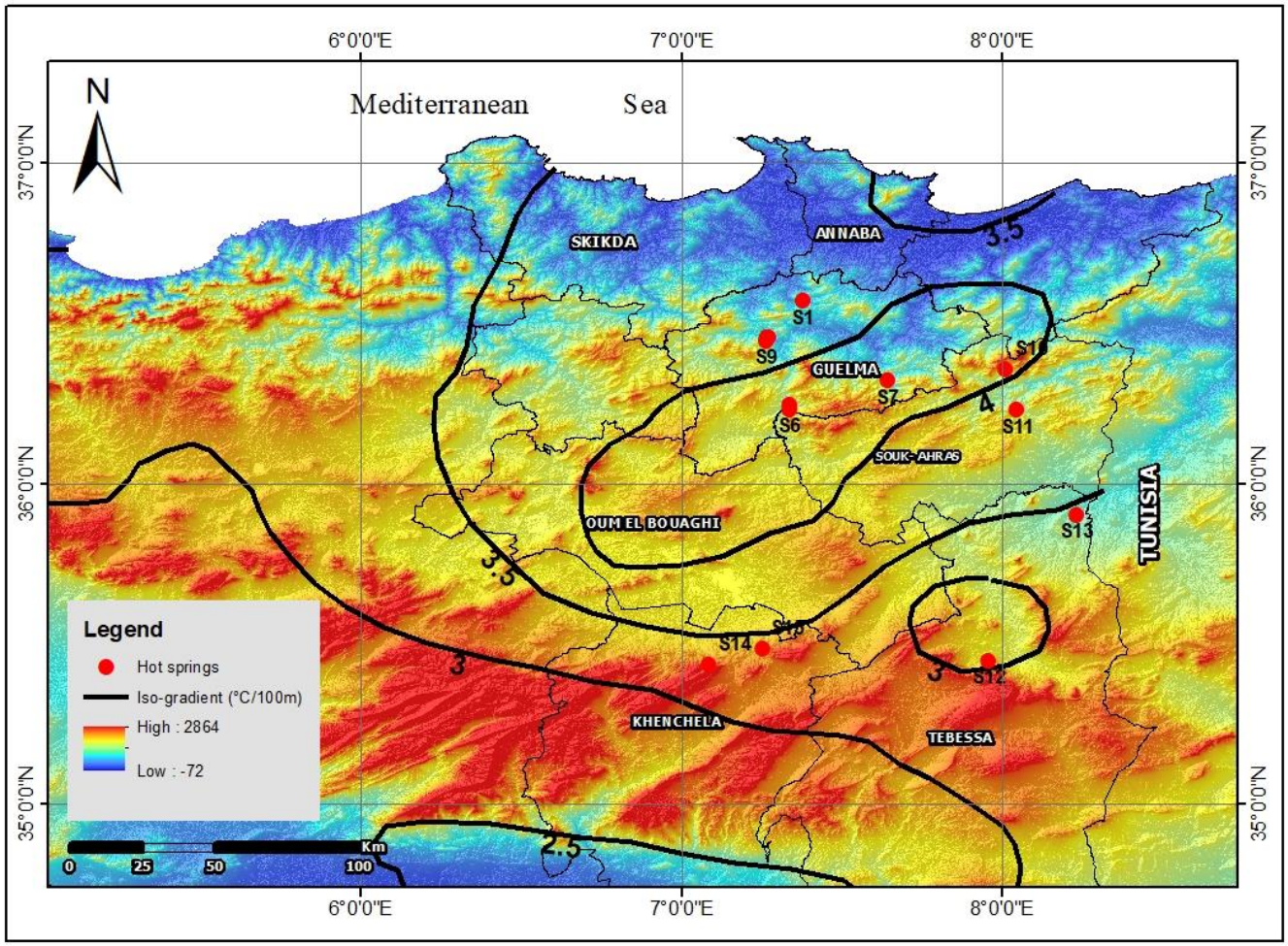


Figure 90 Geothermal Gradient Map of the North-East of Algeria (Adapted from Boucharef-Haouchine, 2012)

4. Estimation of Groundwater Circulation Depths and Temperatures

The estimated temperatures of the sampled waters (Table 32), calculated using Na/K geothermometers, demonstrate greater reliability, ranging from 64.81°C at S10 to 249°C at S1 according to Arnórsson (1983), from 47.38°C at S13 to 261.36°C at S1 based on Fournier (1979), and between 68.89°C at S13 and 273.27°C at S1 as reported by Giggenbach et al. (1983). Notably, an anomaly exists for S13 with the Arnórsson (1983) geothermometer, indicating a lower temperature at depth compared to the surface. This finding is also corroborated by the Na-Ca-K and Mg-Li geothermometers in the context of calcium sulfate water types, suggesting a cation exchange and mineral precipitation, or refer to the limitation of geothermometers' applicability and might indicate that they respond differently to certain mineral equilibria.

For sample S13, a sodium chloride water type with high salinity, this elevated salinity likely causes the anomaly in Arnórsson's geothermometer, alongside the non-equilibrium state of the water. Specifically, the high sodium concentration and undersaturation with key minerals suggest significant ion exchange processes, which possibly disturb the equilibrium assumptions required by Arnórsson's geothermometer. Therefore, results from the Fournier and Giggenbach geothermometers should be considered more reliable for estimating the in-depth temperature.

Although all samples exhibit some level of mineral disequilibrium (Table 26), the geothermometric anomalies (Table 32 in bold) are observed only in the calcium sulfate water type samples (S1, S5, and S6), not in the sodium chloride samples. This difference can be attributed to the distinct geochemical behavior of calcium sulfate waters. In calcium sulfate waters, cation exchange processes involving calcium (Ca^{2+}) and sodium (Na^{+}) are more possibly to occur, especially in the presence of gypsum and anhydrite dissolution. These processes can significantly alter the concentrations of calcium, magnesium, and lithium, disturbing the equilibrium required for the Mg-Li and Na-Ca-K geothermometers. Sodium chloride waters, on the other hand, are more chemically stable and do not experience the same degree of ion exchange, which is why geothermometers such as Na/K perform more reliably in those samples.

While S10, a sodium chloride water type, shares undersaturation with halite like other samples, the observed anomaly in Mg-Li and Na-Ca-K geothermometers probably results from localized variations in water-rock interactions. The distinctive geochemical behavior of the two samples, characterized by magnesium sourced from dolomite dissolution despite its undersaturation, presumably contributes to the observed anomaly in temperature estimation.

Table 36. Estimated temperature in °C in the study zone by different chemical geothermometers

Sample ID	T °C	Estimated T°C Na/K Arnorsson	Estimated °C Na/K Fournier	Estimated T°C Na/K Giggenbach	Estimated T°C Na/Li Kharaka 1982	Estimated T°C Mg-Li Kharaka and Mariner 1989	Estimated T°C Na-K-Ca Fournier 1973
S1	54.6	249.00	261.36	273.27	205.50	**30.24**	**22.85**
S2	94.7	168.44	194.42	211.20	186.92	-	-
S3	69.1	177.74	202.38	218.67	197.39	69.04	76.95
S4	64.4	158.78	186.08	203.36	189.59	69.19	73.72
S5	55.3	164.43	190.96	207.95	158.06	**37.73**	**41.38**
S6	62.2	192.93	215.25	230.69	179.47	**42.69**	**46.00**
S7	42.4	94.32	128.63	148.57	141.31	87.50	130.04
S8	58.6	181.96	205.97	222.03	194.05	65.47	74.65
S9	58.6	176.53	201.35	217.70	194.54	68.18	78.73
S10	57.3	64.81	101.24	122.00	145.96	**44.75**	**34.30**
S11	38.7	92.28	126.76	146.77	155.18	69.42	64.70
S12	34.5	67.65	103.90	124.59	-	-	-
S13	34.5	**8.99**	47.38	68.89	97.91	102.96	80.09
S14	54.7	82.69	117.92	138.21	145.03	69.13	79.85
S15	51	68.52	104.72	125.39	157.03	88.26	74.87

In order to estimate the depth of thermal water reservoirs in the study area, the chemical geothermometer data (Table 32) is combined with the isothermal gradient map of northern Algeria (Figure 90), created by Bouchareb-Haouchine, 2012. This map, based on temperature readings from BHT and DST tests on oil wells, with depths ranging from 196.35 to 6247.63 meters, reveals a notable geothermal gradient in northeastern Algeria. Specifically, in the study region, this gradient ranges from 30°C to 43°C per kilometer. The results are summarized in tables 37 and 38.

The estimated depth (Z) is calculated using the equation:

$$\mathbf{Z = (T_e - T_m)/G}$$

Where:

(T_e): is the temperature estimated at depth

(T_m) is the measured temperature at the surface (the temperature of the water at the source),

(G) is the geothermal gradient, which represents the rate of temperature increase per unit depth, measured in °C/100 m.

Table 37. Estimation of the depths of deep reservoirs in the study area

Sample ID	Gradient C°/100m	Depth (m) Na/K Arnorsson		Depth (m) Na/K Fournier		Depth (m) Na/K Giggenbach		Depth (m) Na/Li Kharaka1982	
		min	max	min	max	min	max	min	max
S1	3.5-4	4859.99	5554.27	5169.04	5907.47	5466.67	6247.63	3772.46	4311.38
S2	3.5 - 4	1843.38	2106.72	2492.90	2849.02	2912.43	3328.49	2305.60	2634.97
S3	3.5 – 4	2715.95	3103.94	3331.99	3807.99	3739.19	4273.36	3207.21	3665.38
S4	3.5 - 4	2359.51	2696.58	3042.07	3476.66	3473.88	3970.15	3129.77	3576.87
S5	4.0 - 4.3	2537.83	2728.17	3154.99	3391.62	3550.06	3816.31	2389.86	2569.10
S6	4.0 -4.3	3040.15	3268.17	3559.27	3826.22	3918.35	4212.23	2727.11	2931.65
S7	4.0 -4.3	1207.38	1297.93	2005.41	2155.82	2469.14	2654.33	2300.15	2472.66
S8	3.5 -4	3083.99	3524.56	3684.33	4210.67	4085.77	4669.45	3386.20	3869.94
S9	3.5-4	2980.83	3406.66	3601.30	4115.77	4010.12	4583.00	3431.04	3921.19
S10	4	675.33	675.33	1585.90	1585.90	2104.99	2104.99	2703.97	2703.97
S11	3.5-4	1339.51	1530.86	2201.60	2516.11	2701.75	3087.71	2912.06	3328.07
S12	3	1104.88	1104.88	2313.27	2313.27	3003.15	3003.15	-	-
S13	3.5	-	-	367.88	367.88	982.49	982.49	1811.84	1811.84
S14	3.0-3.5	799.58	932.84	1806.19	2107.23	2386.12	2783.81	2580.72	3010.84
S15	3.0-3.5	500.57	584.00	1534.79	1790.58	2125.51	2479.76	3029.48	3534.39

Table 38. Estimation of the depths of deep reservoirs in the study area

Samples ID	Depth (m) Na-K-Ca		Depth (m) Mg-Li	
S1	-	-	-	-
S2	-	-	1950.25	1706.47
S3	196.35	224.40	1972.68	1726.09
S4	232.97	266.25	1976.87	1729.76
S5	-	-	-	-
S6	-	-	-	-
S7	2191.11	2504.13	2500.07	2034.94
S8	401.22	458.54	1870.62	1636.79
S9	535.82	612.36	1948.10	1704.58
S10	-	-	-	-
S11	650.05	742.91	1983.47	1735.53
S12	-	-	-	-
S13	1139.79	1302.61	2941.64	2941.64
S14	628.69	718.50	2304.33	1975.14
S15	596.83	682.09	2941.87	2521.61

5. Thermal Water Depth and Temperature of the Reservoir: Plotting the Results

5.1 General Trends Across All Geothermometers

The geothermometer plots (Figure 92) illustrate clear groupings based on specific conditions and processes in the geothermal system. Each geothermometer provides a distinct viewpoint, primarily due to the varying chemical reactions and equilibria it tracks. The following sections will outline these groupings and offer a concise interpretation of the geothermal conditions they reveal.

5.1.1 Grouping of Samples According to Different Geothermometers

a) ***Na/K Geothermometer*** (Fournier, 1979; Arnórsson, 1983; Giggenbach, 1983):

Na/K geothermometers are often reliable for higher temperature reservoirs. S1 stands out as the hottest sample, suggesting a deep reservoir, and the grouping of S2 to S9 suggests waters at mid-range temperatures. The clustering of S7 and S10-S15 could indicate cooler or shallower systems, while S13 appears as an anomaly, potentially due to its chemistry. (Figure 91. a, b, c)

- **G1**: S1. Estimated depth of 4859.99 to 6247.63 m
- **G2**: S2, S3, S4, S5, S6, S9, S8. Depth ranging between 1843.38 and 4583.00 m
- **G3**: S7, S10, S11, S12, S14, S15. Depths are between 500.57 and 3087.71 m
- **G4**: S13. Estimated depth of 367.88 to 982.49 m

b) ***Na/Li Geothermometer*** **:** (Kharaka 1982)

Na/Li geothermometers are sensitive to both temperature and chemical composition changes. The grouping here is slightly different, with S1 still standing out, but the arrangement of mid-depth samples (G2 and G3) varies compared to Na/K, possibly reflecting variations in Li concentrations or chemical processes such as cation exchange (Figure 91. d). Based on Na/Li geothermometry, the following depth estimates can be inferred:

- **G1**: S1. Estimated depth of 3772.46 to 4311.38 m, suggesting a deep-seated geothermal source associated with high-temperature geothermal processes.
- **G2**: S3, S9, S8, S4, S11, S15. Depths ranging between 2305.60 and 3921.19 m, indicating a mid-depth geothermal influence, potentially reflecting moderate thermal gradients and interactions with lithological layers at depth.
- **G3**: S14, S7, S5, S6, S2, S10. Depths estimated between 2300.15 to 3534.39 m, suggesting interactions within both shallow and intermediate geothermal systems, with moderate temperatures.

- **G4**: S13. Estimated depth of 1811.84 m, highlighting a relatively shallower geothermal source. This corresponds to S13's unique chemical profile, including its high salinity and mineral saturation, which could be indicative of evolved water-rock interactions at lower depths.

c) ***Mg/Li Geothermometer*****:** (Kharaka and Mariner 1989)

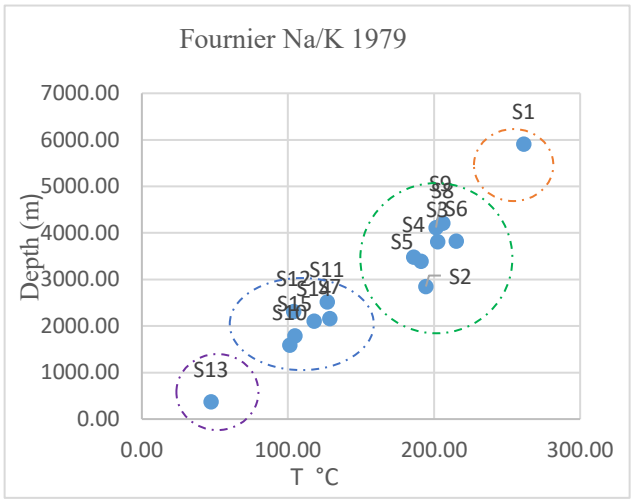
Mg/Li geothermometers can be influenced by water-rock interaction, especially in carbonate systems. In this case, S13 stands out, indicating a lower temperature. The presence of S7 and S15 in G2 suggests deeper or hotter systems than Na/Li would indicate. This geothermometer seems to group cooler, more magnesium-influenced samples differently from others. (Figure 91. e)

- **G1**: S13. Estimated depth 2941.64 m, suggesting a deep-seated geothermal influence, which aligns with S13's complex chemistry, including high salinity and distinctive mineral saturation patterns.
- **G2**: S7, S15. Depths are estimated between 2034.94 and 2941.87 m, indicating moderate geothermal influence. This depth range supports the geochemical profile of S7 and S15, which may be influenced by mid-depth geothermal conditions.
- **G3**: S3, S4, S8, S9, S11, S14. Depth is from 1636.79 to 1983.47 m

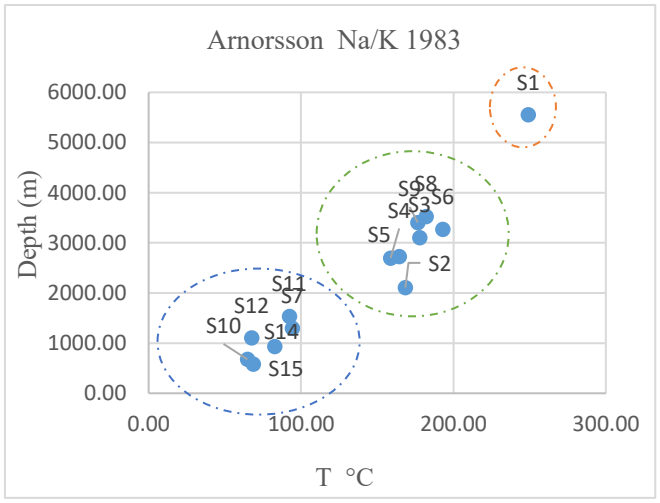
d) Na-K-Ca Geothermometers: (Fournier 1979)

Na-K-Ca geothermometers incorporate calcium, which may be important in systems where cation exchange and carbonate equilibria are active. S7 is grouped as the hottest sample, and S13 again appears distinct, likely due to its sodium chloride water type and its chemical characteristics. (Figure 91. f)

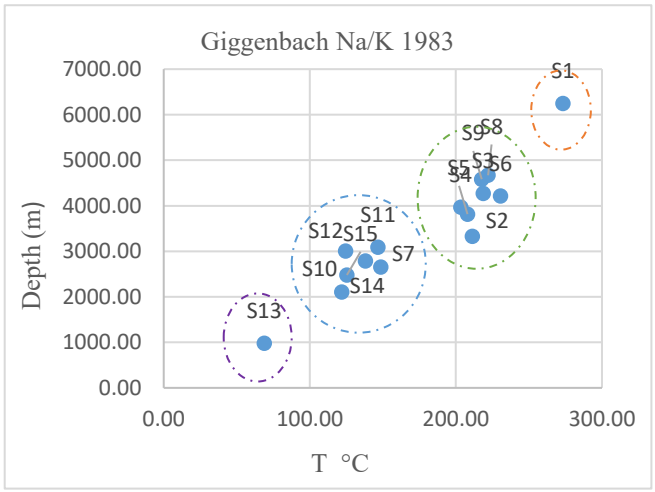
- **G1**: S7. Estimated depths are from 2191.11 to 2504.13 m, indicating a significant deep-seated geothermal source. This sample's characteristics suggest prolonged water-rock interactions, consistent with elevated temperatures.
- **G2**: S13. Estimated depth between 1139.79 and 1302.61 m, suggesting an intermediate geothermal environment.
- **G3**: S8, S9, S11, S14, S15. Depths are estimated from 401.22 to 718.50 m, indicating a relatively shallow geothermal influence.
- **G4**: S4, S3. Estimated depth of 196.35 to 266.25 m, reflecting very shallow geothermal conditions.



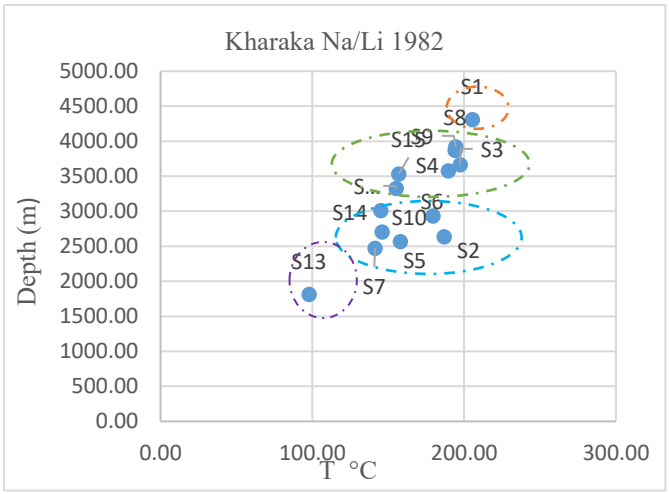
(a)



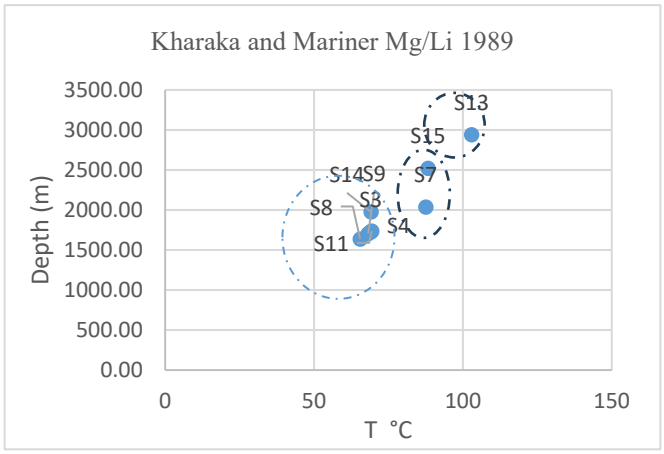
(b)



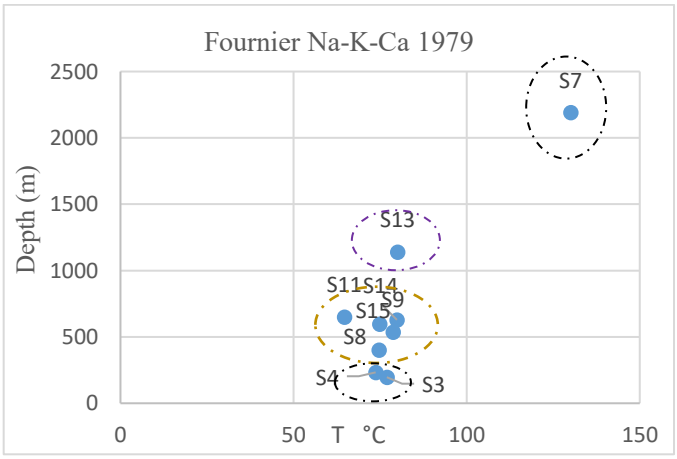
(b)



(d)



(e)



(f)

Figure 91 Plots Illustrating the Depth and Temperature of Thermal Waters in the Study Area

6. Cross-Validation of Geothermometer Reliability Through Index of Maturity and Ternary Diagrams

6.1 Maturity Index

The Maturity Index (MI), as established by (Giggenbach, 1988), is essential for developing geoindicators, such as geothermometers. The maturity index (MI) evaluates the degree of equilibrium between rock and water in geothermal reservoirs (Table 39), regardless of the thermal field's origin. It is a linear combination of sodium (Na^+), potassium (K^+), and magnesium (Mg^{2+}) geothermometers, which helps classify the thermal waters based on their chemical equilibria. Immature waters reflect the impact of rock dissolution rather than equilibration, while partially equilibrated waters exhibit a mature index (MI) of 2 or higher, determined by the following developed formula:

$$\mathbf{MI = 0.315 \cdot (\log (Mg/K) - \log (Na/K))}$$

Table 39. Calculation of the Maturity Index of all samples in the Study area

Sample ID	***S1***	***S2***	***S3***	***S4***	***S5***	***S6***	***S7***	***S8***	***S9***	***S10***	***S11***	***S12***	***S13***	***S14***	***S15***
Na+	38.32	237.2	218.6	231.1	137.4	124.4	1971	218.5	216.7	196.2	462	21.11	4800	568.6	668
K+	6.16	18	18.34	15.73	9.97	12.19	56.05	19.16	17.95	3.35	12.72	0.38	23.3	13.36	12.22
Ca2+	313.5	195.5	197.4	187.6	394.1	390.1	372.8	234.7	175.3	139.1	298.8	70.39	324.3	173.3	206.83
Mg2+	44.54	22.32	25.23	21.42	47.56	52.18	54.85	30.82	24.3	28.92	23.54	21.78	13	24.14	11.34
K/Mg	0.14	0.81	0.73	0.73	0.21	0.23	1.02	0.62	0.74	0.12	0.54	0.02	1.79	0.55	1.08
K/Na	0.16	0.08	0.08	0.07	0.07	0.1	0.03	0.09	0.08	0.02	0.03	0.02	0.00	0.02	0.02
IM	0.52	1.09	1.03	1.12	0.93	0.81	1.55	0.99	1.04	1.47	1.48	1.19	2.39	1.55	1.75

6.2 Ternary Diagram of Giggenbach Na-K-$Mg^{1/2}$

The ternary diagram of Na/1000-K/100-√Mg (Figure 92), proposed by (Giggenbach, 1988), was used to estimate reservoir temperatures, differentiate between mature and immature waters along their flow paths, and cross-check geothermometer reliability. The diagram is divided into three parts to differentiate the types of waters into immature waters, partially equilibrated waters, and fully equilibrated waters.

As shown in Figure 92, only sample S13 is positioned above the Na-K equilibrium line, indicating that it has reached full equilibrium phase and is thus classified as a mature geothermal water. This state of maturity suggests that S13 has achieved a chemical balance within the Na-K system, enhancing the reliability of its Na/K geothermometer results. As a result, these values are likely accurate and reflective of true reservoir temperatures, indicating a stable and well-matured geothermal environment. Consequently, S13 serves as a strong reference point for estimating deeper geothermal conditions, providing reliable indications of reservoir temperature based on its mature state. While

sample S7, located between the Mg corner and the Na-K equilibrium line, demonstrates partial equilibrium, indicating a moderate level of geothermal maturity. This positioning suggests that S7 has undergone significant interaction with geothermal minerals compared to immature waters, though it has not reached full equilibrium in the Na-K system. As a result, S7's Na/K geothermometer values may provide a reasonable approximation of reservoir temperatures but may still be slightly inflated due to residual Mg influences. Therefore, while S7 offers a closer estimate of reservoir conditions than less mature samples, results should be treated with caution, and slight adjustments may be needed to account for its incomplete equilibration. Sample S14 is situated below S7 on the ternary diagram, indicating that it is approaching partial equilibrium but has not yet attained the maturity level of S7. This positioning places S14 between the immature samples near the Mg corner and S7, suggesting it exhibits characteristics of both. The limited cation exchange influence observed in S14 implies a more complex interaction with the geothermal system, although it does not reach full equilibrium within the Na-K system. Consequently, the Na/K geothermometer readings for S14 may reflect intermediate thermal conditions, but they are likely less reliable than those of S7 and more susceptible to overestimation, whereas the rest of our samples are plotted near to Mg^{2+} corner corresponding to immature waters.

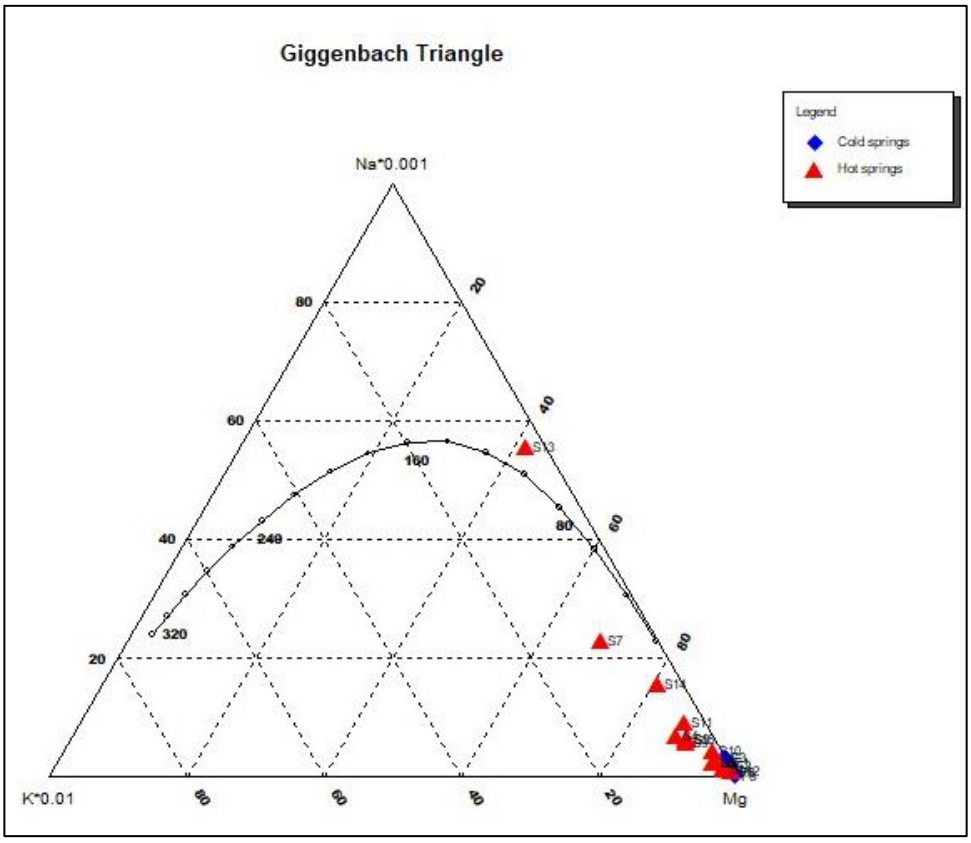


Figure 92 Giggenbach 1988 Ternary Diagram for All Water Samples

6.3 Ternary Diagram of SO4-Cl-HCO3

In the present study, the ternary diagram SO_4-Cl-HCO_3 (Figure 93) is a very useful tool for the classification of geothermal waters to identify the most dominant anionic composition related to geochemical processes and water-rock interactions. On the basis of plotting samples, we can distinguish among sulfate-dominated waters, which generally are indicative of interaction with evaporitic minerals such as gypsum and anhydrite; chloride-dominated waters, which may have interactions with deeper and hotter geothermal reservoirs; and bicarbonate-rich waters, representative of influences from surface or shallow groundwater sources. This diagram helps in understanding the source and evolutionary pathways of each water type and hence supports the cross-validation of geothermometer results and hydrochemical groupings within a wider geothermal context.(Giggenbach, 1991)

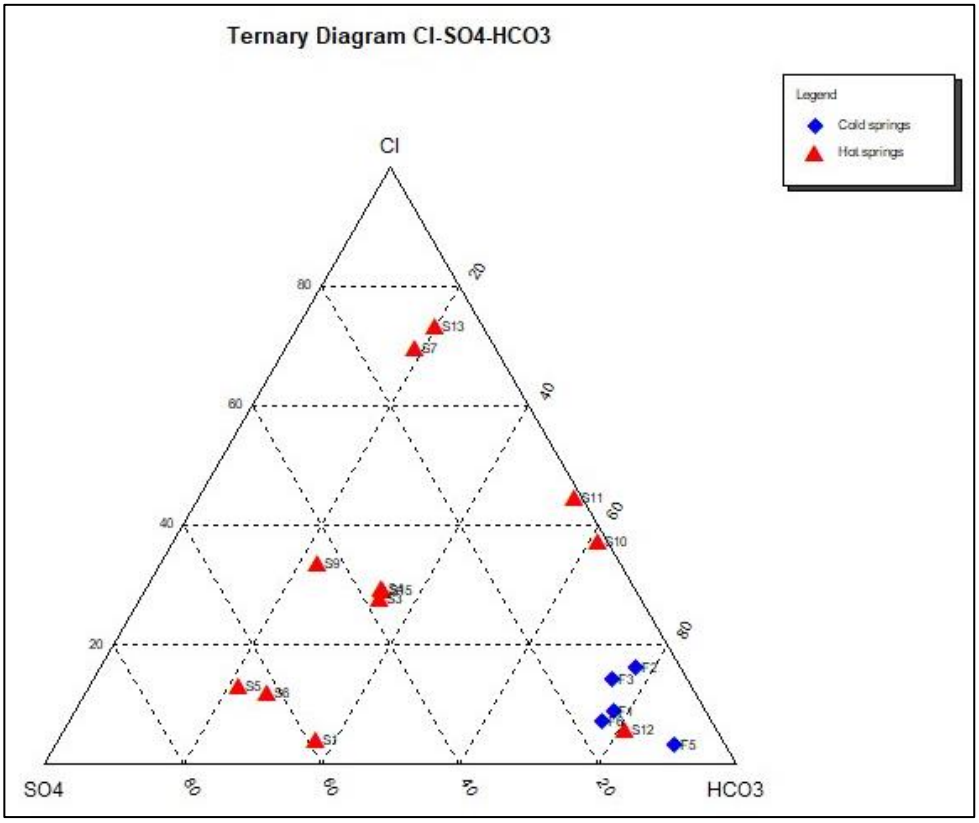


Figure 93 Cl-SO4-HCO3 Ternary Diagram (Giggenbach, 1988) Showing the Position of the Water Samples from the Study Area

The positioning of S7 and S13 in the SO_4-Cl-HCO_3 diagram indicates that these waters are approaching equilibrium conditions. Identified as mature waters, they have likely been in the system long enough to undergo substantial geochemical interactions. This extended residence time facilitates thorough equilibration with surrounding minerals and rock formations, leading to elevated concentrations of sulfate (SO_4^{2-}) and chloride (Cl^-). These characteristics suggest a stable hydrochemical environment that reflects the influence of local geological processes.

S10 and S11 are classified as peripheral waters and plot near the HCO_3 apex on the SO_4–Cl–HCO_3 diagram. This position reflects the dominance of bicarbonate and suggests incomplete water–rock equilibration, where interaction with carbonate formations is present but not fully developed. Their chemical signatures indicate recharge through carbonate-rich terrains, rather than strong evaporitic or saline influence. These waters likely represent an early stage in the water–rock interaction pathway, prior to significant mineral dissolution or ion exchange processes

S1, S5, and S6 are positioned near the sulfate apex of the Cl–SO_4–HCO_3 diagram, indicating sulfate-rich water chemistry. Rather than steam-heated processes, their composition is more consistent with the dissolution of sulfate minerals, particularly gypsum or anhydrite, within the reservoir or along the flow path. The elevated sulfate concentrations may also be influenced by evaporation effects, which further concentrate dissolved ions. This suggests that water–rock interaction and evaporative concentration are the primary controls on the geochemical characteristics of this group.

Waters in Group 4 (S3, S4, S9, S14, S15) exhibit varying degrees of mineralization and are positioned away from the extremes of sulfate and chloride in the SO_4-Cl-HCO_3 diagram. This suggests that they are influenced by local geological conditions and recharge dynamics, resulting in a unique hydrochemical signature. These waters may reflect more recent inputs, possibly due to interactions with surface water or organic contributions. The diversity within this group underscores the complex geochemical processes occurring within the study area.

Group 5 comprises cold springs (F1, F2, F3, F5, F6) and the hot spring (S12), which are positioned near the bicarbonate corner of the diagram. This grouping suggests that these waters are influenced by atmospheric interactions or recent recharge processes, leading to significant bicarbonate concentrations. The presence of S12 as a hot spring indicates geothermal activity, yet its hydrochemical profile reflects a distinct evolution path, likely influenced by surface processes. These waters illustrate a connection between surface and subsurface dynamics, emphasizing their role in regional hydrochemistry.

6.4 Interpretation and Hypotheses

The Na-K-Ca geothermometer is recommended as the most suitable tool for estimating reservoir depth and temperature in this study. It offers consistent results, unlike other geothermometers, such as Na/K, which inaccurately suggest that S1 (51°C, calcium sulfate) is the deepest sample. In contrast, the Na-K-Ca geothermometer accurately indicates deeper reservoir conditions, making it particularly relevant for mature waters like S7 (42°C, sodium chloride) and S13 (34.5°C, sodium chloride) while remaining effective for other samples with notable mineral interactions. This tool considers geochemical interactions among sodium, potassium, and calcium, aligning with the characteristics of most samples and offering reliable temperature estimates for both mature and less mature waters.

Additionally, a maturity index enhances its utility by reflecting longer residence times and substantial mineral interactions. The Na-K-Ca geothermometer is broadly applicable and consistent, though high-temperature samples S3 and S4 show unusually shallow estimated depths relative to their surface temperatures, potentially due to localized geothermal anomalies. Nonetheless, these exceptions do not undermine the tool's reliability, and even the Mg-corrected version shows negligible effects on estimated temperatures, affirming its strength as the primary geothermometer for this dataset.

Based on the Na-K-Ca geothermometer's reliability across samples, especially in distinguishing mature and less mature waters, two hypotheses emerge regarding the geothermal dynamics at play:

- **Hypothesis 1**: S1 as the Deepest Water

S1, characterized by a high surface temperature of 51.4°C, may be affected by rapid flow rates that prevent it from achieving a depth typically associated with prolonged residence times. While geothermometers indicate elevated temperatures for S1, these measurements might not fully reflect the water's geochemical maturity. This discrepancy suggests that, despite its high temperature, S1's rapid movement through the geothermal system along a fault could limit its interactions with surrounding minerals, thus impacting both its thermal and mineral equilibrium.

- **Hypothesis 2:** S7 and S13 as Mature Waters

S7 and S13 demonstrate characteristics indicative of mature waters, including longer residence times and slower flow rates, which facilitate substantial geochemical interactions. These factors contribute to their classification as mature waters within the geothermal system. The Na-K-Ca geothermometer corroborates this classification by aligning with their geochemical profiles, suggesting that both samples reflect deeper reservoir conditions. Despite their relatively lower temperatures (42.5°C, 34.5°C respectively), the strong geochemical evolution observed in S7 and S13 further

reinforces the notion that these waters have undergone significant equilibration with surrounding minerals over extended periods.

The Mg/Li geothermometer is also found to be a valuable and reliable complementary method, particularly effective for cases with pronounced cation exchange or significant geochemical complexity. Its sensitivity to variations in both magnesium and lithium concentrations enhances its applicability, especially in settings where Na-K-Ca may face limitations. For instance, the Mg/Li geothermometer corroborates deeper depth estimations for samples like S7 and S13, which exhibit high salinity and geochemical maturity, while providing reasonable depth estimations for less mineralized or shallow samples.

III. Conclusion

In the hydrochemistry chapter, we explored the chemical compositions, water types, multivariate statistical methods such as Principal Component Analysis (PCA), isotopic variations, and geothermometry estimates of water samples across various sites in the study area, drawing insights into the mineralogical, geochemical, and thermal characteristics of the sampled waters.

The hydrochemical analyses revealed distinct water types, primarily classified as sodium chloride (S2, S3, S4, S7, S8, S9, S10, S11, S13, S14, S15), calcium sulfate (S1, S5, S6), and calcium bicarbonate waters (S12, F1, F2, F3, F5, F6).

Sulfate-Dominated Waters: These waters are typically associated with interactions with evaporitic minerals like gypsum and anhydrite. The presence of high sulfate concentrations suggests geochemical processes involving the dissolution of these minerals, often found in sedimentary environments.

Chloride-Dominated Waters: Chloride-rich waters are often indicative of deeper and hotter geothermal reservoirs. High chloride concentrations usually reflect the influence of brine or saline fluids that have undergone significant thermal evolution, making them crucial for understanding the thermal regime of geothermal systems.

Bicarbonate-Rich Waters: These waters may represent the influence of surface or shallow groundwater sources. High bicarbonate levels often indicate interactions with carbonate minerals or reflect processes such as weathering and dissolution in the upper aquifer systems

The spatial distributions of chemical elements give insights into the hydrogeological characteristics of the area, potentially indicating the influence of geological formations in certain zones. Additionally, high temperatures in thermal waters were found to influence mineral saturation, with

carbonate minerals tending to dissolve under higher temperatures, whereas evaporite minerals, including gypsum and anhydrite, showed a positive correlation with temperature and tended to precipitate.

Principal Component Analysis (PCA) of the second sampling campaign reveals four distinct groups, with PC1 and PC2 explaining 77.44% of the total variance. Group 1 (F1, F2, F3, F5, F6, S12) includes low-mineralized, cool waters with low electrical conductivity. Group 2 (S5, S6) shows high mineral content and elevated temperatures, dominated by calcium and sulfate, indicating influence from evaporitic formations. Group 3 (S1, S3, S4, S9, S10, S11, S14, S15) consists of moderately mineralized waters, balanced in ions such as Mg^{2+}, Ca^{2+}, and SO_4^{2-}. Group 4 (S7, S13) includes chemically distinct, highly mineralized samples with high sodium and chloride levels, reflecting deep circulation and advanced water-rock interaction.

The Hierarchical Cluster Analysis (HCA) of the second campaign grouped the water samples into four distinct clusters based on their chemical characteristics. Group 1 consists of S7 and S13, which are chemically distinct from the other samples. Group 2 includes S12, F1, F2, F3, F5, and F6, representing cooler waters with lower mineral concentrations. Group 3 is made up of S5 and S6, which are characterized by higher levels of calcium and sulfate. Finally, Group 4 contains S1, S3, S4, S9, S10, S11, S14, and S15, which share similar hydrochemical profiles with moderate mineralization. These groupings reveal distinct variations in water chemistry across the study area and provide a clearer understanding of the different water types present. PCA and HCA generated consistent groupings, confirming the strength of the classification and reinforcing hydrochemical differences based on temperature, mineralization, and ion composition.

The PCA of the full dataset, after logarithmic transformation, distinguished six hydrochemical groups. Group 1 includes F1, F2, F3, F5, F6, and S12, characterized by bicarbonate–calcium composition and low temperatures. Group 2 contains high-salinity sodium–chloride samples S7 and S13. Group 3 is made up of thermal waters S1, S2, S3, S4, S5, S6, S8, and S9. Group 4 includes S10, S11, S14, and S15. Group 5 gathers mixed-character hot springs from different sites. Group 6 overlaps with Group 3, including samples S1 to S6 and S14, S15.

The Agglomerative Hierarchical Clustering (AHC) based on regional hydrochemical averages revealed clear spatial patterns. Tebessa and Khenchela formed one group, suggesting similar recharge or geological contexts. Souk Ahras, while somewhat related to this group, showed enough differences to stand alone. Guelma was the most distinct, possibly due to its higher temperatures and unique water–rock interactions. This clustering highlights the regional contrasts in hydrogeochemical conditions across the study area.

The isotopic analysis of ^{18}O and deuterium provided insights into the origin and recharge areas of the water samples, with most samples aligning closely with the Global Meteoric Water Line (GMWL). This alignment suggests meteoric origins, with slight isotopic enrichment observed in samples like S1 and S7, potentially pointing to recharge at lower latitudes or in areas with slightly warmer climates.

The application of various geothermometers provided temperature estimates at depth, though discrepancies emerged due to different geochemical processes, such as cation exchange and mineral precipitation. Notably, calcium sulfate water types, like S1, showed lower estimated temperatures using Mg-Li and Na-Ca-K geothermometers, likely due to these processes. Anomalies were also observed in certain samples with high salinity or elevated sodium levels, particularly in the Na/K geothermometer readings for sample S13. High salinity and non-equilibrium states of samples, such as S13, were considered in interpreting the results, adding complexity to temperature predictions

Sample S13 presents an interesting case where high salinity and non-equilibrium with certain minerals add complexity to its hydrochemical profile. Despite its undersaturation with minerals such as gypsum, dolomite, anhydrite, and halite, S13 is identified as a 'mature water' on the Giggenbach ternary diagram due to the stable phase of its cation ratios, particularly Na/K and Na/Mg. This maturity classification reflects the sample's long-term water-rock interactions, achieving a balanced ionic composition characteristic of evolved geothermal waters. This stable cation ratio phase, indicative of extensive geochemical evolution, supports the mature classification despite the mineralogical non-equilibrium, thus highlighting the complex interplay between water chemistry and mineral saturation in geothermal systems.

Given the high nitrate levels at S13, it is essential to investigate potential contamination sources and determine whether this water is utilized solely for bathing or also for drinking and irrigation purposes. Additionally, assessing for other potential contaminants, such as bacteria or heavy metals, is necessary to evaluate the water's suitability and safety for different uses. Furthermore, as groundwater flows toward the source, it is plausible that iron detected in the water may originate from the El-Ouanza iron deposit, pointing to geological contributions to the water chemistry. These findings underscore the need for comprehensive analysis of water quality in relation to both natural and anthropogenic influences in the area.

Overall, the hydrochemical, isotopic, and thermal analyses indicate a region with complex groundwater interactions influenced by lithology, geochemical processes, and thermal inputs. This study utilizes multiple hydrochemical parameters, including ion concentrations (e.g., Na^+, Ca^{2+}, Cl^-, SO_4^{2-}), saturation indices (e.g., for calcite, dolomite, gypsum), and isotopic markers (e.g., $\delta^{18}O$, δD, d-excess). Additionally, a range of geothermometric approaches such as Na/K, Mg-Li, and Na-K-Ca

geothermometers, provide insights into temperature conditions at depth and help assess the thermal regime's evolution. Integrating these parameters is crucial for a comprehensive understanding of groundwater systems in geothermal and mineral-rich environments.

To further validate and refine these findings, dating thermal waters using isotopic methods (e.g., radiocarbon, tritium, or helium isotopes) is recommended. This approach could confirm assumptions about groundwater residence time and recharge processes, providing temporal context to observed geochemical and isotopic signatures.

Part II

Gravitational Flow Systems in Modern Hydrogeology:

Insights from Tóth's Theory and Application

Preface

بِسْمِ ٱللَّهِ ٱلرَّحْمَٰنِ ٱلرَّحِيمِ

(مَرَجَ ٱلْبَحْرَيْنِ يَلْتَقِيَانِ ﴿19﴾ بَيْنَهُمَا بَرْزَخٌ لَّا يَبْغِيَانِ ﴿20﴾)

سورة الرَّحْمَٰن (آية: 19,20)

Translation:

(19) He released the two seas, meeting [side by side]
(20) Between them is a barrier [so] neither of them transgresses

These verses evoke the wonder and balance of natural systems, where distinct yet connected components interact in harmony. In a similar way, the gravitational flow system theory offers a holistic approach to understanding natural water systems, examining the combined effects of geological, hydrological, and environmental factors, all of which are interconnected.

Our journey with this theory began in 2018, during the IWCF colloquium in Tunisia where we had the privilege of meeting Mr. Joel José Carrillo Riviera (may Allah accord him peace). His dedication inspired us to explore the gravitational flow system theory, guiding us through its principles. Though he sadly passed before we completed our studies, this modest work marks our initial steps in applying the theory despite limited data. Our future goal is to deepen this work, continuing toward a fuller understanding of groundwater flow systems and their functions. Through ongoing application of this methodology, we aim to explore and clarify the intricate workings of these interconnected water systems.

I. History and Definition

The history of gravitational groundwater flow theory traces its origins back to early 20th-century studies on fluid dynamics within geological formations. In 1909, Munn proposed that meteoric water could infiltrate through various sedimentary layers, with its movement influenced by capillary forces, impacting the migration of hydrocarbons. This early work laid a foundational understanding of subsurface fluid dynamics. Later, Fourmanier (1939), following D'Andrimont, R.(1906), expanded on these concepts by exploring the behavior of meteoric water as it moves through strata under gravitational influence, providing valuable empirical insights. In 1940, Hubbert introduced the theory of groundwater motion, emphasizing fluid dynamics and hydraulic potential fields, which offered a theoretical framework to explain groundwater flow under gravitational forces. Building on these foundations, József Tóth's seminal work in 1962 presented a comprehensive theory of regional groundwater flow systems. Tóth introduced the concept of nested flow systems, local, intermediate, and regional, structured by topography and gravity, establishing the bedrock of modern hydrogeology. In the following decade, Freeze and Witherspoon (1966-1968) advanced Tóth's ideas through numerical modeling, showcasing how geological and hydrological variables shape groundwater flow in complex formations. Collectively, these contributions have fundamentally shaped the scope, direction, and evolution of hydrogeology.

Tóth's paper (Tóth, 1963)"A Theoretical Analysis of Groundwater Flow in Small Drainage Basins" is particularly notable, as it introduced the idea of nested flow systems: local, intermediate, and regional within a single groundwater basin. This framework is the basis for what we now call gravitational or regional groundwater flow systems, and it remains influential not only in hydrogeology but also in environmental studies, water management, petroleum exploration, and geotechnical engineering. The concept of nested flow systems has provided paramount insights for understanding fluid movement and resource distribution in subsurface environments, influencing practices in multiple fields reliant on accurate groundwater and fluid flow predictions.

Tóth defined gravitational groundwater flow theory as "Gravity-driven and cross-formational flow of groundwater at spatial and temporal scales that are commensurate with the configuration and dimensions of the natural topographic relief and the human and geologic time scale". Additionally, he defined the groundwater flow system as "a set of flow lines in which any two flow lines adjacent at one point of the flow region remain adjacent through the whole region; they can be intercepted anywhere by an uninterrupted surface across which flow takes place in one direction only." (Tóth, 1963).

The theory has gained widespread acceptance and produced valuable, valid, and logical results. It has been successfully applied globally in countries such as Canada, the USA, Japan, Australia, India, the Netherlands, Switzerland, Sweden, Mexico, and Thailand, as documented by Tóth in 2009, along with numerous other countries in subsequent years.

II. Groundwater Flow Theory: Basic Concepts and Practical Applications

Over the decades, gravitational groundwater flow theory has bifurcated to better illustrate its foundational components (Figure 94). This umbrella theory comprises two sub-theories:

A. The Basic Concepts: The Sub-Theory of the "Hydraulics of Basin-Scale Flow Systems":

1. Flow Patterns in Unit Basins and Their Extension to Complex, Composite Basins:

1.1 The Unit Basin

In basin-scale flow systems, the unit basin serves as a fundamental model to illustrate groundwater flow dynamics, structured around distinct hydraulic regimes that outline groundwater movement across the basin. Three primary regimes: recharge or inflow (R), transfer or throughflow (M), and discharge or outflow (D) define the flow's functional roles, located upslope, adjacent, and downslope relative to the hydraulic midline. In addition to hydraulic head, the flow within these regimes is influenced by regional pore pressure (p), the vertical pressure-gradient, and dynamic pressure increment, which together establish a clear pressure-driven flow pattern. Flow direction varies with each regime: in the recharge (R) regime, groundwater descends from the water table; in the transfer (M) regime, it moves laterally; and in the discharge (D) regime, it ascends. These parameters and pressure patterns combine to create a dynamic yet orderly flow sequence, reflecting the unit basin's basic fluid dynamics.

1.2 The Complex Basin

Owing to the functional relations between boundary conditions and hydraulic head distribution in a flow domain, changes in the geometry of the unit basin modify the patterns of flow and fluid dynamic parameters. Typically, the result is an increase in the complexity of the basic distributions. Regional flow patterns are sensitive to two principal aspects of a **basin's geometry**, namely, the **configuration of the water table** and the relative **depth of the basin**, i.e. its depth-to-width ratio (Tóth, 1963).

In a complex basin, the water table configuration defines flow patterns that, like the basic unit basin, have three distinct flow regimes: recharge, midline, and discharge. However, complex basins exhibit three different orders of flow systems:

- ***Local systems***: Recharge and discharge areas are adjacent, meaning flow paths are short and confined.
- ***Intermediate systems***: These systems lie between local and regional systems, with recharge and discharge areas separated by at least one local flow system but not reaching the basin's main divide or valley bottom.
- ***Regional systems***: These systems link the basin's primary divide and valley bottom (thalweg) hydraulically, covering the longest flow paths and depths.

The depth of flow penetration depends on the local relief and regional slope, allowing flow systems to reach depths over a thousand meters in a uniform rock setting, even with only tens of meters of local relief. With increased flow depth, the spacing between equipotential lines widens, signaling a decrease in flow intensity. This progression from local to regional systems results in longer residence times for water in the deeper regional systems.

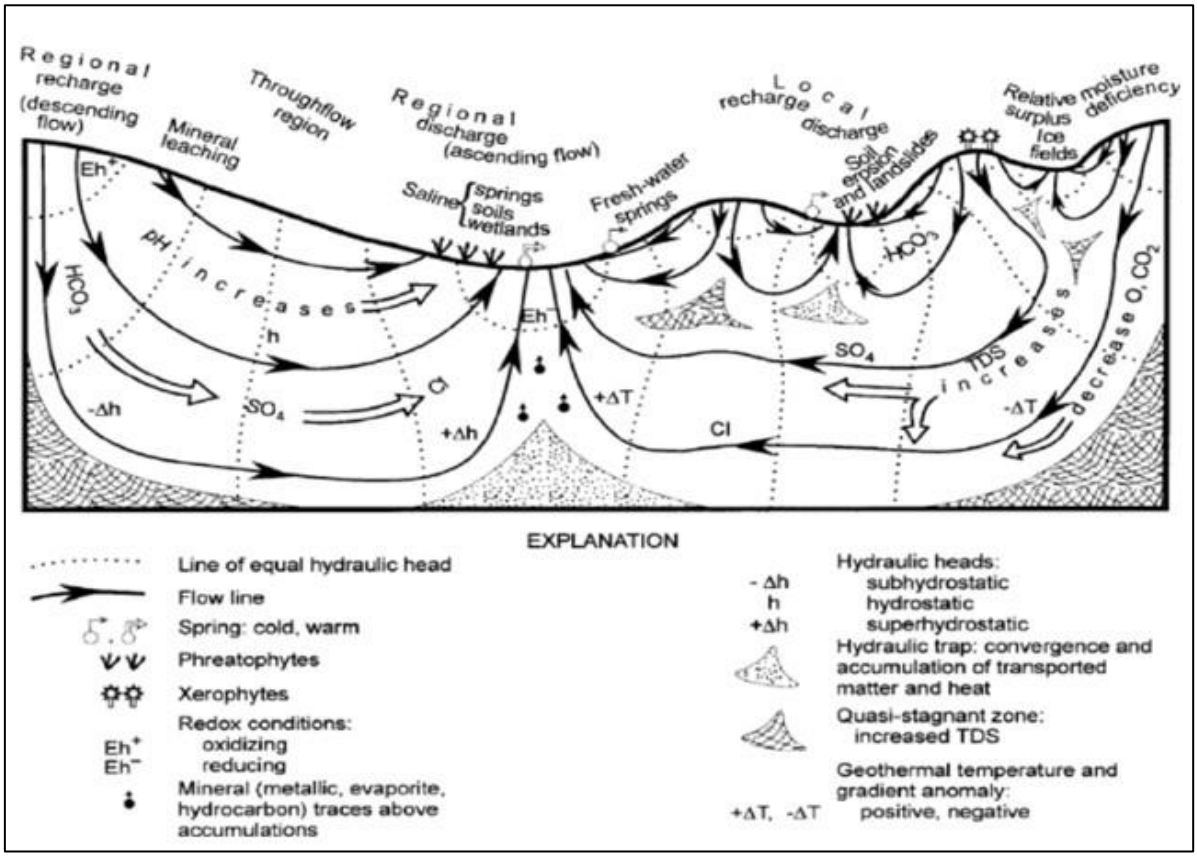


Figure 94 General Groundwater Flow System Conceptual Model

In addition to **basin geometry** (water table relief and depth) and **landforms**, geology, primarily **rock permeability**, is a third major factor shaping basinal groundwater flow patterns. Permeability variations influence how easily water can move through the basin, while the geological structure, including stratification, lenses, faults, and anisotropy, further modifies flow paths. These features can create preferential flow zones or barriers within the system, adding complexity to flow patterns. **Temporal changes in the water table** also affect groundwater flow, as they disrupt equilibrium between boundary conditions and flow regimes, causing shifts in recharge, throughflow, and discharge areas over time. Finally**, hydraulic continuity** across the rock framework allows groundwater, contaminants, and other elements to move throughout the basin. This continuity enables the treatment of the entire system as an interconnected network, where local changes can propagate throughout the basin, influencing both flow patterns and water quality on a regional scale. (Toth J, 2009).

B. The Practical Utilization: The Sub-Theory of the "Geologic Agency of Flow Systems"

The role of groundwater as a geological agent has long been acknowledged across various earth science fields. However, its universal impact wasn't fully appreciated until the 1960s and 1970s, when gravity-driven, basin-scale groundwater flow was recognized as a common underlying cause. Even then, the broad acceptance of groundwater's role in shaping natural systems faced two challenges: (1) the vast diversity of natural phenomena linked to groundwater flow, which often obscured this common cause, and (2) limited knowledge of basin-scale groundwater hydraulics, particularly among specialists in other fields.

Gravity-driven groundwater flow has been shown to generate or influence a wide array of geological and ecological processes, including soil salinization, salt deposits, regional chemical patterns in groundwater, geothermal anomalies, lake eutrophication, types of wetland ecosystems, uranium and sulfide ore deposits, dolomitization, and karst morphology, among others. This realization led to focused studies and models in the 1960s on groundwater flow in small, gravity-driven basins, highlighting the predictable flow patterns within these systems and the natural phenomena associated with different flow segments.

Further research on extensive and deeper basins confirmed that basin-scale groundwater flows operate through hydraulically continuous rock frameworks. These systems exhibit time lags in their response to changing boundary conditions, ranging from human to geological timescales, and are influenced by multiple energy sources. Studies showed that these large-scale flow systems, while distinct in some ways from smaller basin counterparts, also generate diverse geological phenomena.

The recognition of basin-scale groundwater flow across multiple spatial and temporal scales has provided a unified theoretical basis for understanding various natural processes. It has established gravity-driven groundwater flow as a general geological agent, demonstrating this concept through key causes, processes, and observable effects in natural systems.

Two fundamental causes make gravity-driven groundwater a geologic agent: (i) *in-situ* interaction between water and its ambient environment; (ii) transport by flow organized into hierarchical systems of different magnitude. The interaction of water with its surroundings generates various natural processes, products, and conditions. Systematized flow paths, on the other hand, function as sustained mechanisms of distribution of those effects into regular spatial patterns within the basinal flow domain. In basins where groundwater flow is controlled by the topography, the spatial distribution patterns of groundwater's effects are functionally related to identifiable and characteristic segments of the flow systems. Such relations make correlation between cause (groundwater flow) and effect (natural processes, conditions, and phenomena) feasible and verifiable. This is the chief argument for limiting the scope of this discussion to gravity flow (Toth J, 2009).

Three primary types of interactions between groundwater and its hydrogeologic environment have been identified: chemical, physical, and kinetic.

B.1 Chemical Processes

Dissolution is a fundamental process in groundwater chemistry and often marks the first stage in the chemical evolution of water, influencing both gases and solids. Gas dissolution typically occurs within the soil zone, the unsaturated (vadose) zone, and in areas associated with oil and gas deposits. Common dissolved gases in groundwater include nitrogen (N_2), argon (Ar), oxygen (O_2), hydrogen (H_2), helium (He), carbon dioxide (CO_2), ammonia (NH_3), methane (CH_4), and hydrogen sulfide (H_2S). The degree of dissolution depends on mineral solubility, water chemistry (ion concentrations and pH), pressure, and temperature conditions. Highly soluble rocks such as limestone ($CaCO_3$), dolomite ($CaMg(CO_3)_2$), gypsum ($CaSO_4 \cdot 2H_2O$), halite (NaCl), and sylvite (KCl) supply the major ions Ca^{2+}, Mg^{2+}, Na^{+}, K^{+}, Cl^{-}, CO_3^{2-}, and SO_4^{2-} to groundwater. Even silicate and other relatively insoluble rocks can dissolve under specific chemical or thermal conditions, contributing minor and trace elements to the water.

Hydration**:** involves water entering the crystal structure of minerals or bonding to ions in dissolved salts. This process is common in groundwater's chemical evolution and is crucial in mineral weathering, such as transforming anhydrite into gypsum or biotite into vermiculite.

Hydrolysis**:** Breaking down minerals through reaction with water.

***Oxidation–Reduction*:** Altering the oxidation state of elements, often affecting iron, manganese, and sulfur.

Chemical Precipitation: Minerals form solid precipitates as certain ions reach saturation levels.

Base Exchange (Ion Exchange): Swapping of ions between groundwater and surrounding materials, often influencing sodium, calcium, and magnesium levels.

Sulfate Reduction: Sulfates are converted, typically by microbial activity, which can produce hydrogen sulfide.

Concentration of Total Dissolved Solids (TDS)*:* Increasing levels of dissolved minerals through evaporation or other processes.

Concentration by Solution*:* Dissolving more minerals as groundwater flows through soluble rock.

Ultrafiltration by Shale Membranes*:* Filtering of dissolved particles through shale, impacting water composition.

B.2 Physical Processes

The lubrication effect occurs when water infiltrates discontinuities in the rock framework, such as grain surfaces in soils or fractures and fault planes in consolidated rock. This infiltration reduces friction along these surfaces, allowing shear stresses to act more effectively. Consequently, movements can range from minor rearrangements of mineral grains, as seen in compaction, to significant shifts, such as landslides or earthquakes.

Pore-pressure modification involves changes in pore pressure, commonly elevated in discharge areas of groundwater flow systems, which reduce frictional resistance and may lead to shear displacement. Variations in pore pressure, either increases or decreases, can influence geological processes, such as altering reaction rates, gas solubility, and the strength of rocks. These shifts in pore pressure can also affect gas saturation levels in subsurface fluids, impacting rock integrity and altering deformation behavior.

B.3 Kinetic or transport processes

Water transport within flow systems is a fundamental process in groundwater's role as a geological agent. It acts as both a medium for transport and a reactive component in the subsurface environment, contributing to the hydrosphere of the land surface. These flow systems facilitate the gravitational distribution of water, creating distinct moisture conditions between inflow and outflow regions. This process is integral to the hydrologic cycle, influencing the distribution of water bodies,

their chemical characteristics, and the fluctuations of the water table, with significant ecological implications.

The transport of both aqueous and non-aqueous matter through groundwater flow systems is fundamental to subsurface geological processes. Groundwater transports a wide variety of materials, including aqueous solutions of organic and inorganic ions, suspended particulate matter, gases, liquid hydrocarbons, and microorganisms. This transport is crucial for leaching minerals from soils and rocks, delivering nutrients to surface water bodies, forming and redistributing mineral deposits, facilitating the biodegradation of ore and oil accumulations, and concentrating contaminants in favorable subsurface locations.

Heat transport by moving groundwater is a well-established geological process, characterized by water's ability to carry heat due to its specific heat capacity. When a temperature difference exists between the water and its surroundings, heat flows toward the cooler area. The rate of this heat transfer depends on several factors, including the thermodynamic properties of the saturated rock and water, the temperature difference, and the water flow rate. Faster heat exchange reduces the temperature anomaly more quickly.

III. Groundwater Flow Theory: A Fundamental Paradigm Change in Hydrogeology

The "Theory of Regional Groundwater Flow," established sixty years ago, marks a significant paradigm shift in groundwater hydraulics. It transitions from the classical perspective of "pipe flow in confined, or artesian, aquifers," which focuses on direct flow from one outcrop to another, to a more nuanced understanding of "cross-formational water flow in regionally unconfined basin-scale systems."

In this modern paradigm, groundwater movement is seen as flowing from recharge areas where water infiltrates the ground to discharge areas, emphasizing the complex interactions between geological formations. This shift highlights the importance of regional contexts, interconnectedness among various aquifers and geological layers, and the influence of factors such as topography and hydrological processes on groundwater dynamics across larger basinal scales.

While this theory facilitates a broader evaluation of groundwater systems beyond isolated aquifers, there remains a need for clearer definitions regarding terms related to groundwater flow evaluation to interpret complex hydrogeological systems effectively. Discussions among RGFC-IAH

board members have underscored the importance of establishing frameworks for future applications of this theory.

Groundwater flow evaluations at regional scales should incorporate aquifer systems, preferring the term "groundwater basin" over the outdated "artesian basin." Comprehensive assessments require full-groundwater basins for accurate two-dimensional and three-dimensional interpretations, as half-basin assessments can lead to misleading conclusions. Hydraulic continuity is fundamental in evaluating groundwater flow, assuming connectivity across multiple aquifers, aquitards, and faults unless contrary evidence exists. Validating conceptual groundwater flow models with specific field data, numerical simulations, and groundwater flow-related phenomena is crucial. This presentation aims to stimulate discussion on improving the application of regional groundwater flow theory, supported by the National Multidisciplinary Laboratory for Climate Change (Mádl-Szőnyi et al., 2023 Toth J, 2015).

IV. Gravitational groundwater flow system and the science of hydrogeology

Today, hydrogeology is defined as the science and practical application of processes and phenomena arising from the interaction between groundwater and the rock framework. However, its scope and applications have greatly expanded since before the 1960s. At that time, hydrogeology primarily focused on a single objective: sourcing water supplies from underground.

Hydrogeology emerged as a fully-fledged member of the earth sciences within just 30 years, from the late 1950s to the early 1980s, influenced significantly by the concept of gravity-driven groundwater flow systems. Before 1960, the field primarily belonged to geologists, who typically lacked a quantitative understanding of groundwater flow laws or the differential equations that describe them. Meanwhile, hydraulics engineers focused on developing groundwater supplies but struggled with the complexity of geological formations, often simplifying aquifer conditions to permeable or impermeable layers. This rapid conceptual shift was largely driven by the recognition of regional hydraulic continuity within rock formations, which explained groundwater flow as a natural, gravity-influenced system. This development unified hydrogeology and aquifer-well hydraulics, expanding the discipline’s scope to include the interaction of groundwater with large-scale geological structures.

The dual approach to groundwater questions has ancient roots, with two branches developing largely independently until the 1950s. This period marked the beginning of convergence, fueled by scientific curiosity and engineering practicality. Each branch can further be divided into two phases. Initially, explanations for natural water processes were speculative, and groundwater capture methods

were developed through empirical trial and error. Later, however, these explanations evolved, with theories and hypotheses being formulated quantitatively and with mathematical precision (Figure 95).

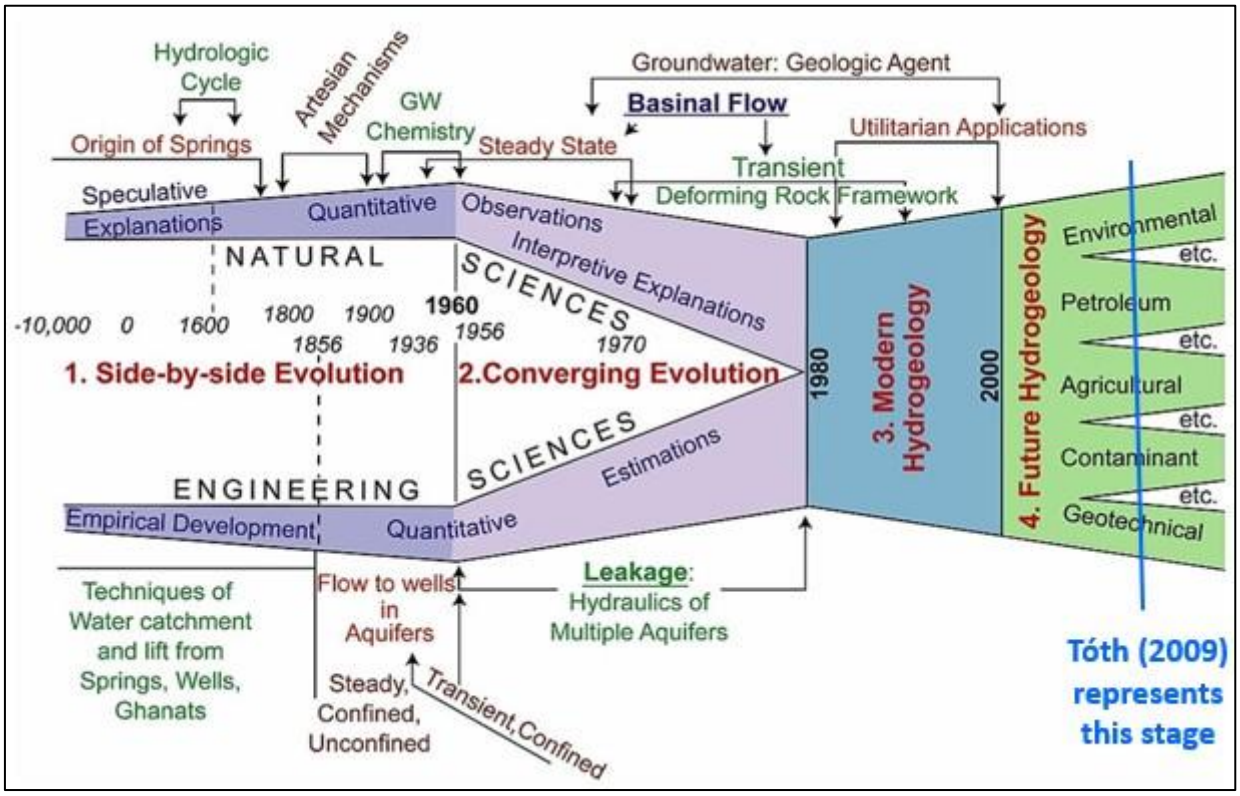


Figure 95 Overview of the Historical Evolution of the Science of Hydrogeology

In the natural sciences branch, speculative explanations about groundwater persisted into the seventeenth century. The earliest recorded inquiries focused on the origin of springs and the hydrologic cycle (Meinzer, 1942). Thinkers from Homer in the eighth century BC to Thales, Plato, Aristotle, Johann Kepler, and René Descartes suggested that springs arose from seawater pressed out of the earth or condensed moisture in caves, dismissing meteoric water as insufficient to sustain rivers. However, Marcus Vitruvius Pollo (86–20 BC) proposed that springs originated from rain infiltration, a theory later supported by Leonardo da Vinci and Bernard Palissy in his 1580 work, Discours admirable de la nature des eaux et fontaines tant naturelles qu'artificielles (Wonderful Discourse on the Nature of Waters and Fountains, both Natural and Artificial).

Quantitative hydrology began in the seventeenth century with Pierre Perrault's rainfall measurements in the Seine basin, showing rainfall vastly exceeded river discharge, findings later confirmed by Edmond Mariotté. Edmund Halley demonstrated that evaporation could explain runoff,

while Jean-Claude La Métherie introduced early concepts of water balance by distinguishing surface runoff from deep infiltration.

The artesian effect, first observed with a well in 1126, was explained in the seventeenth century by Cassini and Vallisnieri, who identified high pressure in confined aquifers as the cause. This understanding laid the groundwork for M. King Hubbert's foundational 'Theory of Ground-Water Motion' (1940), advancing the concept of groundwater basins.

Groundwater chemistry studies beyond practical applications began in the late 19th and early 20th centuries, focusing on classification (e.g., Palmer, 1911; Schoeller, 1935, 1955, 1962) and the factors influencing compositional evolution (e.g., Chebotarev, 1955; Back, 1960).

The first phase of the Engineering Science Branch, lasting until 1856, was focused on practical methods for capturing and lifting water from springs, wells, ghanats, and other subsurface sources. The second phase, marked by Darcy's publication of his law in 1856, spurred significant interest in quantifying groundwater flow and well yields. This led to foundational formulas by Dupuit (1863), Thiem (1906), Theis (1935), Jacob (1940), and Wenzel (1942), which addressed groundwater flow to wells in unconfined and confined aquifers.

In the mid-1950s and 1960s, the idea of absolute impermeability was critically re-examined by both engineers, assessing aquifer and well yields, and geologists, studying groundwater flow in basins. Researchers like Hantush and Jacob (1954), Hantush (1956), and others introduced the concept of leaky aquifers, later expanded into multiple-aquifer systems on a basin scale (Neuman and Witherspoon, 1971, 1972). In natural sciences, Tóth (1962a, 1963) proposed homogeneous unit basins, which Freeze and Witherspoon (1967) later developed into models that considered aquifer and aquitard variations. Field studies and tests (e.g., Geraghty, 1960; Tóth, 1966b; Mifflin, 1968) ultimately confirmed that the rock framework is hydraulically continuous (Tóth, 1995).

The recognition of hydraulic continuity led to the understanding that groundwater flow systems operate across varying spatial and temporal scales (Zijl, 1999), with each scale producing distinct natural processes. This insight unified the view of groundwater as a geologic agent (Tóth, 1999). By around 1980, the convergence of natural and engineering sciences was complete, marking the advent of Modern Hydrogeology. This discipline, now essential to geologic and geotechnical fields, requires both foundational knowledge for broader geological work and specialized expertise, demanding dedicated training and professional focus for hydrogeologists.

Modern hydrogeology rests on two principal paradigms: (i) gravity-driven groundwater flow occurs on a broad spectrum of spatial and temporal scales, and (ii) flowing groundwater is a ubiquitous geologic agent responsible for a broad spectrum of natural processes and phenomena at and to great depths below the surface of the Earth. Now a mature science grounded in both the mathematical rigor of engineering and the creative insight of earth science, hydrogeology is unlikely to experience major conceptual breakthroughs in the near future. Instead, it is expected to further specialize, giving rise to various sub-disciplines such as environmental, contaminant, agricultural, ecological, and petroleum hydrogeology (Figure 95).

V. From Recharge to Discharge: The Study Zone from a Tothian Perspective

V.1 Practical Utilization: Data Projection and Analysis of Primary Indicators

Building on the detailed site description, climatology, geological and structural framework, and water chemistry presented in Part 1, it is now time to briefly summarize these factors and define their relationship to groundwater from a Tóthian perspective to gain further insights into the groundwater flow dynamics in our study area.

A. Surface Indicators of Groundwater

Due to slight differences in the definitions of various indicators related to groundwater characterization, the following terms are briefly explained to facilitate their understanding in the context of the current investigation.(Toth J, 2009)

1. Groundwater and Perennial Surface Water

A surface water body is considered perennial when it remains present year-round, unaffected by seasonal rain or runoff. The portion of stream discharge sustained by groundwater, even during low-flow periods, is termed baseflow. Springs, where water flows directly from the ground, form at locations with adequate hydraulic conductivity, intersecting water tables, topoforms, and soils. Perennial water bodies emerge when this flow is protected from evaporation and nearby plant absorption. In discharge zones, recharge or throughflow processes may also occur, often overlapping with flow systems discharging in other zones. Key indicators of a discharge zone include the permanent presence of water, waterlogging, mud, flooding, and shallow water levels. This indicator is represented by rivers in our case, which run throughout the year, indicating a discharge zone. Additionally, the presence of saline soil (Chott Guaraet et Tarf), situated south of sampling points S14 and S15, acts as a permanent water source.

2. Groundwater Depth

The depth of the groundwater table is important for identifying the hydraulic regime of a groundwater flow system. While groundwater depth serves as a strong indicator, it should be assessed in conjunction with key hydraulic and hydrological characteristics, along with other surface indicators. Shallow groundwater depths are uncommon in recharge zones, whereas in discharge zones, groundwater typically lies at or near the surface. In our case, the depth decreases toward the north, reaching approximately 10 to 30 meters.

3. Groundwater and Soil

Soil is the Earth's surface layer, characterized by distinct properties formed through a combination of factors like material, relief, climate, time, and biota, as defined by Jenny (1994). Soil classification systems typically consider a depth of up to 2 meters and assess soil moisture and temperature regimes in relation to climate conditions. However, these classifications often exclude groundwater's physicochemical properties and effects, which are essential for understanding soil behavior in a regional context and promoting sustainable management. Soil analysis includes taxonomic classification, analytical factors (e.g., pH, salinity, organic matter), and morphological properties (e.g., texture, structure, color), with particular attention to hydromorphic indicators, such as Fe–Mn concretions, that signal redox processes related to soil moisture levels.

4. Groundwater and Vegetation

Globally, plants are categorized as **xerophytes**, which do not rely on groundwater, and **phreatophytes**, which depend heavily on it. However, some plants fall between these groups, depending on groundwater only under specific conditions or as a mix with rainwater. Since local, intermediate, and regional groundwater flow systems can coexist, vegetation may shift its groundwater dependence across these systems, resulting in temporal variations in groundwater usage by volume and quality. Certain vegetation types, recognized as groundwater-dependent ecosystems (GDEs), rely directly on groundwater for their ecosystems.

As mentioned in Part 1, Chapter 1, and considering that plants can adapt to varied conditions, particularly in regions where groundwater availability fluctuates, we can classify the existing vegetation types based on their general dependence on groundwater as follows:

Phreatophytes, including Tamarix (Tarfa), Retama (R'tem), Willows, Junipers, Palm trees, and a variety of fruit trees such as apple, pomegranate, apricot, pear, fig, and olive, as well as Aleppo Pine, Cedar, Holm Oak, Black Pine, Cypress, and Ash, are typically found in discharge zones. These areas have groundwater close to the surface, allowing these deep-rooted plants to access the water

directly. Their presence often indicates regions where groundwater naturally rises or discharges near the surface, supporting a more diverse and dense vegetation structure than in recharge areas.

Xerophytes like Armoise or Chih (Artemisia alba), Guetaf (Atriplex), Salsola, and Jujube (Ziziphus) are indicative of recharge zones. In these areas, water infiltrates deep into the ground and is not readily accessible at shallow depths. Xerophytic plants are highly adapted to dry conditions, able to survive on minimal surface moisture. Their presence suggests that groundwater is recharging beneath them, as they rely primarily on surface water or sporadic rainfall rather than direct groundwater access. This vegetation type characterizes arid and semi-arid landscapes where water conservation is key to survival.

5. Groundwater and Topoforms

Certain topographical features provide the energy needed to drive water movement, influencing the flow patterns and defining regional flow boundaries. According to Tóth's theory, regional relief guides the flow system's direction, with downward flow in elevated areas and upward flow in depressions. However, this flow direction can vary, allowing for both upward and downward movement within systems depending on spatial scale and geomorphological context.

6. Groundwater and Geological Framework

The geological context (Figure 96) influences groundwater presence, flow rate, direction, and physicochemical characteristics, interacting with tectonic activity, surface water, and climate. Variations in groundwater flow (vertical, horizontal, or inclined) are mainly due to media permeability, water table position, and basement rock depth. Rock types can generate different soil and vegetation types, or conversely, similar soils and vegetation may arise from various rock types, as determined by the geological framework, groundwater flow systems, and climate. Groundwater shapes landscapes, but relying solely on surface rock type for regional groundwater flow analysis is oversimplified and was not applied here.

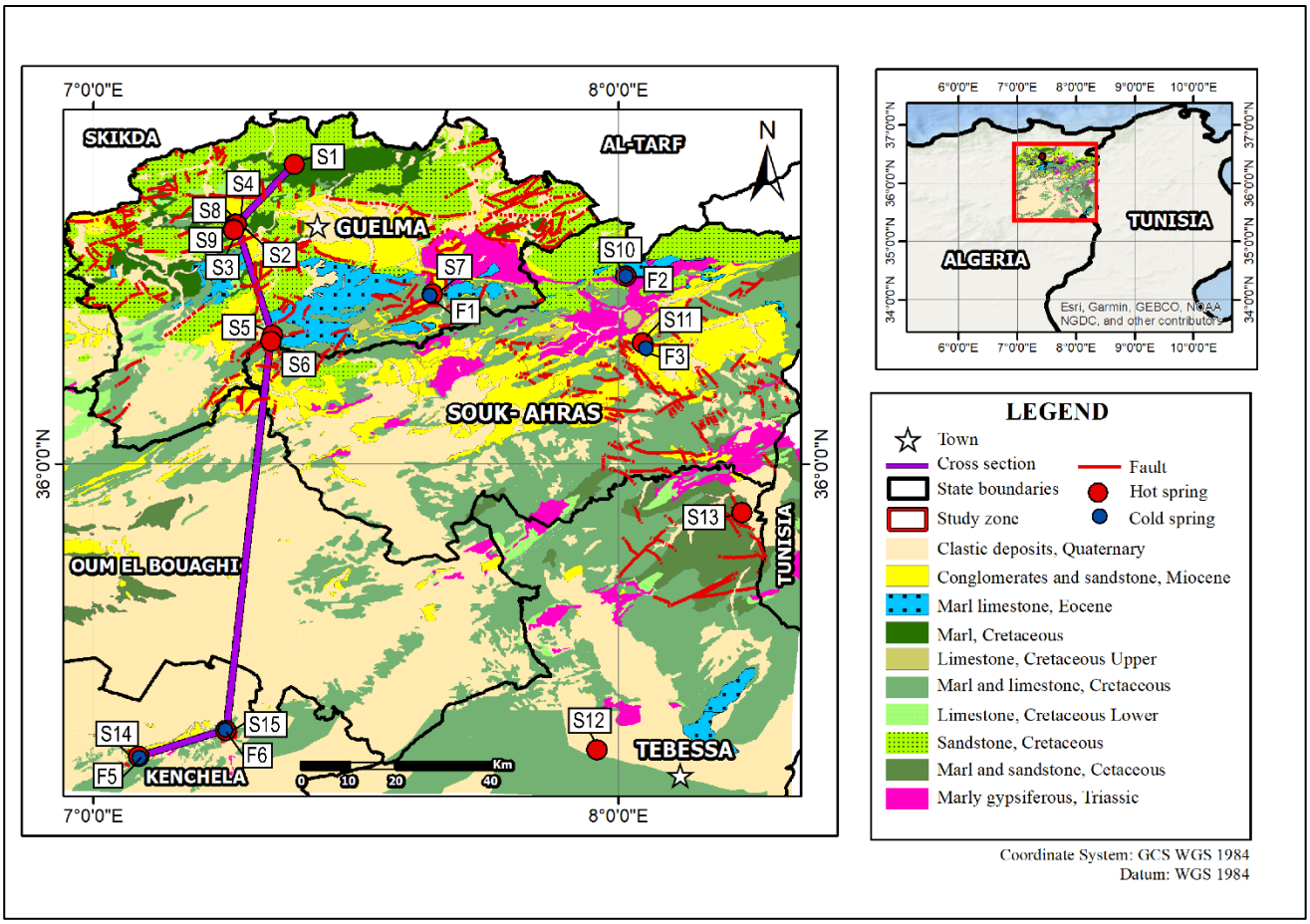


Figure 96 Surface Geological Framework of The Study Area Showing Spring Locations, Major Faults, and The Position of the Cross-Section (Figure 100)

7. Groundwater and Climate

Climate dictates the regional water availability and its distribution, influenced by air temperature, precipitation, and evaporation rates, along with hydrogeological elements. Given the extensive study area and scale of climatic data, climate serves as a regional reference to interpret surface indicators, such as the persistent presence of perennial water bodies even in arid conditions.

8. Discharge, Throughflow, and Recharge Zones

Groundwater reaches its endpoint in discharge zones, where it surfaces or lies close to the surface. These zones are marked by key attributes: (i) a positive potential slope, (ii) a lower-lying position, (iii) water with a distinct, non-local physicochemical composition, and (iv) a unique temperature profile. The manifestation of these characteristics varies based on a range of hydrogeological factors, including air temperature, terrain slope, rock composition and permeability, vegetation, and land use.

Natural features indicating groundwater discharge, either directly or diffusely onto the surface, include perennial water bodies, base flow, springs, geysers, marshes, quicksand areas, salt deposits, landslides, shallow water tables, river valleys, swamps, eutrophic waters, topographic depressions, soil with excess moisture, hydrophilic and halophytic vegetation. Key indicators of a discharge zone are a permanent presence of water, waterlogging, mud, flooding, and shallow water table levels.

In recharge zones, the water table varies seasonally and is usually deep, often with no permanent surface water depending on the area's geological, climatic, and ecological conditions, such as basement rock depth, transmissive rocks, rainfall, and soil-vegetation types. Ideally, the study area would include discharge zones as well. Throughflow zones lie between recharge and discharge zones and lack clear surface indicators typical of either zone.

B. Chemical Indicators

Regional groundwater flow exerts various notable and observable impacts on the chemistry and mineral composition of rocks and water both at and below the surface. Generally, as flow progresses and depth increases, several transformations occur (Figure 97): total dissolved solids (TDS) levels rise; anion types shift from bicarbonate to sulfate, eventually reaching chloride; cation composition transitions from calcium–magnesium to calcium–sodium, then sodium–calcium, and finally to sodium. Concurrently, carbon dioxide and free oxygen levels diminish, redox potential shifts from positive to negative, and pH gradually changes from acidic to alkaline. Partly due to these conditions, mineral dissolution and leaching are prevalent in recharge areas, while deposition and accumulation are characteristic of discharge zones. Salts like $NaSO_4$, NaCl, $Ca(SO_4)_2$, and $CaCO_3$ carried to the surface by discharging groundwater can remain in soils, leading to salinization, or accumulate to form commercially valuable deposits, such as sodium sulfate, halite, gypsum, and calcareous tufa. Groundwater's chemical processes naturally result in the weathering, dissolution, cementation, and diagenesis of various rocks and minerals, as reported in (SALAMA et al., 2013).

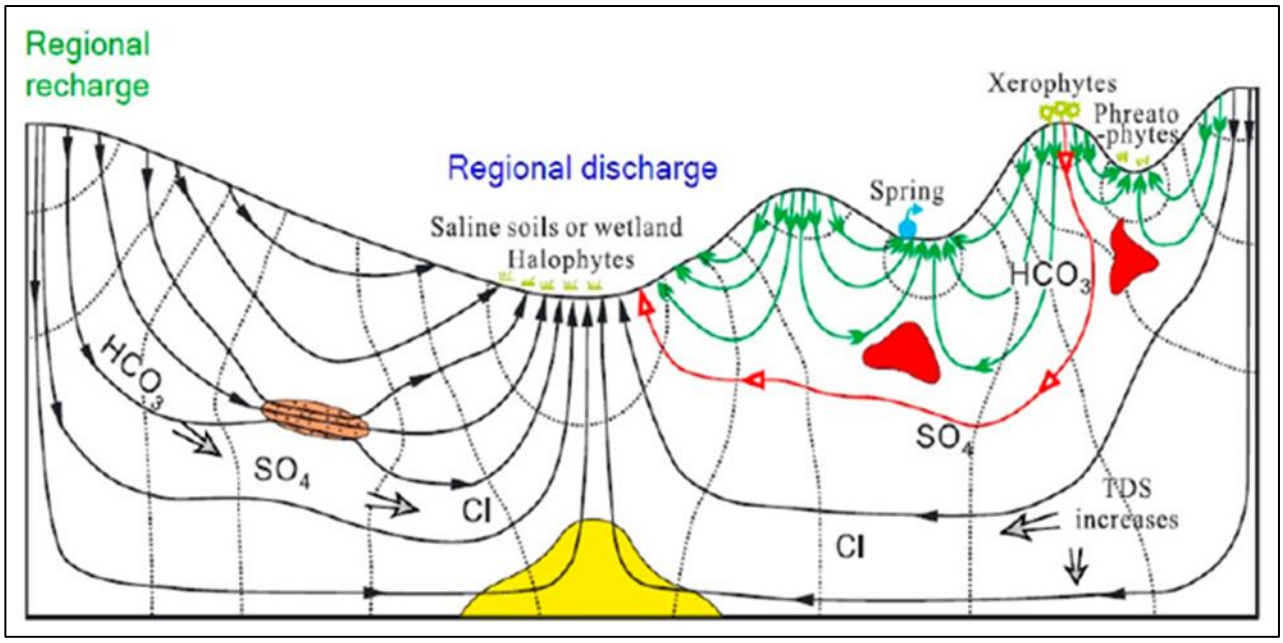


Figure 97 The Schematic Diagram of Groundwater Flow Systems Illustrates Various Processes and Manifestations. The Flow Order, Local, Intermediate, and Regional, is represented by Green, Red, and Black Flowlines, respectively. The two Red Areas Signify Internal Water Traps, While the Yellow Area Indicates a Basin Floor. The Scale is determined by the geological Framework

.

1. Groundwater Facies

In the study area, water temperature among sampled sites varies from 18.7°C to 94.7°C, recorded at F3 and S2, respectively. Sample S2 is noted as one of the hottest spring waters globally, second only to Icelandic geysers, which could reach up to 98°C according to various authors (Dib H, 2008). As anticipated, thermal groundwater samples tend to have higher total dissolved solids (TDS) compared to those from cold springs.

A Piper diagram (Figure 98) was used to examine the relationship between groundwater chemistry and local rock formations. According to Tóth (1995, 2009), anion composition reflects groundwater residence time, as water chemistry evolves from bicarbonate (HCO_3^-) to sulfate (SO_4^{2-}) and eventually to chloride (Cl^-), the latter often resembling seawater composition (SALAMA et al., 2013).

.

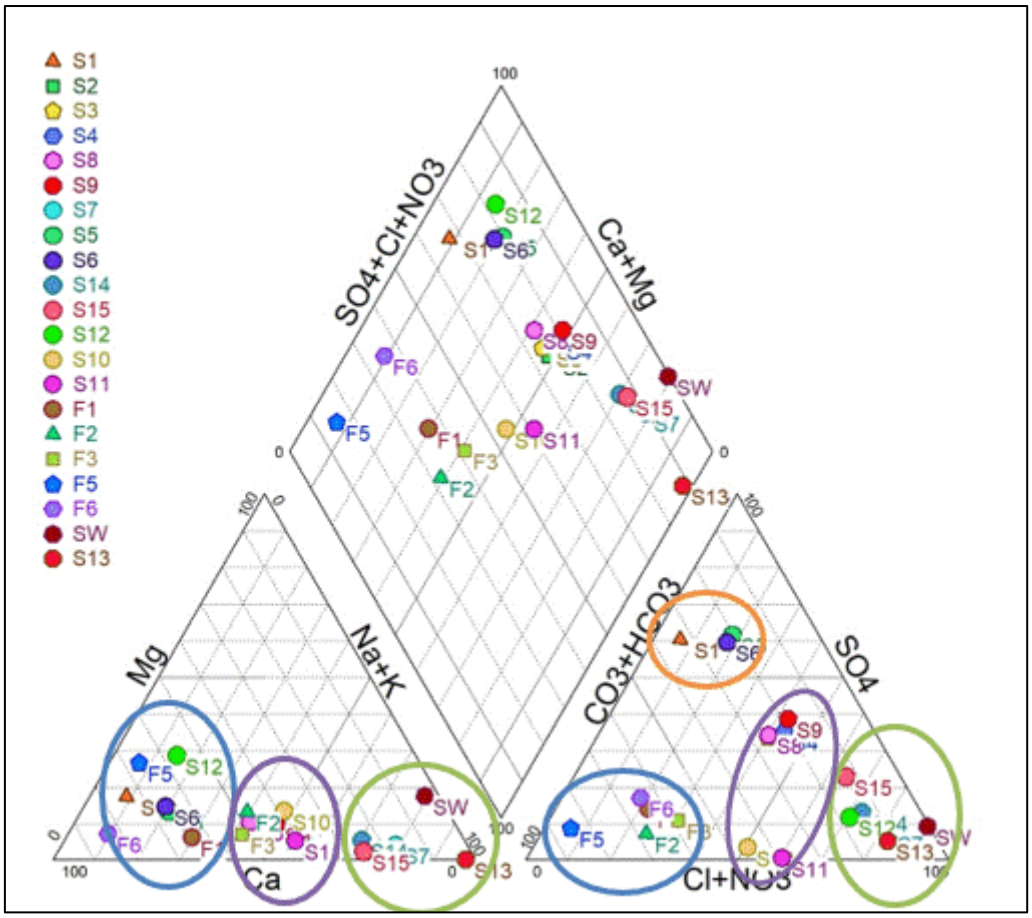


Figure 98. Hydrochemical facies classification using the Piper Diagram

The cation triangle provides insight into the types of rocks the water has interacted with. Group 1, comprising samples S1, S5, S6, S12, F1, F5, and F6, represents a calcium-dominant type, likely influenced by limestone and marl formations. Group 2 includes samples S2, S3, S4, S9, S10, S11, S15, F2, and F3, which originate from a mix of Triassic and Paleozoic rock formations, suggesting a varied mineral source. Group 3, characterized by sodium-potassium dominance (samples S7, S13, S14, S15), shows a composition resembling seawater (SW in Figure 98), indicating interaction with evaporitic formations and more chemically evolved groundwaters.

Following Tóth's criteria, the anion triangle was further subdivided based on inferred residence times:

- ***Subgroup 1***: Younger, cooler, bicarbonate-rich waters represented by samples F1, F2, F3, F5, and F6, indicating recent recharge.
- ***Subgroup 2***: Slightly older sulfate-dominant waters (S1, S5, S6).

- ***Subgroup 3***: Older waters, with higher sulfate and chloride concentrations, include samples S2, S3, S4, S9, and S8, as well as S10 and S11, which exhibit longer residence times.
- ***Subgroup 4***: Chloride-dominant and considered the oldest waters, represented by S7, S13, S14, and S15.

Notably, sample S12, despite its prolonged residence time, appears to have remained relatively shallow (see Geothermometry section in part 1, chapter five), resulting in elevated nitrate (333.22 mg/L) and undetectable lithium levels.

The Piper diagram (Figure 98) for all samples indicates two primary classifications: **Group A**, consisting of chloride-sodium facies with elevated TDS and temperature, and **Group B**, defined by bicarbonate-calcium facies with lower TDS and temperature. These distinctions suggest varying groundwater flow hierarchies, highlighting the influence of the geological formations encountered along each flow path and distinguishing multiple groundwater flow systems. Additionally, **Group C** includes waters with intermediate characteristics, tending toward a sulfate composition.

2. Geochemical Parameters

To avoid duplication in presenting results and their interpretations, the discussions on the saturation index, stable isotopes, ionic ratios, and geothermometry (including geothermometers, index of maturity, ternary diagrams, and the estimation of temperature and reservoir depth) are consolidated in Part 1, Chapter five.

V.2 Innovations in Groundwater Analysis

Tóth's approach employs a nested multistage flow system alongside maps of discharge and recharge, providing a more nuanced understanding of groundwater systems. This methodology allows for a comprehensive analysis of hydraulic head variations across multiple depths and locations, enhancing our understanding of groundwater dynamics. Unlike traditional methods, Tóth does not rely on simple piezometric maps, which may oversimplify groundwater behavior.

Additionally, Tóth critiques classical hydrogeological concepts, particularly mixing and water balance, suggesting that they require a more nuanced understanding. For mixing, Tóth’s model demonstrates the hierarchy of groundwater flow systems: local, intermediate, and regional, which inherently shapes how waters interact. While Tóth acknowledges that groundwater interacts with surface water bodies, such as rivers and lakes, which plays a critical role in hydrological processes and ecosystem health, he argues that deeper and shallower groundwater mixing is more constrained.

Geological barriers and differences in hydraulic conditions limit the degree of interaction between deep and shallow groundwater, leading to a more stratified system with localized exchanges.

Regarding the water balance concept, Tóth finds the classical approach too simplistic and instead proposes a 3-D framework that captures the multi-directional movement of groundwater within a system. His perspective emphasizes the complex interplay between groundwater and surface water, noting that recharge areas provide water that moves both horizontally and vertically through different geological layers, eventually discharging into surface water systems like rivers and lakes. This multi-dimensional balance is essential for understanding both water quantity and quality, highlighting the need for sustainable management practices. Tóth's approach underlines the interconnected nature of these water systems, essential to preserving ecological health and meeting human demands. Statistical methods, in this framework, serve not as conclusive proofs but as tools for cross-checking findings, adding depth to the analysis of groundwater systems.

A. Influence of Faults

After discussing the Surface Indicators of Groundwater and their relationship to the physical characteristics of the study area, we can observe that these indicators often reflect the underlying geological processes, including the influence of faults.

A fault is a fracture or zone of fractures caused by the movement of rock blocks relative to each other along its generally planar and parallel surfaces. Movement along these opposite surfaces can occur repeatedly throughout a region's geological history. Faults often create breaks in permeability, potentially influencing the flow of groundwater or formation fluids by acting as barriers or conduits within the subsurface. Two fundamental hydraulic types of faults are briefly noted: barrier faults and conduit faults.

A **barrier fault** can act as an impermeable boundary and is often modeled this way. However, faults rarely achieve complete impermeability, as true impermeable conditions are mostly theoretical and uncommon in natural systems. Assuming absolute impermeability in faults may lead to misinterpretations of basin flow patterns and groundwater dynamics over time. The barrier effect of a fault on basin flow can diminish due to changes in permeability, which may be caused by mechanical or chemical alterations within the fault, the dissolution and removal of gouge material by fluids, or shifts in the relative positions of aquifers and confining layers on either side of the fault.

Barrier faults can influence groundwater flow in two main ways:

- *Compartmentalization*: Barrier faults divide the flow area into separate sections, where each section has its own flow conditions. Vertical or steeply angled barrier faults create distinct basins side-by-side with reduced horizontal reach (Figure 99. C)
- *Hydraulic Sheltering*: Barrier faults also create areas of limited or "quasi-stagnant" flow, especially beneath the footwall. This effect intensifies as the fault's dip decreases and is strongest beneath horizontal faults, leading to increased sheltered water volumes (Figure 99. b).

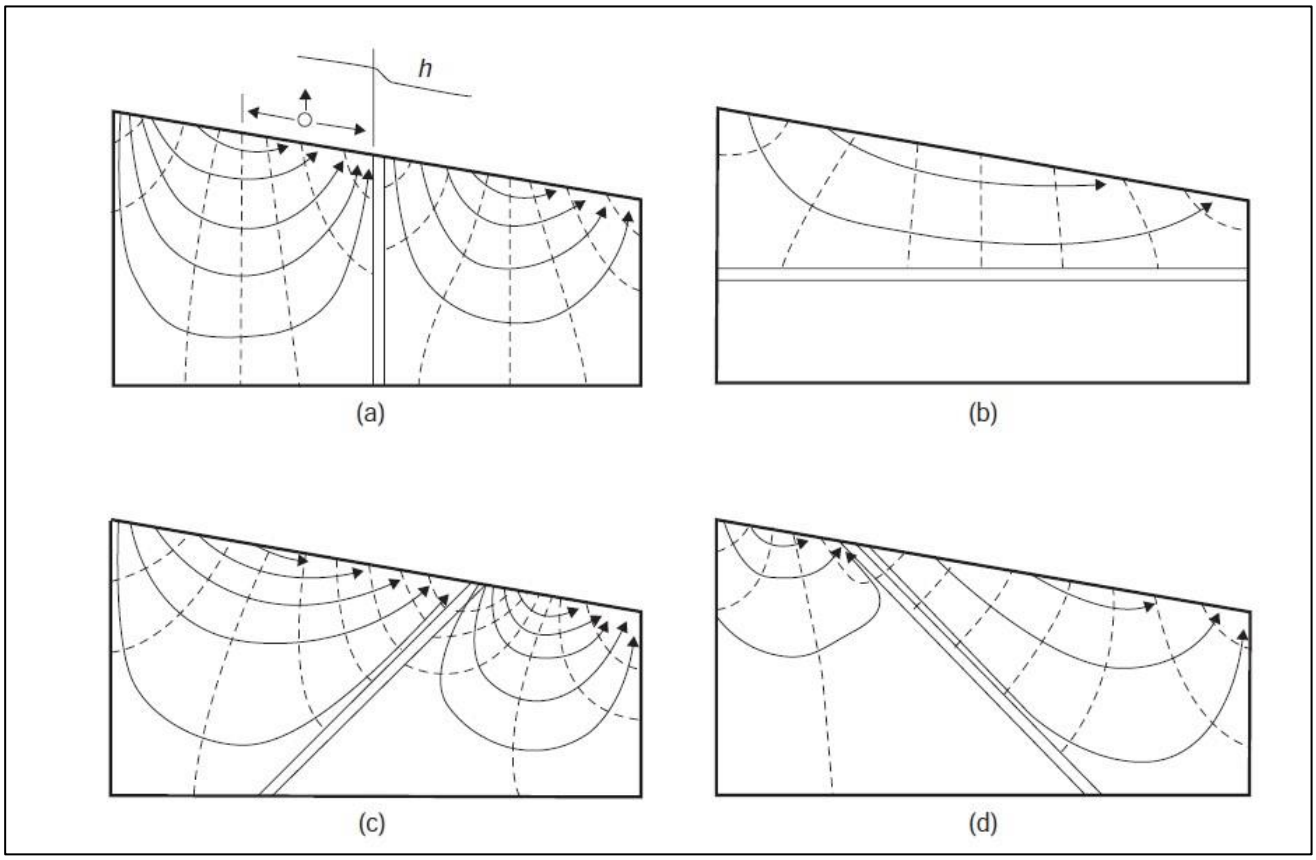


Figure 99 Effects of Barrier Fault on Groundwater Flow Patterns in the Unit Basin:(a) vertical fault, (b) horizontal fault, (c) fault dipping opposite to the direction of regional flow, (d) fault dipping in the direction of regional flow (Toth J, 2009)

A fault is considered a **hydraulic conduit** (Figure 100) if it facilitates water flow through it. Two primary types of conduit faults are distinguished based on the flow path's relative direction: a *conductive conduit fault* (Figure 100. a, b), which allows fluid to move along the fault, and a *barrier conduit fault* (Figure 100. c, d), which directs flow across the fault.

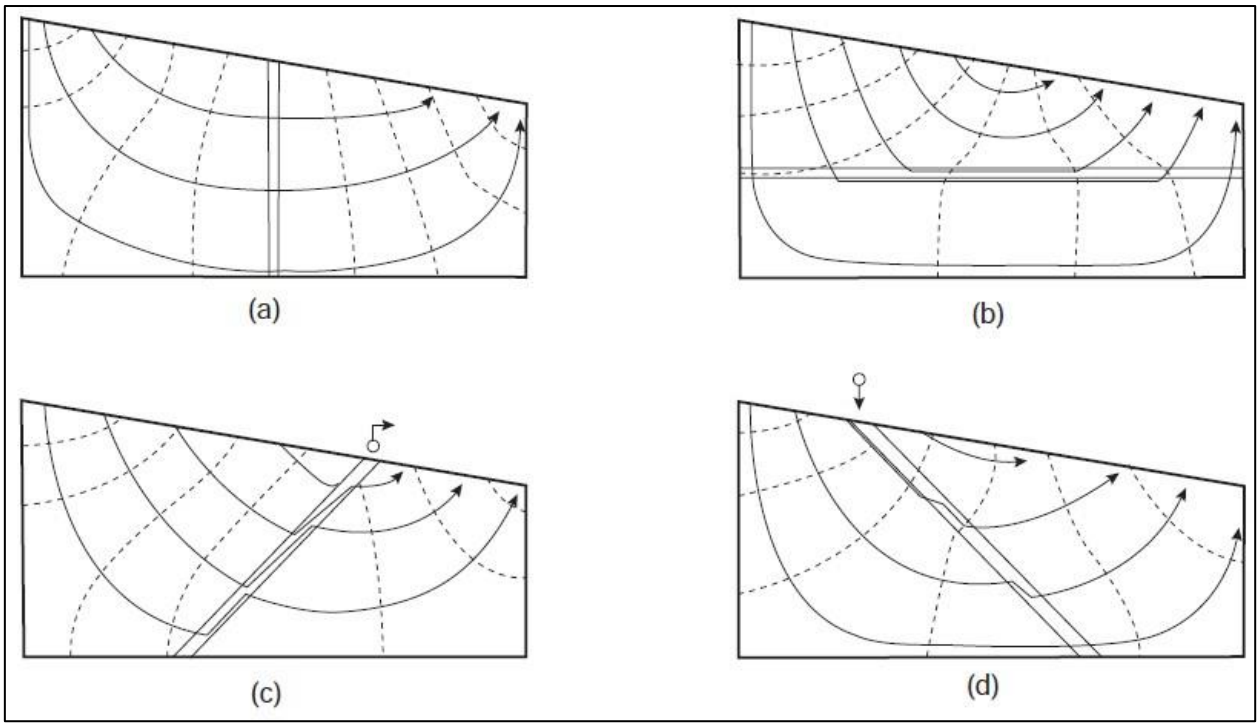


Figure 100 Effect of Faults on Groundwater Flow Patterns in the Unit Basin : (a) vertical fault, (b) horizontal fault, (c) fault dipping opposite to the direction of regional flow, (d) fault dipping in the direction of regional flow (Toth J, 2009).

In the study area, the alignment of springs along fault lines suggests that these features may act as conductive conduit faults and fault springs. This indicates that the faults facilitate groundwater flow by serving as pathways for deeper groundwater to ascend to the surface. When these faults intersect aquifers or allow pressurized water from deeper geological layers to migrate upward, fault springs are often formed at these discharge points.

B. Conceptual Model

The initial conceptual model of groundwater flow systems (Figure 101) requires a foundational geological framework, developed through a hydrogeological cross-section informed by exposed formations (Figure 101) and key references (Bencharef et al., 2022; Hadji, 2013; Nosjean et al., 2020). These publications provide essential details on formation thicknesses and lithological descriptions that characterize the primary subsurface rock structure. Complementary aspects, including water chemistry and geothermal response, were also incorporated. Cold water samples, with their relatively low mineral content, suggest shallow, short-path flow paths, aligning with Tóthian concepts that associate lower chemical concentrations with limited depths and reduced residence times in regional flow systems.

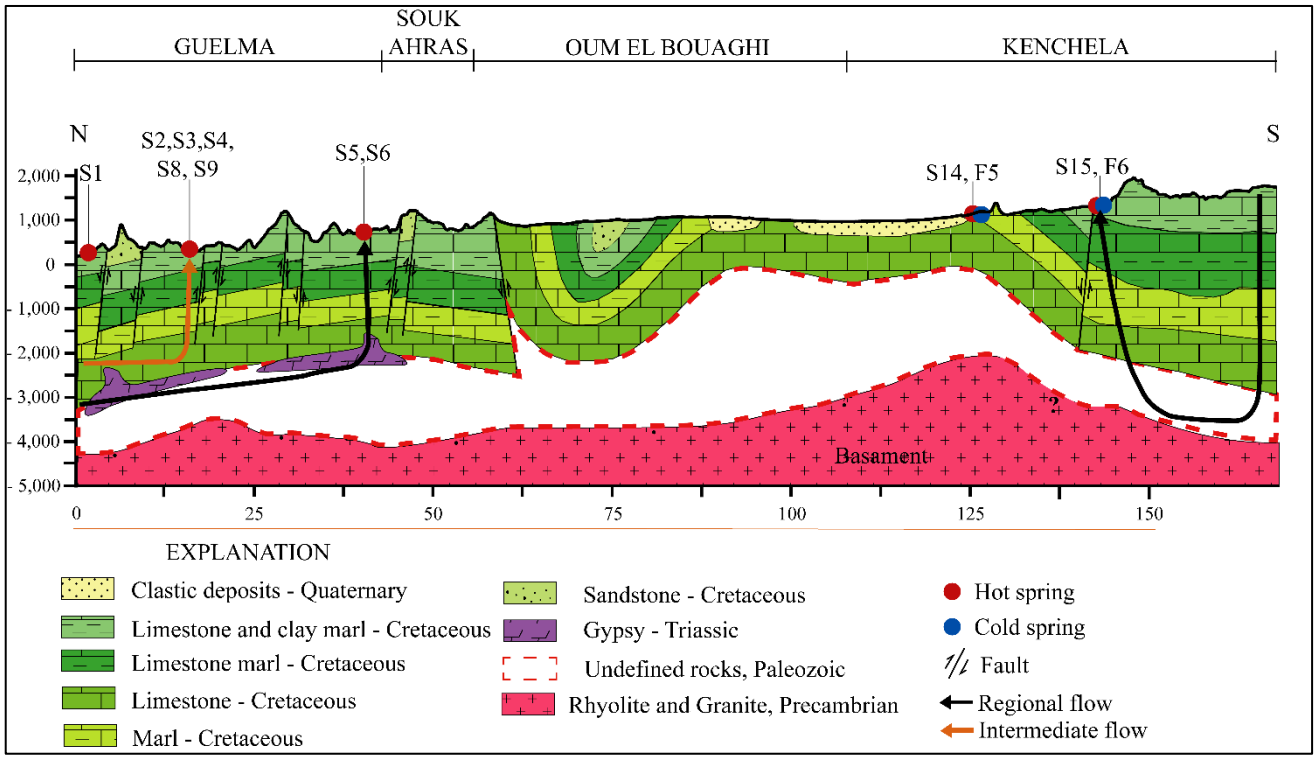


Figure 101 N - S Cross-Section of the Region Illustrating the Hierarchical Flow Systems (credit by Tatiana Aguilar Castillo)

On a regional scale, Figure 101 illustrates a northwest-oriented groundwater flow, with an approximate pathway mapped to identify recharge conditions, throughflow, and discharge zones. The hierarchical flow system, as established by Tóth (1963, 2009), served as a reference framework, supporting a logical classification of the observed data. To deepen our understanding of the hydrogeological dynamics in the region, it is essential to integrate diverse information, including geomorphology (topographic forms), vegetation, soil, climate, stratigraphy, groundwater hydrology, water chemistry (reflecting water-rock interactions), and potential human influences. This conceptual analysis points to the need for a numerical groundwater flow model, although developing such a model is beyond the scope of this work.

Surface features like perennial rivers are key indicators of groundwater discharge zones, as noted by Kachadourian-Marras et al.(2020). Similarly, the presence of saline soils, such as those at Chott Guaraet et Tarf, north of sampling sites S14 and S15, points to a continuous groundwater supply. Soil conditions also reflect groundwater dynamics; for example, vegetation influenced by edaphic factors generally corresponds to depths of about 2 meters. These landscape characteristics affect the direction and energy of groundwater movement, supporting Tóth's theory that topography

governs flow systems, descending in high-relief areas and ascending in low-lying depressions (Kachadourian-Marras et al., 2020).

Vegetation patterns offer further clues: xerophytes, with deep roots, rely on groundwater, while phyreatophyte vegetation often marks discharge areas, as seen at sites S14 and S15. Conversely, S1 and S2 exhibit perennial vegetation, hinting at a shallow water table typical of intermediate or regional discharge zones. In recharge areas, water tables are generally deeper, whereas in discharge zones they can be as shallow as 10–30 meters (Tóth, 2009). The geological setting also plays an important role in shaping groundwater flow, affecting both its flow dynamics and chemical composition, and is further modulated by tectonics, climate, and surface water interactions. In this study, thermal and cold-water circulation was distinguished based on chemical composition and geothermal characteristics.

Cold groundwater, with its low mineral content, typically indicates shallow and short flow paths. In contrast, thermal waters reflect deeper circulation through geological strata, acquiring unique chemical and thermal features along the way. Their geothermal characteristics reveal interactions with deeper geological structures that influence their mineral makeup. This is further supported by the Piper diagram, which shows a strong correlation between water types and specific lithologies in the subsurface, reinforcing the idea that groundwater flow systems are shaped not just by recharge and discharge zones, but also by depth-driven geochemical evolution.

Altogether, the conceptual model developed here synthesizes geological, hydrological, and chemical evidence to describe the movement of cold and thermal groundwater in northeastern Algeria. It underscores the complexity of the system, showing how topography, rock formations, and water chemistry together determine the locations and nature of recharge, flow, and discharge zones

VI. Conclusion

By applying Tóth's framework, which emphasizes the interactions between recharge and discharge zones within regional groundwater flow systems, this research sheds light on the hydrogeological processes influencing the study area. Despite the challenges posed by data limitations and an evolving understanding of the theory, these insights underscore the need for further research to fully leverage the framework’s potential.

The hydrochemical classification of water samples reveals four distinct subgroups, each corresponding to varying residence times and flow path lengths.

- Subgroup 1: (F1, F2, F3, F5, F6, S12): Younger bicarbonate-rich waters associated with recent recharge, indicative of local flow systems.

- Subgroup 2: (S1, S5, S6): Slightly older sulfate-dominant waters, representing intermediate flow systems where mineral interactions moderately influence composition.

- Subgroup 3: (S2, S3, S4, S8, S9, S10, S11): Waters with higher sulfate and chloride concentrations, suggesting advanced mineralization typical of regional flow systems with longer residence times.

- Subgroup 4: (S7, S13, S14, S15): Chloride-dominant waters with the longest flow paths, reflecting the oldest waters in regional flow systems.

To deepen our understanding of these dynamics, future work should include numerical simulations based on the Tóthian model to better represent groundwater flow patterns and enhance data accuracy. This approach will support the "how" of flow systems, translating theory into actionable insights for effective groundwater management. This study not only identifies recharge and discharge zones but also lays the groundwork for an integrated approach to regional water resource management, reinforcing the Tóthian theory's value in creating sustainable groundwater management practices.

General Conclusion

General Conclusion

This study investigated the hydrogeological and hydrochemical characteristics of thermo-mineral springs in the northeastern regions of Algeria, specifically focusing on Guelma, Souk Ahras, Tebessa, and Khenchela. It revealed significant insights into the interconnectedness of these springs and their regional variability. By employing classical methods in hydrogeology alongside modern frameworks such as Toth's flow system theory, we established a comprehensive understanding of the origin, circulation, and emergence conditions of these thermal waters.

The study region, located within Algeria's Tellian Atlas and Saharian Atlas, encompasses Guelma, Souk Ahras, Tebessa, and Khenchela, presenting a varied topography that significantly influences groundwater dynamics. Guelma's landscape is dominated by mountainous reliefs, plains, and limestone peaks, providing diverse infiltration zones and potential aquifer recharge areas. Souk Ahras features rugged terrain, with the Medjerda mountain range in the north and high plains to the south, where groundwater storage and flow are likely influenced by this structural contrast. In Tebessa, the pleated mountains in the north and the Saharan plateau in the south indicate a transition from elevated, structurally complex zones to flat, potentially expansive aquifer systems. Khenchela, characterized by the Aures Mountains and extensive high plains, has a landscape that includes substantial groundwater discharge areas like chotts and sandy soils in the south, which may act as natural discharge zones. This complex physiography establishes a range of hydrogeological conditions, from recharge areas to natural outflows, highlighting the interconnected hydrothermal systems across the region.

The semi-arid climate across Guelma, Souk Ahras, Tebessa, and Khenchela creates seasonal water availability challenges. Winter rainfall enables vital aquifer recharge, especially during the extended humid season, while high summer evapotranspiration leads to significant water deficits. Effective water management is essential to harness seasonal recharge and address water scarcity during dry periods.

The hydrogeological study reveals significant similarities and connectivity across the aquifers of Guelma, Souk Ahras, Khenchela, and Tebessa. Shared geological formations, such as permeable karstic limestones and marly-calcareous rocks, play a vital role in groundwater storage and flow. Triassic evaporitic layers, coupled with tectonic fault activity, contribute to mineral-rich thermal springs. The prevalence of sodium chloride waters, shaped by interaction with evaporitic formations, underscores a consistent lithological influence on groundwater chemistry. These findings highlight

the need for a regional groundwater management approach to enhance water resource sustainability across the interconnected aquifers in the study area.

The hydrochemical and isotopic analysis reveals distinct water types shaped by interactions with geological formations, geothermal processes, and lithological controls across the study area. Sodium chloride, calcium sulfate, and bicarbonate waters reflect varying depths and mineral influences, while isotopic data support meteoric origins. Thermal waters show temperature-dependent mineral solubility, and geothermometric estimates highlight cation exchange and mineral equilibrium dynamics. Sample S13's high salinity and stability of cation ratios underscore its advanced geochemical evolution, while potential contamination concerns emphasize the need for water quality assessments. Overall, the region's groundwater systems exhibit complex interactions driven by lithology, chemistry, and temperature

The Tóthian framework of groundwater flow, a global theory integrating various factors that create an interconnected system, provides a rational and comprehensive approach to understanding regional hydrogeological processes. While its application offers insights into the recharge-discharge dynamics within the study area, limitations in data and evolving theoretical understanding hinder its full implementation at this scale. Given the potential of the framework to yield valuable insights into groundwater behavior, it is recommended to deepen our knowledge of the Tóthian theory to apply it accurately. This would support a clearer understanding of groundwater functioning and contribute to more effective management of this critical resource.

References

Ahmad, M., Akram, W., Ahmad, N., Tasneem, M. A., Rafiq, M., & Latif, Z. (2002). Assessment of reservoir temperatures of thermal springs of the northern areas of Pakistan by chemical and isotope geothermometry. *Geothermics*, *31*(5), 613–631. https://doi.org/10.1016/S0375-6505(02)00009-3

Allan Freeze, R., & Cherry, J. A. (1979). *GROUNDWATER* (Vol. 07632). Prentice-Hall. Inc, Englewood Cliffs, New Jersey.

ANDI. (2013). *Wilaya de Khenchela, rapport de l'agence nationale du developpement des investissements*.

Angert Alon, C. C. D. D. D. J. (2004). Kinetic 17O effects in the hydrologic cycle: Indirect evidence and implications. *Geochimica et Cosmochimica Acta*.

APHA. (2005). *Standard methods for the examination of water and wastewater (21st edi.). American Public Health Association, Washington, USA.*

Appelo, C. A. J., & Postma, D. (2004). Geochemistry, groundwater and pollution, second edition. *Geochemistry, Groundwater and Pollution, Second Edition*, 1–649. https://doi.org/10.1201/9781439833544/GEOCHEMISTRY-GROUNDWATER-POLLUTION-DIEKE-POSTMA-APPELO/RIGHTS-AND-PERMISSIONS

Arnórsson, S. (1983). Chemical equilibria in icelandic geothermal systems—Implications for chemical geothermometry investigations. *Geothermics*, *12*(2–3), 119–128. https://doi.org/10.1016/0375-6505(83)90022-6

Arnorsson S. (2000). *Isotopic and Chemical Techniques in Geothermal Exploration, Development and Use: Sampling Methods, Data Handling, Interpretation*. INTERNATIONAL ATOMIC ENERGY AGENCY. https://www.iaea.org/publications/5733/isotopic-and-chemical-techniques-in-geothermal-exploration-development-and-use-sampling-methods-data-handling-interpretation-edited-by-stefan-arnorsson

Arnorsson, S., Gunnlaugsson E, & Savavrsson, H. (1982). The chemistry of geothermal waters in Iceland. III. Chemical geothermometry in geothermal investigations. *Geochimica et Cosmochimica Acta*, *47*, 567–577.

Askri, H. , Belmecheri, A. , Benrabah, B. , Boudjema, A., Boumendjel K., Daoudi, M., Terkmani, M., & et al. (1993). *Geology of Algeria. Contribution from SONATRACH Exploration Division. Research and Development Centre and Petroleum Engineering and Development Division (SCHLUMBERGER WEC SONATRACH).*

Athamena, M. (2006). *Étude des ressources thermales de l'ensemble allochtone sud sétifien*. http://eprints.univ-batna2.dz/807/1/gha%20Athamena%20Malika.pdf

Bagnouls, F., & Gaussen, H. (1957). Les climats biologiques et leur classification. *Annales de Géographie*, *66*(355), 193–220. https://doi.org/10.3406/GEO.1957.18273

Banton, O., Bangoy, L., Chevalier, S., & Houenou, P. (1997). *Hydrogéologie: multiscience environnementale des eaux souterraines*. https://pascal-francis.inist.fr/vibad/index.php?action=getRecordDetail&idt=6241402

Barkat, A., Bouaicha, F., Mester, T., Debabeche, M., & Szabó, G. (2022). Assessment of Spatial Distribution and Temporal Variations of the Phreatic Groundwater Level Using Geostatistical Modelling: The Case of Oued Souf Valley—Southern East of Algeria. *Water (Switzerland)*, *14*(9). https://doi.org/10.3390/w14091415

Bayou, Y., Abtout, A., Renaut, R. A., Bouyahiaoui, B., Maouche, S., Vatankhah, S., & Berguig, M. C. (2023). The northeastern Algeria hydrothermal system: gravimetric data and structural implication. *Geothermal Energy*, *11*(1). https://doi.org/10.1186/s40517-023-00258-2

Bekkouche mohamed faouzi. (2016). *CARACTERISTIQUES HYDROCHIMIQUES DES SOURCES THERMALES DE L'EXTREME NORD-EST ALGERIEN* [These de doctorat en sciences]. BADJI MOKHTAR-ANNABA UNIVERSITY.

Belhai, M., Nishijima, J., Fujimitsu, Y., & Zohra Bouchareb-Haouchine, F. (2015). Fluid geochemistry of the northern part of Algeria View project groundwater issue including exploration View project Geology, Geothermometry, Isotopes and Gas Chemistry of the Northern Algerian Geothermal System. *Proceedings World Geothermal Congress*, 19–25. https://doi.org/10.13140/RG.2.1.2737.4248

Benaabidate, L. (2000). *Caractérisation du bassin versant de Sebou: hydrogéologie, qualité des eaux et géochimie des sources thermales. These de doctorat en sciences de la terre, Univ. Sidi Mohamed Ben Abdellah, Fes, Morocco.*

Benabid, I. (2024). *Shallow landslides of the Souk Ahras region: influence of soil geotechnical properties and rainfall.* Echahid Cheikh Larbi Tebessi university.

Benamara Abdelwaheb. (2017). *Les eaux thermo-minérales et développement durable; cas de Hammam Meskoutine et Hammam Ouled Ali (Nord-Est Algérien)* [These de doctorat]. université Badji Mokhtar Annaba.

Bencharef, M. H., Boubaya, D., Aboud, E., & Ayfer, S. (2022). Role of an advanced gravity data analysis in improving the geologic understanding of the northern Tebessa region, Northeastern Algeria. *Journal of African Earth Sciences*, *196*. https://doi.org/10.1016/j.jafrearsci.2022.104693

Benmarce, K. (2015). *Caractérisation physico-chimique des eaux souterraines dans la région de Guelma, Nord-Est Algérien.* [Option Hydrogeologie]. Université Badji Mokhtar Annaba.

Berman, E., Levin, N., Landais, A., Li, S., Owano, T., Berman, E. S., & Levin, N. E. (2013). Measurement of δ 18 O, δ 17 O, and 17 O-excess in Water by Off-Axis Integrated Cavity Output Spectroscopy and Isotope Ratio Mass Spectrometry. *Ratio Mass Spectrometry. Analytical Chemistry*, *85*(21). https://doi.org/10.1021/ac402366tï

Boden, D. R. (2016). Geologic fundamentals of geothermal energy. *Geologic Fundamentals of Geothermal Energy*, 1–399. https://doi.org/10.1201/9781315371436

Bouaicha Foued. (2018). *le géothermalisme de la région de Guelma*. http://archives.umc.edu.dz/handle/123456789/136501

Bouaicha Foued, Dib Hénia, Belkhiri Lazhar, Manchar Nabil, & Chabour Nabil. (2017). Hydrogeochemistry and geothermometry of thermal springs from the Guelma region, Algeria. *Journal of the Geological Society of India*, *90*(2), 226–232. https://doi.org/10.1007/s12594-017-0703-y

Boubelli, S. (2017). *Identification et mise en évidence des formations hydrogéologiques de la wilaya de Khenchela (Nord-Est Algerien) Annalyse et synthèse des données*.

Bouchareb-Haouchine, F. Z. (2012). Etude hydrogéochimique des sources thermales de l'Algérie du Nord. In *Potentialités géothermiques.* UNIVERSITÉ DES SCIENCES ET DE LA TECHNOLOGIE « HOUARI BOUMEDIENE » FACULTE DES SCIENCES DE LA TERRE ET DE L'AMENAGEMENT DU TERRITOIRE.

Bouchareb-Haouchine, F.-Z., ISSAADI, A., & BEN DHIA, H. (1994). Estimation et interprétation du gradient géothermique en Algérie du Nord. *Estimation et Interprétation Du Gradient Géothermique En Algérie Du Nord*, *5*(1), 69–74.

Boudoukha, A., & Athamena, M. (2012). Caractérisation des eaux thermales de l'ensemble sud sétifien. Est Algérien. *Revue Des Sciences de l'Eau*, *25*(2), 103–118. https://doi.org/10.7202/1011602AR

Bouri, S., Gasmi, M., Jaouadi, M., Souissi, I., Lahlou Mimi, A., & Ben Dhia, H. (2009). Etude intégrée des données de surface et de subsurface pour la prospection des bassins hydrogéothermiques: cas du bassin de Maknassy (Tunisie centrale) / Integrated study of surface and subsurface data for prospecting hydrogeothermal basins: case of the Maknassy basin (central Tunisia). *Https://Doi.Org/10.1623/Hysj.52.6.1298*, *52*(6), 1298–1315. https://doi.org/10.1623/HYSJ.52.6.1298

Bourmada, A., Khammar, H., Ramzi, H., Chaffai, A., Bouchema, N., & Hamida, B. (2024a). Integrated assessment of groundwater quality in Algeria's Souk Ahras region: Implications for sustainable and management water for drinking and irrigation purpose. *Desalination and Water Treatment*, *320*. https://doi.org/10.1016/j.dwt.2024.100827

Bourmada, A., Khammar, H., Ramzi, H., Chaffai, A., Bouchema, N., & Hamida, B. (2024b). Integrated assessment of groundwater quality in Algeria's Souk Ahras region: Implications for sustainable and management water for drinking and irrigation purpose. *Desalination and Water Treatment*, *320*. https://doi.org/10.1016/j.dwt.2024.100827

Bouroubi Ouadfel, Y., Benzagouta, M. S., Khiari, A., Souffi Moulla, A., Ait ouali, A., Saadali, B., & Khaska, S. (2021). Hydrogeochemistry and geothermal potential of thermal waters: case study of the Triassic diapir area in Northeastern Algeria. *Euro-Mediterranean Journal for Environmental Integration*, *6*(3). https://doi.org/10.1007/s41207-021-00278-z

Bouroubi-Ouadfel, Y., Djebbar, M., & Khiari, A. (2018). Hydrothermal complex of the Souk Ahras Basin: geological and hydrogeochemical approaches (north east of Algeria). *Journal of Fundamental and Applied Sciences*, *8*(3), 894. https://doi.org/10.4314/jfas.v8i3.13

BRGM, & DIVISION NATIONALE DES EAUX BUREAU DE RECHERCHES MINÉRALES ET THERMALES GÉOLOGIQUES ET MINIÈRES. (1999). *Les géothermomètres chimiques, note technique n°13*.

Brown, C. E. (1998). Applied Multivariate Statistics in Geohydrology and Related Sciences. *Applied Multivariate Statistics in Geohydrology and Related Sciences*. https://doi.org/10.1007/978-3-642-80328-4

Camille Risi. (2009). *les isotopes stables de l'eau: applications à l'étude du cycle de l'eau et des variations du climat*. université de Paris 6.

Carrillo-Rivera, J. J., Cardona, A., & Moss, D. (1996). Importance of the vertical component of groundwater flow: a hydrogeochemical approach in the valley of San Luis Potosi, Mexico. *Journal of Hydrology*, *185*(1–4), 23–44. https://doi.org/10.1016/S0022-1694(96)03014-4

Castany, G. (1982). *Bassin sédimentaire du Sahara septentrional (Algérie, Tunisie). Aquifères du Continental intercalaire et du complexe terminal [nappe captive, système multicouche, hydrodynamique, gestion des ressources en eau, milieu aride]. Bulletin du Bureau de Recherches Géologiques et Minières Section 3 Hydrogéologie Géologie de l'Ingénieur.*

Castany, G. (1986). *Principes et méthodes de l'hydrogéologie. Paris, France: Dunod Université, p. 236 (in French).*

Celle-Jeanton, H., Travi, Y., & Blavoux, B. (2001). Isotopic typology of the precipitation in the Western Mediterrenean region at the three different time scales. *Geophysical Research Letters*, *28*(7), 1215–1218. https://doi.org/10.1029/2000GL012407

Chabbi, A. (2017). *Les nappes telliennes de la région Nord de Souk Ahras (NE algérien) : Etude géologique et structurale.* [These de doctorat en science]. université de Badji Mokhtar Annaba.

Chaffai, H., Toubal, A., Michel, L., Boubelli, S., & Djabri, L. (2013). *Hydrogeologie d'un systeme aquifere en zone semi-aride, cas de la région de Khenchela (Algérie)*.

Chenaker, H., Houha, B., & Vincent, V. (2018). Hydrogeochemistry and geothermometry of thermal water from north-eastern Algeria. *Geothermics*, *75*, 137–145. https://doi.org/10.1016/J.GEOTHERMICS.2018.04.009

Clark, I. D., & Fritz, P. (1997). *Environmental Isotopes in Hydrogeology* (1st Edition). CRC Press. https://doi.org/10.1201/9781482242911

CRAAG. (n.d.). *Centre de la recherche en Astronomie, Astrophysique et Géophysique*. Retrieved November 14, 2024, from www.craag.dz

Craig, H. (1961). Isotopic Variations in Meteoric Waters. *Science*, *133*(3465), 1702–1703. https://doi.org/10.1126/SCIENCE.133.3465.1702

Craig, H., & Gordon, L. I. (1965). *Deuterium and Oxygen 18 Variations in the Ocean and the Marine Atmosphere*. https://books.google.dz/books/about/Deuterium_and_Oxygen_18_Variations_in_th.html?id=6wIKAQAAIAAJ&redir_esc=y

Cruz, J. V., & França, Z. (2006). Hydrogeochemistry of thermal and mineral water springs of the Azores archipelago (Portugal). *Journal of Volcanology and Geothermal Research*, *151*(4), 382–398. https://doi.org/10.1016/J.JVOLGEORES.2005.09.001

Curetti, P. (1964). *Synthèse des études exécutées sur la station thermale d'Hammam Meskoutine, département de Bone. Document ANRH, Bir Mourad Raïs*.

Dansgaard, W. (1964). Stable isotopes in precipitation. *Tellus*, *16*(4), 436. https://doi.org/10.3402/TELLUSA.V16I4.8993

De Launay. (1889). *Recherche, captage et aménagement des sources thermominérales. Béranger, Paris.*

Deleau, P. (1938). *Etude géologique des régions de Jemmaps, Hammam Maskoutine et du col des oliviers. Thèse, Bulletin: Service de la Carte Géologique de l'Algérie*.

Deleau P. (1952). Le pays constantinois. In *CiNii Books*.

DERIAS, T. (2013). *Hydrogéologie du bassin versant de l'Oued Ksob (Tebessa): vulnerabilité et protection de la ressource*. https://www.pnst.cerist.dz/detail.php?id=74812/

Derias Tarek. (2013). *Hydrogéologie du bassin versant de l'Oued Ksob (Tebessa); Vulnerabilté et protection de la ressource* .

Derradji, T. (2023). *Régionalisation et cartographie des précipitations et des indices de sécheresse dans les bassins versants du Nord-Est Algérien (Constantinois-Seybouse-Mellègue)* [These de doctorat]. science de la terre et l'univers.

DHW Guelma. (2011). *Direction de l'hydraulique de la wilaya de Guelma (rapports des données)*.

DHW Tebessa. (1975). *Direction de l'hydraulique de la wilaya de Tebessa*.

Dib H. (1985). *Le thermalisme de l'Est algérien*. https://scholar.google.com/scholar?q=related:6OvAR0GwrJAJ:scholar.google.com/&scioq=DIB+Adjoul.+H+(1985)+Le+thermalisme+de+l%27Est+Alg%C3%A9rien&hl=fr&as_sdt=0,5

Dib H. (2008). *Guide pratique des sources thermales de l'Est algérien. Service géologique national.* https://scholar.google.com/scholar?hl=fr&as_sdt=0%2C5&q=28.%09Dib.+H%2C+2008.+Guide+pratique+des+sources+thermales+de+l%27Est+alg%C3%A9rien.+Editions+du+Service+G%C3%A9ologique+national+%28Alger%29&btnG=#d=gs_cit&t=1695052137901&u=%2Fscholar%3Fq%3Dinfo%3ARVncIYt9yxkJ%3Ascholar.google.com%2F%26output%3Dcite%26scirp%3D0%26hl%3Dfr

Dixon, W. , & Chiswell, B. (1992). The use of hydrochemical sections to identify recharge areas and saline intrusions in alluvial aquifers, southeast Queensland, Australia. *Journal of Hydrology*.

Djaafri, I., Seghir, K., Valles, V., & Barbiero, L. (2024). Regional Hydro-Chemistry of Hydrothermal Springs in Northeastern Algeria, Case of Guelma, Souk Ahras, Tebessa and Khenchela Regions. *Earth (Switzerland)*, *5*(2), 214–227. https://doi.org/10.3390/earth5020011

Djaafri Ibtissem. (2018). *Contribution to the hydro-structural study of the thermo-mineral waters of the Guelma region (East Algerian)* (International Water Forum Conference 2018, Ed.).

Djaafri Ibtissem, & Djeliel hassina. (2015). *L'impact de la tectonique sur la température, le chimisme, et la répartition des eaux dans la région de Guelma et les massifs du Nord* [These de master].

Djaafri Ibtissem, Seghir karima, & Carrillo-Rivera Jose joel. (2019). *Tóthian flow systems contribution to the hydro-structural study of the thermo-mineral waters of Guelma region (East Algeria)*.

Djaafri Ibtissem, Seghir Karima, & Carrillo-Rivera Jose joel. (2021). A hydrogeochemical study of thermal water (Geysers Hammam Debegh & Ouled Ali) using Toth's theory in Eastern Algeria. *International Symposium on Geofluids*.

Djabri, L., Bouhsina, S., Hani, A., Chaffai, H., Trabelsi, F. Z., Rouaibia, F., & Bouderbala, A. (2020). Origin and Quality of Groundwater of the Taoura Syncline Aquifer in North-Eastern of Algeria. In *Handbook of Environmental Chemistry* (Vol. 97, pp. 29–52). Springer Science and Business Media Deutschland GmbH. https://doi.org/10.1007/698_2020_523

Dotsika, E., Dalampakis, P., Spyridonos, E., Diamantopoulos, G., Karalis, P., Tassi, M., Raco, B., Arvanitis, A., Kolios, N., & Michelot, J. L. (2021). Chemical and isotopic characterization of the thermal fluids emerging along the North–Northeastern Greece. *Scientific Reports*, *11*(1). https://doi.org/10.1038/s41598-021-95656-6

Drias Tarek. (2013). *Hydrogeologie du bassin versant de l'oued ksob (Tebessa); vulnerabilité et protection de la ressource. These de magister.* Université des Sciences et de la Technologie Houari Boumediene (USTHB.

Dubourdieu, G. (1956). *Geological study of the Ouenza*. https://scholar.google.com/scholar?hl=fr&as_sdt=0%2C5&q=Dubourdieu+G+%281956%29+Geological+study+of+the+Ouenza+region++%28Algerian%E2%80%93Tunisian+borders%29+%28Bulletin+10%29.+Service+de+la+carte++ge%CC%81ologique+de+l%27Alge%CC%81rie%2C+Alger%2C+p+659+%28in+French%29&btnG=

Durand-Delga M. (1955). *Etude géologique de l'Ouest de la chaîne numidique. Thèse Sc. Paris, B. S. C. G. A. (2) Stratigra., Descrip., région., Bull. n 24, 533p, 143 fig.16 pl. photo. 10 pl. h. t., Alger*.

Earthquakelist.org. (2024). *Earthquakelist.org*. Earthquakelist.org

Edmunds, W. M., Kay, R. L. F., & McCartney, R. A. (1985). Origin of saline groundwaters in the Carnmenellis Granite (Cornwall, England): Natural processes and reaction during Hot Dry Rock reservoir circulation. *Chemical Geology*, *49*(1–3), 287–301. https://doi.org/10.1016/0009-2541(85)90162-7

Edmunds, W. M., Smedley, P. L., & Spiro, B. (1996). *Controls on the geochemistry of Sulphur in the East Midlands Triassic aquifer, United Kingdom*.

Ellis, A. J., & Mahon, W. A. J. (1977). *Chemistry and Geothermal Systems Academic Press New York 392pp*.

Everitt, B., Landau, S., & Leese, M. (2001). *Cluster analysis: Vol. 4th edn*. https://scholar.google.com/scholar?hl=fr&as_sdt=0%2C5&q=Everitt%2C+B.+S.%2C+Landau%2C+S.%2C+%26+Leese%2C+M.+%282001%29.+Cluster+Analysis+%284th+ed.%29.+Arnold.&btnG=

Fabre, J. (1976). *Introduction à la géologie du Sahara algérien et des régions voisines: La couverture phanérozoïque (Vol. 1). publisher not identified ED.*

Fehdi, C., Boudoukha, A., Rouabhia, A., & Salameh, E. (2011). Origin of groundwater salinity in the Morsott-El Aouinet basin, Northeastern Algeria: Hydrochemical and environmental isotopes approaches. *Desalination and Water Treatment*, *36*(1–3), 1–12. https://doi.org/10.5004/dwt.2011.1205

Fekraoui, A., & Kedaid, F.-Z. (2005). Geothermal Resources and Uses in Algeria: A Country Update Report. *Proceedings World Geothermal Congress*, 24–29.

Firat Ersoy, A., & Çalik Sönmez, S. (2014). Hydrogeochemical and isotopic characteristics of the Ilica geothermal system (Erzurum, Turkey). *Environmental Earth Sciences*, *72*(11), 4451–4462. https://doi.org/10.1007/S12665-014-3345-Z/METRICS

Fisher, R. S. , & Mullican, I. W. F. (1997). Hydrochemical evolution of sodium-sulfate and sodium-chloride groundwater beneath the northern Chihuahuan Desert, Trans-Pecos, Texas, USA. *Hydrogeology Journal*.

Fisher, R. S., & Mullican, W. F. (1997). Hydrochemical evolution of sodium-sulfate and sodium-chloride groundwater beneath the Northern Chihuahuan Desert, Trans-Pecos, Texas, USA. *Hydrogeology Journal*, *5*(2), 4–16. https://doi.org/10.1007/S100400050102/METRICS

Fouillac, C., & Michard, G. (1981). *SODIUM/LITHIUM RATIO IN WATER APPLIED TO GEOTHERMOMETRY OF GEOTHERMAL RESERVOIRS* (Vol. 10, Issue 1).

Fournier R. (1979). A revised equation for the Na/K geothermometer. *GRC Transactions*, *3*, 221–224. https://cir.nii.ac.jp/crid/1570854174249891072

Fournier, R. O. (1977). Chemical geothermometers and mixing models for geothermal systems. *Geothermics*, *5*(1–4), 41–50. https://doi.org/10.1016/0375-6505(77)90007-4

Fournier, R. O. (1991). Water geothermometers applied to geothermal energy. *Cir.Nii.Ac.Jp*. https://cir.nii.ac.jp/crid/1571417124958408320

Fournier, R. O., & Potter, R. W. (1982). An equation correlating the solubility of quartz in water from 25° to 900°C at pressures up to 10,000 bars. *Geochimica et Cosmochimica Acta*, *46*(10), 1969–1973. https://doi.org/10.1016/0016-7037(82)90135-1

Fournier, R. O., & Truesdell, A. H. (1973). An empirical Na-K-Ca geothermometer for natural waters. *Geochimica et Cosmochimica Acta*, *37*(5), 1255–1275. https://doi.org/10.1016/0016-7037(73)90060-4

Frohlich, K., Gibson, J. J., & Aggarwal, P. K. (2002). *DEUTERIUM EXCESS IN PRECIPITATION AND ITS CLIMATOLOGICAL SIGNIFICANCE*.

Fu, C. , Li, X. , Ma, J. , Liu, L. , Gao, M. , & Bai, Z. (2018). A hydrochemistry and multi-isotopic study of groundwater origin and hydrochemical evolution in the middle reaches of the Kuye River basin Applied Geochemistry, 98, 82-93. *Applied Geochemistry,*.

Fu, C., Li, X., Ma, J., Liu, L., Gao, M., & Bai, Z. (2018). A hydrochemistry and multi-isotopic study of groundwater origin and hydrochemical evolution in the middle reaches of the Kuye River basin. *Applied Geochemistry*, *98*, 82–93. https://doi.org/10.1016/J.APGEOCHEM.2018.08.030

Gat, J. R. (1996). OXYGEN AND HYDROGEN ISOTOPES IN THE HYDROLOGIC CYCLE. *Annu. Rev. Earth Planet. Sci*, *24*, 225–262. www.annualreviews.org

Gemici, Ü., Tarcan, G., Çolak, M., & Helvaci, C. (2004). Hydrogeochemical and hydrogeological investigations of thermal waters in the Emet area (Kütahya, Turkey). *Applied Geochemistry*, *19*(1), 105–117. https://doi.org/10.1016/S0883-2927(03)00112-4

Ghreib, L. (2011). *IMPACT DE LA MINÉRALISATION DES FORMATIONS TRIASIQUES SUR LA QUALITÉ DE L'EAU ET DU SOL EN ZONE SEMI-ARIDE : Cas de la plaine Bekkaria-Tébessa (Extrême Nord-est Algérien).* Badji Mokhtar-Annaba University.

Ghrieb, L., Maoui, A., Boudjebieur, E., & Gueroui, Y. (2021). Physicochemical Characterization of the Quality of Groundwater: Case Study of the Tebessa Plain (North-East Algeria). *Civil and Environmental Engineering Reports*, *31*(3), 18–36. https://doi.org/10.2478/ceer-2021-0032

Giggenbach, W. F. (1988). Geothermal solute equilibria. Derivation of Na-K-Mg-Ca geoindicators. *Geochimica et Cosmochimica Acta*, *52*(12), 2749–2765. https://doi.org/10.1016/0016-7037(88)90143-3

Giggenbach, W. F. (1991). Chemical techniques in geothermal exploration. *Application of Geochemistry in Geothermal Reservoir Development*. https://cir.nii.ac.jp/crid/1570572699730688640

Giggenbach, W. F., Gonfiantini, R., Jangi~, B. L., & Truesdell, A. H. (1983). ISOTOPIC AND CHEMICAL COMPOSITION OF PARBATI VALLEY GEOTHERMAL DISCHARGES, NORTH-WEST HIMALAYA, INDIA. *Geothermics*, *12*(3), 199–222.

Giménez, R., Bartolomé, M., Gázquez, F., Iglesias, M., & Moreno, A. (2021). Underlying Climate Controls in Triple Oxygen (16 O, 17 O, 18 O) and Hydrogen (1 H, 2 H) Isotopes Composition of Rainfall (Central Pyrenees). *Frontiers in Earth Science*, *9*, 209. https://doi.org/10.3389/FEART.2021.633698/BIBTEX

Goldscheider, N., Mádl-Szőnyi, J., Erőss, A., & et al. (2010). Thermal water resources in carbonate rock aquifers. *Hydrogeology Journal*. https://doi.org/https://doi.org/10.1007/s10040-010-0611-3

Gorelick, N., Hancher, M., Dixon, M., Ilyushchenko, S., Thau, D., & Moore, R. (2017). Google Earth Engine: Planetary-scale geospatial analysis for everyone. *Remote Sensing of Environment*, *202*, 18–27. https://doi.org/10.1016/J.RSE.2017.06.031

Guigue, S. (1947). *Les sources thermo-minérales de l'Algérie, étude géochimique (Tome II)*. Service de la carte géologique de l'Algérie .

Hadji, R. (2013). *Shallow landslides in the region of Souk Ahras, Algeria (Thèse de doctorat)*.

Hafid Feyrous. (n.d.). *Mise en évidence d'une alimentation du champs captant, Ain Chabro-Hammamet par les formations calcaires de Youkous*.

Hatvani, I. G., Smati, A. E., Erdélyi, D., Szatmári, G., Vreča, P., & Kern, Z. (2023). Modeling the spatial distribution of the meteoric water line of modern precipitation across the broader Mediterranean region. *Journal of Hydrology*, *617*, 128925. https://doi.org/10.1016/J.JHYDROL.2022.128925

Hotelling, H. (1933). ANALYSIS OF A COMPLEX OF STATISTICAL VARIABLES INTO PRINCIPAL COMPONENTS 1. *Journal of Educational Psycology*.

Houha, B. (2007). *Etude du fonctionnement hydrogéologique et salin d'un bassin semi-aride. Rémila–Khenchela (Doctoral dissertation, PhD Thesis, faculty of Earth Sciences, University of Annaba, Algeria).*

Hydrographic basins agency Constantinois-Seybouse- Mellegue. (2009). *Quality of surface water in Kebir-Rhumel, Seybouse, and Medjerda-Mellegue bassins 2004-2007* (Vol. 12).

Issaadi, A. (1992). *Le thermalisme dans son cadre géostructural, apports à la connaissance de la structure profonde de l'Algérie et de ses ressources géothermales. Thèse de doctorat d'état, University of Science and Technology Houari Boumedienne, Algiers.*

Issaadi, A., -Zohra BOUCHAREB -HAOUCHINE, F., Alia, E., Ezzouar, B., & -Algérie, A. (1997). Estimation du flux de chaleur en Algérie du Nord à partir de la Thermométrie silice Heat flow estimate in the North of Algeria by the silica temperature. In *Bulletin du Service Géologique de l Algérie* (Vol. 8, Issue 1).

Jakemann·, A., Randall, O., Huntt·, J., & Andrewwross, J.-D. (2016). *Integrated Groundwater Management Concepts, Approaches and Challenges*.

Jenny, Hans. (1994). *Factors of soil formation : a system of quantitative pedology*. Dover.

Jiang, X. W., Wan, L., Ge, S., Cao, G. L., Hou, G. C., Hu, F. S., Wang, X. S., Li, H., & Liang, S. H. (2012). A quantitative study on accumulation of age mass around stagnation points in nested flow systems. *Water Resources Research*, *48*(12). https://doi.org/10.1029/2012WR012509

Joel Carrillo-Rivera, J., Ouysse, S., & Hernández, G. (2013). *Identification of Groundwater Flow Systems response in Draa basin (Morocco)*. https://www.researchgate.net/publication/270592233

Kachadourian-Marras, A. , A.-M. M. M. , C.-R. J. J. , M. E. , H.-A. F. , & S. R. (2020). Characterization of surface evidence of groundwater flow systems in continental Mexico. *Water*.

Kachadourian-Marras, A., Alconada-Magliano, M. M., Carrillo-Rivera, J. J., Mendoza, E., Herrerías-Azcue, F., & Silva, R. (2020). Characterization of surface evidence of groundwater flow systems in continental Mexico. *Water (Switzerland)*, *12*(9). https://doi.org/10.3390/w12092459

Kachi, S., Kherici, N., & Kachi, N. (2007). Vulnerability and Pollution Risks in the Alluvial Aquifer of Tebessa-Morsott. In *American Journal of Environmental Sciences* (Vol. 3, Issue 4).

Kedaid F. (2002). Algerian geothermal country report. *Kgvrs.Mine.Kyushu-u.Ac.Jp*. https://kgvrs.mine.kyushu-u.ac.jp/GVR%20report/No11/algeria.pdf

Kharaka, Y. K., Hull, R. W., & Carothers, W. W. (1985). Water-Rock Interactions in Sedimentary Basins. *Relationship of Organic Matter and Mineral Diagenesis*, 79–176. https://doi.org/10.2110/SCN.85.03.0079

Kharaka, Y. K., Lico, M. S., & Law-Leroy M. (1982). Chemical geothermometers applied to formation waters, Gulf of Mexico and California basins. *Archives.Datapages.ComYK Kharaka, MS Lico, LM LawAapg Bulletin, 1982•archives.Datapages.Com*. https://archives.datapages.com/data/bulletns/1982-83/data/pg/0066/0005/0550/0588a.htm

Kharaka, Y. K., & Mariner, R. H. (1989). Chemical Geothermometers and Their Application to Formation Waters from Sedimentary Basins. *Thermal History of Sedimentary Basins*, 99–117. https://doi.org/10.1007/978-1-4612-3492-0_6

Kowalski, W., & l', M. H.-B. du S. G. de. (2000). Diapirisme polyphasé ou glacier de sel albien? Dilemme du matériel triasique des confins algéro-tunisiens. *Researchgate.NetWM Kowalski, M HamimedBulletin Du Service Géologique de l'Algérie, 2000•researchgate.Net*. https://www.researchgate.net/profile/Messaoud-Hamimed/publication/354556026_Diapirisme_polyphase_ou_glacier_du_sel_Albien_Dilemme_du_materiel_triasique_des_confins_algero-tunisiens/links/613fc5e5185c504a1abfc57a/Diapirisme-polyphase-ou-glacier-du-sel-Albien-Dilemme-du-materiel-triasique-des-confins-algero-tunisiens.pdf

Kowalski, W. M., Boudoukha, A., Hemila, M. L., & Pharisat, A. (1997). *Les stades d'effondrement du graben de Tébessa (confins Algéro-Tunisien) et la tectonique plicative Plio-Quaternaire*.

KOWALSKI, W. M., Hamimed, M., & Pharisat, A. (2002). LES ETAPES D'EFFONDREMENT DES GRABENS DANS LES CONFINS ALGERO-TUNISIENS. *Bulletin Du Service Géologique de l'Algérie*, *13*(2), 131–152.

La Région de Guelma, Étude Spéciale Des Terrains Tertiaires. Bull. Du Service de La Carte Géologique de l'Algérie, Alger, 2emmesérie, N°5. (1910).

Landais, A., Barkan, E., & Luz, B. (2008). Record of δ18O and 17O-excess in ice from Vostok Antarctica during the last 150,000 years. *Geophysical Research Letters*, *35*(2). https://doi.org/10.1029/2007GL032096

Langmuir, D. (1997). *Aqueous Environmental Geochemistry. Prentice-Hall, Inc., Englewood Cliffs, 601. - References - Scientific Research Publishing*. https://www.scirp.org/reference/referencespapers?referenceid=1651828

Legrioui, R. (2019). *Contribution à la connaissance de l'aquifère karstique des calcaires du Maestrichtien de la région SW de Tébessa (N-E Algérien)*.

LEGRIOUI, R. (2019). *Contribution à la connaissance de l'aquifère karstique des calcaires du Maestrichtien de la région SW de Tébessa (NE Algérien)*. https://www.ccdz.cerist.dz/admin/notice.php?id=000000000000009501590000922

Lenntech. (2005, January). *Composition of seawater. Water Condition and Purification magazine*. https://www.lenntech.com/composition-seawater.htm

Luz, B., & Barkan, E. (2010). Variations of 17O/16O and 18O/16O in meteoric waters. *Geochimica et Cosmochimica Acta*, *74*(22), 6276–6286. https://doi.org/10.1016/j.gca.2010.08.016

Mádl-Szőnyi, J., Molson, J., Batelaan, O., Verweij, H., Jiang, X.-W., Carrillo-Rivera, J. J., & Tóth, Á. (2023). *Evolving concepts and communication: what do we need to evaluate better regional groundwater flow?* https://doi.org/10.5194/egusphere-egu23-14159

Mádl-Szőnyi, J., Pulay, E., Tóth, Á., & Bodor, P. (2015). Regional underpressure: a factor of uncertainty in the geothermal exploration of deep carbonates, Gödöllő Region, Hungary. *Environmental Earth Sciences*, *74*(12), 7523–7538. https://doi.org/10.1007/S12665-015-4608-Z/METRICS

Mádl-Szőnyi, J., & Tóth, Á. (2015). Modèle conceptuel d'écoulements d'eau souterraine à l'échelle d'un basin pour une région carbonatée épaisse libre et captive. *Hydrogeology Journal*, *23*(7), 1359–1380. https://doi.org/10.1007/s10040-015-1274-x

Mahon, W. A. J. (1970). Chemistry in the exploration and exploitation of hydrothermal systems. *Geothermics*, *2*(PART 2), 1310–1322. https://doi.org/10.1016/0375-6505(70)90449-9

Maouche, S., Abtout, A., Merabet, N.-E., Aïfa, T., Lamali, A., Bouyahiaoui, B., Bougchiche, S., & Ayache, M. (2013). Tectonic and Hydrothermal Activities in Debagh, Guelma Basin (Algeria). *Journal of Geological Research*, *2013*(1), 409475. https://doi.org/10.1155/2013/409475

Merdas Brahim. (2006). *Contribution à l'étude géologique et gitologiquedes minéralisations de la région de Hammam N'bails (Nord-Est Algérien)*.

Mook, W. G., Rozanski, K., & Froehlich, K. (2000). Environmental isotopes in the hydrological cycle: principles and applications. *Technical Documents in Hydrology*, *1*(39). https://www.hydrology.nl/images/docs/ihp/Mook_III.pdf

Morel, F. (1957). *Etude geologique de Djebel Belkfif (Tebessa)*.

Murtagh, F., Classification, M. F.-J. of, & 2001, undefined. (2001). Pattern Classification, by Richard O. Duda, Peter E. Hart, and David G. Stork. *Elibrary.Ru*. https://elibrary.ru/item.asp?id=816540

Nassima, S., & Djabri, L. (2014). *Contribution of hydrochemistry to the characterization and assessment of groundwater resources: the case of Tebessa alluvial aquifer (Algeria) Contribution of hydrochemistry to the characterization and assessment of groundwater resources: the case of Tebessa alluvial aquifer (Algeria)*. *364*. https://www.researchgate.net/publication/266023581

Nieva, D., & Nieva, R. (1987). Developments in geothermal energy in Mexico—part twelve. A cationic geothermometer for prospecting of geothermal resources. *Heat Recovery Systems and CHP*, *7*(3), 243–258. https://doi.org/10.1016/0890-4332(87)90138-4

Nosjean, N., Khamitov, Y., Rodriguez, S., & Yahia-Cherif, R. (2020). Fracture corridor identification through 3D multifocusing to improve well deliverability, an Algerian tight reservoir case study. *Solid Earth Sciences*, *5*(1), 31–49. https://doi.org/10.1016/j.sesci.2019.11.009

Nyamgerel, Y., Han, Y., Kim, M., Koh, D., & Lee, J. (2021). Review on applications of17O in hydrological cycle. *Molecules*, *26*(15). https://doi.org/10.3390/molecules26154468

Othmanine, A. (1987). *Les minéralisations en fluorine, barytine, Pb, Zn et fer sidéritique autour du fossé de Tébessa-Morsott. Relation entre la paléogéographie albo-aptienne*. https://pascal-francis.inist.fr/vibad/index.php?action=getRecordDetail&idt=7785015

Ouali salima. (2015). *Contribution à l'étude de quelques réservoirs géothermiques en Algérie* [These de doctorat en science]. L'Université des Sciences et de la Technologie Houari Boumediene (USTHB).

Ouali Salima. (2015). *Contribution à l'étude de quelques réservoirs géothermiques en Algérie* [Faculté des Sciences de la Terre, de la Géographie et de l'Aménagement du Territoire]. https://www.cder.dz/vlib/cder_ft/cder_ft_00143.pdf

Ouysse S. (2012). *Approche régionale par intégration des indicateurs hydrogéologiques et biotiques en vue de comprendre la réponse des ressources en eau dans le bassin du Draa aux variabilités climatiques. Submitted Ph.D Thesis Cadi Ayyad University Marrekech Morroco*.

Papp, D. C., & Niţoi, E. (2006). Isotopic composition and origin of mineral and geothermal waters from Tuşnad Băi Spa, Harghita Mountains, Romania. *Journal of Geochemical Exploration*, *89*(1–3), 314–317. https://doi.org/10.1016/J.GEXPLO.2005.12.008

Parkhurst, D., & Appelo, C. (2013). *Description of Input and Examples for PHREEQC Version 3-A Computer Program for Speciation, Batch-Reaction, One-Dimensional Transport, and Inverse Geochemical Calculations: Vol. Chapter A43*. http://www.hydrochemistry.eu

Pauwels, H., Fouillac, C., & Fouillac, A. M. (1993). Chemistry and isotopes of deep geothermal saline fluids in the Upper Rhine Graben: Origin of compounds and water-rock interactions. *Geochimica et Cosmochimica Acta*, *57*(12), 2737–2749. https://doi.org/10.1016/0016-7037(93)90387-C

Pearson, K. (1901). LIII. On lines and planes of closest fit to systems of points in space. *The London, Edinburgh, and Dublin Philosophical Magazine and Journal of Science*, *2*(11), 559–572. https://doi.org/10.1080/14786440109462720

Peñuela-Arévalo, L. A., & Carrillo-Rivera, J. J. (2013a). Discharge areas as a useful tool for understanding recharge areas, study case: Mexico Catchment. *Environmental Earth Sciences*, *68*(4), 999–1013. https://doi.org/10.1007/s12665-012-1803-z

Peñuela-Arévalo, L. A., & Carrillo-Rivera, J. J. (2013b). Discharge areas as a useful tool for understanding recharge areas, study case: Mexico Catchment. *Environmental Earth Sciences*, *68*(4), 999–1013. https://doi.org/10.1007/S12665-012-1803-Z/METRICS

Peybernès, B., Chouabbi, A., & Vila, J. M. (2002). Reconstitution du substratum jurassique-crétacé basal du domaine des Sellaoua (marge sud-téthysienne, Algérie nord-orientale) à partir des galets du bassin mio-pliocène d'Hamman N'Baïls. *Comptes Rendus Palevol*, *1*(8), 681–688. https://doi.org/10.1016/S1631-0683(02)00081-7

Pfeiffer, T. (2024). *The Volcano Discovery Website*. https://www.Volcanodiscovery.com/fr/siesmes/derniers.html

Plummer, L. N., & Busenberg, E. (1982). The solubilities of calcite, aragonite and vaterite in CO2-H2O solutions between 0 and 90°C, and an evaluation of the aqueous model for the system CaCO3-CO2-H2O. *Geochimica et Cosmochimica Acta*, *46*(6), 1011–1040. https://doi.org/10.1016/0016-7037(82)90056-4

Porowski, A. (2019). Mineral and Thermal Waters. *Environmental Geology*, 149–181. https://doi.org/10.1007/978-1-4939-8787-0_978

Pu, J., Yuan, D. , Zhang, C. , & Zhao, H. (2013). Hydrogeochemistry and possible sulfate sources in karst groundwater in Chongqing, China. *Environmental Earth Sciences, 68, 159-168.* https://doi.org/https://doi.org/10.1007/s12665-012-1726-8

Rodier, J., Geoffray, C., & Rodi, L. (1996). *L'analyse de l'eau, eau naturelle, eau résiduaire, eau de mer: chimie, physico-chimie, bacteriologie, biologie.Dunod*.

Rouabhia, A., Baali, F., & Fehdi, C. (2010). Impact of agricultural activity and lithology on groundwater quality in the Merdja area, Tebessa, Algeria. *Arabian Journal of Geosciences*, *3*(3), 307–318. https://doi.org/10.1007/S12517-009-0087-4

Rouaibia, F., & Djabri, L. (2017). Caractéristiques chimiques des eaux de la nappe du synclinal de Taoura, Souk Ahras (Nord-Est de L'Algérie). Chemical characteristics of waters aquifer of the syncline of Taoura, Souk Ahras (North-east of Algeria). In *Rouaibia & L. Djabri Rev. Sci. Technol., Synthèse* (Vol. 35).

Rozanski, K., Araguás-Araguás, L., & Gonfiantini, R. (2013). *Isotopic Patterns in Modern Global Precipitation* (pp. 1–36). https://doi.org/10.1029/gm078p0001

Saad, M. A., Seghir, K., Touahri, A., Bendekkoum, M., Bellaoueur, A., & Pulido-Bosch, A. (2024). Study of the influence of the Tebessa region wastewaters on the hydrochemical quality of the alluvial aquifer groundwater's Tebessa-Ain Chabro (N-E Algeria). *RBRH*, *29*. https://doi.org/10.1590/2318-0331.292420230134

SALAMA, M. M., El Ebaidi, S. K., & DAVID P.STICKLEY. (2013). *WATER CHEMICAL ANALYSIS FOR DIFFERENT STAGES IN TOBRUK DESALINATION PLANT*. https://www.researchgate.net/publication/289249278

Salhi, M., & Ouanassi, M. (2022). *La géologie général de la wilaya de khenchela (ville de kais)*.

Seghir, K. (2008). *Vulnérabilité à la pollution, protection des ressources en eaux et gestion active du sous système aquifère de Tebessa Hammamet (Est Algérien)* [Doctor degree thesis]. Badji Mokhtar Annaba University.

Serra, H. , & Sunjuan, B. (2004). Synthese bibliographique des géothermometres chimiques appliqués aux eaux géothermales: rapport final. BRGM, France. In *rapport final. BRGM, France*. https://scholar.google.com/scholar?hl=fr&as_sdt=0%2C5&q=synthese+bibliographique+des+g%C3%A9othermometres+chimiques+appliqu%C3%A9s&btnG=

Service de la carte géologique de l'Algérie. (1977). *Carte Geologique de l'Algérie, Khenchela, première édition, feuille N°203, Ministère de l'industrie et l'énergie, direction des mines et de la géologie, .*

Sogréah, (Societé française d'ingénierie). (2005). *Etude d'actualisation et de finalisation du plan national de l'eau. Région hydrographique Centre et Est*.

Sridhar, H. (2020). *The Impact of Boundary Condition on Groundwater Flow: Topography v/s Recharge Controlled HARSHITHA SRIDHAR*.

Stamboul, M. E. (2017). *Analyses de l'état quantitatif et qualitatif des eaux superficielles et souterraines de la zone El Aouinet- El ouanza et son impact sur l'environnement (Wilaya de Tebessa)(Doctoral dissertattion* . Earth and univers sciences.

Steig, E. J., Gkinis, V., Schauer, A. J., Schoenemann, S. W., Samek, K., Hoffnagle, J., Dennis, K. J., & Tan, S. M. (2014). Calibrated high-precision 17O-excess measurements using cavity ring-down spectroscopy with laser-current-tuned cavity resonance. *Atmospheric Measurement Techniques*, *7*(8), 2421–2435. https://doi.org/10.5194/AMT-7-2421-2014

Sunjuan B, & Millot R. (2009). *Bibliographical review about Na/Li geothermometry and lithium isotopes applied to worldwide geothermal waters Final report HiT/ Géosciences pour une Terre durable brgm*.

Tonami, F. (1970). Geochemical methods of exploration for geothermal energy. *Geothermics*, *2*(PART 1), 492–515. https://doi.org/10.1016/0375-6505(70)90049-0

Tóth, Á., Kovács, S., Kovács, J., & Mádl-Szőnyi, J. (2022). Springs regarded as hydraulic features and interpreted in the context of basin-scale groundwater flow. *Journal of Hydrology*, *610*. https://doi.org/10.1016/j.jhydrol.2022.127907

Tóth, J. (1963a). A theoretical analysis of groundwater flow in small drainage basins. *Journal of Geophysical Research*, *68*(16), 4795–4812. https://doi.org/10.1029/jz068i016p04795

Tóth, J. (1963b). A theoretical analysis of groundwater flow in small drainage basins. *Journal of Geophysical Research*, *68*(16), 4795–4812. https://doi.org/10.1029/JZ068I016P04795

Toth, J. (1978). *WATER RESOURCES RESEARCH* (Vol. 14, Issue 5).

Toth J. (2009). *Gravitational systems of groundwater flow: theory, evaluation, utilization* (N. Y. Cambridge university press, Ed.). www.cambridge.org/9780521886383

Tóth, J. (2015). Geothermal phenomena in the context of gravity-driven basinal flow of groundwater. *Central European Geology*, *58*(1–2), 1–27. https://doi.org/10.1556/24.58.2015.1-2.1

Toth J. (2015). *Regional Grundwater Flow Theory*.

Toth, J. (2016). *The Evolutionary Concepts and Practical Utilization of the T thian Theory*.

Toth Jozsef. (2015). *The basic Concepts and Practical utilization of the Regional Groundwater Flow*.

Truesdell A. H. (1976). Summary of section III-geochemical techniques in exploration. *Cir.Nii.Ac.Jp*, *1*. https://cir.nii.ac.jp/crid/1573950399451321344

USGS. (n.d.). *Earthquake Hazard program*. Retrieved November 14, 2024, from usgs.gov

Verdeil, P. (1974). *Carte au 1/50000 des eaux minérales, thermales et thermominérales de l'Algérie . Comm. Eaux Miner., A.I.H., Eforie Nord.*

Verdeil, P. (1982). Algerian thermalism in its geostructural setting -- how hydrogeology has helped in the elucidation of Algeria's deep-seated structure. *Journal of Hydrology*, *56*, 107–117.

Vila, J. M. (1977). *Carte géologique de l'Algérie à 1:20000, feuille P-Q- 3- 5 Constantine, avec notice expl. 53 p, Publ. Serv.Géol.Algérie/Sonatrach*.

Vila J-M. (1977). *Explanatory note of the geological map of Khenchela (203), Direction des mines et de la géologie, service de la carte géologique de l'Algérie et SONATRACH (division des hydrocarbures, direction d'exploration)*. Direction of exploration, .

Vila, J. M. (1978). *Carte structurale au 1/500000 de la chaine alpine d'Algérie orientale et des confins Algéro-Tunisiens. C.N.R.S & B.E.I.CP.France* .

Vila J. M. (1980). *La chaine alpine de l'Algerie orientale et des confins Algero-Tunisiens* [These de doctorat]. Pierre et Marie Curie, Paris.

Vila, J. M., Busnardo, R., Devries, A., Magne, J., & Sigal, J. (1986). Données stratigraphiques sur la série renversé et charriée du Djebel Bou Sba et étude de son cadre structural (région de Guelma, Constantinois,Algerie). *La Société Geologique de France*.

Ward, J. H. (1963). Hierarchical Grouping to Optimize an Objective Function. In *Source: Journal of the American Statistical Association* (Vol. 58, Issue 301).

White, D. E. (1970). *Geochemistry applied to the discovery, evaluation, and exploitation of geothermal energy resources. Geothermics 3 (spec. issue 2)*.

Winter, T. C., Harvey, J. W., Franke, O. L., & Alley, W. M. (1998). *Groundwater and surface water A single resource. U.S. Geological Survey Circular1139*. https://pubs.usgs.gov/circ/circ1139/

Yang, P., Cheng, Q., Xie, S., Wang, J., Chang, L., Yu, Q., Zhan, Z., & Chen, F. (2017). Hydrogeochemistry and geothermometry of deep thermal water in the carbonate formation in the main urban area of Chongqing, China. *Journal of Hydrology*, *549*, 50–61. https://doi.org/10.1016/J.JHYDROL.2017.03.054

Yang, P., Luo, D., Hong, A., Ham, B., Xie, S., Ming, X., Wang, Z., & Pang, Z. (2019). Hydrogeochemistry and geothermometry of the carbonate-evaporite aquifers controlled by deep-seated faults using major ions and environmental isotopes. *Journal of Hydrology*, *579*. https://doi.org/10.1016/j.jhydrol.2019.124116

Yelles-Chaouche, A. K., Boudiaf, A., Djellit, H., & Bracene, R. (2006). La tectonique active de la région nord-algérienne. *Comptes Rendus - Geoscience*, *338*(1–2), 126–139. https://doi.org/10.1016/j.crte.2005.11.002

Yelles-Chaouche, Aidi Ch, Beldjoudi, & Benajma. (2022). *The recent seismicity of northern Algeria: the 2006 - 2020 catalogue*.

Zhu, Y., An, F., & Tan, J. (2011). Geochemistry of hydrothermal gold deposits: A review, Geoscience Frontiers 2(3) (2011) 367-374. *Geoscience Frontiers*.

Appendices

Table 40. Calculated Mineralization of all samples (Appendices)

Samples	Conductivité	Factor	Mineralization
S1	1459	0.8465351	1235.09
S3	2030	0.8465351	1718.47
S4	2130	0.8465351	1803.12
S5	2380	0.8465351	2014.75
S6	2410	0.8465351	2040.15
S7	9300	0.8465351	7872.78
S9	1972	0.8465351	1669.37
F1	645	0.79896672	515.33
S10	1770	0.8465351	1498.37
S11	3360	0.8465351	2844.36
F3	736	0.79896672	588.04
F2	544	0.79896672	434.64
S12	667	0.79896672	532.91
S13	16850	0.94908211	**15992.03**
S14	3390	0.8465351	2869.75
S15	2190	0.8465351	1853.91
F5	556	0.79896672	444.23
F6	531	0.79896672	424.25

Table 41. Air Temperature in the region of Guelma during the period 2000 to 2022 downloaded from GEE (Appendices)

Year	Sept	Oct	Nov	Dec	Jan	Feb	Mar	Apr	May	Jun	July	Aug	SUM	Average
2000	38.07	25.57	20.75	15.97	21.87	20.97	22.78	26.38	32.64	37.00	42.05	45.43	349.47	53.76
2001	35.05	30.14	19.83	12.82	12.88	15.10	24.98	24.99	29.36	38.07	40.96	42.56	326.75	50.27
2002	35.85	30.40	17.05	13.15	13.79	18.47	21.70	26.82	35.91	43.71	40.18	39.05	336.08	51.70
2003	32.66	27.64	18.49	13.40	11.64	12.39	21.09	22.58	28.35	37.76	41.52	41.64	309.16	47.56
2004	35.35	30.85	15.69	12.41	11.96	15.98	20.04	21.84	23.93	31.68	37.88	38.22	295.83	45.51
2005	36.42	29.22	21.89	12.28	11.30	11.40	18.51	23.12	31.38	36.94	40.45	39.26	312.15	48.02
2006	37.06	32.15	21.88	13.91	10.05	14.13	21.86	26.66	31.34	37.23	43.22	40.49	329.97	50.77
2007	34.51	28.05	16.43	12.79	15.21	15.05	18.61	20.92	28.79	35.48	41.11	41.28	308.23	47.42
2008	35.37	26.73	18.21	11.52	13.77	16.52	20.84	26.07	28.96	37.54	41.48	42.07	319.08	49.09
2009	32.64	25.40	19.33	13.90	11.19	12.40	18.89	21.62	28.96	36.51	41.87	41.24	303.95	46.76
2010	36.04	27.37	16.83	10.70	11.69	17.67	19.89	23.01	27.10	34.63	41.35	41.38	307.66	47.33
2011	36.03	26.80	18.67	14.65	13.54	14.08	17.79	25.05	27.05	34.22	38.88	41.21	307.97	47.38
2012	34.59	30.13	19.22	14.14	11.43	12.16	20.79	22.89	29.54	38.49	40.28	42.56	316.21	48.65
2013	32.11	31.63	17.22	13.35	12.93	12.69	19.81	25.84	29.26	36.91	41.63	41.81	315.18	48.49
2014	37.90	30.74	24.53	13.61	13.41	16.19	17.39	24.32	30.92	36.77	40.36	40.98	327.13	50.33
2015	33.41	26.58	19.12	15.25	13.18	10.60	20.04	25.33	31.93	37.48	44.18	40.73	317.81	48.89
2016	34.50	28.90	20.14	15.41	15.19	15.10	19.46	23.31	29.81	36.41	41.56	41.25	321.02	49.39
2017	37.46	28.84	20.27	12.29	10.61	15.49	23.67	26.73	34.21	41.60	44.07	44.75	339.98	52.30
2018	34.11	23.25	17.85	14.68	14.75	12.59	18.15	23.17	26.95	33.99	38.56	36.57	294.61	45.32
2019	30.37	26.47	15.77	14.33	10.84	14.67	20.27	22.08	26.16	36.90	39.52	39.92	297.29	45.74

2020	33.32	27.45	21.69	12.72	12.85	18.54	17.09	21.59	30.64	36.51	41.80	42.21	316.43	48.68
2021	35.19	27.38	18.07	13.40	12.81	17.32	20.26	23.36	27.85	35.44	41.71	42.27	315.07	48.47
2022	35.84	28.75	26.46	29.21	13.98	17.39	17.23	23.40	30.68	40.96	44.75	41.81	350.47	53.92
Average	34.95	28.28	19.36	14.17	13.08	15.08	20.05	23.96	29.64	37.05	41.28	41.25		

Table 42. Precipitation of the region of Guelma during the period 2000 to 2022 according to GEE (Appendices)

Year	Sept	Oct	Nov	Dec	Jan	Feb	Mar	Apr	May	Jun	July	Aug	Sum	Average
2000	30.94	57.54	35.82	90.76	27.27	24.26	37.99	37.89	117.89	27.17	0.20	9.48	497.21	41.43
2001	74.93	26.05	52.85	52.67	128.57	45.72	37.26	41.38	54.02	7.29	0.54	8.36	529.64	44.14
2002	31.73	36.44	129.03	101.88	25.94	37.82	53.24	44.20	23.19	11.68	11.31	44.64	551.10	45.93
2003	51.97	55.09	52.85	125.96	183.04	78.40	35.97	99.78	52.25	11.02	2.37	8.97	757.68	63.14
2004	38.63	32.85	115.29	181.07	62.48	31.15	77.00	60.12	73.47	33.80	0.40	16.81	723.07	60.26
2005	21.11	21.49	29.02	119.71	45.89	90.86	42.01	79.14	15.19	19.57	6.93	12.39	503.32	41.94
2006	23.82	34.03	35.60	134.37	137.29	71.65	37.70	40.76	61.67	13.87	8.33	13.84	612.94	51.08
2007	41.60	55.47	57.12	98.16	37.88	59.95	118.48	57.33	34.86	28.53	4.46	9.44	603.29	50.27
2008	52.42	37.87	54.45	74.71	34.50	23.04	75.75	49.57	61.53	13.27	7.15	13.50	497.77	41.48
2009	55.55	52.38	40.65	84.62	171.98	68.88	75.21	126.63	65.19	6.24	5.08	20.30	772.69	64.39
2010	30.08	57.83	104.01	51.08	103.51	49.30	66.48	65.86	69.65	25.38	2.63	9.55	635.37	52.95
2011	31.85	97.08	47.32	83.61	44.67	132.90	71.80	73.10	66.73	23.36	4.90	7.24	684.56	57.05
2012	45.94	54.40	47.66	47.24	41.99	113.71	82.60	67.37	25.55	10.09	4.04	9.54	550.13	45.84
2013	41.36	38.54	95.95	56.95	87.84	117.02	75.15	50.65	24.59	7.76	5.73	30.09	631.63	52.64
2014	29.76	37.42	40.08	109.48	93.73	59.73	142.13	28.25	33.80	17.41	2.50	4.15	598.45	49.87
2015	34.36	60.68	76.29	19.84	131.02	138.29	81.62	16.15	38.39	10.37	0.85	24.79	632.65	52.72
2016	34.84	24.73	53.27	44.53	42.78	57.36	87.45	60.54	47.88	15.15	2.14	6.15	476.83	39.74
2017	15.91	39.62	97.24	85.41	67.07	55.20	19.44	40.21	16.89	21.06	1.73	5.96	465.74	38.81
2018	31.57	95.90	40.31	40.23	29.30	50.73	73.85	52.28	65.46	15.17	2.74	31.70	529.24	44.10
2019	75.15	68.14	92.64	94.20	116.87	71.98	79.68	52.68	66.67	8.83	4.31	35.47	766.62	63.88
2020	51.34	23.77	103.17	93.89	37.61	15.12	106.06	61.50	18.48	15.30	1.77	10.62	538.62	44.89
2021	21.63	27.63	39.14	72.01	64.27	43.55	57.83	61.80	50.10	15.96	1.50	8.67	464.11	38.68
2022	34.87	25.96	66.00	39.27	46.95	29.28	66.15	45.93	36.36	7.40	5.13	8.69	411.99	34.33
sum	901.36	1060.90	1505.77	1901.67	1762.48	1465.88	1600.86	1313.11	1119.79	365.69	86.77	350.37		
average	39.19	46.13	65.47	82.68	76.63	63.73	69.60	57.09	48.69	15.90	3.77	15.23	584.12	

Table 43. Air temperature of the Souk Ahras region in the period from 2000 to 2022(Appendices)

Years	Sept	Oct	Nov	Dec	Jan	Feb	Mar	Apr	May	Jun	July	Aug	Average
2000	21.94	15.46	12.40	9.04	4.67	7.78	11.06	14.83	20.10	21.45	26.53	26.45	15.98
2001	21.59	20.31	11.41	6.49	7.94	7.23	14.29	12.88	17.84	23.73	27.02	26.46	16.43
2002	20.34	17.77	12.06	8.81	5.87	8.44	11.43	14.04	18.65	24.73	25.23	23.97	15.95
2003	20.92	18.44	11.80	6.89	6.87	5.91	9.72	13.87	17.98	24.41	28.15	27.46	16.04
2004	20.62	19.79	9.72	7.68	6.83	9.03	10.66	12.26	15.10	20.79	25.06	25.90	15.29
2005	20.32	17.21	11.86	6.29	4.56	4.32	10.03	13.39	19.49	23.11	26.79	24.29	15.14
2006	21.56	18.74	12.52	8.36	4.90	6.57	10.80	15.84	20.10	23.99	26.23	24.96	16.21
2007	21.78	16.69	10.23	6.96	8.45	8.94	9.21	13.00	17.48	23.73	26.04	26.09	15.72
2008	21.54	16.80	10.21	6.59	7.11	8.09	9.99	14.14	18.17	21.62	27.00	26.39	15.64
2009	20.32	15.48	11.97	10.22	6.84	6.51	9.29	11.30	17.93	23.23	28.03	26.07	15.60
2010	20.92	16.62	11.71	8.54	8.00	9.34	11.18	14.44	15.77	21.97	26.23	25.63	15.86
2011	22.53	15.81	12.00	7.71	7.40	6.61	9.42	14.38	16.71	20.95	25.89	26.27	15.47
2012	21.64	18.44	13.85	8.02	6.13	3.86	10.15	13.73	18.23	25.76	27.52	28.38	16.31
2013	21.11	20.55	10.73	7.24	7.03	6.06	11.49	14.92	17.01	21.09	25.72	24.81	15.65
2014	23.96	18.36	13.99	7.69	7.97	8.89	8.74	14.04	17.25	22.54	25.63	26.74	16.32
2015	21.99	17.72	11.55	7.87	6.35	5.84	9.48	14.54	19.26	22.34	27.25	26.03	15.85
2016	21.09	19.04	12.66	9.34	8.67	9.60	10.17	15.86	18.26	22.83	26.24	24.88	16.55
2017	21.59	15.99	10.60	6.85	5.25	9.50	12.07	13.83	20.46	24.92	27.74	28.27	16.42
2018	22.42	16.00	11.45	8.54	8.71	6.99	11.17	15.03	16.94	22.03	28.69	23.63	15.97
2019	22.12	17.44	10.76	9.57	5.87	6.59	9.73	12.92	15.25	25.47	28.07	27.19	15.92
2020	21.03	16.26	13.65	8.30	7.19	10.16	10.60	14.55	20.15	22.93	26.55	27.47	16.57
2021	24.68	16.14	11.59	8.20	8.55	11.06	10.28	14.30	19.96	25.84	28.42	29.01	17.34
2022	24.42	19.63	13.71	11.73	5.98	8.56	10.28	13.87	19.59	27.73	28.64	26.90	17.59
Average	21.76	17.60	11.85	8.13	6.83	7.65	10.49	14.00	18.16	23.36	26.90	26.23	

Table 44. Precipitation of the region of Souk Ahras from 2000 to 2022 (Appendices)

Years	Sept	Oct	Nov	Dec	Jan	Feb	Mar	Apr	May	Jun	July	Aug	average
2000	39.30	68.06	26.42	67.67	22.63	20.57	29.78	36.34	135.36	32.82	4.70	9.49	41.10
2001	74.64	28.21	35.52	36.25	81.13	36.15	35.68	32.94	67.33	8.30	4.39	7.76	37.36
2002	28.35	33.70	100.85	75.63	26.39	28.16	51.22	42.14	31.92	17.72	31.34	46.44	42.82
2003	64.38	65.62	43.20	157.23	185.97	71.69	35.07	94.33	53.37	15.96	6.07	8.48	66.78
2004	35.64	36.99	102.13	138.64	56.61	24.15	76.08	57.19	67.46	44.30	5.60	20.40	55.43
2005	23.19	38.04	26.10	97.63	40.51	57.86	37.34	63.61	16.65	27.22	13.13	13.51	37.90
2006	23.23	39.92	27.38	97.66	125.74	41.81	35.99	47.66	65.90	14.70	16.10	15.98	46.01
2007	45.12	55.87	39.67	75.68	32.83	45.30	98.55	67.04	40.45	29.35	6.42	10.88	45.59
2008	65.55	37.48	34.04	61.82	31.21	16.54	58.05	48.10	62.19	17.53	10.49	17.54	38.38
2009	69.41	48.64	29.44	64.06	158.34	45.49	58.74	157.68	65.36	6.70	11.81	20.80	61.37
2010	38.79	48.08	85.59	33.27	97.51	37.01	52.52	80.17	64.97	23.13	11.40	10.57	48.58
2011	28.85	93.78	36.42	65.75	44.68	114.41	61.42	66.10	75.53	22.85	12.50	7.74	52.50
2012	50.59	67.31	35.17	26.03	58.19	86.82	88.94	61.80	30.79	10.91	10.66	13.42	45.05
2013	40.40	42.37	60.24	55.94	69.76	69.46	63.57	53.74	25.91	8.59	12.70	25.04	43.98
2014	36.90	45.21	45.39	68.28	92.76	52.63	107.56	23.70	38.79	18.75	6.35	6.01	45.19
2015	45.85	59.25	63.93	14.74	108.09	120.95	68.16	15.80	38.73	14.97	4.70	32.72	48.99
2016	36.17	33.90	46.56	47.16	42.58	37.87	90.26	56.37	55.19	17.36	4.27	5.89	39.47
2017	16.68	48.59	72.66	56.67	62.75	41.88	22.74	45.28	27.49	23.92	6.29	5.37	35.86
2018	33.44	105.72	35.41	41.02	25.82	44.03	66.15	52.10	67.49	21.96	6.68	30.27	44.17
2019	62.73	50.39	68.40	71.78	94.53	61.50	78.56	54.73	70.72	8.85	7.25	33.89	55.28
2020	40.51	28.46	71.96	83.00	37.76	12.49	83.80	61.19	22.83	20.16	4.44	12.39	39.92
2021	21.09	37.35	25.14	44.85	47.01	40.96	59.63	56.79	48.91	16.51	5.26	9.04	34.38
2022	38.63	25.64	43.98	30.42	49.24	22.86	74.65	53.63	33.10	11.51	8.74	10.50	33.58
average	41.71	49.50	50.24	65.70	69.22	49.16	62.37	57.76	52.46	18.87	9.19	16.27	

Table 45. Air temperature of the region of Tebessa from 2000 to 2022 (Appendices)

Years	Sept	Oct	Nov	Dec	Jan	Feb	Mar	Apr	May	Jun	July	Aug	Average
2000	20.83	13.86	10.50	7.27	3.12	6.08	9.92	14.06	18.83	21.02	25.93	25.05	14.71
2001	20.11	18.39	9.70	4.86	6.04	5.65	13.53	12.68	17.76	23.67	26.91	25.55	15.40
2002	19.30	15.81	10.04	6.79	4.48	7.22	10.38	12.64	17.47	23.20	25.25	23.39	14.66
2003	19.80	17.40	10.02	5.10	4.82	4.01	7.99	12.32	17.17	22.84	27.33	25.60	14.53
2004	18.93	18.69	8.38	5.81	5.25	7.90	9.45	11.54	14.07	20.28	24.50	25.20	14.17
2005	19.88	15.27	9.88	4.07	3.22	3.03	9.20	12.77	19.62	22.04	26.96	24.00	14.16
2006	19.32	17.16	10.40	6.24	2.88	4.91	10.00	15.23	18.86	22.13	24.96	24.23	14.69
2007	20.40	15.52	8.90	5.29	6.81	7.37	7.76	11.30	16.86	23.00	25.08	25.08	14.45
2008	20.51	14.65	8.12	4.36	5.30	6.27	9.11	13.72	17.46	20.92	26.49	25.36	14.35
2009	18.66	13.90	10.64	8.24	4.99	4.77	8.18	10.07	16.34	22.66	27.02	24.87	14.19
2010	19.68	14.62	9.55	6.96	6.08	7.78	10.64	13.89	15.86	22.05	25.53	25.58	14.85
2011	21.69	13.95	9.88	5.90	5.88	4.89	7.39	13.34	15.42	20.45	25.70	24.95	14.12
2012	20.33	17.18	11.95	6.40	4.31	2.08	8.37	12.80	17.64	24.94	27.03	27.14	15.01
2013	20.02	18.39	8.99	5.64	5.49	4.77	10.72	14.33	16.79	21.09	24.83	23.53	14.55
2014	22.78	17.21	12.04	5.75	6.06	7.27	7.15	13.58	17.14	21.50	25.70	26.48	15.22
2015	21.03	16.25	10.01	6.65	4.87	4.19	8.10	14.02	18.93	21.73	25.84	24.68	14.69
2016	19.88	17.72	10.72	7.32	7.09	8.05	8.99	15.35	17.84	22.66	25.55	24.21	15.45
2017	20.68	14.31	9.15	5.06	3.17	7.73	10.71	12.61	19.20	23.48	26.27	26.70	14.92
2018	21.02	14.07	9.76	7.42	7.11	5.39	10.15	13.81	16.15	21.34	28.52	22.07	14.73
2019	21.05	15.77	8.63	7.92	4.17	4.94	8.55	12.09	14.88	24.98	27.08	26.16	14.69
2020	19.99	15.12	11.59	6.49	5.57	9.31	9.19	13.11	19.47	22.23	25.24	26.71	15.34
2021	23.63	14.88	9.76	6.69	6.80	9.21	8.74	13.63	19.92	25.76	28.00	28.03	16.25
2022	23.09	17.63	11.91	10.12	4.78	7.38	8.19	12.62	18.52	26.73	27.30	25.76	16.17
Average	20.55	15.99	10.02	6.36	5.14	6.10	9.24	13.11	17.49	22.64	26.22	25.23	

Table 46. Precipitation data of Tebessa from 2000 to 2022 (Appendices)

Year	Sept	Oct	Nov	Dec	Jan	Feb	Mar	Apr	May	Jun	July	Aug	average	sum
2000	37.06	32.62	15.07	19.98	8.74	8.55	23.21	26.61	66.65	34.72	7.39	10.31	24.24	290.90
2001	66.08	23.23	15.21	14.59	21.47	11.50	20.22	13.43	46.52	8.25	7.86	8.85	21.43	257.22
2002	25.92	28.48	62.46	27.98	9.20	11.19	17.57	24.90	30.97	22.45	23.33	45.35	27.48	329.79
2003	52.42	57.29	26.61	71.29	54.72	23.36	26.59	68.45	28.26	22.57	7.01	11.77	37.53	450.34
2004	31.76	25.49	53.49	41.75	14.69	8.20	46.36	36.63	24.13	53.56	11.78	31.58	31.62	379.42
2005	35.37	45.85	24.62	49.78	10.88	16.61	23.94	29.05	14.94	31.25	7.65	19.86	25.82	309.81
2006	37.29	31.72	14.84	45.34	31.81	16.45	13.81	47.84	38.58	23.28	12.32	18.30	27.63	331.59
2007	58.91	24.44	11.93	30.05	12.69	21.70	48.17	72.71	27.95	32.45	9.86	20.59	30.95	371.45
2008	75.62	39.43	14.26	27.81	11.69	7.10	25.31	26.59	35.38	22.84	13.14	22.32	26.79	321.48
2009	85.22	18.51	12.27	18.90	70.88	10.65	24.89	86.32	36.24	11.46	12.76	18.72	33.90	406.84
2010	49.32	37.56	55.12	17.24	28.26	11.50	22.48	60.54	26.73	24.33	13.00	12.24	29.86	358.32
2011	21.32	52.89	17.18	18.62	12.45	33.76	38.15	37.52	41.06	27.23	17.26	14.69	27.68	332.15
2012	38.57	45.88	19.29	7.76	19.59	21.82	51.36	42.06	23.86	13.05	8.19	18.17	25.80	309.60
2013	71.96	39.14	24.94	30.16	20.38	12.02	24.49	31.29	13.23	10.66	15.13	17.23	25.89	310.64
2014	41.12	30.98	36.86	16.80	19.61	19.97	38.57	17.66	22.46	24.89	8.83	11.35	24.09	289.12
2015	55.74	37.48	25.25	8.05	25.17	38.00	40.54	11.64	16.69	28.81	5.76	58.58	29.31	351.72
2016	46.02	35.04	22.23	44.81	12.00	10.95	41.05	42.26	40.66	14.33	3.25	10.41	26.92	323.01
2017	25.72	35.46	28.74	14.22	15.44	16.69	20.78	42.63	24.11	21.39	8.70	10.04	21.99	263.93
2018	37.77	76.96	23.99	15.26	5.89	18.42	26.16	34.46	43.54	22.55	7.94	43.11	29.67	356.04
2019	59.56	26.98	33.69	25.59	15.25	20.28	62.85	38.64	38.05	10.76	9.71	45.04	32.20	386.39
2020	45.77	20.75	22.27	27.55	8.90	5.92	53.00	32.50	17.41	31.12	9.33	10.19	23.73	284.70
2021	18.26	31.46	11.39	12.08	9.96	13.59	23.94	27.68	24.95	16.01	4.82	21.82	18.00	215.99
2022	56.24	13.93	19.99	11.58	15.53	13.98	46.19	30.59	18.78	19.64	9.76	18.47	22.89	274.68
sum	1073.03	811.56	591.72	597.20	455.20	372.22	759.64	882.02	701.15	527.59	234.78	499.02		
Average	46.65	35.29	25.73	25.97	19.79	16.18	33.03	38.35	30.48	22.94	10.21	21.70		

Table 47. Air temperature of the Khenchela region from 2000 to 2022 (Appendices)

Years	Sept	Oct	Nov	Dec	Jan	Feb	Mar	Apr	May	Jun	July	Aug	average
2000	20.35	13.20	9.66	6.80	2.97	6.06	9.67	13.81	18.88	20.88	25.98	24.79	14.42
2001	20.69	18.32	8.83	4.65	5.45	5.16	13.15	12.40	17.36	23.61	26.99	25.38	15.17
2002	19.31	15.46	9.12	6.27	4.37	6.88	10.00	12.18	17.56	23.17	25.17	23.40	14.41
2003	19.47	16.44	9.20	4.34	3.97	3.49	8.12	12.41	17.34	22.63	27.17	24.86	14.12
2004	18.97	17.67	7.65	4.90	4.57	7.39	9.37	11.10	13.65	20.23	24.24	25.10	13.74
2005	19.60	15.34	9.33	3.70	2.59	2.20	8.95	12.44	19.21	21.86	26.95	24.24	13.87
2006	18.80	17.00	9.94	5.41	2.47	4.39	9.57	14.88	18.84	22.24	24.89	24.39	14.40
2007	20.25	14.96	7.97	4.43	6.27	6.96	7.46	11.42	16.35	22.92	25.31	25.12	14.12
2008	20.26	14.14	7.12	3.64	4.87	5.99	8.88	13.46	17.42	21.10	26.49	25.14	14.04
2009	18.14	13.59	10.13	7.28	4.12	4.16	7.83	9.28	16.06	22.34	26.82	24.88	13.72
2010	19.55	14.37	8.85	6.13	5.37	6.98	10.24	13.55	15.11	21.82	25.30	25.45	14.39
2011	21.81	13.61	9.19	5.30	5.41	4.36	7.29	13.22	15.38	20.01	25.31	24.97	13.82
2012	20.02	16.68	11.11	5.71	3.75	1.40	8.42	12.16	17.58	24.79	27.04	26.99	14.64
2013	20.00	18.45	8.31	4.86	4.54	4.09	9.94	13.89	16.61	21.14	25.17	23.67	14.22
2014	22.63	16.67	11.25	4.81	5.48	6.61	6.99	13.40	16.99	20.87	25.72	26.47	14.82
2015	20.41	15.54	9.59	6.58	3.95	3.50	7.86	14.35	18.76	21.25	25.88	24.80	14.37
2016	20.14	17.46	9.90	6.63	6.63	7.42	8.41	14.88	17.58	22.47	25.50	23.99	15.08
2017	20.21	14.06	8.66	4.53	2.77	7.71	10.43	12.45	19.27	23.21	26.27	26.49	14.67
2018	20.80	13.52	9.03	6.80	6.20	4.52	9.14	13.56	15.64	21.25	28.37	21.58	14.20
2019	20.82	15.50	7.96	7.41	3.34	4.79	8.34	12.02	14.83	24.64	26.80	26.12	14.38
2020	20.09	15.09	11.08	5.99	5.27	9.14	9.17	13.05	19.25	22.30	25.43	26.67	15.21
2021	23.76	14.83	9.02	6.18	5.88	9.22	8.64	13.52	19.65	25.77	28.19	27.97	16.05
2022	22.87	17.42	11.40	9.28	4.51	7.16	8.13	12.63	17.97	26.68	27.23	25.65	15.91
average	20.39	15.62	9.32	5.72	4.56	5.63	8.96	12.87	17.27	22.49	26.18	25.14	

Table 48. Precipitation of Khenchela region during 2000 to 2022 (Appendices)

Years	Sept	Oct	Nov	Dec	Jan	Feb	Mar	Apr	May	Jun	July	Aug	average
2000	48.76	36.12	25.96	35.65	14.94	16.50	35.32	22.57	89.29	23.85	2.36	9.06	30.03
2001	52.91	25.67	38.60	18.08	73.00	21.21	25.97	23.86	54.84	6.89	5.49	11.01	29.79
2002	19.83	33.00	66.05	29.04	21.23	22.71	31.10	28.75	24.36	15.74	16.68	53.35	30.15
2003	36.64	59.27	34.87	62.15	115.56	31.66	69.74	71.98	41.70	20.19	6.12	13.98	46.99
2004	44.97	32.00	106.35	95.36	34.85	19.10	74.45	54.69	58.96	52.32	6.72	25.77	50.46
2005	26.63	25.87	29.06	42.81	27.81	36.75	43.33	31.56	18.23	21.55	8.46	11.79	26.99
2006	32.89	26.71	36.17	64.04	60.26	41.11	23.04	48.98	78.11	22.36	11.58	11.76	38.08
2007	76.89	35.91	27.09	23.79	22.57	29.67	60.99	48.28	33.44	11.92	4.65	12.33	32.29
2008	47.34	47.27	28.54	38.17	19.11	13.10	48.76	23.79	71.08	16.33	19.34	30.32	33.60
2009	87.87	25.62	18.61	30.09	94.23	22.47	48.71	63.75	56.68	10.54	9.64	14.15	40.20
2010	31.72	35.81	54.45	22.56	50.69	24.05	46.41	51.31	45.81	28.84	6.39	10.30	34.03
2011	34.88	89.58	21.07	25.57	25.62	53.18	58.38	56.77	61.53	25.46	8.47	15.11	39.63
2012	21.11	33.00	37.37	11.03	32.12	48.41	62.18	36.67	28.75	15.49	4.08	12.67	28.57
2013	42.20	37.08	37.30	28.75	40.51	27.61	49.57	38.74	19.04	20.56	9.15	33.21	31.98
2014	36.03	24.27	30.45	25.01	30.07	29.35	80.86	23.11	36.06	25.93	2.41	8.34	29.32
2015	27.42	54.04	33.53	8.71	42.78	51.71	54.78	16.10	22.27	23.35	3.94	54.95	32.80
2016	27.11	19.71	37.82	16.07	23.72	20.54	47.34	57.28	50.14	14.85	3.91	9.64	27.34
2017	21.37	27.25	36.99	24.62	38.18	18.32	22.39	41.88	26.10	26.42	3.45	11.87	24.90
2018	31.01	72.06	17.90	10.14	13.64	23.34	56.61	43.92	73.59	16.12	5.96	44.61	34.07
2019	44.03	40.57	60.17	30.51	37.58	26.71	89.98	46.86	51.68	9.69	10.06	33.44	40.11
2020	24.98	23.82	23.29	36.87	17.07	11.73	78.72	39.63	38.99	20.27	4.57	8.28	27.35
2021	21.80	21.08	23.99	11.68	17.91	16.76	38.96	30.04	46.15	18.87	0.93	14.49	21.89
2022	33.75	17.24	24.53	19.24	16.84	27.10	48.64	40.56	27.23	12.02	12.82	17.11	24.76
	872.12	842.93	850.13	709.93	870.28	633.10	1196.21	941.08	1054.06	459.56	167.16	467.54	
average	37.92	36.65	36.96	30.87	37.84	27.53	52.01	40.92	45.83	19.98	7.27	20.33	











Figure 102. Cascade of Guelma highlights (Appendices)